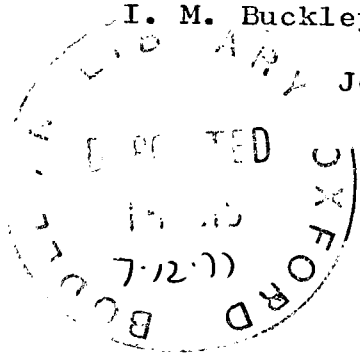
PROPERTIES OF LOW DISLOCATION DENSITY METAL CRYSTALS

I. M. Buckley-Golder, B.Sc., M.I.M.

Jesus College



A thesis submitted for the degree of Doctor of Philosophy
in the University of Oxford

September, 1977

PREFACE

This thesis describes the work carried out by the author in the Department of Metallurgy and Science of Materials, in the University of Oxford, from October, 1973, to September, 1977. The work included herein has not been submitted to any other University for any other degree and is original. However, where the work of others has aided the investigations it has been drawn upon freely and due acknowledgement is given.

Various sections of the thesis have been presented in the following journals and conferences:-

Chapter I	Journal of Crystal Growth, 1977 (in press)
Chapter III	Fourth European Crystallographic Meeting, Oxford, 1977
Chapter IV	Journal of Applied Crystallography, 1977 (in press)

Ian Buckley-Golder

Jesus College, Oxford

September, 1977

ACKNOWLEDGEMENTS

The author wishes to thank:-

Professor Sir Peter Hirsch, F.R.S., for the provision of Laboratory facilities and encouragement.

Dr. C. J. Humphreys for his great kindness and encouragement.

Dr. B. K. Tanner (University of Durham) for his interest in the work carried out; for very kindly providing portions of his very valuable time on the Daresbury Synchrotron, NINA, thus allowing the experiments in Chapter IV to be performed; and for his enthusiastic encouragement.

Dr. D. K. Saldin for leaving the much researched world of electron diffraction theory, grasping X-ray diffraction theory, and helping to generate the results discussed in Chapter III.

Dr. P. Rez for imparting to the author an insight into the mechanics of computing: for his help in streamlining the computer work presented in Chapter II.

Dr. J. Wilks (Clarendon Laboratory) for providing the diamond crystal briefly discussed in Chapter III.

Mr. G. Dixon-Brown, Mr. G. Norton and Mr. R. Cripps for maintaining the troublesome X-ray apparatus.

Mr. D. Tansley for so ably manufacturing bits of apparatus to the author's designs; for help in maintaining the Elliot GX6 generator and for many interesting conversations.

Mr. J. Short for his wit, help and interest in the experimental problems of crystal growth.

Mr. A. Fairless, Mr. D. Penfold, Mr. J. Stead and Mr. S. Miles for constructing apparatus and for their banter.

Mr. A. McKnight and Mr. S. Bowers for their photographic assistance and professionalism!

The Science Research Council for a grant from October, 1973, to October, 1976.

Metals Research Ltd., Royston, Herts., for a grant from October, 1976, to October, 1977.

My dear Mother and Father for paying for the final thesis costs and my sister Delphine for her effervescent nature.

Stephen Malcolm and John Aggleton for keeping the real values of life in perspective during many happy hours in the "Rose and Crown", North Parade!

Stephen and Christine Druce for all their help, kindness and true friendship.

Carine Slade for typing this work and putting up with a seemingly endless series of telephone calls.

And finally, to dearest Debs for her inimitable help, kindness, affection and friendship during the latter stages of thesis production.

ABSTRACT

This thesis describes the growth, X-ray diffraction assessment and tensile deformation properties of dislocation-free copper single crystals. As such it has been possible to conveniently section the work carried out into these three main areas within this thesis. Consequently, each chapter may be read almost independently of the others with references and further work suggestions being incorporated at the end of each chapter. This format, it is felt, does not disjoint the work: rather, it enables the central theme (i.e. the title of this thesis) to be developed in a much more continuously clear way than is normally apparent in a thesis where conclusions, further work suggestions and references are not drawn together until the end of the volume.

Chapter I opens with a brief outline of the crystal growth methods which could have been used to produce low dislocation density ($<10^6 cm/cm^3$) crystals by utilising the three fundamental phase transitions, i.e. solid to solid, vapour to solid and liquid to solid. The Czochralski method is then discussed in detail since it was used by the author to produce dislocation-free copper single crystals. The technological problems in obtaining such crystals are extensively enumerated and solutions presented. For instance, melt surface vibrations were eliminated by using a continuous flow of cooling water, by standing the complete crystal puller on a bed of foam, and by rigidly clamping the R.F. coil. It is emphasised that these technological problems must be solved before the scientific aspects of the growth of dislocation-free crystals can be studied. It is further

shown that the author's modified crystal growing technique can be reliably used to grow dislocation-free crystals of copper each time, providing adequate care is taken over growth rates (≈1.2 cm/hr); specimen shape (a long thin "double-neck" must precede the required crystal to eliminate dislocations propagating from the seed and to act as a heat flow resistance); and crystal cooling rates (a long "tail" allowed the crystal to reach the ambient temperature slowly thereby minimising dislocation by thermal stresses and/or vacancy condensation). In the future, it is suggested, an automated crystal pulling system would be advantageous and a study of crystal growth in a synchrotron X-ray beam could be potentially definitive experiment on crystal growth.

Chapter II looks at the theoretical aspects of Czochralski crystal growth with the aid of a new model which has been analysed on the Oxford University Computer. The model assumes a crystal-neck-seed configuration to be "sitting" on a liquid and examines the influence of geometric changes of the seed-neck-crystal and of radiation changes on the temperature gradients, primarily at the growth front. Four elements were chosen for study in this way: Si, Ge, Ag, Cu, i.e. four elements which have been grown dislocation-free. It was found that the seed size and shape played a small part in determining the interfacial temperature gradients, $DT_c(0)$, of all the elements. The neck, however, could have a marked influence on $DT_c(0)$ values in metals but not so much in semiconductor crystals. By geometric control alone it was found that the best way to reduce $DT_c(0)$ values was to grow a large diameter crystal.

The influence of radiation losses was found to be marked for semiconductor crystals but not for metal crystals. Finally, it is concluded that to minimise $DT_c(0)$ values then the seed and neck must be long and thin and the crystal fat. These results fit in well with experimental knowledge. Further work to be carried out could consider the influence of a varying ambient temperature and convective heat losses on the interfacial temperature gradients.

Chapter III is concerned with the interaction of X-rays with perfect crystals. The Lang-Borrmann X-ray topography technique is examined, and the experimental methods used to obtain X-ray topographs taken throughout this work are discussed. The major part of the chapter takes up the discussion of the theoretical interaction of X-rays with a perfect crystal set to diffract such X-rays. It is demonstrated that for a plane-wave incident on a cylindrical crystal, for the boundary condition to be satisfied the dispersion surface tie-points are displaced as the crystal traverses the incident X-ray beam. Thus the crystal wave-vectors no longer exactly satisfy the Bragg condition. This effect was never unambiguously monitored experimentally because of the incident beam divergence. It is suggested that a future study could consider this problem in more detail.

The Takagi-Taupin-Uragami generalised X-ray diffraction theory is reviewed and then used to calculate the intensity in the diffracted beam of a traverse topograph from a perfect cylindrical copper crystal. This computer simulation is also compared to an experimental condition. In both cases it is

found that the Bragg surface of the crystal produces a very intense reflection whilst the remainder of the crystal gives a much reduced diffracted intensity in comparison. This asymmetric profile is interpreted in terms of absorption mechanisms which are strong at the centre of the crystal but not at the surface. The general agreement between theory and experiment is considered to be good although a few discrepancies arose, e.g. the lateral extent of the Bragg surface peak was found to be larger for the experiment than for the theory. Continued research in this area must explore further these small discrepancies; and it is suggested that a possible line of future study would be to examine theoretically and experimentally the X-ray diffraction from dislocation-free cylindrical crystals which possess low absorption coefficients (e.g. aluminium, silicon) for harder radiations (e.g. $M_{oK\alpha_1}$, $Ag_{K\alpha_1}$). It should then be possible to produce interference fringes and then it should be possible to examine the effects of a strain gradient on fringe spacing and visibility.

Chapter IV sets out to discuss the tensile deformation behaviour of $[\bar{1}\bar{2}3]$ growth axis, dislocation-free, chromium plated copper single crystals. This is done using the results from two sets of coupled experiments: an Instron deformation study and a synchrotron deformation investigation. It is first shown that chromium plating can destroy the perfection of the crystal unless care is exercised over plating temperatures and times. It was finally found that after plating for 10 seconds at 55C ($\approx$1 μm of Cr deposited) that there was no indication of lattice dislocation. The stress-strain curve of a chromium plated

dislocation-free copper crystal (Cr thickness ≥ 1 μm) is shown to exhibit a yield point commensurate with that for a non-plated, dislocation-free copper crystal, i.e. ≈ 90 g/mm^2. The work hardening curve is shown to be comprised of three distinct regions: an initial rapid work hardening rate; a transitionary work hardening rate; and a stabilised work hardening rate up to a shear strain of 6%. In straining the crystal through these regions the work hardening rate progressively decreased.

For a plated crystal which is dislocation-free initially it is shown that serrations in the flow curve occur, whilst for all other crystals these are shown to be absent. Such serrations are argued to occur by a source suppression and new source operation mechanism during the early deformation stages ($\approx$1% shear strain), and then by a crack formation mechanism at the copper-chromium interface during the later stages of deformation. The initial work hardening rates ($\approx$18 kg/mm^2) were found to be independent of coating thickness (0.5 μm and 1 μm) but in the latter two regions the thicker coating imparted a higher work hardening rate to the crystal than the thinner layer, e.g. for a 0.5 μm chromium layer the work hardening rate was ≈ 1.65 kg/mm^2 in region iii and for a 1 μm chromium layer it was 2·97 kg/mm^2 in region iii. It is tentatively suggested that the chromium layer affected mobile dislocation motion rather than dislocation generation.

The synchrotron work produced no evidence to support the argument that dislocation motion up the elastic line took place. Yielding was found to occur at a stress level similar to that measured in the Instron work. The complex stress

system imposed by the deformation jig and the lack of resolution rendered it impossible to decide where the dislocation sources were located. Further increases in the load on the crystal produced double slip and this was argued to prematurely occur because of the combination of torsion, bending and tension which the crystal experienced. Certain interfacial dislocation activity was registered but this was not readily analysed in terms of surface sources. The yielding behaviour was inhomogeneous and appeared to be remote from the few slip bands induced by specimen transport. After yielding evidence was found for dislocation pile-up at the centre of the crystal. It is pointed out that future studies should use a better design of deformation jig so as to apply only a tensile stress to the crystal. Plating thickness and specimen size could be further explored.

CONTENTS

		Page Number
PREFACE		i
ACKNOWLEDGEMENTS		ii
ABSTRACT		iv
CONTENTS		x
CHAPTER I:	THE EXPERIMENTAL ASPECTS OF LOW DISLOCATION DENSITY CRYSTAL GROWTH	1
CHAPTER II:	THEORETICAL MODELLING OF CZOCHRALSKI CRYSTAL GROWTH	52
CHAPTER III:	ASSESSING THE DEFECT DENSITY OF LOW DISLOCATION DENSITY ($<10^6/cm^2$) CRYSTALS ABOVE A 1 μm RESOLUTION LIMIT	84
CHAPTER IV:	A STUDY OF THE TENSILE DEFORMATION PROPERTIES OF CHROMIUM PLATED $[1\bar{2}3]$ GROWTH AXIS DISLOCATION-FREE COPPER CRYSTALS	128

CHAPTER I

THE EXPERIMENTAL ASPECTS OF LOW DISLOCATION DENSITY CRYSTAL GROWTH

List of Symbols Used in this Chapter

X	= Fraction of recrystallised material
B, n^1	= Constants
t	= Time
K, K_p	= Reaction rate constant
C_H	= Solubility of a gas in a metal
P	= Partial pressure
X_t	= Mean diffusion distance
D	= Diffusion coefficient

CONTENTS

		Page Number
	Contents	1
1.1	Introduction	3
1.2	Crystal Growth Methods	4
1.2.1	Solid → Solid Crystal Growth	5
1.2.2	Vapour → Solid Crystal Growth	7
1.2.3	Liquid → Solid Crystal Growth	10
1.2.3 (i)	The Bridgman-Stockbarger-Stöber Method	11
1.2.3 (ii)	The Kyropoulos Method	14
1.2.3 (iii)	Floating Zone Crystal Growth	15
1.2.3 (iv)	The Pedestal Method	18
1.2.3 (v)	Verneuil Crystal Growth	19
1.2.3 (vi)	Czochralski Crystal Growth	20
1.3	The Growth of Dislocation-Free Copper Crystals	21
1.3.1	Preamble	21
1.3.2	The Basic Crystal Growing Equipment	22
1.3.3	The Basic Experimental Technique	25
1.3.4	The X-ray Topography Examination Method	29
1.3.5	The X-ray Topography of the Crystals Grown by the Basic Experimental Method	31
1.3.6	The Modified Experimental Technique	33
1.3.6 (i)	The R.F. Susceptor	33
1.3.6 (ii)	The R.F. Susceptor Liner	34
1.3.6 (iii)	The Growth Atmosphere	35
1.3.6 (iv)	Melt Surface Vibrations	38
1.3.6 (v)	The Afterheater	39

1.3.6 (vi)	Crystal Rotation	40
1.3.6 (vii)	"Double-Necking"	41
1.3.6 (viii)	The "Cooling Tail"	42
1.4	Conclusions	44
1.5	Further Work Suggestions	44
	References	47

'As Frank has written (Crystal Growth p.54) "The completely perfect crystal will not grow in any circumstance: the conditions which would cause it to grow would also soon make it imperfect". In fact, it could not exist except as an abstraction, for a perfect crystal would have to be infinite in all dimensions. Any surface forces would mar its perfection.'

Dame Kathleen Lonsdale

"Fifty Years of X-ray Diffraction", Ed. by P. P. Ewald, p.233

1.1 Introduction

Dame Kathleen Lonsdale's reiteration and extension of Frank's seemingly definitive philosophical statement about crystal growth is no less true from the purists' viewpoint today than it was in 1962 when she was writing. It is indeed true that a finite crystal (a periodically repeating three dimensional structure of atoms) will experience boundary forces which will tend to relax the three dimensional structure in size and shape locally; hence, the finite crystal, irrespective of internal considerations will not be perfect. To be perfect it must be boundless, therefore: this is conceivable but hardly likely. Likewise, for a perfect crystal to grow it must possess a boundary onto which atoms may condense: but the possession of a boundary is a sign of imperfection in the crystal, and so the perfect crystal (not possessing a boundary) will not grow.

These apparently completely self-contained and cyclic arguments seem to destroy the original fundamental aim of this thesis: to grow, examine and study perfect crystals. Frank's and Dame Kathleen's statements were and are absolute and definitive: therefore, this cannot be a thesis about perfect crystals. Yet, as Dame Kathleen added in her rider to Frank's statement, "..... it (the perfect crystal) could not exist except as an abstraction .....": the perfect crystal is therefore separated from matter.

Matter, however, is at the inescapable centre of this thesis. In particular this is a thesis about the second nearest cousin to the perfect crystal: the dislocation-free crystal.

Such a crystal is the nearest it has yet been possible to approach the perfect crystalline state. The nearest cousin to the perfect crystal would be the dislocation-free crystal at absolute zero, at which point the vacancies too would be removed.

Whilst the perfect crystal does not exist and will not grow, the dislocation-free crystal will grow and does exist. In consequence it is the first aim of this chapter to present the ways in which low dislocation density and dislocation-free crystals have been grown in the past. And it is the second aim of this chapter to present a detailed account of the growth of dislocation-free copper crystals by the author.

It will be shown that dislocation-free crystals of copper can be produced easily and on a repetitive basis provided adequate care is taken both prior, during and after growth: for it is the technological problems which all too often dictate the rate of advance of the science of crystal growth: and it is these technological problems which, when uncontrolled, turn the science into an art.

1.2 Crystal Growth Methods

There are three fundamental transitions which can be exploited to promote the growth of a crystal:-

Solid ——→ Solid (S→S)

Vapour ——→ Solid (V→S)

Liquid ——→ Solid (L→S)

Other, hybrid, changes may also be controlled to expedite crystal growth, e.g. the S→L→S→L .... mechanism of Pfann[1],

otherwise known as "zone-refining". These three transitions will now be treated in a little more detail with a view to determining the disadvantages and advantages of each. All the time the theme will be to investigate the ways in which low dislocation density crystals have been grown.

1.2.1 Solid → Solid Crystal Growth

In metallurgical terms solid → solid crystal growth falls under two main headings: recrystallisation and grain growth. The former of these two is dependent on deformation history; temperature of recrystallisation; time of recrystallisation; initial grain size; and composition. In practice the deformed material (strained ≈1-5%) to be recrystallised is heated to a temperature at which grain boundary motion can be rapid (usually $0.13T_M$ for pure metals and $0.5T_M$ for alloys, where T_M is the melting point of the material). In all probability adjacent grains will have vastly different dislocation densities (e.g. $10^{11}/cm^2$ in one and $10^6/cm^2$ in the other), and so the least dislocated crystal can grow into the most dislocated crystal with a consequent reduction in dislocation line energy. Hence, the internal energy of the crystal is reduced; this being the driving force for recrystallisation. The fraction (X) of the material which has recrystallised can be described by an Avrami[2] equation:-

$$X = 1 - \exp\left(-Bt^{nl}\right) \qquad (1.1)$$

where,

B, n^1 = constants
t = time

When n^1 lies between 1 and 2 one dimensional recrystallisation is argued to have operated, and when n^1 is between 2 and 3 then two dimensional recrystallisation is argued to have taken place.

Crystal growth rates (recrystallisation rates) can vary over a very wide range, e.g. from 0cm/hr for passive grains (pinned by impurities) to 600cm/hr for very glissile grains in highly pure metals. In the literature Minari[3] et al have produced metal crystals good enough for Borrmann x-ray topography (a dislocation density of $\approx 10^3/cm^2$ was necessary) by this method but only, "When the operation was successful ....". Other workers[4,5,6,7] produced aluminium single crystals with a very low dislocation density ($\approx 10^2$—$10^3/cm^2$) but none were ever completely free from line defects.

Consequently, solid state transitions are to be regarded as a last resort for the production of large (1cm x 1cm x 1mm) single crystals of metals with very low dislocation densities. The only advantage of recrystallisation methods is that a large, useful crystal can be surrounded at both ends by a complex of finer grains, thereby allowing easier specimen handling, e.g. for tensile deformation (see Minari[3] et al for a useful exposition of this method).

The second phenomenon, grain growth, was originally used by early researchers to produce very large single crystals from recrystallised metals. The driving force in this case was the reduction in grain boundary surface energy and so the internal energy of the crystal was accordingly diminished. A good example in this area is the work of Williamson and Smallman[8], who were able to grow single crystals of aluminium

and its dilute alloys (principal additions were 2% of Cu, Zn, Ag) 2' long, $\frac{1}{2}$" wide and 0.039" thick. Unfortunately in 1953 when this work was published there was no direct method of imaging dislocations, and so it is impossible to state whether low dislocation density crystals were produced too. The only indication is that if the original material was recrystallised then the dislocation density could have been low; hence, the final line defect density could have been very low indeed. A comprehensive review of the physical metallurgy of these two areas can be found in Christian's book[9] and Cotterill and Mauld's book[10].

1.2.2 Vapour→Solid Crystal Growth

Vapour to solid transitions normally produce low dislocation density ($\approx 100/cm^2$), very pure crystals. Metal crystal platelets have been grown by this method but the examples of large crystal growth are isolated[11,12]. Dislocation-free metal crystal whiskers have also been grown[13], but such small crystals ($\approx 1\mu m$ diameter) are not of interest here. Since the ratio of the density of atoms in the solid:vapour is large, however ($\approx 1:10,000$), growth rates are often slow ($\approx 0.6\mu m/min$); the control of both equipment and crystal shape can be very difficult; and a seed is normally needed. But vapour growth does find wide acceptance in many electronic micro-processing areas where epitaxial crystal layers are required which are thin (a few hundred microns at most), of high purity and low defect density, e.g. photocathodes made from GaAs/GaAlAs/GaAs sandwiches.

Two intrinsic vapour growth methods are available: the first involving mass transport whereby two or more gases are reacted together over a substrate at high temperatures (to accelerate gas-gas and vapour-substrate reaction rates) as shown in Fig. 1.1a. And the second method is to use sublimation, in which a solid is heated to a high temperature, sublimated, and then deposited on a single crystal substrate, Fig. 1.1b. Both versions of vapour growth depend on a significant amount of surface diffusion (see Sears's article[14] for an account of this phenomenon) taking place, i.e. the surface layer of the crystal may be amorphous by the immediate addition of the depositing atoms, and so atomistic diffusion is required to order the surface.

A typical example of the first variation is:-

$$SiHCl_3 + H_2 \longrightarrow Si + 3HCl \qquad (1.2)$$

The reaction rate can be easily controlled by the partial pressures (P) of the reactants and products from the expression:-

$$K_p = \frac{P_{SiHCl_3} \cdot P_{H_2}}{P_{Si} \cdot P^3_{HCl}} \qquad (1.3)$$

Where K_p is the reaction rate constant.

Obviously, to promote the forward reaction the partial pressure of the HCl must be minimised, and this is best done by flushing the gases through reasonably quickly so that the partial pressure of the HCl does not exceed the equilibrium value. Silicon doping can be easily effected by adding BCl_3 or PCl_3 to the $SiHCl_3$.

Fig. 1.1 Vapour Growth Methods (V → S)

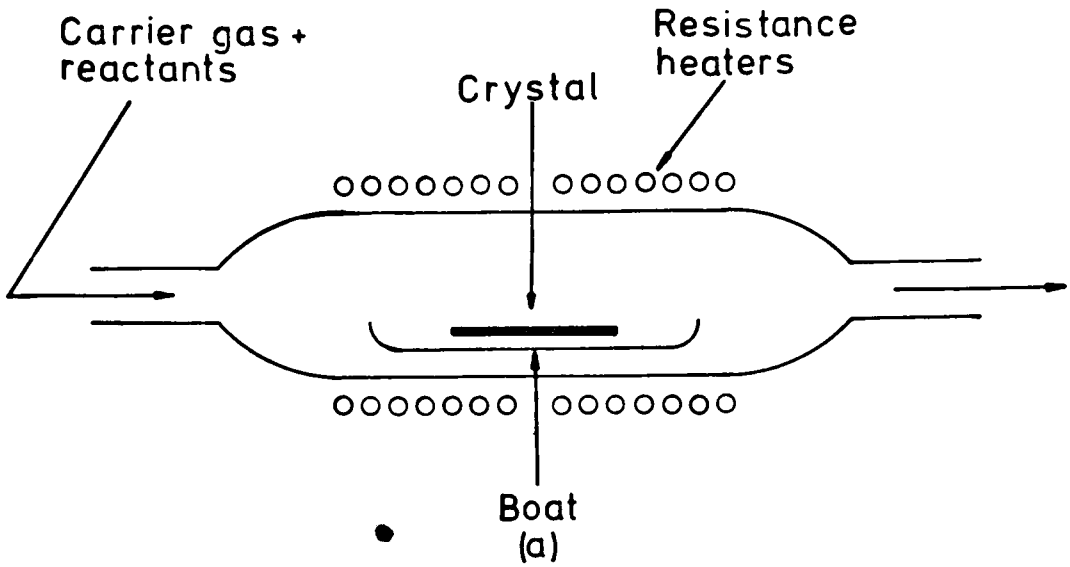
a. Mass Transport

Two or more gases are reacted over a substrate at a high temperature. Precipitation from the gas takes place causing the crystal substrate to grow

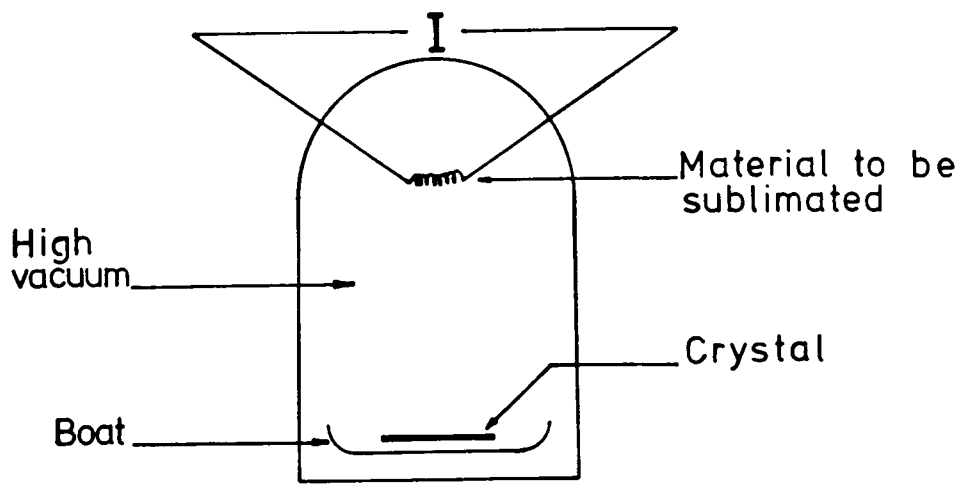
b. Sublimation

The material to be grown is sublimated by resistance heating under a high vacuum. Deposition on a seed crystal occurs producing crystal growth.

In both these cases layer compounds are possible


Carrier gas + reactants
Crystal
Resistance heaters
Boat

(a)


I
Material to be sublimated
High vacuum
Crystal
Boat

(b)

Experimentally, the apparatus for this vapour growth method is relatively rudimentary: plentiful sources of reagents are required; plus a resistance wound tube furnace in which to place the silica tube, seed crystal and boat. The resistance heating normally comes from a current carrying conductor laid into a ceramic embedding material (e.g. alumina), with the heat being partly dissipated in the crucible and charge, Fig. 1.1a. Typical furnace winding materials are Kanthal A-1(Fe + 22%Cr, 5.5%Al, 0.5%Co) which will operate to about 1300C; Kanthal Super ($MoSi_2$) which will go another 350C higher than Kanthal A-1; molybdenum (≈2370C maximum working temperature); and vitreous carbon for very high temperatures (≈3000C). Unfortunately, resistance heating may not always be completely reliable; for example, the elements may burn out because of local resistance increases which lead to hotspots. Therefore, new elements need to be commissioned slowly giving enough time for local resistance increases to anneal out. Oxidation of metal windings can also be a significant problem leading to premature failure. To reduce the incidence of breakdown by this fault the windings are often cooled with an inert (Ar) or a reducing (H_2) gas.

From Fig. 1.1b it would seem that vapour growth by sublimation methods is experimentally simple: but this is not the case since the experimental chamber must be clinically clean; a pressure of 10^{-5} Torr at least is necessary; and high current leads need to be fed into the chamber. Because vacuum vapour growth is needed multiple layers can be problematical. This is not an insurmountable problem, however, as many current leads and sublimants can be used: but inter-sublimate

contamination can occur. A typical example of crystal growth by this method is CdS[15]. In this example growth under a vacuum was very necessary for the following reasons:-

i. To reduce oxidation of the sublimated material - especially important for metals.

ii. To increase the rate of sublimation: the greater the partial pressure of the sublimate over the surroundings the greater the rate of sublimation.

iii. To increase the mean free path (m.f.p.) of the sublimated atoms (e.g. the m.f.p. at 10^{-6} Torr is 5000 metres[16]), which aids growth rates and reduces secondary ionisation.

Despite all of these drawbacks both methods of vapour growth have been greatly exploited to produce many good crystals. Exhaustive details of the processes can be found in reference 17.

1.2.3 Liquid → Solid Crystal Growth

All of the six methods in this category use the simple fact that when a liquid metal cools below its fusion temperature it is possible to produce a single crystal as a result. These six types are:-

i. Bridgman-Stockbarger-Stober[18]

ii. Kyropoulos[19]

iii. Float zone[20]

iv. Pedestal[21]

v. Verneuil[22]

vi. Czochralski[23]

All of these techniques have similarities; for instance, from Figs. 1.2, 1.3 and 1.4 it is clear that the crystals produced

are usually cylindrical and that seeding is often used to provide a desired orientation. Also, it is usually important to produce very large crystals, e.g. in the Czochralski method[23] silicon single crystals weighing 10 kg, with a length of 1 metre and a diameter of 10 cm are often grown[24]. Each technique will now be more thoroughly and critically reviewed.

1.2.3i. The Bridgman-Stockbarger-Stöber Method (BSS)[18]

Bridgman's version of this method was to fill a split mould refractory (e.g. Al_2O_3, graphite) with the material from which the crystal was to be grown. All contaminating gaseous species (e.g. O_2) were then evacuated and the whole charge melted by a resistance furnace, Fig. 1.2a. Crystal growth was activated by lowering the crucible down through the furnace so that heat would be lost, thus ensuring that of the one or two crystals nucleated at the sharp point one large crystal would grow. As shown in Fig. 1.2a it is also possible to melt only a portion of the charge by using a triangular furnace profile, thereby saving on furnace size and running cost. Additionally, a preferred orientation crystal can be grown by seeding the base of the crucible: in this case visibility of the solid seed must be maintained initially to ensure that it does not completely melt. Subsidiary furnace windings can also be used; to anneal out micro-segregation in the growth of alloys, for instance.

Stockbarger's variation of the basic Bridgman technique was simple: instead of moving the crucible he moved the furnace. The prime advantage of his apparatus was that

Fig. 1.2 Liquid ⟶ Solid Crystal Growth (L ⟶ S)

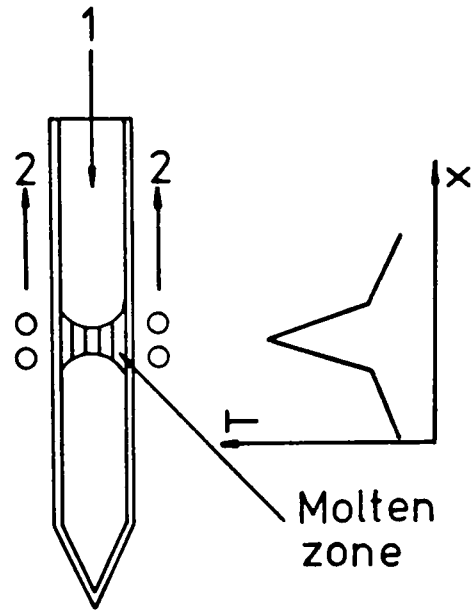
a. Bridgman -Stockbarger-Stöber (BSS)

A crucible containing the material to be crystallised is lowered through the hot zone of a furnace (Bridgman 1). Alternatively (a), the furnace could be raised over the crucible (Stockbarger[2]), or, the furnace temperature could be lowered with the whole molten charge inside (Stöber). In all cases large single crystals can be produced. Also, a small portion of the charge could be melted by using a triangular furnace profile (T = temp., x = dist.)

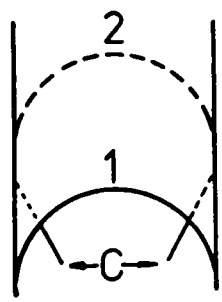
b. By using a highly convex growth face (1) secondary crystals (C) could be quickly grown out of the main crystal as the growth front moved forward. This is only if they occurred in the first place.

c. The Kyropoulos Method

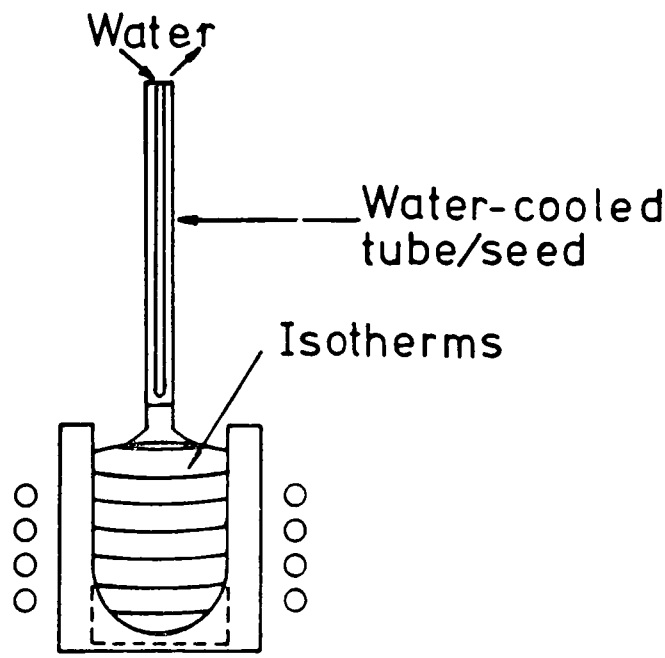
By dipping a water cooled seed or tube (with a sharp tip) into a melt large scale crystallisation could occur.


1
2
2
x
T
Molten
zone

(a)


2
1
C

(b)


Water
Water-cooled
tube/seed
Isotherms

(c)

secondary nucleation at the growth front, or ahead of the growing interface, could be reduced: in the Bridgman method such secondary nucleation was encouraged by melt vibrations from the lowering motor. Lately, highly convex solid-liquid interfaces have been used[25] so that any secondary crystals at the growth front will quickly grow out to the mould wall, Fig. 1.2b.

Both variations suffer from one major drawback: in the solid-liquid interface region, the cooling crystal and the liquid are always in contact with the crucible. In one respect this is advantageous because the grown crystal will always assume the inside shape of the crucible; hence, polyhedral crystals are feasible[26,27]. However, this attribute aside, it will always be difficult to completely eradicate the following three problems:-

i. Contraction stresses between the crucible and the solid crystal.

ii. Spurious growth events at the growth front (e.g. dislocations) arising primarily from the interaction between the irregular surface of the crucible and the solid-liquid interface.

iii. Contamination of crystal and liquid either by the crucible itself or by elements contained in its walls.

A very early and successful attempt was made to minimise (i) above by growing the crystals in open horizontal boats[28]. The obvious disadvantage of this approach was the lack of crystal shape control. The most notable compromise to all these problems for metals was put forward by Young and his co-workers[29,30,31] in the early to mid 1960's. Young's aim

was to produce very low dislocation density ($\approx 100/cm^2$) copper crystals with which to study initial work hardening behaviour and dislocation dynamics.

Young's group first chose a high purity starting material, i.e. 99.999%Cu, thus reducing the constitutional stresses which can be deleterious to perfection as the solute segregates or "bands" during growth. "Banding" can be regarded as a wavelength type fluctuation of the solute distribution as a crystal is grown. This can be caused by thermal fluctuations, incomplete liquid mixing, dislocation segregation (e.g. into sub-grain boundaries) and so on. Young's workers minimised crystal-crucible bonding by highly polishing the inside wall of the halogenated high purity graphite mould. Unidirectional heat flow was increased by placing a mullite sleeve around the crucible and growth took place by the Stockbarger method (purposefully to reduce vibrations) at 10^{-5} Torr; this latter measure reduced crystal contamination from the absorbed gaseous chemicals in the graphite. Furthermore, after growth the crystals were annealed either in hydrogen or at 10^{-6} Torr for periods of up to six weeks at 1075C. One further problem which Young faced was an impurity layer which floated on the top of the melt and which could give rise to secondary nucleation from the top free surface. This was solved by employing two crucibles connected by a narrow passageway: the charge was melted in the top half, ran down to the bottom half and left the impurity layer behind in the constriction. Growth then took place as normal in the bottom crucible.

Only by exercising such particular care was Young able to produce low dislocation density copper crystals. It must also be made clear that the density of the as grown crystals was approximately $10^4 - 10^5$ lines/cm^2, and only by annealing and subsequent slow cooling could the density be reduced further to $\approx 10^2$ lines/cm^2.

Work on other metals (Zn^{32} Mg^{33} Cd^{34} Al^{35}) using techniques very similar to, but not derived from, those of Young has been carried out and achieving a low dislocation density has met with some success. It must be added that a strong feature of all these studies was that the crystals were all cooled slowly ($\approx$5C/hr), thereby minimising dislocation multiplication stresses and to give vacancies enough time to diffuse to the only sink, i.e. the surface (otherwise vacancy clusters and loops can form). Further information on the BSS methods can be found in Brice's books[36,37].

1.2.3ii. The Kyropoulos Method[19]

This technique is a small step from the BSS methods. As shown in Fig. 1.2c the molten material to be crystallised was held at just above its melting point in a smooth-sided crucible. Secondary nucleation from the sharp corners at the bottom of the crucible was eliminated by machining the base into a hemisphere. A water cooled seed or tube (with a sharp point) was then lowered into the melt. At the seed crystallisation began (the melt temperature was sometimes reduced to induce this) and provided mechanical stability and thermal symmetry was maintained the whole melt would grow with the

orientation of the seed; or, in the case of the tube, randomly. In either case a very large single crystal was normally produced. Heat was usually provided by resistance or R.F. methods.

In theory there is no limit to the crystal size attainable. To take typical examples, Menzies and Skinner[38] have grown NaCl and KBr crystals 3" deep and 4" in diameter; Weller and Grandits[39] have grown large sodium tungsten bronzes (1" x 1" x 1"); and the author has grown copper crystals $1\frac{1}{8}$" in diameter and $1\frac{1}{2}$" long, which were later used for T.E.M. discs. Alloys can be a problem with this method because long annealing times may be necessary to redistribute the inhomogeneous spread of alloying constituents. Also, contraction stresses and contamination can be a problem, just as in the BSS methods; hence, dislocation densities are considered to be high although no systematic study has ever been carried out. In essence, therefore, the Kyropoulos method is very similar to the Stöber variation of the original Bridgman technique. Controlled solid-liquid interface motion is encouraged by lowering the temperature of a stationary growth system and not a moving one. Today, the Kyropoulos crystal growth technique has found little favour in the production of low dislocation density crystals. Such lack of use has stemmed from the greater attractions of the Czochralski and float zone methods. For further basic information the reader is directed to the limited available literature.

1.2.3iii. Floating Zone Crystal Growth[20]

This technique is an interesting combination of both sophistication and elegance, incorporating a number of novel

ideas. Dislocation-free silicon crystals have been produced[40] by a necking procedure (discussed later), and the only major requirement is that the surface tension of the material to be grown be high. An added minor requirement is that the solid-liquid vapour pressures must be low. Reasonably low dislocation density niobium crystals have also been grown from polycrystalline stock by Miltat[41], and so it is possible to consider the growth of good metal crystals by this means too.

Fig. 1.3a shows the system in outline. Within a high vacuum chamber ($\approx 10^{-5}$ Torr or better) a cylindrical (normally) rod of the material to be grown is held at either end by two chucks. A very narrow region of the rod is melted by a circular beam of electrons emanating from a cathode. Alternatively, a single turn R.F. coil can be used to heat the sample; in either case contamination-free heating can be produced. In the example depicted in Fig. 1.3a electron focussing takes place with the aid of a negatively biased grid, and growth occurs when the grid and cathode move upwards. The molten zone so produced and traversed is kept from sliding down the sides of the rod by surface tension forces alone; it is therefore clear that these forces must be large as mentioned earlier.

Although very similar in the basic method to the BSS techniques, float zoning is advantageously different in that crucible-melt contact is excluded; consequently, melt contamination by the crucible is eliminated. Where even trace impurity levels can significantly influence crystal properties this has been a major reason for using float zoning. In this context silicon is the most notable example where oxygen can reduce

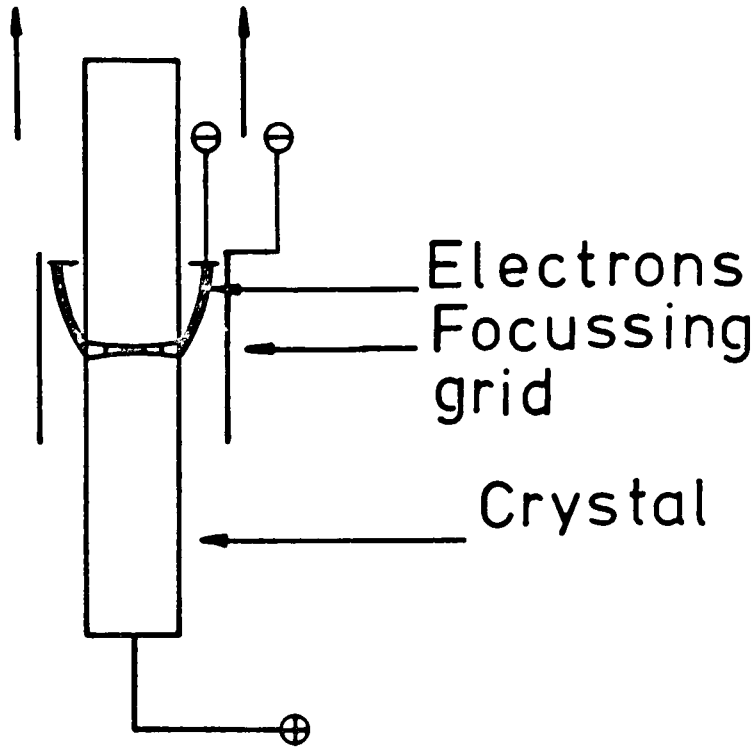
Fig. 1.3 Liquid ⟶ Solid Crystal Growth (L ⟶ S)

a. Float Zone

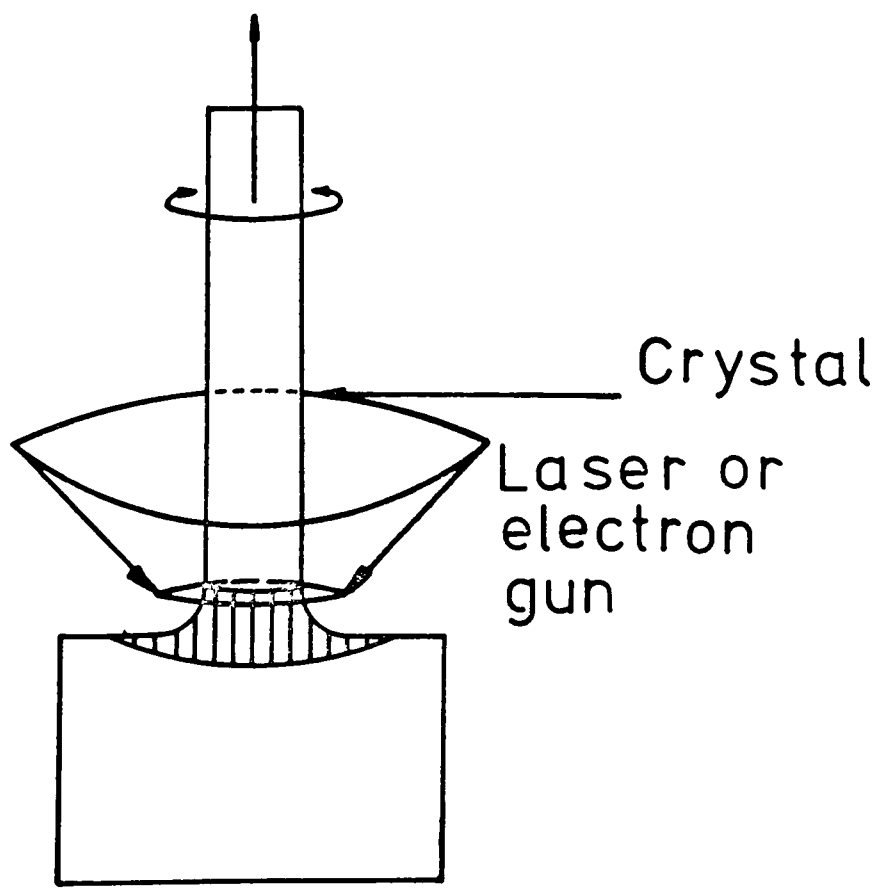
A cylindrical rod supported at either end is melted in a very narrow region by a beam of electrons. Crystal growth is advanced by moving this zone up the rod

b. Pedestal

This is very similar to float zoning. A beam of electrons, a laser or thermally imaged radiation melts a portion of a solid block. From this pool a crystal is grown by dipping in a seed and withdrawing it.


Electrons
Focussing grid
Crystal

(a)


Crystal
Laser or electron gun

(b)

electronic device efficiency. Using float zoning the oxygen impurity level can be reduced to 1 part in 10^9: the best yet achieved by the competitive Czochralski process is 1 part in 10^6 (42). With patience much purer crystals still could be grown by repeatedly float zoning the same crystal as in the method of Pfann(1). At this juncture it is important to note that float zoning belongs to a sub-section of the six categories considered in this section. Others in this sub-section are the Bridgman and Stockbarger methods, and all three incorporate two solid-liquid interfaces: one continuously melting and one continuously fusing. Therefore, in the very narrow molten region it is easy to envisage the latent heat of fusion from the one becoming a part of the latent heat of melting for the other.

As stated in the beginning float zoning is a sophisticated technique and so it has inherent problems. First, a good clean high vacuum is mandatory ($\approx 10^{-5}$ Torr) otherwise the electrons will cause secondary ionisation and eventually contamination. The electron beam can also crack hydrocarbons which leads to contamination. Such a level of evacuation is also needed for the reasons stated on P.10. A further problem arises when growing crystals for which the surface tension plot against orientation (a Wulff plot) shows a marked deviation from uniformity. In this case an initial cylinder can become ellipsoidal, for instance. To annul this problem the crystal must normally be rotated. In turn this implies a need for synchronously driven chucks which are capable of linked variable speeds. A further technical problem is power source

stability since any fluctuations in power, or electron beam position (due to contamination) will clearly give rise to zone melt changes and thus crystal diameter variations.

In conclusion float zoning can be used to grow metal crystals (some with high melting points), e.g. W, Fe, Ni, Cu and, dislocation-free crystals of high purity can likewise be grown (see reference 43 for a readable review). However, the technique is restricted to high surface tension materials and the technical problems are many.

1.2.3iv. The Pedestal Method[21]

This crystal growing system is in many respects a hybrid of the float zone (P.15) and Czochralski methods (P.20). As shown in Fig. 1.3b, a seed crystal is lowered into a pool of molten material (c.f. Czochralski) which sits on a solid block of the same material. Surface tension forces keep the pool intact (c.f. float zoning) and it is clear that the liquid must not wet its own solid. Heating is normally carried out by an electron gun[44] (c.f. float zone), a focussed laser beam[45] or by thermal imaging[46]. Growth rates are obviously material dependent but are usually low (a few mm/hr for metals but higher for semiconductors) and rotation rates are likewise low (a few r.p.m.). Also, depending on material parameters and heating methods a vacuum may or may not be necessary with all the attendant problems (P.10, P.17). In the literature on metal crystals only niobium has been grown dislocation-free[47], but the research into semiconductor crystal growth by this method has been extensive. See, for instance, the work of A. J. R. de Kock et al[48] on the growth of dislocation-free silicon. A detailed survey of these zone melting techniques can be found in reference 49.

1.2.3v Verneuil Crystal Growth[22]

This is analogous to the industrial technique of "metal spraying", where powder (≈50μm → 100μm in diameter) is fed through a flame (Fig. 1.4a) in which it melts. Then either by gravity feed or by forced gas feed molten droplets impinge on a seed crystal where growth occurs. Crystal symmetry can easily be maintained by seed rotation, but the fundamental problem is to balance the rod withdrawal rate with the powder feed rate. Growth rates are usually in the range 1 — 20mm/hr.

Verneuil's method has normally been used to grow middle to high melting point materials, e.g. emerald (melting pt. = 1400C), and zirconia (ZrO_2, melting pt. 2700C). Ruby, however, has been the major material to be grown, up to 50 mm in diameter. The only metal to have been grown was niobium[50] and then not dislocation-free. This latter observation is hardly surprising because the melt would vibrate from the repeated impulses of molten droplets; the thermal stresses would be high since the crystal would cool down from a high temperature quickly; and the risk of contamination from a "dirty flame" would be high. Crystal reduction or oxidation by the flame or its combustion products could further lead to constitutional and/or impurity stresses. Other heating methods have been used, e.g. high frequency induction heating[51] which was obviously much "cleaner" and less susceptible to instabilities from contamination itself.

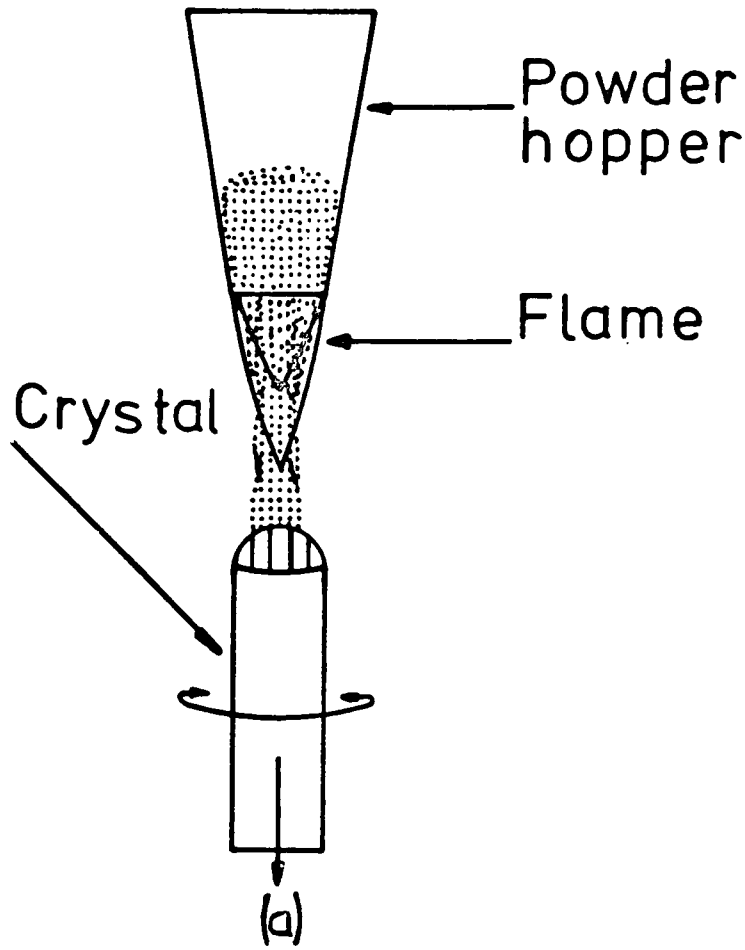
Fig. 1.4 Liquid-solid Crystal Growth (L⟶S)

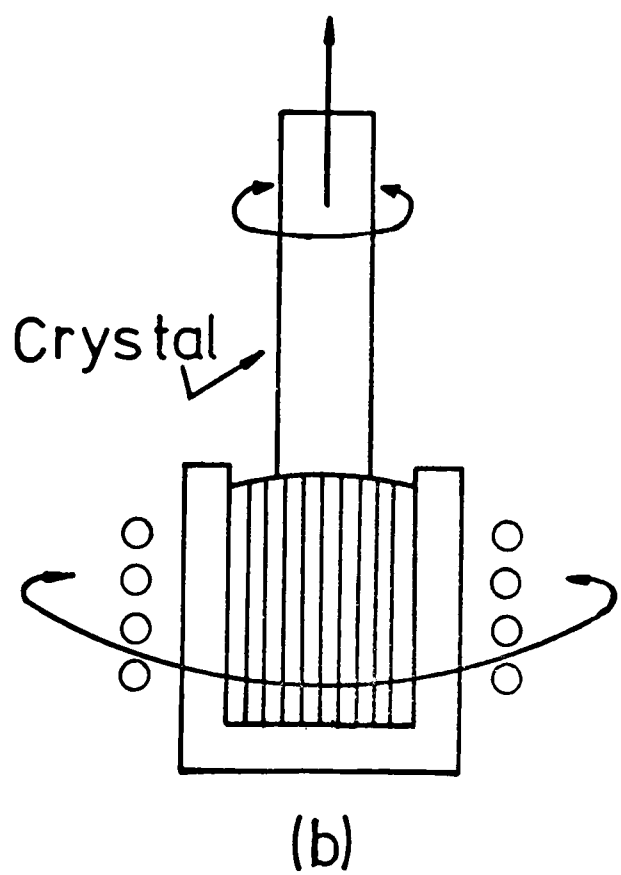
a. Verneuil's Method

Small powder particles (50—100 μm in diameter) fall through a flame in which they melt. Below the flame they hit a crystal seed and growth occurs as the seed is withdrawn.

b. Czochralski's Method

An oriented seed is dipped into a crucible containing the material to be grown. By simultaneously pulling and rotating extra crystal is grown.


Powder
hopper
Flame
Crystal
(a)


Crystal
(b)

1.2.3vi. Czochralski Crystal Growth[23]

To complete this introductory crystal growing account the Czochralski method will be briefly treated. A much more detailed account will follow in the next section.

Fig. 1.4b shows the schematic outline of the method: a seed crystal (usually of known orientation) is dipped into a melt which is either inductively or resistance heated, and by a combination of pulling and rotation extra cylindrical crystal can be grown. Crucible contamination has proved to be a problem in a number of instances (see references 48 and P.25 of this chapter for examples) but this has been controlled by either growing under a vacuum or under a suitable atmosphere. Alternatively the float zone method has been used in preference when very low impurity silicon was required[48].

Many metal crystals have been grown by this method (e.g. Al^{52}, Ag^{53}, Cu^{54}) and a number of these have been grown dislocation-free[52,53,54]. Very complex oxides have been grown too (although not dislocation-free) with crucible rotation being included to aid melt component mixing. Typical examples here are $BaTiO_3$[55] and $Dy_3Al_5O_{12}$[56]. The basic technique has also been adapted to grow highly volatile materials such as GaP[57] and GaAs[58] under pressure (≈25 atmospheres). It is therefore clear that Czochralski crystal growth is versatile and, under the right conditions, can produce very low dislocation density ($0 \rightarrow 10/cm^2$) crystals.

1.3 The Growth of Dislocation-free Copper Crystals

1.3.1 Preamble

It can now be readily understood which particular problems a crystal grower faces when attempting to manufacture low dislocation density (if not dislocation-free) metal crystals, no matter what the technique. Very necessary is a mechanically and chemically stable crystal growing installation; electrical power control and stability is an added necessity; and, probably most important of all, the crystals grown must be good enough for subsequent experiments every time. Even a success rate of 1 in 2 is not really creditable since it indicates a lack of control on the part of the grower, and it represents a 50% waste of crystal growing time.

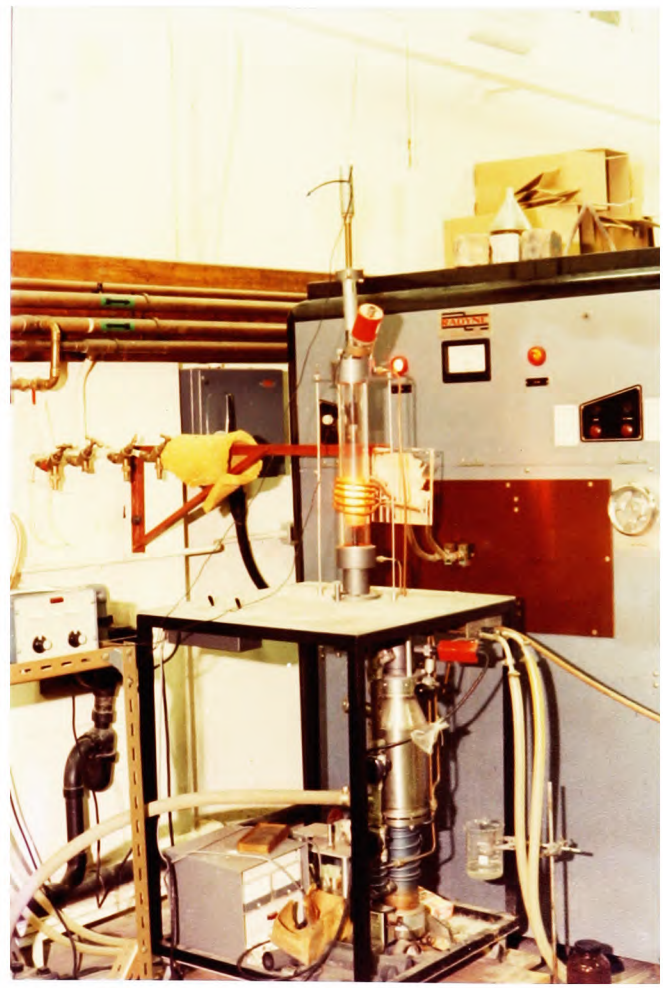
Czochralski crystal growth was chosen for the growth of the dislocation-free copper crystals described in this thesis because it was, quite simply, a tried and tested technique. The particular adaptation of the method used in this work had to incorporate a number of very important conditions in addition to the three broad and exacting requirements mentioned above. First, good diameter control was essential and this meant adequate visibility of the solid-liquid interface region. Secondly, the crystal should not touch any other object except its seed at one end and the completely clean melt free surface at the other; in Bridgman growth, for instance, it has already been pointed out what effects crystal-crucible contact could have (P.12). This being the case, it is further important to use a Czochralski crystal puller where the diameter can

either be adjusted automatically or else easily changed by operator intervention. It is additionally clear that the shape and size of the crystal cannot be dictated by the crucible (as in Bridgman growth); hence, the necessity for good solid-liquid interface visibility is strengthened. Thirdly, the crystal must cool down slowly giving no opportunity for dislocation generation and multiplication by thermal stresses or by vacancy condensation.

1.3.2 The Basic Crystal Growing Equipment

The crystal growth equipment used in this work is shown in Fig. 1.5. It consisted of a Metals Research B.C.G.265 crystal puller, incorporating an inner silica growth tube and an outer pyrex tube. Inside the silica was situated the radio frequency susceptor, the crucible and the metal to be melted. Cooling water (from a closed circuit or mains source) flowed between the two tubes to prevent the glass from cracking. (The normal water flow rate was about 9 litres/min., being 6 litres more than the recommended flow rate[59].) It must be noted at this point that when the ambient temperature outside the building was low and the inside ambient temperature normal, that cooling with the mains water has caused significant condensation on the outer surface of the pyrex tube which greatly impaired visibility. Such a problem has never been faced using the closed circuit water supply because it is at a slightly higher incoming temperature. However, the closed circuit system did suffer from other more disastrous problems which will be dealt with later.

Fig. 1.5 The Crystal Growing Apparatus



The growth chamber could be completely sealed off and operated under either a vacuum (2×10^{-6} Torr was the best achieved), normal atmospheric pressure with a suitable gas (Ar), or a slightly positive pressure (Sworn[60] suggested no more than 2 atmospheres). The gas was supplied from a free standing cylinder. Evacuation was affected by a combination of rotary and diffusion pumps, the latter being cooled by the same water systems as the furnace tubes. A liquid nitrogen cold trap was also built into the diffusion pump to increase the pumping efficiency. The tubes were easily disassembled for cleaning and/or replacement, although a straight vertical lift was necessary otherwise torsional and bending stresses would very easily fracture the glass. If the tubes are accidentally broken, new and, probably more financially important, reconditioned replacements may be bought from T. E. Brown, The Cavendish Laboratory, Madingley Road, Cambridge; or preferably the same supplier at The Old Vicarage, Foxton Road, Barrington, Cambs.

Tube cleaning was best done by using a normal domestic cleaner (e.g. Ajax) to remove compounds sometimes deposited from the water; followed by a thorough rinse in distilled water. Deposits on the inside of the silica tube have been easily removed using the same cleaning agent and a large bottle brush. Again a very thorough distilled water rinse was needed afterwards plus drying with a hot air blower. The aluminium ferrules on the ends of the furnace tubes sometimes needed lightly cleaning too, with wire wool: water deposits were again the main problem in this respect.

Heat was inductively supplied by a Radyne R.F. generator (type CC240) which was capable of a power range from 0 to 25 kW. This power could be very finely tuned via a system of three power control variacs each being graduated in increasingly finer power steps. The oscillator valve in the generator was force air cooled by the transformer and induction coils were water cooled. In the past the interior induction coils have overheated and failed catastrophically owing to silted-up cooling lines. This led to a flow switch being installed inside the machine which has been known to trip twice during a growth. The cause of such tripping was traced to other water users coupling into the closed circuit water system which consequently reduced the pressure and flow rate in the Radyne generator below the flow switch level. Consequently, to avoid the repeated failure of the Radyne for such a reason the much more reliable, although it seems less clean, mains water has been used. As mentioned in another context before the mains water could cool the R.F. work coil so efficiently that condensation occurred on the coil. This was not deleterious, but what could cause trouble is condensation actually inside the generator, e.g. water dropping onto a hot valve could cause fracture and subsequent failure. Frequent inspection of the generator with this in mind has so far failed to substantiate this concern. Since the machine relies very heavily on many large expensive and not easily obtained valves a 15 minute running-in period was always used before switching on the R.F. (manufacturer's recommendation). Also, the cooling water was always left running for 1 hr. to ensure that the components were cool at the end of the run. To prevent the furnace tubes from cracking they too were water cooled to room temperature (usually $\approx 2\frac{1}{2}$ hours was needed) after a growth cycle.

As manufactured the crystal growth equipment was capable of growing crystals by the Czochralski, Kyropoulos and Bridgman methods. It has been used by the author to successfully grow crystals by the first two of these. The Czochralski pulling attachment could be clamped to the top of the furnace tubes with pulling and rotation rates being continuously variable from 0 to 7.8 cm/hr and 40 r.p.m. respectively.

1.3.3 The Basic Experimental Technique

Much of the early work on the growth of dislocation-free crystals has been built on in this work. For instance, the earliest record of the controlled growth of dislocation-free silicon was by Dash[61] in 1958; later in a longer publication[62] Dash gave details of his method, and it is this method which forms the basis for the experimental technique described here.

In Fig. 1.6 are schematically depicted the essential elements of the growth chamber from Fig. 1.5. The <123> growth axis copper seed and melt, the graphite R.F. susceptor and the alumina afterheater were all thoroughly cleaned by the following method:-

Repeat 2x:

i. Immerse in running water (10 secs)

ii. "Clean" in concentrated nitric acid (≈1 min with agitation)

iii. Wash in methanol (agitate for ≈30 secs)

iv. Wash in running water with agitation for ≈15 secs)

v. Wash in running water for 5 mins.

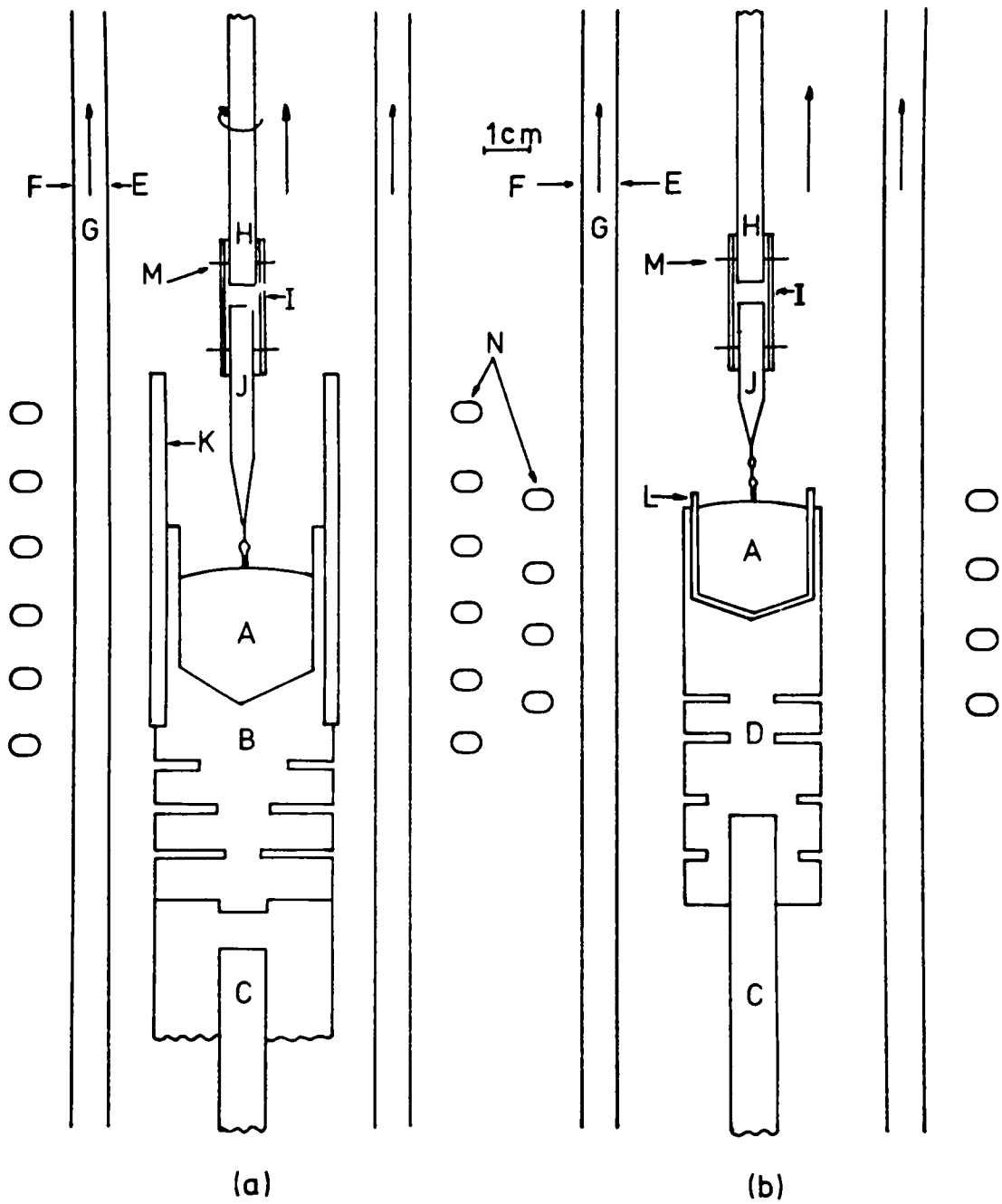
vi. Dry on a cold air metallographic specimen drier

Fig. 1.6 The Two Forms of Czochralski Crystal Puller

a. Original components

b. Modified components

A. 99.999% purity copper melt
B. Graphite susceptor (Morganite EY9)
C. Stainless steel support rod
D. Molybdenum susceptor
E. Silica tube
F. Pyrex tube
G. Cooling water
H. Stainless steel pulling rod
I. Stainless steel chuck
J. 99.999% purity copper seed
K. Alumina afterheater
L. Vitreous carbon crucible
M. Set screws
N. R.F. coil (water-cooled)


F
E
G
H
M
I
J
K
A
B
C
(a)
1cm
F
E
G
H
M
I
N
J
L
A
D
C
(b)

When assembled, the chamber was evacuated to 10^{-6} Torr for approximately 12 hrs. Then, while still being evacuated, the charge was almost melted and the pumping was continued for 30 mins. in an attempt to remove any remaining volatile compounds. The pumps were then switched off; the chamber filled with standard purity argon; and the charge melted.

The crystal was grown (refer to Fig. 1.7a for a pictorial sequence of the events to be described; this is for a later modified rig, but the events are similar) by dipping the seed into the melt (the temperature of which was adjusted from experience to enable growth to begin) and then withdrawing it for 3-4 cms at approximately 6 cm/hr. At the same time the crystal was rotated at 15 r.p.m. and the R.F. power was slowly increased, so that the diameter progressively decreased. Owing to the presence of the long alumina afterheater, Fig. 1.6, it was impossible to view the crystal normally and so ascertain its diameter. Such a measurement could only be inferred from the presence of the "halo" around the crystal at the solid-liquid interface when looking down the seed with almost grazing incidence. This halo can be readily seen in Fig. 1.7a and has been thought to arise from the increased emissivity of this region over the surroundings thus causing it to radiate more and so appear brighter[61]. On reflection the author can envisage no fundamental reason why this should be so and feels the origin of the "halo" is quite different. In short, the growing crystal will always locally pull-up the liquid by surface tension forces, Fig. 1.7b, so that a curved surface will be produced. This curved surface will act as a mirror and focus radiation falling on it in preferential directions; hence it appears brighter.

Fig. 1.7 Solid-liquid Interface Phenomena

a. The crystal growth halo in the vicinity of the growth interface
The complete set of four pictures also shows a typical growth cycle
Growth rate = G.R. Rotation rate = R.R.

i. "Necking" down to the second "neck".
The first neck is clearly visible
G.R. = 1.2 cm/hr
R.R. = 0 r.p.m.
Somewhere down this neck the dislocations stop

ii. The initiation of the desired dislocation-free volume
G.R. = 1.2 cm/hr
R.R. = 0 r.p.m.

iii. Part-way down the gauge length of the crystal
G.R. = 1.2 cm/hr
R.R. = 0 r.p.m.

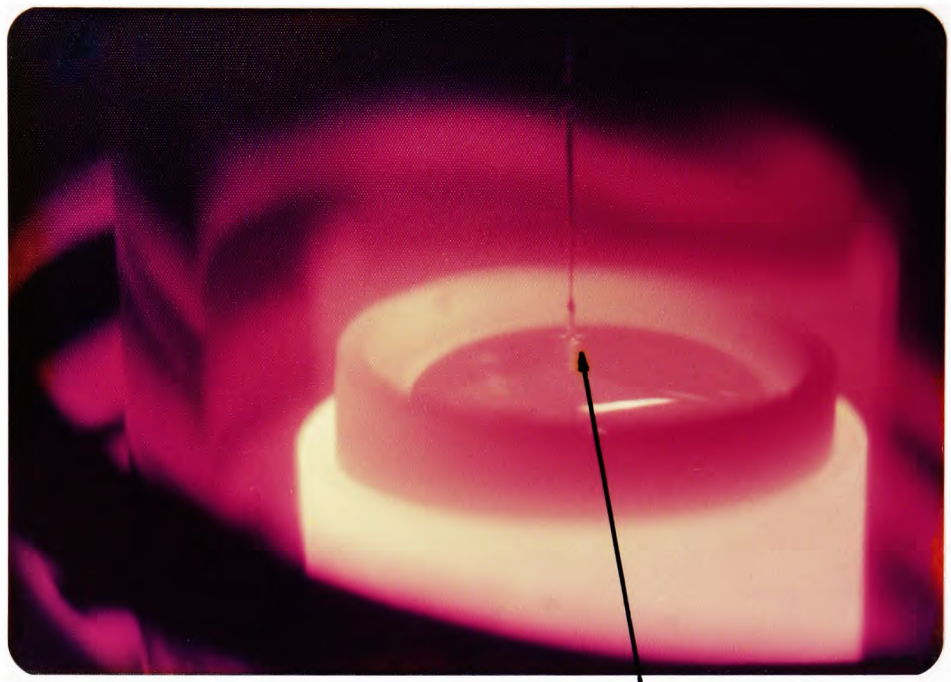
iv. Growing the "tail"
G.R. = 1.2 cm/hr
R.R. = 0 r.p.m.

Scale mark = 10 mm

These pictures refer to growth using the modified crystal puller, but the basic details are also relevant to the original system

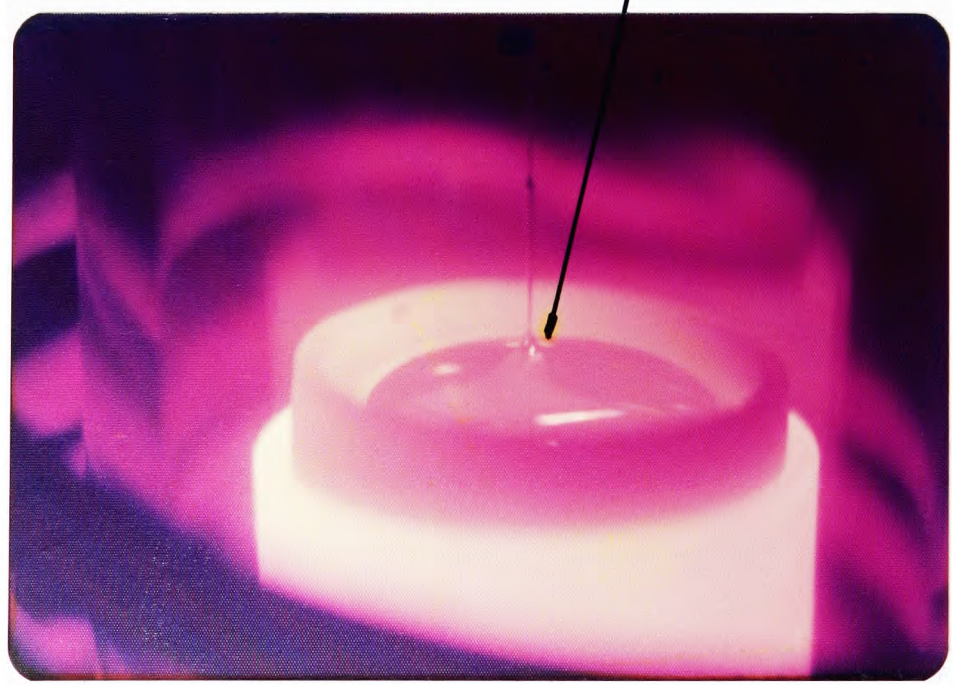
b. Because of surface tension forces the seed crystal (C) will always pull the melt up locally. This liquid (L) will have a curved surface (S) which will tend to preferentially focus light giving rise to the halo

c. It is feasible to grow a dislocation-free crystal from a polycrystalline seed. This can be done by a system of "necks" whereby grain boundaries and dislocations are simply grown out of seed

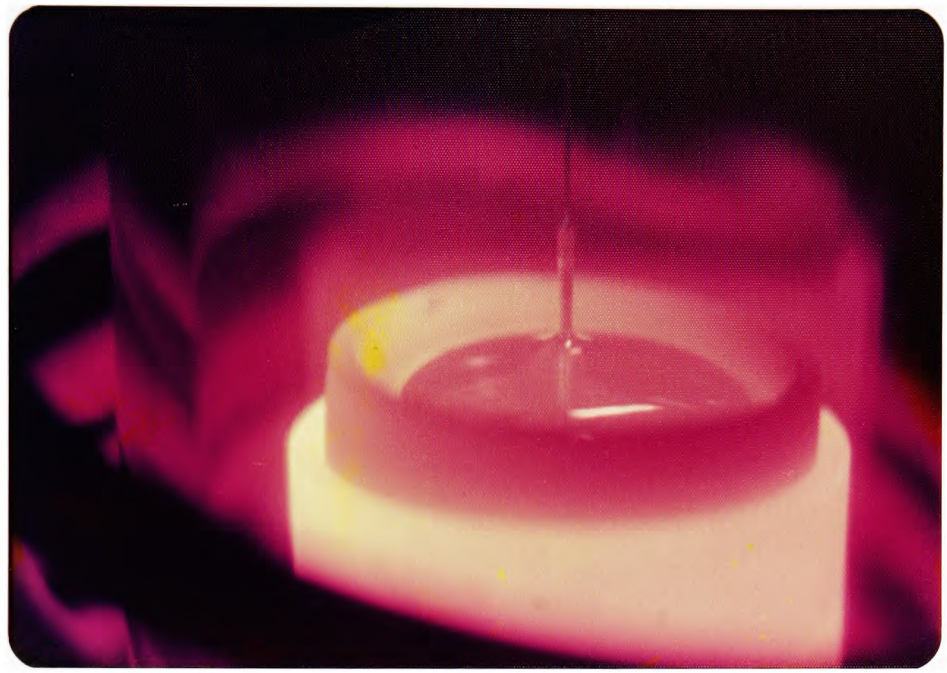


a i

Halo



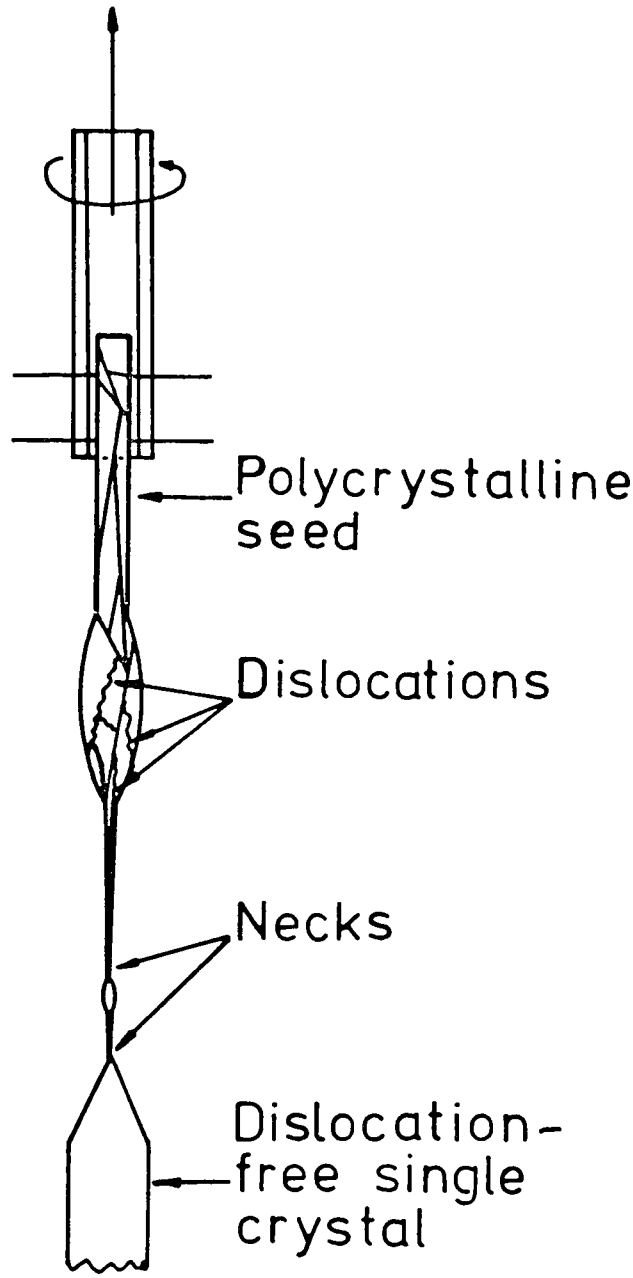
a ii



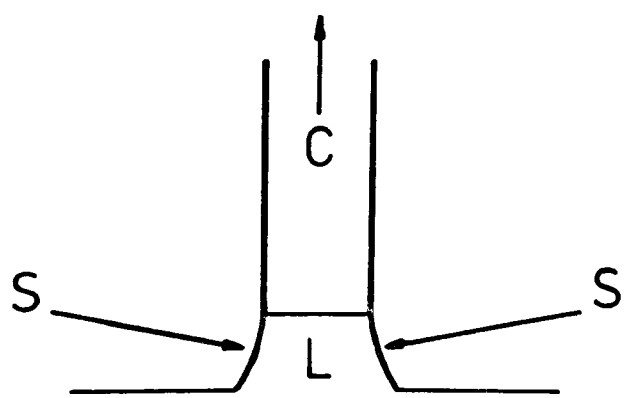
a iii



a iv


Polycrystalline seed
Dislocations
Necks
Dislocation-free single crystal

(c)

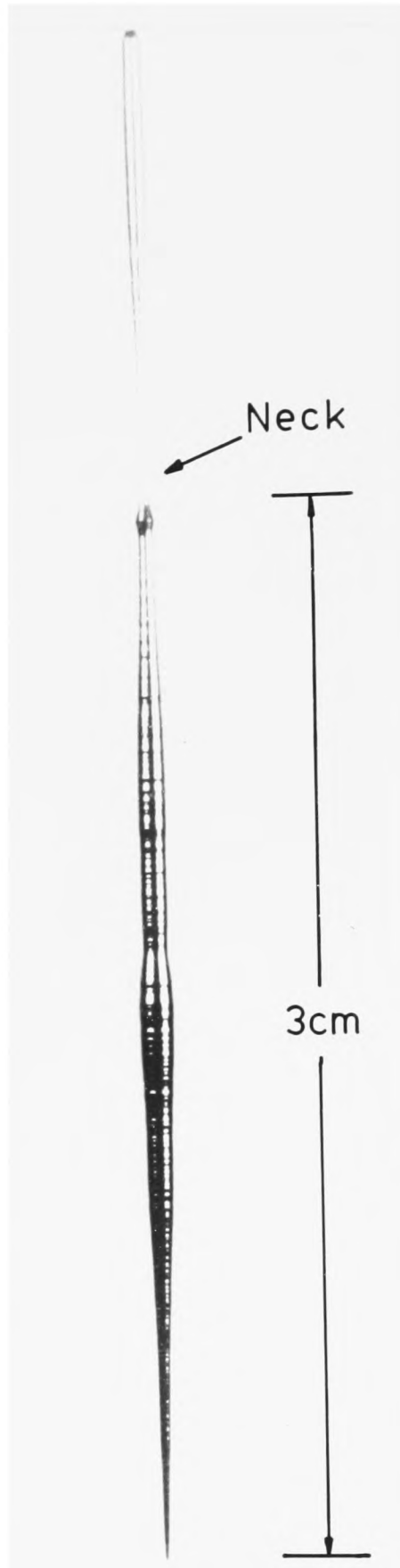

C
S
S
L

(b)

The diameter was reduced to approximately $\frac{1}{3}$ mm and then kept constant for ≈ 2-4 mm. This process was originally termed "necking" by Dash and was used by many subsequent crystal growers[52,53,54,64,65,66,67,68,100] to emulate the conditions which Dash had found necessary for the growth of dislocation-free silicon. "Necking", it was argued, performed two very important roles: the first was that dislocations intersecting the solid-liquid interface would simply be grown out, since the slip planes would be inclined to the <123> growth axis, Fig. 1.7c. And the second was that when the pulling rate was reduced and the diameter increased to produce a large, now dislocation-free, crystal volume, that the thermal stresses in the crystal would be too low to produce defects; since the long, thin neck then acted as a very efficient heat flow resistance (see Chapter II for more work on this problem).

In this study the growth rate was reduced to 3 cm/hr and the diameter increased to ≈1-2 mm at the end of the neck. In order that the crystal be useful for subsequent tensile deformation studies a "dog bone" profile was grown, Fig. 1.8. After growing for ≈2 cm the temperature of the melt was again increased so that a long "tail" approximately 2 cm in length was attached to the previous 2 cm of crystal. This latter measure allowed the crystal to cool down slowly, and when it had grown out of the melt it was pulled further up inside the alumina afterheater but never out of it. The system was then switched off and left for not less than $2\frac{1}{2}$ hrs. to cool down to room temperature before removing the crystal for subsequent X-ray topography.

Fig. 1.8 An optical picture of a typical crystal-neck arrangement. Note the "dog-bone" profile which was necessary for later experiments


Neck
3cm

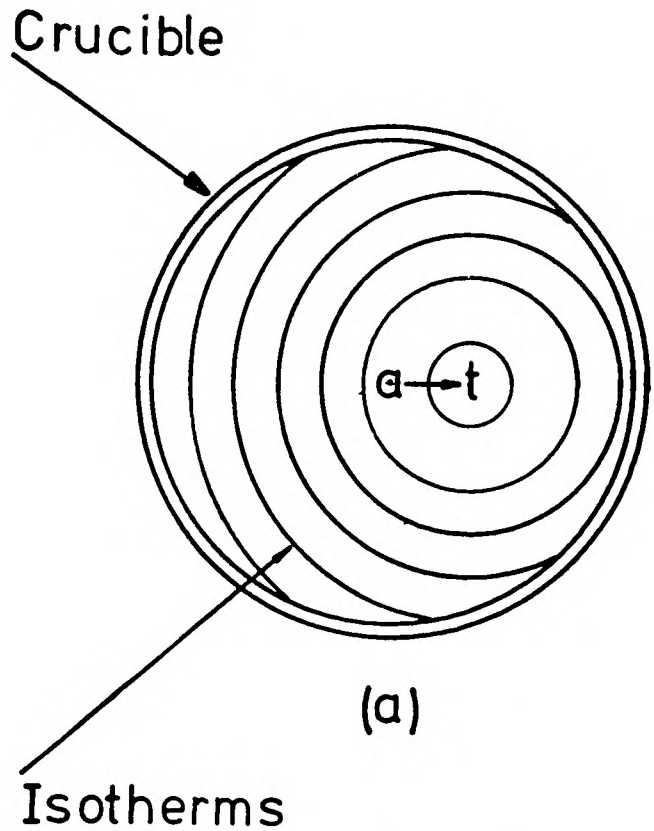
Two important crystal growing phenomena were noticed at various stages during this work and they are included here for completeness. The first involves seed alignment in the chuck and the crucible alignment in the R.F. coil. If the pulling axis of the Czochralski head, the growth axis of the crystal and the longitudinal thermal axis of the melt were co-linear, then the crystal would clearly grow along this line. If, however, one of these three conditions were not true then the crystal would grow to the thermal minimum of the melt over a few cms of growth, Fig. 1.9.

The second observation was with reference to the vertical position of the melt in the R.F. coil. Originally the R.F. coil consisted of six turns, with the lower three being occupied by the melt and the upper three by the afterheater. If the melt was raised too high in the coil, however, it was noticed that when the dislocation-free volume was being grown then a position was reached at which the complete melt surface would begin to freeze, Fig. 1.10a. Obviously, the crystal was absorbing more heat than the melt could provide, resulting in accelerated radial growth. Conversely, if the melt was too low then secondary solidification would take place from the base, Fig. 1.10b. Both these effects were undesirable: but only the former could be quickly controlled, since with the latter almost the whole melt would solidify before being noticed, and then avoiding action was usually too late. The best position was found to be such that the whole melt was surrounded by the R.F. coil.

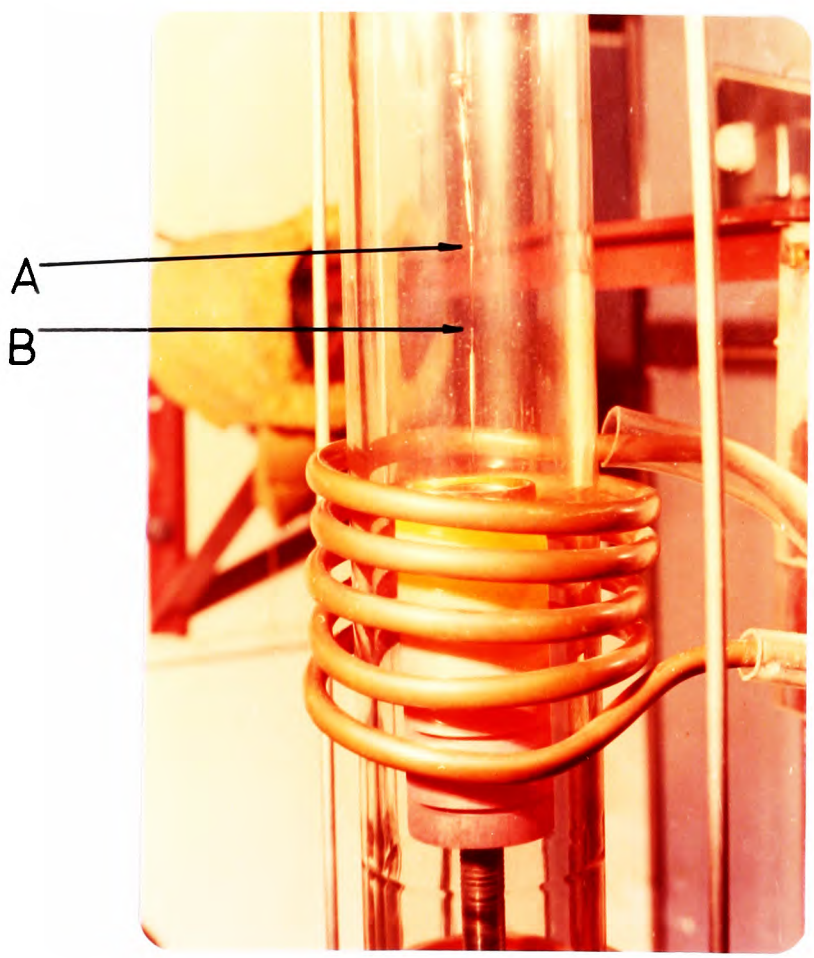
Fig. 1.9 The Effect of Crystal, Crucible, Puller Misalignment

a. If the growth axes of the seed and crystal pulling rod (a) are not co-linear with the thermal axis of the crucible (t), then the crystal will grow towards the thermal minimum of the crucible (t)

b. An actual example of the type of behaviour described in (a). The seed crystal began growing at A, grew across the melt to B as it was pulled, and then grew straight along the thermal minimum of the crucible thereafter



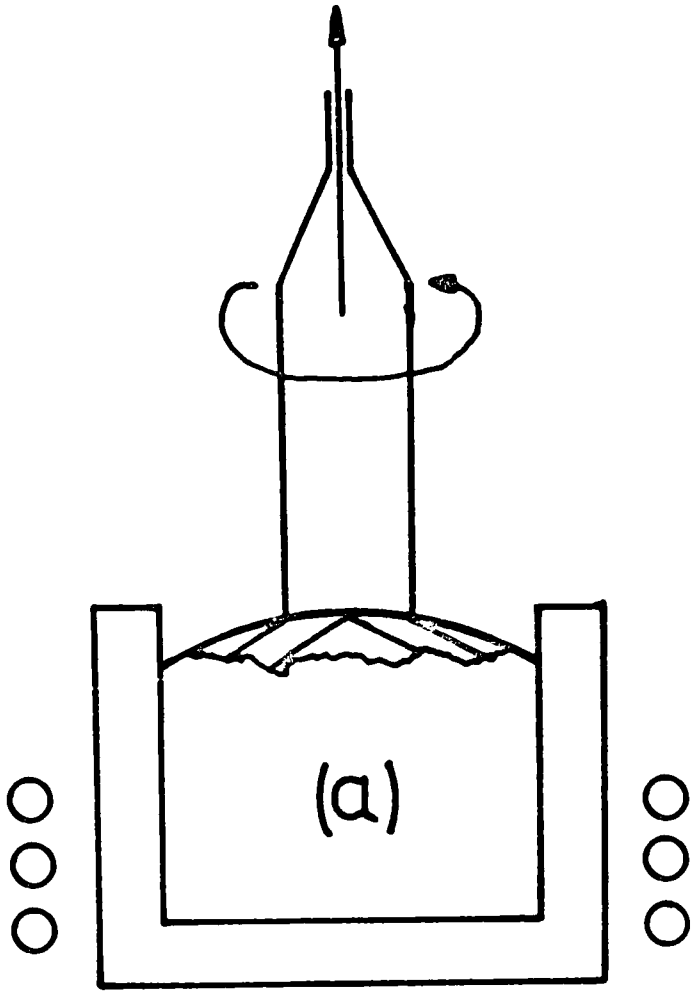
(a)

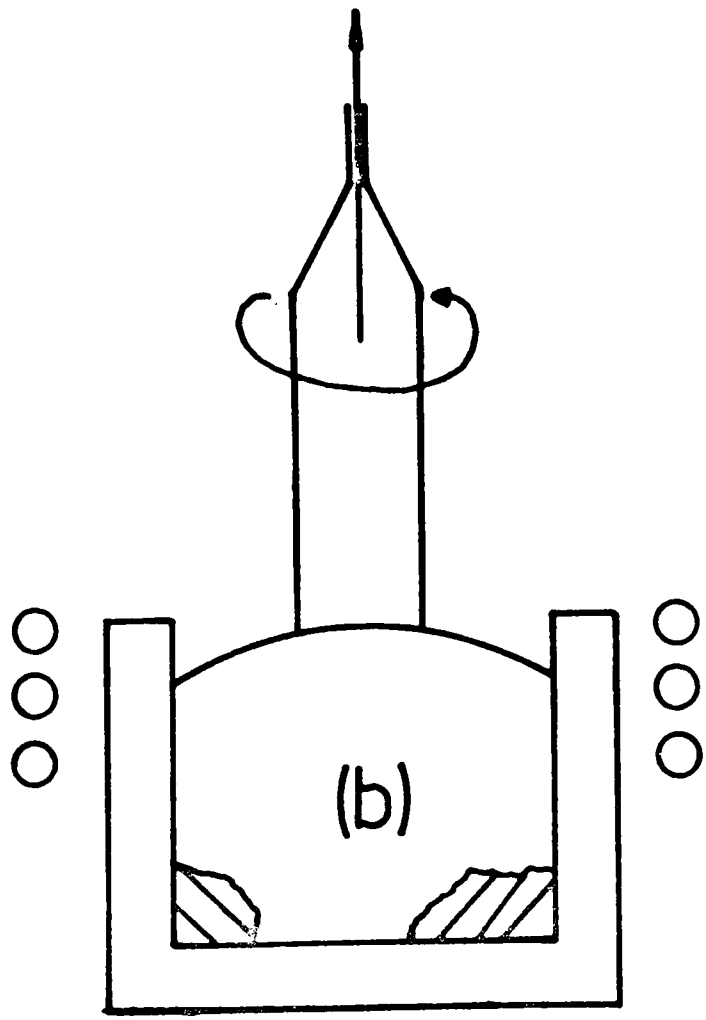


(b)

Fig. 1.10 Incorrect Positioning of the Melt in the R.F. Coil

If the melt was too high in the R.F. coil (a) then rapid solidification occurred at the surface; conversely, if the melt was too low (b) then secondary solidification could occur at the base of the crucible


(a)


(b)

1.3.4 The X-ray Topography Examination Method

The reader most interested in X-ray topography is advised to read Chapter III, because this section is only meant to be a basic account of the way in which the crystal was handled and examined to assess its defect distribution after growth.

At this stage it is important to remember that a crystal growing recipe had been strictly adhered to, and so the crystal should have been dislocation-free. (The crystal now looked as shown in Fig. 1.8). To maintain this supposed state of perfection, the seed and crystal were always kept as vertical as possible to minimise handling damage and to reduce dislocation propagation from the neck into the dislocation-free volume of interest. Bending at the neck was a repetitive problem. Further precaution against the elements was afforded by supporting the seed and crystal vertically inside a glass jar. The jar was then carried very carefully the $\frac{1}{4}$ of a mile to the X-ray camera!

Whilst remaining vertical the crystal was Lang[69] topographed in the Borrmann[70] mode using an Elliott GX6 rotating anode X-ray generator operating at 50 kV and 35 mA. The $K_{\alpha 1}$ characteristic radiation from a molybdenum target was used (wavelength = 0.70926A^{o}) which rendered a value for the Bragg angle (Θ_B) of 9.78^{o}. The 111 g-vectors were always used because:-

i. The complete crystal could be imaged at once, Fig. 1.11, implying a large diffracting volume; thereby rendering diffracted beam location that much easier and reducing exposure times.

ii. The 111 anomalous transmission coefficients are the highest of all for copper[71], implying the highest relative diffracted intensity and consequently the shortest relative exposure times for the Ilford L4 50μm plates. Exposure times were between 1 hr/mm. and 5 hr/mm. depending on crystal thickness.

Using anomalous transmission through thick specimens, dislocations locally reduce this anomalous transmission and hence appear as light lines on a darker background on the original topograph plate, and also on the pictures presented in this thesis (the plate processing technique outlined by Lang[72] and described in Chapter III was used throughout). Three points should be borne in mind in the interpretation of the topographs: first, since the growth axis of the crystal was <123> no axial screws could grow out of the neck and into the specimen; second, using a 111 type reflection it is conceivable that dislocations could appear "invisible" by g.b. = 0 criteria (see Chapter III for a clear exposition of these criteria); and thirdly, such factors as emulsion grain size, photoelectron track lengths etc., combine to limit the resolution of the X-ray technique to at best 1 μm. The first point is useful in that axial screws were not problematical, whilst the second observation would seem critical since the perfection assessment method would appear to be inconclusive. However, Tanner[68] has shown using non-coplanar g-vectors that crystals can indeed be dislocation-free. Hence, within the confines of the third observation it seems fair, at this stage, to assert that down to a 1 μm resolution, when the Lang-Borrmann topograph shows no intra-image contrast (i.e. no light lines) then the crystal is indeed dislocation-free. Chapter IV considers this fundamental question of perfection on a sub-micron level in much more detail.

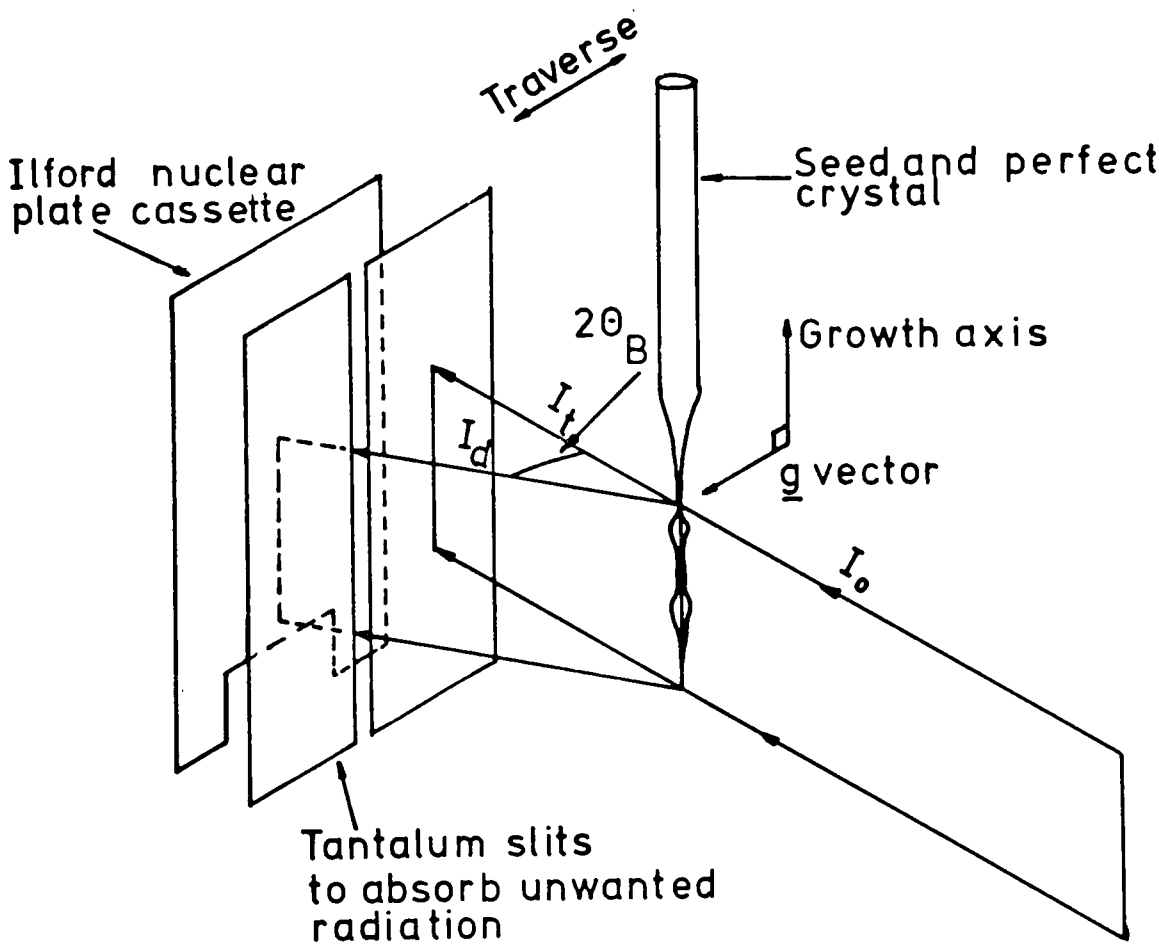
Fig. 1.11 X-ray Diffraction Set-up (Schematic)

I_o = Incident beam

I_d = Diffracted beam

I_t = Forward transmitted beam

Θ_B = Bragg angle


Traverse
Ilford nuclear plate cassette
Seed and perfect crystal
$2\theta_B$
Growth axis
I_t
I_d
g vector
I_o
Tantalum slits to absorb unwanted radiation

1.3.5 The X-ray Topography of the Crystals Grown by the Basic Experimental Method

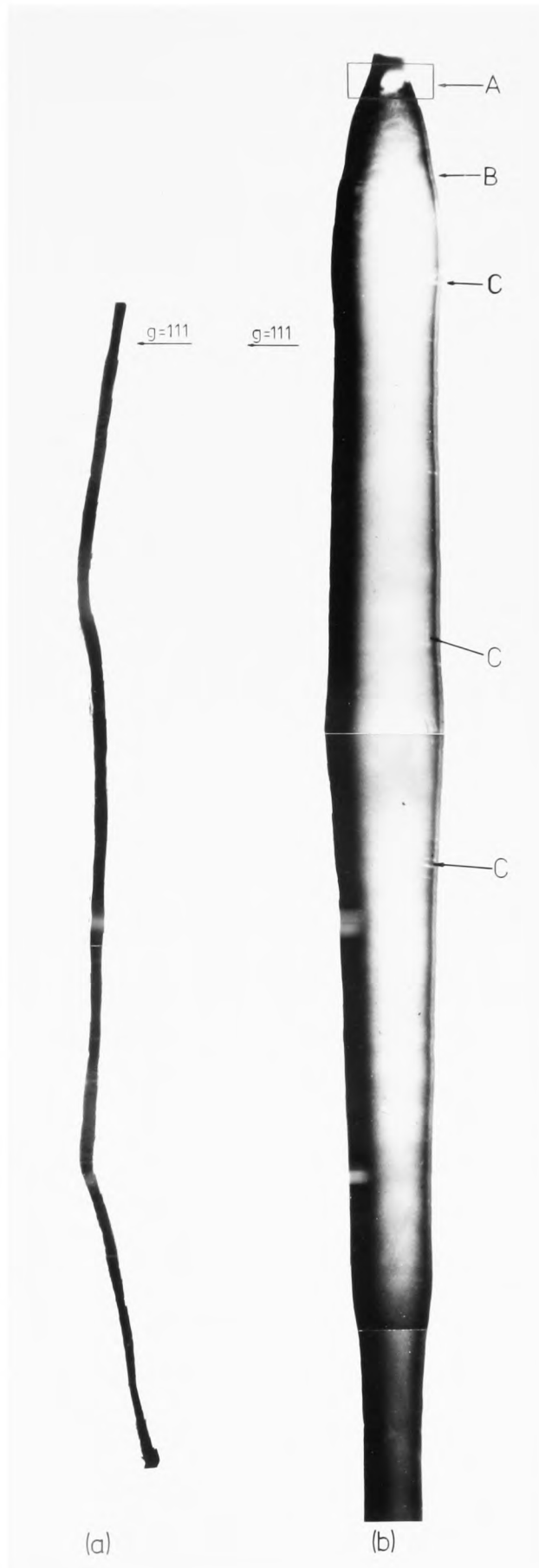
Some 40 crystals were produced in the manner outlined above and not one was completely free from dislocations. In the many cases where the crystals turned out to be heavily dislocated no anomalous transmission was ever recorded; Fig. 1.12a shows a good example of this where only a surface reflection could be monitored. In this and subsequent pictures the tail has been partly eliminated to allow as high a magnification as possible of the "crystal" to be achieved. In another case where encouraging anomalous transmission was obtained other effects were noticed. These are shown in Fig. 1.12b where it is obvious that the vast majority of dislocations did indeed stop in the neck; however, a few always managed to propagate down into the region of interest. Such observations have been made by Schwuttke[73] and Tanner[74] too. These are not handling dislocations induced during transportation, because they are not straight as would be expected from stage I plastic deformation processes (see the topographs of Fred Young et al in reference 75 for a clear indication of this type): rather, these are dislocations straggling down during growth. They appear wavy because of the climb processes which are operative at the high temperatures of growth (≈1083C). In the same picture it is easily possible to see the effects of minor growth accidents, such as those labelled 'C'.

Sworn[60] in his thesis has noticed these 'C' contrast features too; in the published literature Steinemann and Zimmerli[66], Sworn and Brown[67], and Kamada and Tanner[76]

Fig. 1.12 The Effects of Crystal-scum/particle Collisions

When the melt free surface was covered with a copper oxide scum dislocated growth resulted and only a surface reflection could be obtained (a). On the rare occasion when scum-free growth happened it was consistently noticed that the majority of dislocations stopped at the end of the neck (A in (b)), but others grew into the main body of the crystal of interest (B in (b)). Crystal graphite collisions produced small surface defects (C in (b)) which were localised, i.e. post collision growth was dislocation-free

g-vector = $\frac{1}{2}$ mm


A
B
C
C
C
g=111
g=111
(a)
(b)

have also observed such phenomena. These previous workers put such effects down to crystal-particle collisions near the growth front, i.e. foreign, contaminating particles moved incontrollably across the melt free surface impinging on the growing crystal and produced defects. Sworn[60] calculated that the impact stress would be ≈ 3.0 g/mm^2 and when superimposed on the thermal stress dislocation could occur.

Although no data exists on yield stresses in this temperature region for dislocation-free Czochralski Cu, the order of magnitudes involved do appear to be realistic. Taking the room temperature yield stress data of Kamada and Tanner[76] and extrapolating to $\approx$1000C it is clear that a yield stress of about $0 \rightarrow 30$ g/mm^2 could be expected. Also, Gallagher's[77] experiments show that the yield stress of Bridgman crystals is $0 \rightarrow 50$ g/mm^2 at around 1045C in Cu.

If minor growth collisions could give rise to small surface defects, it is conspicuously clear that permanent contact with a completely contaminated melt would give rise to the kind of contrast feature in Fig. 1.12a, i.e. a wholly dislocated crystal. Much effort was directed towards eliminating this layer of copper oxide scum which invariably grew across the melt free surface. Floating graphite particles were also a problem.

Preliminary attempts to remove the oxidants in the porous graphite mould by prolonged vacuum pumping (2×10^{-6} Torr) at high temperatures ($\approx$1000C) for long periods (6 hrs.) were never entirely satisfactory: the scum always returned on melting the charge. The use of high purity argon (impurity levels:

4vpm O_2, 1 vpm H_2, 15 vpm N_2, hydrocarbons 1 vpm, total impurities 20vpm) in the chamber, in an attempt to fill the graphite "pores" with a better inert medium also proved useless. Continuous pumping during growth was impracticable since evaporated copper condensed and solidified on the walls of the apparatus which significantly reduced visibility (the saturated vapour pressure of copper at its melting point is 6×10^{-7} Torr[78]). Only Fehmer and Uelhoff[54] have published work on the growth of copper under vacuum; they were successful because their system was so much larger. Melt vibrations arising from the backing pump also significantly contributed to the loss of perfection (to be shown later).

1.3.6 The Modified Experimental Technique

The visibility problems have previously been referred to and the crystal-scum interactions have been clearly shown to destroy the perfection of the crystal. An obvious need therefore arose to eliminate such problems and to grow dislocation-free crystals every time. This was done through the following eight modifications.

1.3.6i. The R.F. Susceptor

Graphite is a moderately good conductor of electricity and heat; it is relatively inert itself to molten copper; and it can be used many times over. However, the Morganite EY9 graphite originally used was 17% porous (Table 1.1) and consequently very difficult to evacuate. As an R.F. susceptor it was very good, being quick to respond to power changes and exhibiting a good "skin depth" (Fig. 1.13), implying that it heated up rapidly (charge melting could be easily obtained in 5 mins.).

TABLE 1.1

Typical Properties of Morganite EY9 Graphite** Vitreous Carbon** and Molybdenum*

	Morganite EY9 Graphite	Vitreous Carbon	Molybdenum
Density (g/cm^3)	1.7	1.47	10.2
Porosity (%)	17	0.05	0
Permeability to gases (cm^2/sec)	0.015	2.5×10^{-11}	0
Young's modulus ($kg/cm^2 \times 10^4$)	4.9-13.33	21-28	273
Coefficient of linear expansion ($\times 10^6/C$)	1.8	3.2	4.9
Thermal conductivity (cal/cm/sec.C)	0.11-0.14	0.01-0.02	0.35
Electrical resistivity (10^{-4} Ω.cm)	19-39	30-80	0.2

* Kindly supplied by Murex Refractory Metals, Rainham, Essex, England.

** Taken from reference 77

Fig. 1.13 A Comparison of the R.F. Susceptors

Of the three materials (Mo, vitreous carbon, (V.C.) graphite (G)) used in the susceptor-crucible combination, vitreous carbon possessed the greatest skin depth (δ). δ is defined as that distance into the material over which the R.F. falls to $1/e$ of its surface value. The curves opposite were calculated for the crucible diameter, (25 mm), and using a frequency of 0.5MHz. They represent the depreciation of the surface R.F. current I(r)% versus distance into the material as a proportion of the radius (r)

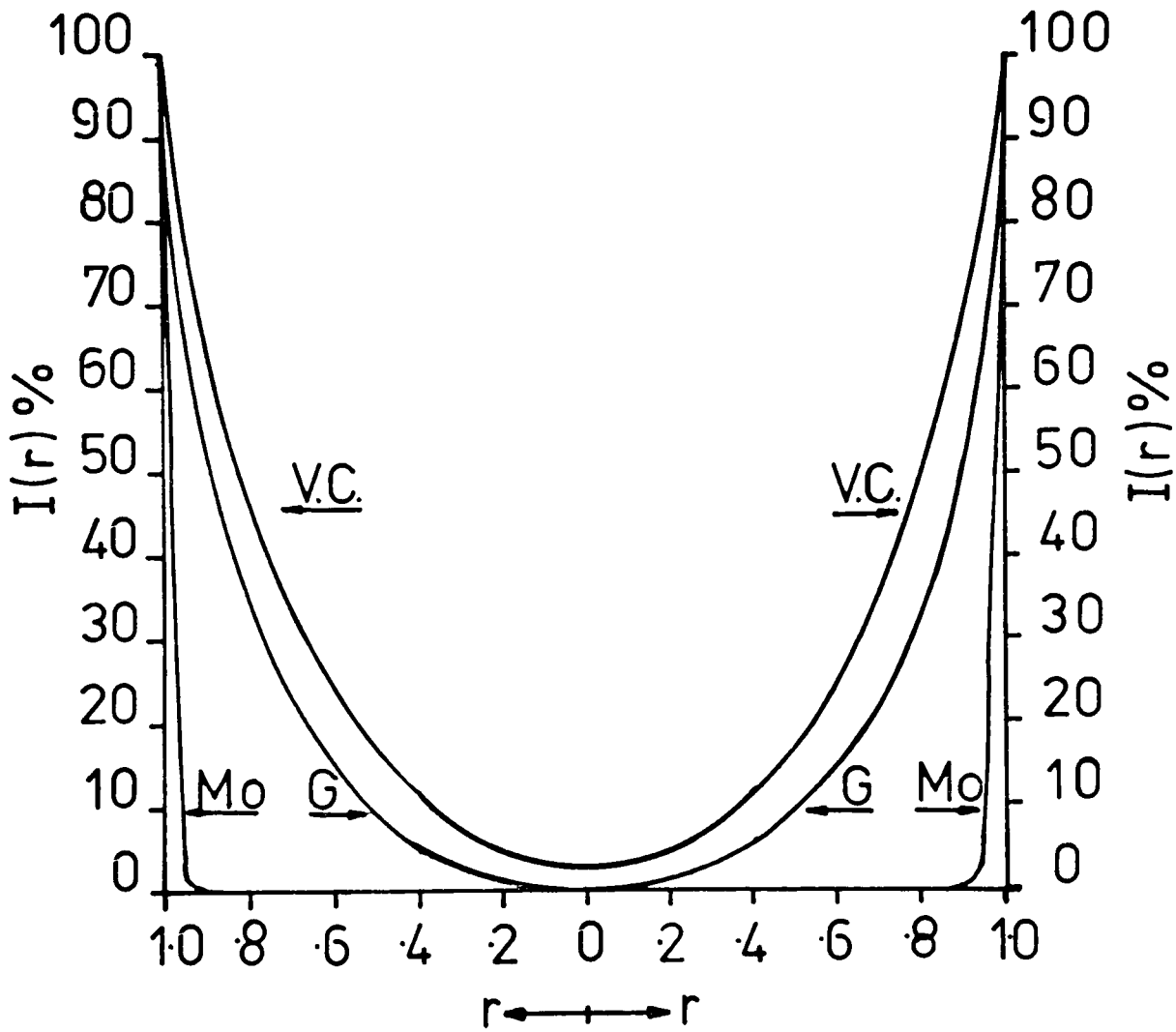
δ was calculated from the expression:-

$$\delta = \frac{1}{2}\left(\frac{\rho \times 10^7}{\mu \nu}\right)^{\frac{1}{2}}$$ (Taken from reference 16, p.333)

Where ρ = resistivity of the material
ν = frequency being used
μ = permeability of the material (= 1 here)

The values of δ so calculated were:-

Mo	0.225 mm
Graphite	2.52 mm
Vitreous carbon	3.57 mm


100
90
80
70
60
50
40
30
20
10
0
I(r) %
V.C.
Mo
G
G
Mo
V.C.
1·0 ·8 ·6 ·4 ·2 0 ·2 ·4 ·6 ·8 1·0
r r

Molybdenum was chosen as a replacement for the graphite because it was impervious to contaminating species; because it displayed excellent high temperature oxidation and creep properties; and, because it was a good conductor of heat and electricity, Table 1.1. The design used is shown in Fig. 1.6b. (The actual component was built to this design by Murex Refractory Metals, Rainham, Essex, RM13 9DP, England.) As can be seen from Fig. 1.6b radial slots were cut into the susceptor to reduce longitudinal heat losses and to conserve generator power.

Two disadvantages were apparent with the molybdenum, however: first, it was wetted by molten copper; and second, it only had an R.F. "skin depth" of 0.225 mm, Fig. 1.13. This latter condition prolonged melting times because of the higher thermal mass of the molybdenum and the smaller depth which was electro-magnetically coupled to the work coil. Melting took about 16 minutes with this new susceptor.

1.3.6ii. The R.F. Susceptor Liner

The second of the previous two disadvantages was an unfortunate condition of using molybdenum, and without changing the generator frequency it could not be circumvented. But the first disadvantage needed further attention. It was readily solved by using a vitreous carbon liner (produced by the Beckwith Carbon Corporation, 16140 Raymer Street, Van Nuys, California, 91460, U.S.A.) inside the molybdenum, Fig. 1.6b.

Vitreous (glassy) carbon is produced by the thermal degradation of selected organic polymers (c.f. graphite which

is produced from coal) and can be used to high temperatures (3000C) in controlled atmospheres. It is impervious to contaminants; cleans very easily; and is not wetted by copper. For an enthusiastic review of its properties and uses the reader is directed to the paper by Cawlard and Lewis[79]. Selected properties are tabulated in Table 1.1.

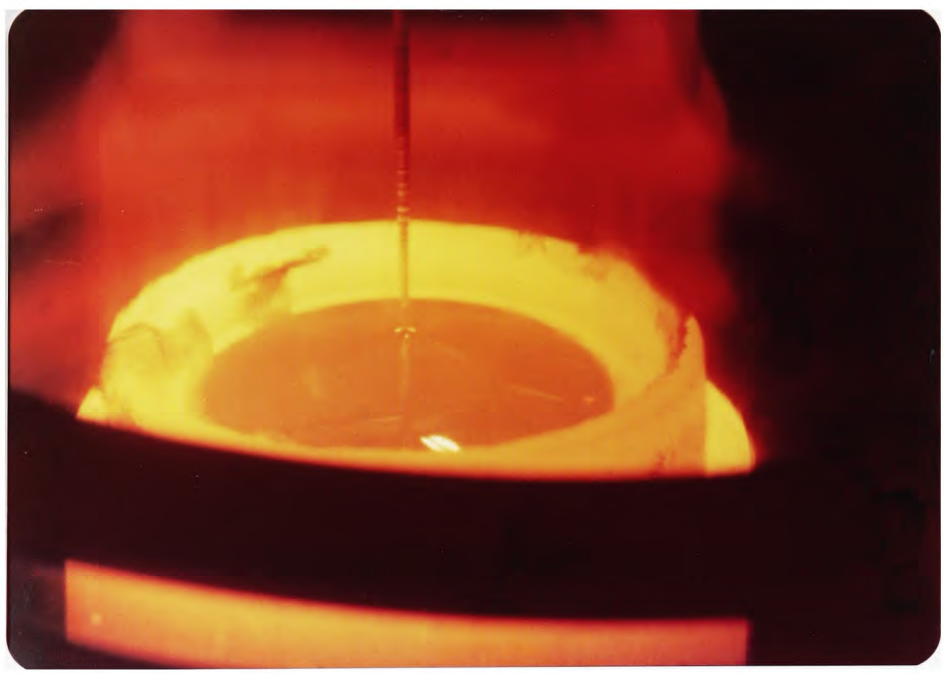
Only two minor disadvantages have been monitored using a vitreous carbon liner. The first was that it suffered from a very large "skin depth" (3.57 mm at the 0.5MHZ produced by the R.F. generator). This was noticed at times in the form of slight melt surface vibrations owing to the thin walled liner (wall thickness=2.36 mm). However, by raising the top of the liner so that it was just out of the direct R.F. field and therefore not directly coupled to it, these vibrations became imperceptible. Other workers have also noticed such vibrations[80] arising from electromagnetic coupling effects. The second was that the liner wall degraded at the top, and flaked off; this is shown well in Fig. 1.14. Such degradation began after approximately 50 growth runs over a year's work. It was eliminated by careful inspection and removal prior to assembly.

1.3.6iii. The Growth Atmosphere

On P.32 it has already been pointed out that the use of high purity argon in an initial attempt to reduce oxidation of the melt proved to be useless. It was much more satisfactory to use a special gas mixture of 95% argon, 5% hydrogen, which was sufficiently reducing in nature to maintain the melt free surface scum-free, under a static 1 atmosphere pressure, for

Fig. 1.14 Crucible Liner Degradation

Over a period of a year, and 50 growth runs the vitreous carbon crucible began to flake at the top edge. This was easily removed prior to growth



the complete growth cycle. This was produced in the first stages of growth by continuously flushing the mixture through the chamber for ≈5 minutes, during which time any surface oxides of copper were completely reduced.

Only two side effects were originally conceivable with the introduction of hydrogen. The first was the explosive nature of the gas, but since the concentration of the hydrogen in the mixture was only just over the lower explosion level (4.65%)[81] this was not of great concern and it has never been a problem. And the second side effect was the possibility of atomic hydrogen being retained in the crystal as grown from the melt, diffusing to form gas bubbles and dislocating the lattice thereby. (The argon was very insoluble in copper[36] and was therefore not a problem). In a pure atmosphere of hydrogen the amount which is soluble in pure, liquid copper at 1083C is ≈5.3 cm^3/100g; the amount which is soluble in the solid at 1083C is ≈2.0 cm^3/100g.[82] Using Sievert's law of gas solubilities[83]:-

$$C_H = \left(KP_{H_2}\right)^{\frac{1}{2}} \qquad (1.4)$$

where, C_H is the solubility of the gas in the metal

K is a reaction rate constant (for $H_2 \longrightarrow 2\ H$)

P_{H_2} is the ambient pressure of hydrogen

H refers to atomic hydrogen

H_2 refers to molecular hydrogen

and assuming that the reaction rate constant K is independent of hydrogen pressure, then the hydrogen solubility values in liquid and solid copper at 1083C for a 95% Ar, 5% hydrogen mixture are 1.185cm^3/100g and 0.447cm^3/100g respectively.

Consequently, during crystallisation, the solid must lose 0.738 cm^3/100g of hydrogen to maintain equilibrium. This can only be done by diffusion mechanisms.

Hydrogen diffuses in crystalline copper by an interstitial mechanism[84] and this is therefore a comparatively rapid process. The crystals were finally grown at 1.2 cm/hr (to be explained later) or 3.33 μm/sec. Since the diffusion coefficient (D) of interstitial, atomic hydrogen in solid copper at around its melting point is $\approx 3.1 \times 10^{-4}$ cm^2/sec[85], the mean distance (X_t) the hydrogen can be reliably thought to diffuse in a time (t) of 1 second is given by[86]:-

$$X_t = (Dt)^{\frac{1}{2}} \qquad (1.5)$$

This yields a value for X_t of approximately 170 μm/sec, i.e. well above the growth rate and so hydrogen retention in the crystal lattice would not be expected, and the 0.738 cm^3/100g could feasibly be lost to the melt and/or surrounding ambient. In Bridgman grown crystals hydrogen induced dislocations have been observed, e.g. refer to the work of Young and Sherrill in reference(87). Here, such hydrogen rejection by the crystal was useful because it is easily possible to envisage the growing crystal, in the solid-liquid region, moving through a slightly higher hydrogen concentration than elsewhere owing to this rejected hydrogen. The possibility of local growth interface transient oxidants being reduced more quickly is therefore increased. In passing it is worthwhile mentioning that the impurity level of the grown crystals was below 1 ppm[88].

1.3.6iv Melt Surface Vibrations

During the early stages of this work it was noticed that the surface of the liquid copper charge vibrated intermittently. Such vibrations resulted in unusual topographic contrast; typically, patches of locally dislocated growth occurred as displayed in Fig. 1.15, and in many cases large volumes of a crystal would only give very weak anomalously transmitted beams of X-rays. (Fig. 1.15b shows this feature well.) Closer examination of the topographs in Fig. 1.15 further shows that when the vibrations stopped dislocation-free growth was resumed almost immediately; conversely, when the vibrations started again dislocations were produced. It therefore appears that once a neck has been grown and once dislocation-free growth has been established, then a further neck is unnecessary to re-establish such growth if it is ever lost. These observations fit in well with the work of Sworn and Brown[67], Steinemann and Zimmerli[66] and, Kamada and Tanner[76] who all recorded the effects of crystal-scum collisions and found them to be localised.

The particular sources of the vibrations and their elimination were as follows:-

i. The closed circuit cooling water was found to be pulsating. By switching over to mains water the vibrations diminished.

Fig. 1.15 The Deleterious Effect of Melt Vibrations

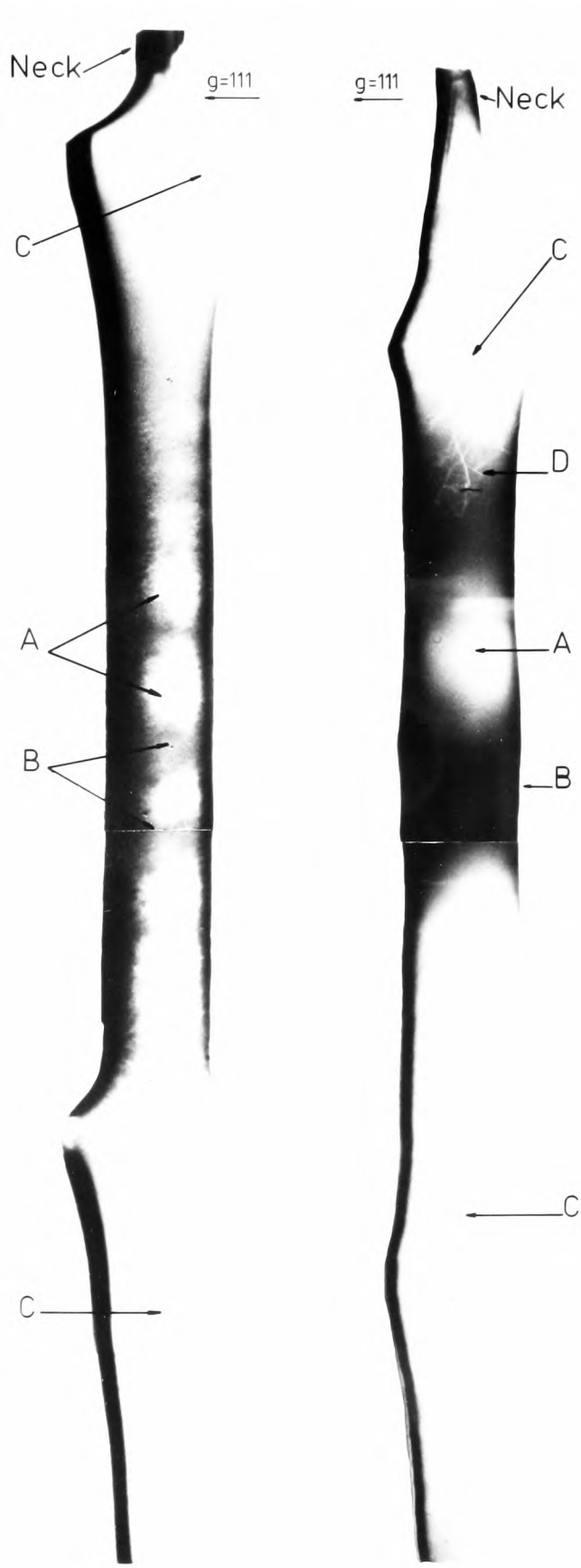
A. Local loss of perfection

B. Vibrations stop and dislocation-free growth resumed

C. Almost total loss of anomalous transmission arising from large vibrations

D. Dislocation propagation from the neck into the main body of the crystal

Length of the g-vector = $\frac{1}{2}$ mm


Neck
g=111
C
A
B
C
(a)
g=111
Neck
C
D
A
B
C
(b)

ii. Because of all the inherent moving parts the generator vibrated, causing such vibrations to be conducted to the melt through the floor and apparatus. A 3" thick foam rubber pad on which the complete puller was situated again reduced the vibrations.

iii. The R.F. work coil moved up and down slowly causing melt instability. This was securely clamped to the wall.

At this stage of rebuilding, the melt was perfectly clean on the surface and no melt vibrations could be detected. Also if any one of the above three steps were relaxed the vibrations returned.

1.3.6v. The Afterheater

It is clear from Fig. 1.6b that the afterheater was essentially eliminated by introducing the much shorter vitreous carbon liner. The afterheater length varied from 1 to 5 mm depending on the number of crystals already grown from the melt. In the original equipment the afterheater had been 3-4 cms long, the aim being to minimise longitudinal and radial temperature gradients in the crystal puller near to the region of crystal growth. Experimentally there was very good published evidence to suggest including the afterheater was very necessary, e.g. Sworn and Brown[67] could not grow dislocation-free copper crystals without one. Theoretically too the arguments for an afterheater were considerable. The most noted work in this field being that of Kobayashi and Arizumi[89] who calculated temperature distribution profiles in a Czochralski crystal under various conditions. They found that above a critical length of afterheater the crystal could actually receive radiation overall rather than lose it; hence, the conclusion was that the crystal would grow into a much improved thermal environment, and so possibly not dislocate by cooling stresses.

The prime reason for going against this previous work and growing crystals with such a short afterheater was so that diameter control, and especially neck diameter control, would be far easier; since it would then be possible to view the crystal normal to its growth axis and maintain continuous growth. The growth rate was lowered to 1.2 cm/hr and dislocation-free crystals were produced (Fig. 1.16) subject to conditions vii and viii to follow. In a further experiment it was noticed that once dislocation-free growth had been initiated at 1.2 cm/hr, the growth rate could be increased to 3 cm/hr without further loss of perfection (Fig. 1.17). This indicates that a slow growth rate was only a preliminary pre-requisite to dislocation-free growth; and, that the thermal stresses both at the growth front and in the as grown crystal body were insufficient to cause dislocation when the crystal grew faster. <110> growth axis dislocation-free crystals were also grown without any further problems as shown in Fig. 1.18. This last result fits in well with the work of Sworn and Brown[67] and, Tanner[74] who found that <111>, <110>, <100> and <123> crystals could all be grown dislocation-free. However, Fehmer and Uelhoff[54] found that only <100> crystals would grow dislocation-free. It is hard to advance reasons for this minor discrepancy; indeed the experimental tangle is still unravelled. The answer may be size effect and growth rate related, however.

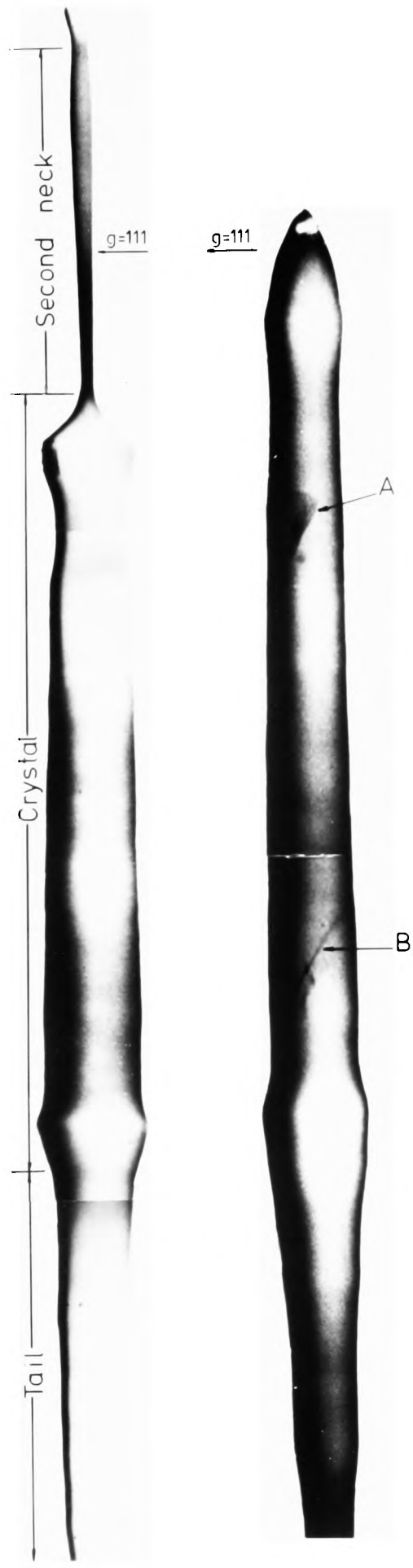
1.3.6vi. Crystal Rotation

This was stopped. All other authors have emphasised the need to rotate the seed and crystal, and so homogenise

Fig. 1.16 <123> Growth Axis Dislocation-free Crystals

Using a double necking procedure these completely dislocation-free crystals were grown at 1.2 cm/hr and without rotation. The intra-image contrast in (b) (regions A and B) arises from secondary, overlapping, Laue images

Length of g-vector = 0.75 mm



(a) (b)

Fig. 1.17 The Effect of Growth Rate on Perfection

Half of the crystal, in each case, was grown at 1.2 cm/hr and the other half was grown at 3 cm/hr. The result was that the crystals remained dislocation-free along the total length grown. A slow growth rate was therefore only initially necessary

Scale mark = 1mm

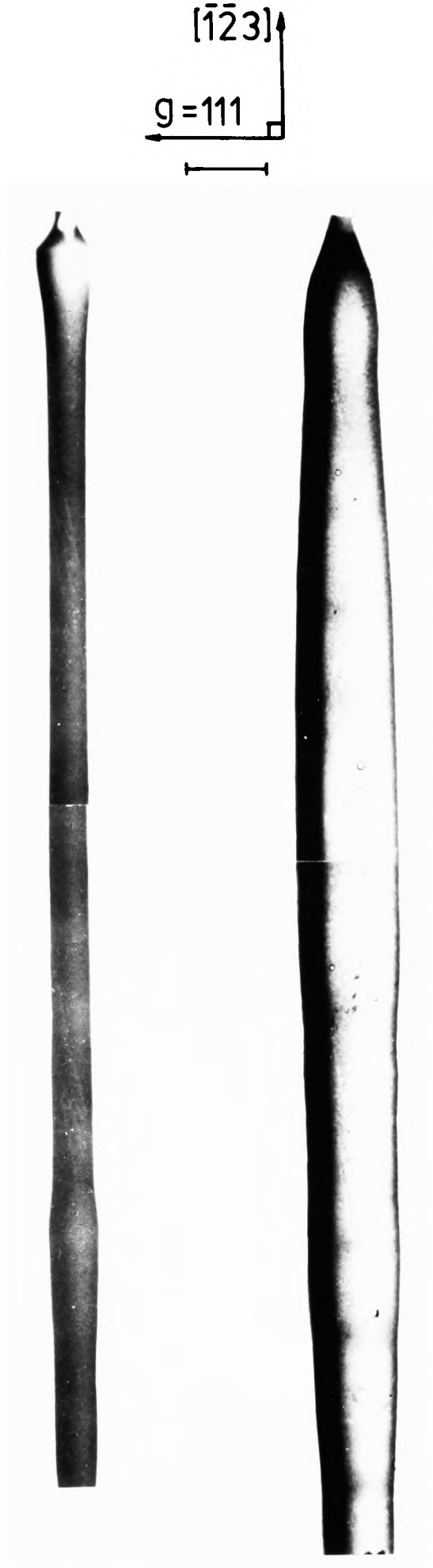
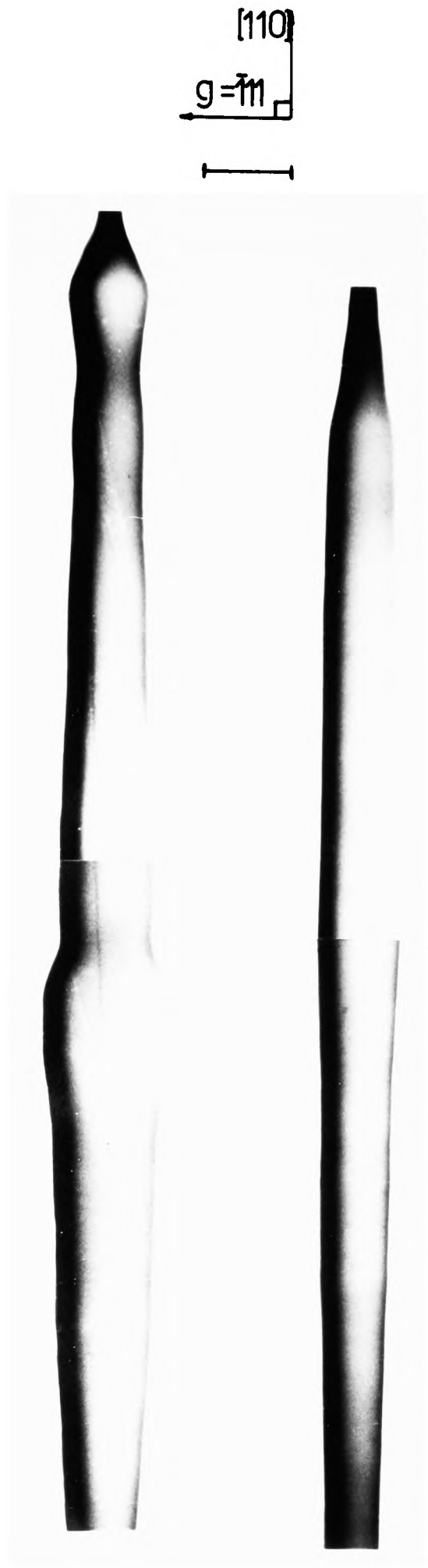

[1̄2̄3]
g=111

Fig. 1.18 <110> Growth Axis Dislocation-free Crystals

Contrary to the work of Fehmer and Uelhoff[52], these <110> crystals have been grown free from dislocations. These results are, however, supported by the work of Sworn and Brown[65], and Tanner[72]

Length of the g-vector = 1.2 mm


[110]
g = 111

radial temperature gradients (and hence stresses). Once again the experimental and theoretical evidence in support of crystal rotation was convincing. Excellent work by Penning[93] and, Nikitenko et al[94] has been done to show that if the isotherms in the crystal puller are not concentric with the growth axis of the crystal, then both shape and stress perturbations can occur leading to dislocation generation. Here, no adverse effects have ever been noted by cutting out rotation.

The major difference between these crystals and those grown by Fehmer and Uelhoff[54], for example, was one of size: the crystals described here occupied only 1/800 of the melt free surface area, whereas for Fehmer and Uelhoff this ratio was 1/36. Consequently, it can be argued, these crystals were not so susceptible to the melt temperature variations as the German crystals and larger crystals in general. It was additionally noticed that seed perfection, size and shape did not noticeably affect the final quality of the crystal: it was the neck which critically determined the final perfection.

1.3.6vii. "Double-necking"

A few dislocations always used to run into the dislocation-free volume of interest, thereby ruining the crystal for subsequent experiments. This effect is clearly shown in Fig. 1.12b and Fig. 1.15. Causes for this phenomenon are not specifically understood, but it was effectively controlled by a "double-necking" procedure, i.e. during growth a neck was grown; then the diameter was slightly increased to promote dislocation-free growth; a second neck was then grown

leaving behind the few remaining propagating dislocations; finally, the desired diameter and length of crystal was grown. Fig. 1.16a clearly shows the dislocations stopping at the end of the first diameter increase. Thereafter, dislocation-free growth proceeded. In later experiments the double-neck proved useful for handling the dislocation-free volume with tweezers.

1.3.6viii. The "Cooling Tail"

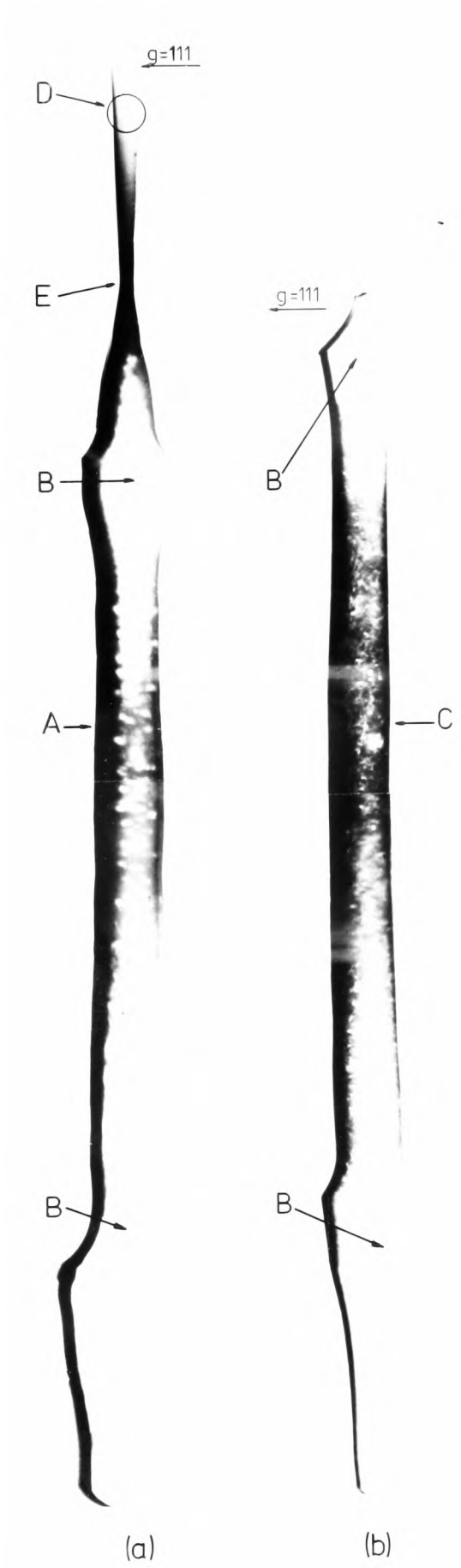
When the desired diameter and length of crystal had been grown the temperature of the melt was slowly increased to reduce the diameter. A cone was therefore grown which had the effect of slowly cooling the crystal down, i.e. cooling stresses were insufficient to dislocate the crystal and excess vacancies could migrate out of the crystal. If the diameter was suddenly reduced then defects were definitely generated throughout the crystal as shown in Fig. 1.19. A noticeable distribution of "spotty defects" was always recorded, Fig. 1.19a, and dislocations were sometimes imaged too, Fig. 1.19b.

Unfortunately the resolution limit (1μm) of the X-ray examination technique prohibits any definitive statement on the type of these "spotty defects". It is tempting to label them as large vacancy loops, but they are approximately 400μm in diameter which is rather large for a single loop. Other workers[95] have noticed such large loops in metals, however. They are more likely to be dislocation tangles and loops combined. Chapter IV provides much more experimental information on the likely origin, structure and type of these defects.

Fig. 1.19 The Effect of a Short Tail on Perfection

Short "tails" induced defects to be generated. These defects were sometimes "spotty" (e.g. region A in (a), and sometimes line defects (e.g. region C in (b)). The defect density was very diameter dependent (Compare regions A, B and E). Also, note that in (a) even the upper part of the neck had "spotty" defects generated in it (region D in (a)).

Length of the g-vector = 1.0 mm


g=111
D
E
B
A
B
(a)
g=111
B
C
B
(b)

Previous early research in this field by Penning[93] and Wagner[96] on semiconductor crystals has been convincing. Wagner, for instance, performed a very simple series of experiments by growing germanium crystals under high and low growth and cooling temperature gradients. Crystals grown under a high interfacial temperature gradient but cooled slowly suffered a much lower dislocation density than crystals grown under a high interfacial temperature gradient but cooled quickly. Metal crystals initially good enough for X-ray topography have also been examined during heating, at elevated temperatures and on subsequent cooling[95,96,97]. Representative work in this field by Nøst and Sorensen[95] has clearly shown that when aluminium crystals were cooled only a few degrees from 350C long straight dislocations lying in <110> directions were produced. As the temperature decreased the density of such defects increased, and as the rate of temperature fall increased the defect density markedly increased. Nøst and Sorensen argued these to be vacancy loops in a long row produced by a helical climb source such as that described by Amelinckx and Bontinck[99]. A critical vacancy supersaturation was required of 1.1 to promote this loop production, and the intervals between loops represented the times during which the vacancies had to be built up following the nucleation of a previous loop.

Consequently, cooling rates are extremely influential in determining the final defect densities of all types of crystal. Moreover, in this study the reason for the long tail is made further clear. Given these modifications no major problems have been experienced in growing dislocation-free copper crystals.

1.4 Conclusions

a. The crystal must only be in contact with its own continuously clean melt and its seed; otherwise dislocations occur. Hence, the Czochralski technique was very suitable for the production of dislocation-free crystals.

b. A "double-neck" was found to be necessary otherwise dislocation propagation into the volume of interest took place.

c. An afterheater and crystal rotation were unnecessary to promote the dislocation-free growth of small crystals; and seed perfection, size and shape were immaterial.

d. Melt vibrations and a "cooling tail" were to be eliminated and included respectively.

e. The inclusion of a reducing gas mixture, a molybdenum susceptor and a vitreous carbon liner produced the desired effect of eliminating melt surface contaminants completely.

1.5 Further Work Suggestions

There are very many ways in which the work previously discussed could be extended. A selection of these possible avenues of investigation will now be presented.

a. Dislocation-free crystals have been grown for almost twenty years now and it is still not known why the crystals should grow in this form. Intuitively, as mentioned previously (P.27), the dislocations are grown out by using a long thin neck: then, the dislocation-free crystal will not subsequently dislocate because the thermal stresses are too small. To examine the growth of a typical dislocation-free copper crystal

in situ would be rewarding. And the obvious way to do this would be in a synchrotron X-ray beam. Considerable thought would need to be brought to bear on crystal puller design, automation of the apparatus, etc., so that the X-ray plate exposure time would be less than the necessary growth rate. It would then be possible to study dislocation processes in the neck-crystal region during the critical stage of necking down. This would not be an easy experiment, but it would be potentially definitive.

b. Growing dislocation-free crystals is boring for the operator: this process should be completely automated. Methods are already available in the literature[101,102,103] to enable automation to be carried out when the crystal profile required is simply rectangular, i.e. for a cylindrical crystal. In this study it has been made demonstrably clear that for reasons of crystal cooling and subsequent experiments, a much more complicated profile is necessary, e.g. a "dog-bone". Such a profiling attachment would simply be a small computer which would be programmed with a particular desired profile to alter the power imput to the R.F. susceptor such that the temperature varied to yield this crystal profile. It would be necessary to either weigh or image the crystal at the solid-liquid interface, to allow a comparison between the actual crystal diameter and the programmed diameter to be made. This would allow compensatory action to be taken by the computer if deviations between the two occurred. A fully automatic crystal puller is definitely a prerequisite to any in situ synchrotron studies of dislocation-free growth.

c. There is no reason why other materials should not be grown dislocation-free by this method, e.g. zinc, nickel, gold. Also, alloys could be attempted, but to reduce the constitutional stresses the temperature difference between the solidus and liquidus must be small. The alloy must therefore be chosen carefully.

d. For many studies (e.g. deformation and diffusion experiments) a cylindrical crystal is not the best shape to use. Recently, a process known as edge-defined, film-fed growth[104, 105, 106] has been developed in which the liquid to be grown is seeded through a capillary former, the inside shape of which dictates the crystal shape. Hollow cylinders, square cylinders and polyhedral crystals have been produced by this method. By exercising care over the choice of materials to be grown and to act as a capillary, dislocation-free shaped crystals could be manufactured, which would lend themselves to easier experimentation than the cylindrical variety. In conjunction with this change it would be advantageous to redesign the crystal puller so that larger crystals could be grown (see, for example, the work of Fehmer and Uelhoff[54] on the growth of dislocation-free copper).

CHAPTER I REFERENCES

1. W. G. Pfann, "Zone Melting", Acad. Press, 1966

2. M. Avrami, J. Chem. Phys., 7, 1103, 1939

3. F. Minari, B. Pichaud and L. Capella, Phil. Mag., 31, 275, 1975

4. B. Nøst, Phil. Mag., 11, 183, 1965

5. M. Fremiot and G. Champier, C.R.A.S., Paris, 265, 1331, 1967

6. A. R. Lang and G. Meyrick, Phil. Mag., 4, 878, 1959

7. A. Authier, C. Rogers and A. R. Lang, Phil. Mag., 12, 547, 1965

8. G. K. Williamson and R. E. Smallman, Acta. Met., 1, 487, 1953

9. J. W. Christian, "The Theory of Phase Transformations in Metals", Pergamon Press, Oxford, 1965

10. P. Cotterill and P. R. Mauld, "Recrystallisation and Grain Growth", Surrey University Press, 1976

11. D. Michell and G. J. Ogilvie, Phy. Stat. Sol., (a) 15, 83, 1966

12. A. Fordeaux, A. Berghezan and W. Webb, J.A.P., 31, 918, 1960

13. S. S. Brenner, Acta. Met., 4, 62, 1956

14. G. W. Sears, J. Chem. Phys., 25, 637, 1955

15. W. W. Piper and S. J. Polich, J.A.P., 32, 1278, 1961

16. J. S. Shah in "Crystal Growth", Ed. B. R. Pamplin, Pergamon, 1975, opp. p.380

17. D. K. Wickenden and R. W. Brander, same as (16), Ch. 10

18. P. W. Bridgman, Proc. Amer. Acad. Arts Sci., 60, 305, 1925
D. C. Stockbarger, Rev. Sci. Instr., 7, 133, 1936
F. Stober, Z. Krist., 61, 299, 1925

19. S. Kyropoulos, Z. Phys., 63, 55, 1930
S. Kyropoulos, Z. Phys., 154, 308, 1926

20. P. H. Keck and M. J. E. Golay, Phys. Rev., 89, 1297, 1953

21. R. P. Poplawsky, J.A.P., 33, 1616, 1962

22. A. Verneuil, C.R.A.S., Paris, 135, 791, 1902

23. J. Czochralski, Z. Phys. Chem., 92, 219, 1918

24. R. J. C. Draper, "Crystal Growth", Ed. B. R. Pamplin, Pergamon, 1975, opp. p.498

25. D. Bartholomew, D. Phil. Thesis, University of Oxford, 1974

26. J. Budke, J. Sci. Instr., 34, 815, 1963

27. W. Bosenberg, Z. für Angew. Physik, 9, 347, 1957

28. P. Kapitza, Proc. Roy. Soc., 119A, 358, 1928

29. F. W. Young, J.A.P., 33, 963, 1962

30. F. W. Young, J.A.P., 3553, 1963

31. F. W. Young and J. R. Savage, J.A.P., 35, 1917, 1964

32. C. G. G'Sell and G. Champier, Phil. Mag., 32, 283, 1975

33. A. S. T. Badrick and K. E. Puttick, Phil. Mag., 23, 585, 1971

34. R. Vale, Ph.D. Thesis, University of Birmingham, 1976

35. A. R. Lang, Acta Met., 5, 358, 1957

36. J. C. Brice, "The Growth of Crystals from the Melt", North-Holland, 1967

37. J. C. Brice, "The Growth of Crystals from Liquids", North-Holland, 1973

38. A. C. Menzies and J. Skinner, "Crystal Growth" Disc. Farad. Soc., 5, 1949, p.306

39. P. F. Weller and D. M. Grandits, J.C.G., 12, 63, 1972

40. N. Miyamoto and J. Nishizawa, Sci. Rept. Ritu., B15, 13, 1963

41. J. E. A. Miltat, D. Phil. Thesis, University of Oxford, 1971

42. See for example:-
J. R. Patel and B. W. Batterman, J.A.P., 34, 2716, 1963
J. R. Patel, J.A.P., 44, 3903, 1973
J. R. Patel, "Int. Summer School on X-ray Dynamical Theory and Topography", Limoges, France, 1975

43. R. R. Haberecht and E. L. Kern, Semiconductor Silicon, Electrochemical Society, N.Y., 1969

44. H. Naramoto and K. Kamada, J.C.G., 24/25, 145, 1974

45. D. B. Gasson and B. Cockayne, J. Mat. Sci., 5, 100, 1970

46. R. P. Poplawsky, J.A.P., 33, 1616, 1962

47. H. Naramoto and K. Kamada, J.C.G., 30, 145, 1975

48. See for example:-
A. J. R. de Kock et al, J.C.G., 22, 311, 1974
A. J. R. de Kock et al, J.C.G., 28, 125, 1975

49. J. Goorissen, Philips Tech. Rev., 21, 185, 1959/60

40. T. B. Reed, J.A.P., 32, 2534, 1961

51. G. Busch and O. Vogt, Helv. Phys. Acta, 33, 437, 1960

52. S. Howe and C. Elbaum, Phil. Mag., 6, 1227, 1961

53. B. K. Tanner, Z. für Naturforsch, 289, 676, 1973

54. H. Fehmer and H. Uelhoff, J.C.G., 15, 195, 1972

55. F. H. Horn, J.A.P., 33, 1615, 1962

56. B. Cockayne, J. Mat. Sci., 4, 236, 1969

57. D. Richman, J. Phys. Chem. Sol., 24, 1131, 1963

58. P. C. Leung and W. P. Allred, J.C.G., 19, 356, 1973

59. T. E. Brown, Cavendish Laboratory, Cambridge, Priv. Comm.

60. C. H. Sworn, Ph.D. Thesis, University of Cambridge, 1971

61. W. C. Dash, J.A.P., 29, 736, 1958

62. W. C. Dash, J.A.P., 30, 459, 1959

63. J. C. Brice, "The Growth of Crystals from Liquids", North-Holland, 1973, p.239

64. B. Okkerse, Philips Tech. Rev., 21, 340, 1959

65. U. Zimmerli and Z. Steinemann, Z. für Angew. Phys., 30, 145, 1965

66. Z. Steinemann and U. Zimmerli, J. Phys. Chem. Sol., Supp. 1, 1, 1967

67. C. H. Sworn and T. E. Brown, J.C.G., 15, 195, 1972

68. B. K. Tanner, J.C.G., 16, 86, 1972

69. A. R. Lang, J.A.P., 30, 1748, 1959

70. G. Borrmann, W. Hartwig and H. Irmler, Z. für Naturforsch. 13a, 423, 1958

71. F. W. Young, T. O. Baldwin and A. Merlini, Phys. Rev., 163, 591, 1967

72. A. R. Lang, "Modern Diffraction and Imaging Techniques in Material Science", Ed. S. Amelinckx et al, North-Holland, 1969

73. G. H. Schwutke, I.B.M. Scientific Rept., Prepared for AFCRL, Number AFCRL-70-0110

74. B. K. Tanner, University of Durham, Priv. Comm.

75. F. W. Young and F. A. Sherrill, J.A.P., 42, 230, 1971

76. K. Kamada and B. K. Tanner, Phil. Mag., 29, 309, 1974

77. P. C. J. Gallagher, Ph.D. Thesis, University of Cambridge, 1964

78. Hultgren et al, "Selected Values of the Thermodynamic Properties of the Elements", A.S.M. Handbook, 1973

79. F. C. Cawlard and J. C. Lewis, J. Matl. Sci., 2, 507, 1967

80. R. I. Miller, J.C.G., 20, 310, 1970

81. C. R. C. "Handbook of Chemistry and Physics", 55th Edition, 1974-75, p.D86

82. C. J. Smithells, Ed: "Metals Ref. Book", III, p.606

83. L. Darken and R. Gurry, "Physical Chemistry of Metals", McGraw-Hill, 1953, p.132

84. J. D. Fast, "Gases in Metals", Philips Tech. Lib., N. V. Philips Gloeilampenfabricken, Eindhoven, 1976

85. W. Eichenauer, W. Löser and H. Witte, Z. Metallkunde, 56, 287, 1956

86. A. H. Cottrell, "An Introduction to Metallurgy", Arnold, 1967, p.152

87. F. W. Young and F. A. Sherrill, Canad. J. Phys., 45, 757, 1967

88. Supplied for the author by A. Y. Stathopoulos following spectrographic analysis at A.E.R.E. Harwell on a copper crystal grown from the same melt as the dislocation-free variety

89. N. Kobayashi and T. Arizumi, J.C.G., 13/14, 615, 1972

90. J. C. Brice, J.C.G., 2, 395, 1968

91. B. Cockayne et al, J. Matl. Sci., 4, 236, 1969

92. W. R. Runyan, Silicon Semiconductor Technology, McGraw-Hill, N.Y., 1965, p.29

93. P. Penning, Philips Res. Repts., 13, 79, 1958

94. V. I. Nikitenko and V. L. Indenbom, Soviet Phys.-Cryst., 6, 341, 1961

95. B. Nøst and G. Sorensen, Phil. Mag., 13, 1975, 1966

96. R. S. Wagner, J.A.P., 29, 1679, 1958

97. B. Nøst et al, "Crystal Growth", Suppl. to J. Phys. and Chem. of Solids, Ed. H. Peiser, 1967, 801

98. B. Baudelet and G. Champiers, Cryst. Lattice Defects, 4, 95, 1973

99. S. Amelinckx and W. Bontinck, Acta Met., 5, 345, 1957

100. M. Kuriyama, W. J. Boettinger and H. E. Burdette, 47, J.A.P., 5064, 1976

101. U. Gross and R. Kersten, J.C.G., 15, 85, 1972

102. R. C. Reinert and M. A. Yatsko, J.C.G., 21, 283, 1974

103. H. J. A. Van Dijk et al, Acta Electronica, 17, 1, 1974

104. H. E. Labelle, Mater. Res. Bull., 6, 581, 1971

105. B. Chalmers, H. E. Labelle and A. I. Mlavsky, J.C.G., 13/14, 84, 1972

106. V. A. Tatarchenko and G. A. Satunkin, J.C.G., 37, 285, 1977

CHAPTER II

THEORETICAL MODELLING OF CZOCHRALSKI CRYSTAL GROWTH

List of Symbols Used in This Chapter

L_c, L_n, L_s	Furthest distance of the crystal, neck and seed respectively from the melt free surface
R_c, R_n, R_s	Radii of the crystal, neck and seed respectively
A_c, A_n, A_s	Areas of the crystal, neck and seed respectively
T_A	Temperature of the ambient
T_M	Temperature of the melt
$T(z)$	Temperature at a point z in the model
$DT(z)$	Temperature gradient in the rod at a point z
DT_{MA}	Relative temperature drop
$DDT_c(0\text{-}L_c)$	Temperature gradient difference quotient
Δz	Element of the rod
c	Specific heat capacity
ϱ	Density
t	Time factor
K	Thermal conductivity
P	Circumference of the rod
h_R	General heat radiation coefficient
h_{Rc}, h_{Rs}	Heat radiation coefficients of the crystal and seed respectively
h_c	Convection constant
n	Constant
B_i	General Biot number
B_c, B_n, B_s	Biot numbers of the crystal, neck and seed respectively
C_{1-7}	Integration constants
σ	Stefan-Boltzmann constant
ϵ	Emissivity
(Q/A)	Heat radiated/unit area/second

CONTENTS

		Page Number
	Contents	52
2.1	Introduction	53
2.2	Formulation of the Model	54
2.3	Advantages and Limitations of the Model	60
2.4	Determination of Fundamental Constants relevant to the Model	62
2.5	Introduction to the Two Types of Simulation carried out	64
2.6a	Radiation Changes	64
2.6a.i	The Non-Radiating Case	65
2.6a.ii	A Comparison of the Low and High Radiating Cases	67
2.6b	Geometric Changes of the Seed, Neck, Crystal, i.e. Fat, Thin, Short, Long?	69
2.6b.i	The Seed	70
1.	Varying the Seed Length	70
2.	Varying the Seed Radius	70
2.6b.ii	The Neck	71
1.	Varying the Neck Length	71
2.	Varying the Neck Radius	72
2.6b.iii	The Crystal	74
1.	Varying the Crystal Length	74
2.	Decreasing the Crystal Radius	74
3.	Increasing the Crystal Radius	75
2.7	Conclusions	76
2.8	Suggestions for Further Work	78
	Appendix A	79
	Appendix B	80
	References	83

2.1 Introduction

It was shown in Chapter I that Czochralski crystal growth could be reliably and repeatedly used to manufacture dislocation-free copper crystals under fairly relaxed crystal growing conditions. It was also pointed out that specific growth profiles were necessary to produce the desired dislocation-free crystal, e.g. a thin neck before the actual crystal was mandatory, and a long "cooling tail" was required. From a heat flow standpoint it is intuitively easy to understand the general reasons for a neck and a tail, i.e. the neck is a heat flow resistance which reduces heat conduction up the crystal by virtue of its small cross-sectional area; and the tail allows the crystal to cool down slowly, thereby minimising cooling stresses.

Clearly, in a growing crystal the thermal stresses which it inevitably experiences can be of sufficient magnitude to produce dislocations either directly at the growth front, or, during cooling (see Fig . 1.19, - for examples). In this work it was profitable to study the crystal growth regime from a theoretical standpoint more fully, because the factors most influencing dislocation-free Czochralski crystal growth have never been fully elucidated.

A simple new model has been derived with which temperature and temperature gradient distributions in the seed, neck and crystal could be studied; also, with the aid of the model, the analysis was broadened to include copper, silver, germanium and silicon (i.e. the four main materials to be grown dislocation-free) so that key similarities and differences

could be highlighted; and finally, the model was used to show which parameters (e.g. crystal dimensions, radiation losses, etc.) are important in determining the thermal history of Czochralski crystals.

Past theoretical analyses of the temperature and temperature gradient distributions in a Czochralski crystal[1-7] have always been restrictively applied to a single element, and the thermal behaviour of different elements has not been compared. In addition, although it is widely held that the neck critically controls the inception of dislocation-free growth in both metals and semiconductors[8-14], no systematic study of neck diameter and length influence on temperature gradients has been performed previously.

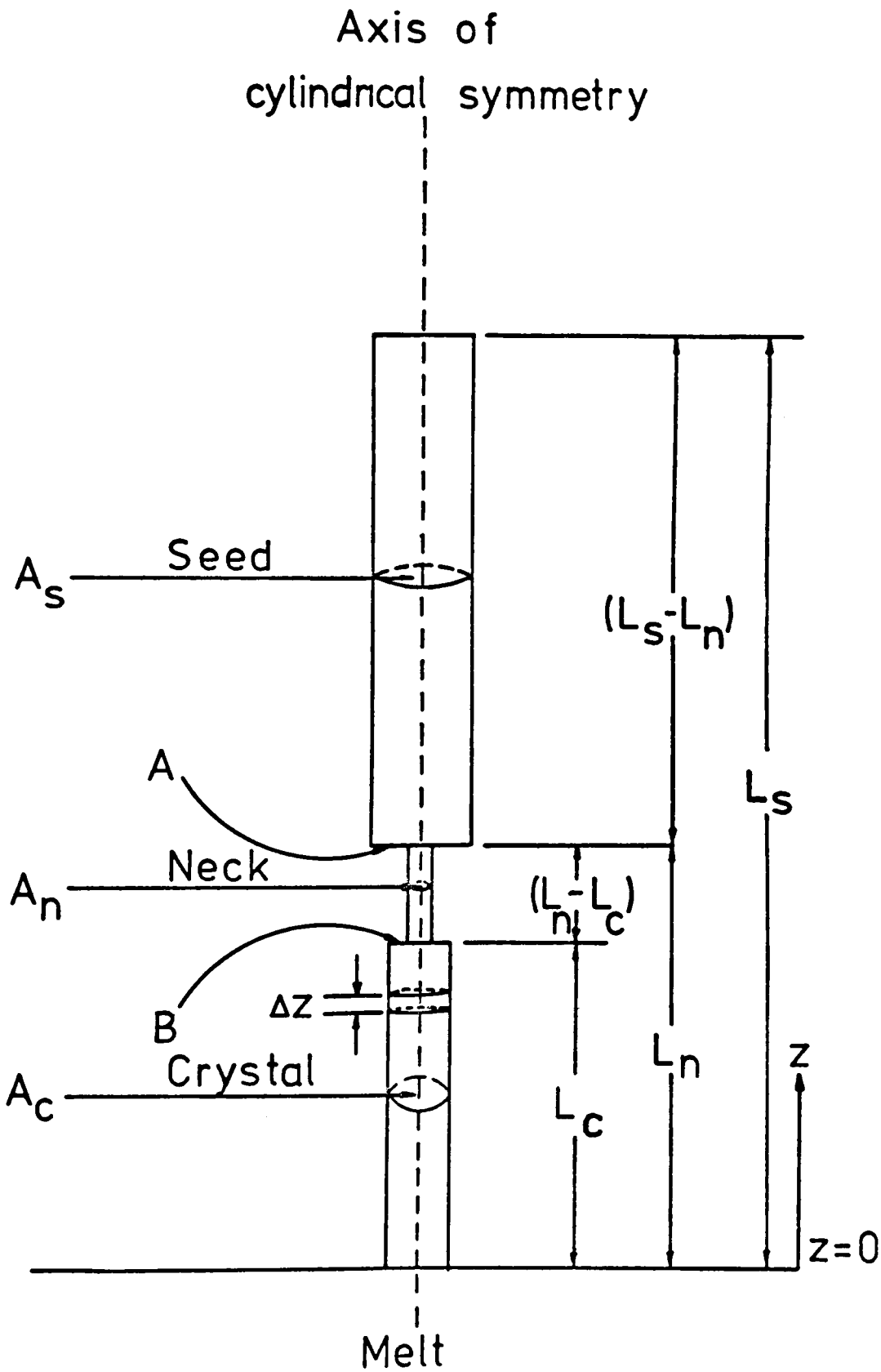
2.2 Formulation of the Model

Consider a seed, neck and crystal to be "sitting" on a liquid as in Fig. 2.1. Let the element in the liquid, seed, neck and crystal be the same throughout and assume the model to exhibit cylindrical symmetry, with the longitudinal axes of the seed, neck, crystal and liquid being coincident. Then, let the crystal have a length L_c and cross sectional area A_c; let the neck have a length (L_n-L_c) and cross sectional area A_n; and let the seed have a length (L_s-L_n) and cross sectional area A_s. Assume that the crystal grows into a constant ambient temperature T_A, and that only two heat transfer processes occur:-

i. Conduction up the crystal

ii. Radiation from surfaces such as A and B in Fig. 2.1

Fig. 2.1 The Crystal Growth Model


Axis of
cylindrical symmetry
Seed
A_s
(L_s-L_n)
A
L_s
Neck
A_n
(L_n-L_c)
B
Δz
Crystal
A_c
L_n
z
L_c
z=0
Melt

Assuming radial temperature gradients are negligible (see Section 2.3) the heat flow equation for a cylindrical rod is[13]:-

$$c\rho\frac{A\partial T(z)}{\partial t} = \frac{KA\partial^2 T(z)}{\partial z^2} - h_R P(T(z)-T_A) \qquad 2.1$$

where, c = specific heat capacity of the element considered

ρ = density

A = cross sectional area of the rod

$T(z)$ = temperature at a given point z in Fig. 2.1

t = time factor

K = thermal conductivity

h_R = a heat radiation coefficient

T_A = ambient temperature

P = circumference of the rod

(The complete derivation of equation 2.1 can be found in Appendix A)

Equation 2.1 consists of three terms:-

i. The left hand side which describes the heat lost with time from an infinitesimal element of the rod Δz, Fig. 2.1.

ii. The first right hand side term which accounts for the rate of gain of heat by the element due to thermal conduction up the rod.

iii. The second right hand side term. When $T_A \approx T(z)$, as is normally the case in practice, $(T(z)-T_A)$ is a good approximation to the Stefan-Boltzmann Law, $(T(z)^4-T_A^4)$.

In the time independent condition, i.e. when $\frac{\partial T(z)}{\partial t} = 0$, equation 2.1 reduces to:-

$$\frac{d^2T(z)}{dz^2} = \frac{\partial^2 T(z)}{\partial z^2} = n^2(T(z)-T_A) \qquad 2.2$$

where, $$n^2 = \left(\frac{h_R P}{KA}\right) = \left(\frac{2h_R}{RK}\right) = \left(\frac{2B_i}{R^2}\right) \qquad 2.3$$

R = radius of the rod

$B_i = \left(\frac{h_R P}{K}\right)$ and is called the Biot number 2.4

(The Biot number gives a measure of the proportion of radiative to conductive heat losses, and is a dimensionless quantity)

The solution of 2.2 is:-

$$T(z) = T_A + C_1 \text{Cosh}\left(\frac{(2B_i)^{\frac{1}{2}}}{R} z\right) + C_2 \text{Sinh}\left(\frac{(2B_i)^{\frac{1}{2}}}{R} z\right) \quad 2.5$$

where C_1 and C_2 are integration constants

Given that the diameters of the seed, neck and crystal remain constant along their lengths, then for each of these three sections an expression such as 2.5 may be written:-

$$\text{i.} \quad T_c(z) = T_A + C_1 \text{Cosh}\left(\frac{(2B_c)^{\frac{1}{2}}}{R_c} z\right) + C_2 \text{Sinh}\left(\frac{(2B_c)^{\frac{1}{2}}}{R_c} z\right)$$

$$\text{ii.} \quad T_n(z) = T_A + C_3 \text{Cosh}\left(\frac{(2B_n)^{\frac{1}{2}}}{R_n} z\right) + C_4 \text{Sinh}\left(\frac{(2B_n)^{\frac{1}{2}}}{R_n} z\right) \quad 2.6$$

$$\text{iii.} \quad T_s(z) = T_A + C_5 \text{Cosh}\left(\frac{(2B_s)^{\frac{1}{2}}}{R_s} z\right) + C_6 \text{Sinh}\left(\frac{(2B_s)^{\frac{1}{2}}}{R_s} z\right)$$

where the subscripts c, n, s refer to the crystal, neck and seed respectively

The constants C_1-C_6 were determined from a set of boundary conditions which were chosen as follows:-

$$\text{i.} \quad z = 0, \; T_c(o) = T_M$$

$$\text{ii.} \quad z = L_c, T_c(L_c) = T_n(L_c)$$

$$\text{iii.} \quad KA_c \frac{dT_c}{dz}(L_c) = KA_n \frac{dT_n}{dz}(L_n) + h_{Rc}(A_c - A_n)(T_c(L_c) - T_A)$$

$$\text{iv.} \quad z = L_n, \; T_n(L_n) = T_s(L_n) \quad 2.7$$

$$\text{v.} \quad KA_n \frac{dT_n}{dz}(L_n) = KA_s \frac{dT_s}{dz}(L_s) + h_{Rs}(A_s - A_n)(T_n(L_n) - T_A)$$

$$\text{vi.} \quad z = L_s, \; T_s(L_s) = T_A$$

Substituting 2.7(i) into 2.6(i):-

$$C_1 = (T_M - T_A) \quad 2.8$$

Hence,

$$T_c(z) = T_A + (T_M - T_A) \text{Cosh}\left(\frac{(2B_c)^{\frac{1}{2}}}{R_c} z\right) + C_2 \text{Sinh}\left(\frac{(2B_c)^{\frac{1}{2}}}{R_c} z\right) \quad 2.9$$

Substituting 2.7(vi) into 2.6(iii)

$$C_5 = - C_6 \text{Sinh}\left(\frac{(2B_s)^{\frac{1}{2}}}{Rs} L_s\right) \quad 2.10$$

Whence,

$$T_s(z) = T_A + C_7 \text{ Sinh } \left(\frac{(2B_s)^{\frac{1}{2}}}{R_s}(L_s - z)\right) \qquad 2.11$$

Where,

$$C_7 = \frac{-C_6}{\text{Cosh}\left(\frac{(2B_s)^{\frac{1}{2}}}{R_s} Ls\right)} \qquad 2.12$$

Using the remaining boundary conditions to set up equations in C_2, C_3, C_4 and C_7:-

$\underline{z = L_c}$, $T_c(L_c) = T_n(L_c)$

Equating 2.6(i) to 2.6(ii) at $z = L_c$,

$$C_3\left(\text{Cosh } \left(\frac{(2B_n)^{\frac{1}{2}}}{R_n} L_c\right)\right) + C_4\left(\text{Sinh } \left(\frac{(2B_n)^{\frac{1}{2}}}{R_n} L_c\right)\right) - C_2\left(\text{Sinh } \left(\frac{(2B_c)^{\frac{1}{2}}}{R_c} L_c\right)\right) =$$

$$(T_M - T_A)\text{Cosh}\left(\frac{(2B_c)^{\frac{1}{2}}}{R_c} L_c\right) \qquad 2.13$$

$$\underline{z=L_c}, \quad KA_c \frac{dT_c(L_c)}{dz} = KA_n \frac{dT_n(L_c)}{dz} + h_{Rc}(A_c - A_n)(T_c(L_c) - T_A)$$

Equating derivatives of 2.6(i) and 2.6(ii) at $z = L_c$,

$$C_3\left(KA_n \frac{(2B_n)^{\frac{1}{2}}}{R_n} \text{Sinh}\left(\frac{(2B_n)^{\frac{1}{2}}}{R_n} L_c\right)\right) + C_4\left(KA_n \frac{(2B_n)^{\frac{1}{2}}}{R_n} \text{Cosh}\left(\frac{(2B_n)^{\frac{1}{2}}}{R_n} L_c\right)\right) +$$

$$C_2\left(h_{Rc}(A_c - A_n)\text{Sinh}\left(\frac{(2B_c)^{\frac{1}{2}}}{R_c} L_c\right) - KA_c \frac{(2B_c)^{\frac{1}{2}}}{R_c} \text{Cosh}\left(\frac{(2B_c)^{\frac{1}{2}}}{R_c} L_c\right)\right) = \qquad 2.14$$

$$\left(KA_c \frac{(2B_c)^{\frac{1}{2}}}{R_c}(T_M - T_A)\text{Sinh}\left(\frac{(2B_c)^{\frac{1}{2}}}{R_c} L_c\right) - h_{Rc}(A_c - A_n)(T_M - T_A) \text{x} \text{Cosh}\left(\frac{(2B_c)^{\frac{1}{2}}}{R_c} L_c\right)\right.$$

$\underline{z = L_n}$, $T_n(L_n) = T_s(L_n)$

Equating 2.6(ii) to 2.6 (iii) at $z = L_n$,

$$C_3\left(\text{Cosh}\left(\frac{(2B_n)^{\frac{1}{2}}}{R_n} L_n\right)\right) + C_4\left(\text{Sinh } \left(\frac{(2B_n)^{\frac{1}{2}}}{R_n} L_n\right)\right) - C_7\left(\text{Sinh}\left(\frac{(2B_s)^{\frac{1}{2}}}{R_s}(L_s - L_n)\right)\right) = 0 \qquad 2.15$$

$\underline{z = L_n}$,

$$KA_n \frac{dT_n(L_n)}{dz} = KA_s \frac{dT_s(L_n)}{dz} + h_{Rs}(A_s - A_n)(T_s(L_n) - T_A)$$

Again, inserting the first derivatives of 2.6(ii) and 2.6(iii) into the above condition and reducing to a simple form,

$$C_3\left(KA_n\frac{(2B_n)^{\frac{1}{2}}}{R_n}\,\mathrm{Sinh}\,\left(\frac{(2B_n)^{\frac{1}{2}}}{R_n}L_n\right)\right) + C_4\left(KA_n\frac{(2B_n)^{\frac{1}{2}}}{R_n}\,\mathrm{Cosh}\,\left(\frac{(2B_n)^{\frac{1}{2}}}{R_n}L_n\right) + \right. \qquad 2.16$$

$$\left. C_7\left(KA_s\frac{(2B_s)^{\frac{1}{2}}}{R_s}\,\mathrm{Cosh}\,\left(\frac{(2B_s)^{\frac{1}{2}}}{R_s}(L_s-L_n)\right) - h_{Rs}(A_s-A_n)\mathrm{Sinh}\,\left(\frac{(2B_s)^{\frac{1}{2}}}{R_s}(L_s-L_n)\right)\right) =\right.$$

The temperature at every point in the model is given by solving the four simultaneous equations 2.13, 2.14, 2.15 and 2.16 for C_2, C_3, C_4, C_7 and then using equations 2.6. For convenience 2.13, 2.14, 2.15 and 2.16 were solved numerically on the University Computer (an ICL 1906A) by writing these equations in matrix form (see Appendix B for the programme) as follows:-

$$
\begin{bmatrix}
-\sinh\left[\left(\frac{2B_n}{R_n}\right)^{\frac{1}{2}} L_c\right] & 0 & 0 \\
\left[h_{Rc}(A_c-A_n)\sinh\left[\left(\frac{2B_c}{R_c}\right)^{\frac{1}{2}} L_c\right] - KA_c\left(\frac{2B_c}{R_c}\right)^{\frac{1}{2}}\cosh\left[\left(\frac{2B_c}{R_c}\right)^{\frac{1}{2}} L_c\right]\right] & 0 & 0 \\
0 & -\sinh\left[\left(\frac{2B_s}{R_s}\right)^{\frac{1}{2}} (L_s-L_n)\right] & 0 \\
0 & \left[\left(\frac{2B_s}{R_s}\right)^{\frac{1}{2}} LA_s\cosh\left[\left(\frac{2B_s}{R_s}\right)^{\frac{1}{2}} (L_s-L_n)\right] - h_{Rs}(A_s-A_n)\sinh\left[\left(\frac{2B_s}{R_s}\right)^{\frac{1}{2}} (L_s-L_n)\right]\right] & 0
\end{bmatrix}
\begin{bmatrix} C_3 \\ C_4 \\ C_2 \\ C_7 \end{bmatrix}
=
\begin{bmatrix}
(T_M-T_A)\cosh\left[\left(\frac{2B_c}{R_c}\right)^{\frac{1}{2}} L_c\right] \\
KA_c\left(\frac{2B_c}{R_c}\right)^{\frac{1}{2}}(T_M-T_A)\sinh\left[\left(\frac{2B_c}{R_c}\right)^{\frac{1}{2}} L_c\right] - h_{Rc}(A_c-A_n)(T_M-T_A) \times \cosh\left[\left(\frac{2B_c}{R_c}\right)^{\frac{1}{2}} L_c\right] \\
0 \\
0
\end{bmatrix}
$$

$$\begin{bmatrix} \cosh\left[\left(\frac{2B_n}{R_n}\right)^{\frac{1}{2}} L_c\right] & \sinh\left[\left(\frac{2B_n}{R_n}\right)^{\frac{1}{2}} L_c\right] \\ \left(\frac{2B_n}{R_n}\right)^{\frac{1}{2}} KA_n \sinh\left[\left(\frac{2B_n}{R_n}\right)^{\frac{1}{2}} L_c\right] & \left(\frac{2B_n}{R_n}\right)^{\frac{1}{2}} KA_n \cosh\left[\left(\frac{2B_n}{R_n}\right)^{\frac{1}{2}} L_c\right] \\ \cosh\left[\left(\frac{2B_n}{R_n}\right)^{\frac{1}{2}} L_n\right] & \sinh\left[\left(\frac{2B_n}{R_n}\right)^{\frac{1}{2}} L_n\right] \\ \left(\frac{2B_n}{R_n}\right)^{\frac{1}{2}} KA_n \sinh\left[\left(\frac{2B_n}{R_n}\right)^{\frac{1}{2}} L_n\right] & \left(\frac{2B_n}{R_n}\right)^{\frac{1}{2}} KA_n \cosh\left[\left(\frac{2B_n}{R_n}\right)^{\frac{1}{2}} L_n\right] \end{bmatrix}$$

The values of C_1 to C_7 being determined, it was then possible to define the first derivatives of 2.16 (i.e. the temperature gradients) as follows:-

$$\text{i.} \quad DT_c(z) = -\frac{dT_c(z)}{dz} = -C_1\frac{(2B_c)^{\frac{1}{2}}}{R_c}\,\text{Sinh}\,(\frac{(2B_c)^{\frac{1}{2}}}{R_c}z) - C_2\frac{(2B_c)^{\frac{1}{2}}}{R_c}\,\text{Cosh}\,(\frac{(2B_c)^{\frac{1}{2}}}{R_c}z)$$

$$\text{ii.} \quad DT_n(z) = -\frac{dT_n(z)}{dz} = -C_3\frac{(2B_n)^{\frac{1}{2}}}{R_n}\,\text{Sinh}\,(\frac{(2B_n)^{\frac{1}{2}}}{Rn}z) - C_4\frac{(2B_n)^{\frac{1}{2}}}{R_n}\,\text{Cosh}\,(\frac{(2B_n)^{\frac{1}{2}}}{R_n}z) \qquad 2.18$$

$$\text{iii.} \quad DT_s(z) = -\frac{dT_s(z)}{dz} = -C_7\frac{(2B_s)^{\frac{1}{2}}}{R_s}\,\text{Cosh}\,(\frac{(2B_s)^{\frac{1}{2}}}{R_s}(L_s-z)$$

2.3 Advantages and Limitations of the Model

The model considers heat flow in one direction (z) in a three dimensional body. Thus the temperature distribution is a function not only of the lengths but also of the radii of the seed, neck and crystal (equation 2.6).

Over the lengths considered ambient temperatures are seldom constant and to assume so is therefore erroneous. In turn such an error would influence $(T(z)-T_A)$ in 2.1: but unless a finite difference numerical analysis method is employed (see Fox[17]), the varying ambient temperature cannot easily be incorporated into the model. It is similarly arguable why the Stefan-Boltzmann function $(T(z)^4-T_A^4)$ cannot also be included in this study.

By its very nature crystal growth is a time dependent process, thereby rendering expressions (2.6) incomplete. However, it has been shown that[3] at z = 0 (for a long crystal) the

error involved in such an omission is, at a maximum estimate, about 20% of $DT_c(o)$ under static conditions, i.e. with the temperature dependence included $DT_c(o)$ increases by 20%. Consequently, care must be exercised over the interpretation of the absolute values generated by the computations: yet it is still beneficial to use this model for study, because influences and trends in thermal behaviour can be examined.

If the model is essentially "quasi-linear" and if the radial temperature gradients are of negligible consequence, then clearly the model best simulates the small crystal situation. In particular, the radial and longitudinal dimensions can be no more than approximately 4 mm and 100 mm respectively. If these dimensions are exceeded then first the above considerations become important; and secondly, the computer results have no meaning, e.g. $DT_c(L_c) > 0$. Furthermore, if large crystals are to be studied (e.g. 2 cm in diameter and 30 cm long) then recourse must be made to the methods of Kobayashi and Arizumi[5] or Brice[2]. The former authors' excellent model treated the two dimensional problem of heat flow (cylindrical symmetry was assumed) by solving a Laplacian equation of the type:-

$$\nabla^2 T = 0 \qquad 2.19$$

by a numerical analysis method, subject to very rigorous boundary conditions. Brice[2] and Billig[1] on the other hand, relaxed the boundary conditions so that radiation was accounted for by a $(T(z)-T_A)$ term and analytically solved 2.19. The radial element of the heat flow was incorporated into these latter models by a series of Bessel functions. All of the models, however, considered the crystal to be a free-standing cylinder on its own liquid, i.e. the neck and seed were omitted from the analysis.

This thesis considers for the first time a mathematical theory for the complete Czochralski seed-neck-crystal system. Although the mathematics is approximate, the approximations are considered to be valid for the small diameter crystals studied.

2.4 The Determination of Fundamental Constants Relevant to the Model

Before any calculations were performed values had to be assigned to L_c, L_n, L_s, R_c, R_n, R_s, h_{Rs}, h_{Rc}, B_i and T_A for the four elements chosen. The geometric constants were easy to determine: the values chosen were representative of the kind of copper crystal grown by the author, as shown in Table 2.1. It is acknowledged that silicon and germanium rarely conform to these dimensions (3" in diameter and 3' long is the norm!), but for reasons of compatibility with the model (the small crystal situation is being discussed) and ease of comparison such values were considered appropriate.

Ambient growth temperatures (T_A) were not to hand in the literature for Si, Ge and Ag, meaning that arbitrary values had to be assigned to T_A for these three elements. For the case of copper, Sworn[4] measured the temperature of the growth ambient versus distance away from the melt free surface. Over the distance considered in this model ($\approx$10 cm in toto) the temperature averaged over $\approx$10 cm in Sworn's puller was $\approx$980C. In Fig. 2.2 it is readily seen that a similar value held for the author's crystal puller. Consequently, T_A for copper was chosen to be 983C. Furthermore, so that each element experienced the same temperature drop between the melt and the ambient, a new

TABLE

THE BASIC VALUES USED

Property → / Element ↓	A_c (mm^2)		A_n (mm^2)		A_s (mm^2)		K^*	T_M^*
	R_c (mm)	L_c (mm)	R_n (mm)	L_n (mm)	R_s (mm)	L_s (mm)	(W/mm/K)	(C)
	3.141		7.068×10^{-2}		2.827×10^{1}		0.363	961.9
Ag	1.0	20	0.15	23	3.0	83		
	3.141		7.068×10^{-2}		2.827×10^{1}		0.342	1083.0
Cu	1.0	20	0.15	23	3.0	83		
	3.141		7.068×10^{-2}		2.827×10^{1}		1.67×10^{-2}	937.4
Ge	1.0	20	0.15	23	3.0	83		
	3.141		7.068×10^{-2}		2.827×10^{1}		2.51×10^{-2}	1410.0
Si	1.0	20	0.15	23	3.0	83		

* Values Taken From Reference 18

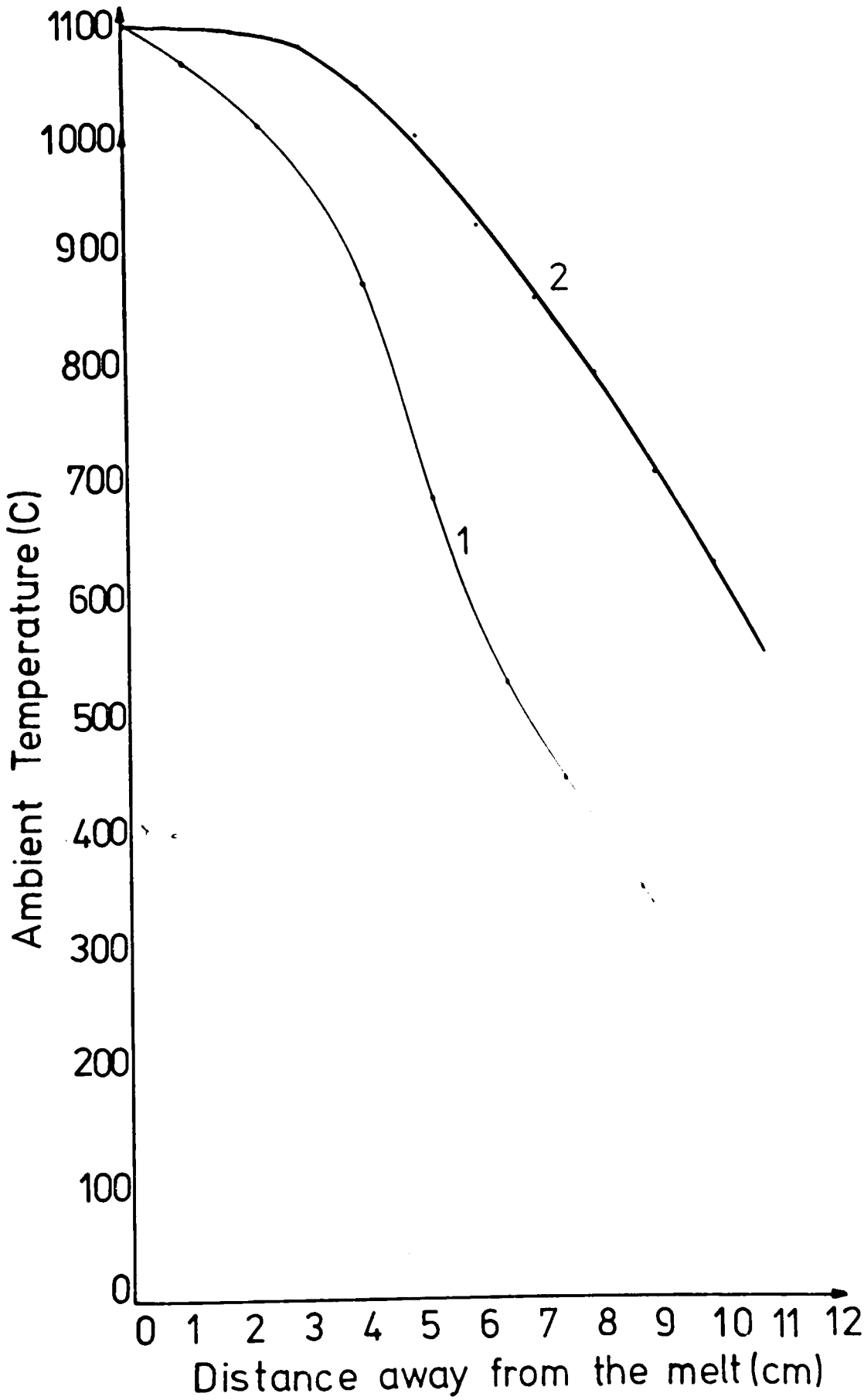
2.1

IN THE CALCULATIONS

(Heat radiation coefficient was arbitrarily increased by a factor of 14 between the low and high radiation cases.)

T_A	DT_{MA}	ϵ^*	$h_{Rs} = h_{Rc}$	B_i
(C)		(At 0.65μm)	($W/mm^2/K$)	Crystal Neck Seed
872.0	0.907	0.07	2.678×10^{-5}	7.37×10^{-5} 1.658×10^{-6} 6.631×10^{-4}
			Low Radiation	
			3.749×10^{-4}	1.03×10^{-3} 2.31×10^{-5} 9.26×10^{-3}
			High Radiation	
983.0	0.907	0.10	5.05×10^{-5}	1.47×10^{-4} 3.30×10^{-6} 1.32×10^{-3}
			Low Radiation	
			7.07×10^{-4}	2.05×10^{-3} 4.61×10^{-5} 1.84×10^{-2}
			High Radiation	
850.2	0.907	0.53	1.912×10^{-4}	1.44×10^{-2} 2.564×10^{-4} 0.1025
			Low Radiation	
			2.676×10^{-3}	0.1596 3.39×10^{-3} 1.4361
			High Radiation	
1279.0	0.907	0.46	4.421×10^{-4}	1.769×10^{-2} 3.98×10^{-4} 0.1592
			Low Radiation	
			6.189×10^{-3}	0.2476 5.57×10^{-3} 2.2805
			High Radiation	

Fig. 2.2 The variation of the ambient temperature with distance away from the melt free surface for the puller described in Chapter I without an afterheater, 1. With an afterheater, 2.


1100
1000
900
800
700
600
500
400
300
200
100
0
Ambient Temperature (C)
0 1 2 3 4 5 6 7 8 9 10 11 12
Distance away from the melt (cm)
1
2

parameter (the relative temperature drop = DT_{MA}) was defined which would circumvent the lack of information in the literature for the other three elements:-

$$DT_{MA} = \frac{(T_M - T_A)}{T_A} \qquad 2.20$$

For copper, DT_{MA} was 0.907 (T_M = 1083C, T_A = 983C); hence, T_A for the Si, Ge and Ag could be calculated using DT_{MA} for copper and the respective values of T_M.

T_A being known it was then possible to assign values to the heat radiation coefficients h_{Rs}, h_{Rc} ($h_{Rs} = h_{Rc}$) as follows. It is customary to use the well known Stefan-Boltzmann distribution to describe radiated energy losses:-

$$(Q/A) = \sigma \epsilon (T(z)^4 - T_A^4) \qquad 2.21$$

where (Q/A) is the energy radiated/unit area/second
σ is Stefan's constant
ϵ is the emissivity of the radiating body
$T(z)$ is the temperature of the radiating body
T_A is the temperature of the surrounding medium

When, however, $T_A \approx T(z)$ it is justifiable to use a simplified version of 2.21 (see Grober, Erk and Grigull[16]):-

$$(\frac{Q}{A}) = h_R(T(z) - T_A) \qquad 2.22$$

Where h_R can be derived by equating 2.21 to 2.22 to produce:-

$$h_R = \sigma\epsilon(T(z)^3 + T(z)^2 T_A + T(z)T_A^2 + T_A^3) \qquad 2.23$$

h_R is not a constant and in these simulations T(z) was approximated to T_M for each element so that the value for h_R was representative of the whole crystal.

Since $h_{Rc} = h_{Rs}$ was then known for every element considered, B_c, B_n and B_s were easily calculable from expression 2.4. Table 2.1 lists the values for h_{Rs}, h_{Rc} and also the Biot numbers which were used in these calculations.

2.5 Introduction to the Two Types of Simulation Carried Out

Perturbations may be included in the model in two distinct ways:-

a. Radiation changes via B_i

b. Geometric changes via L_c, L_n, L_s, R_c, R_n, R_s

In consequence, the results and associated discussion will therefore take the following form: an appraisal of the non-radiating case; a comparison of the low and the high radiating cases, and finally, a study of the way in which crystal temperature gradients may be reduced by careful control of the crystal-neck-seed sizes. This latter analysis was aimed at ameliorating the condition where crystals must be grown under a harsh thermal environment (for instance, when the radiation losses are very high) and the only means available of reducing $DT_c(z)$ is by geometric control alone.

2.6a Radiation Changes

The radiation changes were chosen to be always positive with respect to the crystal, implying that the crystal always suffered a radiative heat loss. This particular approach differed from that of Kobayashi and Arizumi[5] in that it was a special case of their more general study where the crystal could lose or gain a net heat radiation flux, e.g. in the radiation gain condition the afterheater of the crystal puller was long and effective. All of the other remaining computer simulations of Czochralski growth have assumed the radiation losses to be positive with respect to the crystal too.

2.6a.i. The Non-Radiating Case

This is the limiting case for which conduction is the only heat transfer mode considered.

The salient features depicted in Fig. 2.3a show that the seed, neck and crystal sub-divide into three well defined regions, this being an inherent part of the model (refer to equations 2.6). At the junctions of the crystal-neck and neck-seed the temperature gradient was discontinuous as seen in Fig. 2.3b. Obvious also is the fact that the greatest temperature drop and therefore the greatest temperature gradient occurred in the neck: the smallest of both these parameters was always to be found in the seed. It is therefore clear that the neck, by virtue of its relatively small diameter, acted as a very effective thermal resistance in all the cases studied. In reality, of course, the discontinuity monitored in the temperature gradients would never occur because the transition from the crystal to the neck, for example, would be much more gradual than the model allows. Suffice it to observe here that the change in the temperature gradient in these regions would be as rapid as the change in cross sectional area.

For each of the elements considered $DT_c(z)$ was always less than 1 C/mm, and in Fig. 2.3b it is interesting to note that the crystals of germanium and silver displayed similar characteristics, e.g. $DT_c(z)$ was 0.545 C/mm in Ge and 0.516 C/mm in Ag (from Table 2.2.). Viewed overall the $DT_c(z)$ values increased in the order Ge-Ag-Cu-Si, and in this respect the two metals were bounded by the two semi-conductors. This latter trend was directly linked to the (T_M-T_A) variation, thus

TABLE 2.2

Property → / Element ↓	$DT_c(z)$ C/mm	$DT_n(z)$ C/mm	$DT_s(z)$ C/mm	$DT_c(z) : DT_n(z) : DT_s(z)$	$\frac{1}{A_c} : \frac{1}{A_n} : \frac{1}{A_s}$
Ag	0.561	24.971	6.243×10^{-2}	9:400:1	9:400:1
Cu	0.625	27.777	6.944×10^{-2}	9:400:1	9:400:1
Ge	0.545	24.221	6.055×10^{-2}	9:400:1	9:400:1
Si	0.818	36.388	9.097×10^{-2}	9:400:1	9:400:1

$B_i = 0$ i.e. The No Radiation Condition

Fig. 2.3 The Non-Radiating Case (N)

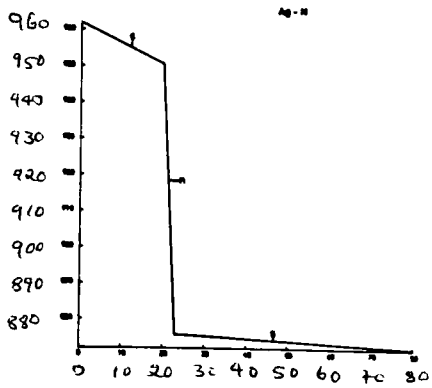
a. Temperature (T) versus distance (z)

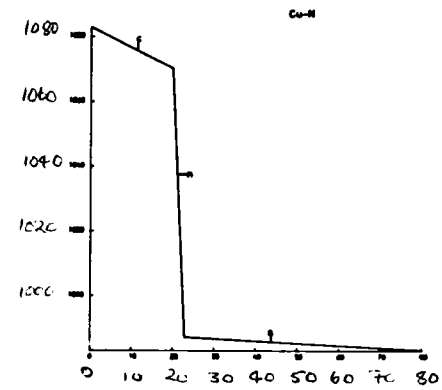
The greatest temperature drop and therefore temperature gradient always occurred in the neck

b. Temperature gradient (DT) versus distance (z)

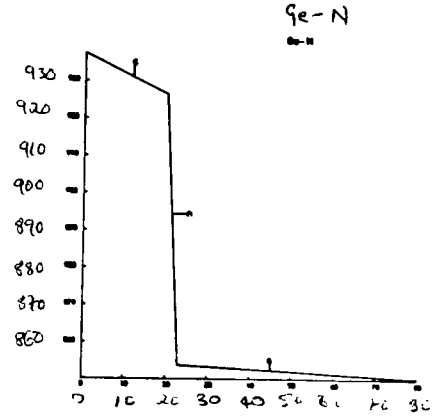
The temperature gradients were discontinuous at the crystal-neck and seed-neck boundaries, this being an inherent part of the model (Equations 2.6)

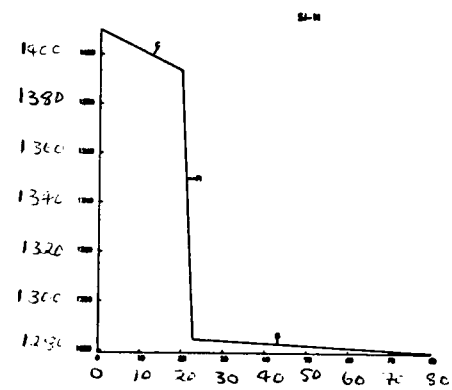
c = crystal; n = neck; s = seed


960
950
940
930
920
910
900
890
880
0 10 20 30 40 50 60 70 80

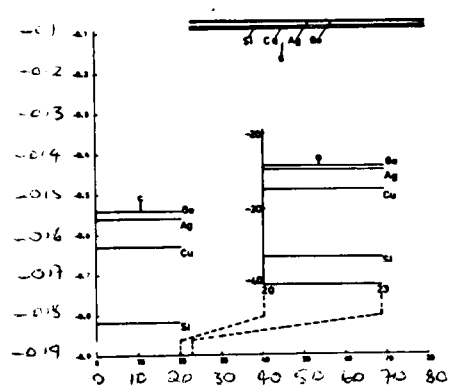

1080
1060
1040
1020
1000
0 10 20 30 40 50 60 70 80

Ge-N


930
920
910
900
890
880
870
860


1400
1380
1360
1340
1320
1300
0 10 20 30 40 50 60 70 80

(a)


Au
Ag
Cu
Si
0 10 20 30 40 50 60 70 80

(b)

implying that to effect intrinsic reductions in $DT_c(z)$ values then (T_M-T_A) must be small, i.e. an afterheater would be advantageous. Further, from the boundary conditions in 2.7, when $h_{Rc} = h_{Rs} = 0$ then:-

$$A_c \frac{dT_c(L_c)}{dz} = A_n \frac{dT_n(L_n)}{dz}$$

and,

$$A_n \frac{dT_n(L_n)}{dz} = A_s \frac{dT_s(L_n)}{dz} \qquad 2.24$$

The temperature gradients consequently varied with the area ratios as $\frac{1}{A_c} : \frac{1}{A_n} : \frac{1}{A_s}$ and this is shown in the results in Table 2.2. It is now pertinent to add that if the area ratios control the relative magnitudes of $DT_c(z) : DT_n(z) : DT_s(z)$ then their absolute magnitudes were dictated by (T_M-T_A) as shown above. In this simulation, therefore, the thermal conductivity was a redundant quantity; also, to reduce crystal temperature gradients (T_M-T_A) must be minimised and $A_c : A_n$ must be maximised: these conclusions are to be expected, but they are also important as indicated in Chapter I. There it was shown that a long thin neck was a very necessary prerequisite to dislocation-free growth (p.41), and that the price to be paid for greatly reducing the afterheater length was a reduction in growth rate. This latter measure obviously increased (T_M-T_A) as shown in Fig. 2.2. thereby increasing the temperature gradient and stress on the stationary crystal. When the crystal grew, the radiative and convective losses which it could sustain before dislocating were consequently reduced.

2.6a.ii. A Comparison of the Low and the High Radiating Cases

(ARBITRARY CHANGE)

Low ——— x14 ———→ High

$$B_c = \begin{bmatrix} 7.37 \times 10^{-5} & (Ag) \\ 1.47 \times 10^{-4} & (Cu) \\ 1.14 \times 10^{-2} & (Ge) \\ 1.76 \times 10^{-2} & (Si) \end{bmatrix} \qquad B_c = \begin{bmatrix} 1.03 \times 10^{-3} & (Ag) \\ 2.05 \times 10^{-3} & (Cu) \\ 0.1596 & (Ge) \\ 0.2476 & (Si) \end{bmatrix}$$

In both radiation conditions the crystal-neck-seed suffered a positive radiation loss. Furthermore, the Biot numbers have been given different values from element to element because what is low radiation for germanium, say, would be incomparably high for silver if they were all the same. As a result, although the absolute radiation losses are different in each case, in terms of the relative radiation loss that the material sustains these values render the elements comparable. Taking such conditions as read, the aim of this low-high radiation comparison was to highlight the principal differences to be expected when the crystal growth environment was harsh, i.e. B_i was very large, compared to when it was not so harsh, i.e. B_i was small but finite; in practice this could be effected by utilising a short or a long afterheater respectively.

Under a low radiating condition silicon and germanium displayed very similar interfacial temperature gradients, i.e. from Table 2.3 and Fig. 2.4 *$DT_c(0)$ was 4.3 C/mm in silicon and 4.14 C/mm in germanium. The metals too were similar but they were not so well correlated as in the semi-conductor case, i.e. $DT_c(0)$ was 0.675 C/mm in copper and 0.592 C/mm in silver.

*The field of view in this figure and in all subsequent figures has been purposefully restricted to 33 mm in the horizontal direction to enable a better appreciation of crystal-neck thermal characteristics to be produced. In later work it will be adequately shown that the seed remains of little determining influence as far as $DT_c(0)$ values are concerned, and so such a step was justified.

TABLE

COMPARISON OF THE LOW-HIGH

Property / Element	$DT_c(0)$ C/mm L.R.	$DT_c(0)$ C/mm H.R.	% Increase Between $DT_c(0)$ LR & HR	$DT_c(L_c)$ C/mm L.R.	$DT_c(L_c)$ C/mm H.R.	$DDT_c(0\text{-}L_c)$ L.R.
Ag	0.592	0.975	64.6	0.559	0.531	0.059
Cu	0.675	1.307	93.6	0.621	0.574	0.086
Ge	4.149	18.450	344	0.293	2.303×10^{-2}	13.16
Si	4.300	20.990	388	0.566	1.781×10^{-2}	6.59

Low B_c = $\begin{bmatrix} 7.37\times10^{-5} & (Ag) \\ 1.47\times10^{-4} & (Cu) \\ 1.14\times10^{-2} & (Ge) \\ 1.76\times10^{-2} & (Si) \end{bmatrix}$ ——— x14 ———→

ARBITRARY CHANGE.

2.3

RADIATION CONDITIONS (L.R.⟶H.R.)

$DDT_c(0\text{-}L_c)$ H.R.	$DT_n(L_c)$ C/mm L.R.	$DT_n(L_c)$ C/mm H.R.	% Diff.in $DT_n(L_c)$ HR & LR	$DT_s(L_n)$ C/mm L.R.	$DT_s(L_n)$ C/mm H.R.	% Diff.in $DT_s(L_n)$ HR & LR
0.836	24.90	24.04	3.4	6.22×10^{-2}	6.00×10^{-2}	3.53
1.277	27.663	26.24	5.1	6.91×10^{-2}	6.54×10^{-2}	5.35
800	16.258	1.531	90.5	3.87×10^{-2}	1.97×10^{-3}	94.9
1177	28.565	5.16	81.9	6.97×10^{-2}	7.90×10^{-3}	88.6

⟶ High B_c = $\begin{bmatrix} 1.03\times10^{-3} & (Ag) \\ 2.05\times10^{-3} & (Cu) \\ 0.1596 & (Ge) \\ 0.247 & (Si) \end{bmatrix}$

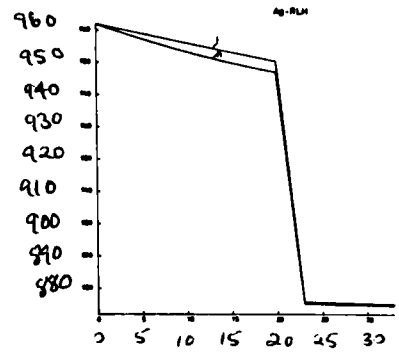
Fig. 2.4 The Low-High Radiation Comparison (RLH)

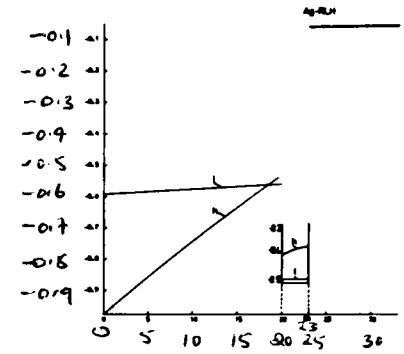
a. T(z) - vs - z

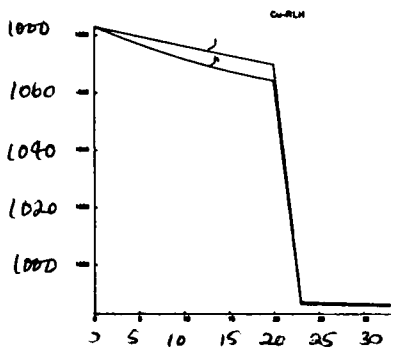
b. DT(z)- vs - z

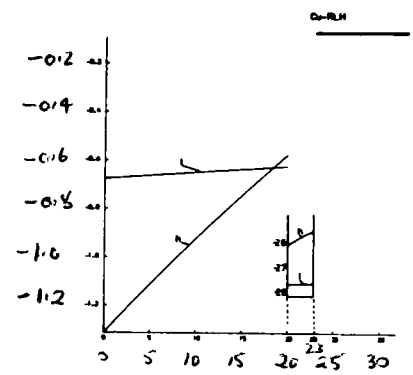
The semiconductors were much more susceptible to radiation changes than metals. This susceptibility, in turn, reduced the thermal resistance effectiveness of the neck for germanium and silicon but not so much for the metals

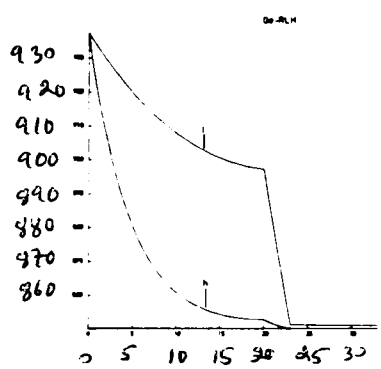
l = low radiation; h = high radiation

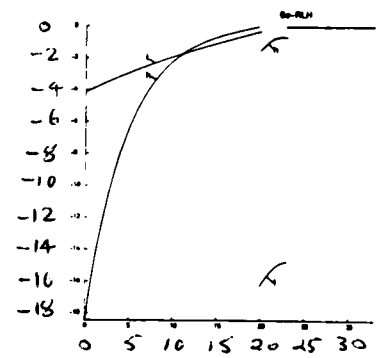

960
950
940
930
920
910
900
890
880
0 5 10 15 20 25 30

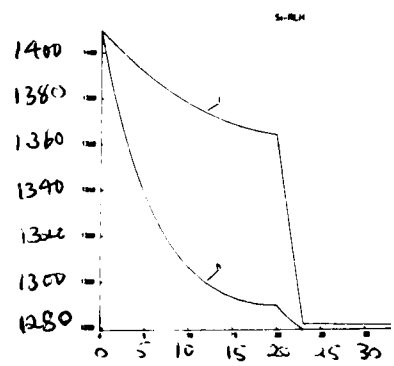

-0.1
-0.2
-0.3
-0.4
-0.5
-0.6
-0.7
-0.8
-0.9
0 5 10 15 20 25 30


1000
1060
1040
1020
1000
0 5 10 15 20 25 30

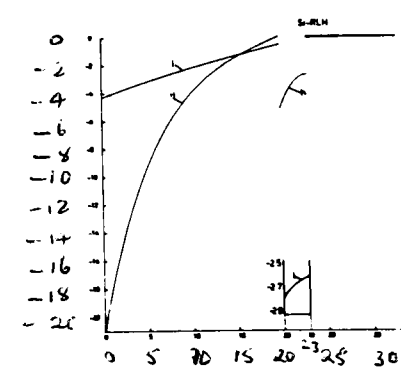

-0.2
-0.4
-0.6
-0.8
-1.0
-1.2
0 5 10 15 20 25 30


930
920
910
900
890
880
870
860
0 5 10 15 20 25 30


0
-2
-4
-6
-8
-10
-12
-14
-16
-18
0 5 10 15 20 25 30


1400
1380
1360
1340
1320
1300
1280
0 5 10 15 20 25 30

(a)


0
-2
-4
-6
-8
-10
-12
-14
-16
-18
-20
0 5 10 15 20 25 30

(b)

It is therefore clear that the metals and semi-conductors do order into two well defined groups once the radiation condition has been imposed. This is to be contrasted to the non-radiating condition where such division was not apparent.

Fig. 2.4a shows that the change from a low to high radiating situation in semi-conductors was much more pronounced than in metals; for example, from Table 2.3 $DT_c(0)$ for silver was raised by 64.6%, whereas in germanium the increase in $DT_c(0)$ was 344%. As a direct result of this the temperature gradients in the neck were correspondingly reduced further, e.g. for the two examples chosen above, $DT_n(L_c)$ for silver was decreased by 3.4% and for germanium 90.5% (Table 2.3). Clearly, these changes were directly dependent on the Biot number; and it is also clear that the metals were least affected by the radiation changes. The imposition of increasingly higher radiation losses was therefore to increasingly diminish the importance of the neck in the semi-conductors, but nowhere near as much in the metals. Again this was a Biot number linked response, with the thermal resistance effectiveness of the neck in silicon (B_c = 0.2476), for instance, being approximately five times less than the copper ($B_c = 2.05 \times 10^{-3}$), as measured by the relative $DT_n(L_c)$ values from Fig. 2.4b and Table 2.3.

The information in Fig. 2.4b also exhibits another interesting trend: as the radiation level increased so the temperature gradient difference quotient ($DDT_c(0\text{-}L_c)$) defined by:-

$$DDT_c(0\text{-}L_c) = (DT_c(0) - DT_c(L_c))/DT_c(L_c) \qquad 2.25$$

also increased quite markedly. Typically, in germanium the value of $DDT_c(0\text{-}L_c)$ was 13.16 when B_c was 1.14×10^{-2} and 800 when B_c was 0.1596; while in silver, $DDT_c(0\text{-}L_c)$ was 0.059 when B_c was 7.37×10^{-5} and 0.836 when B_c was 1.03×10^{-3} (Table 2.3). These results imply that the range of temperature gradients in the semi-conductors was much broader than in the metals, and the effect of raising the radiation level was to accentuate this phenomenon. In practical terms the difference between the two types of crystal growth action becomes a lot more obvious now: since the $DT_c(z)$ values in the semi-conductors fall so rapidly as z increases, Fig. 2.4b, only a relatively short afterheater is required, while in a metal the $DT_c(z)$ magnitudes were alike throughout the length of the crystal and so a relatively long afterheater would be needed to minimise $DT_c(z)$ over the whole crystal. Also, in this context, it is pertinent to add that the value of $DT_c(L_c)$ was 2.30×10^{-2} C/mm in germanium and 1.78×10^{-2} C/mm in silicon; on the other side, the $DT_c(L_c)$ values were 0.574 C/mm in copper and 0.531 C/mm in silver.

The seed was of minor interest since the large perturbations imposed affected $DT_s(L_n)$ only slightly, e.g. in silicon and copper in going from a low to a high radiating environment $DT_s(L_n)$ decreased by a mere 6.78×10^{-2} C/mm and 3.70×10^{-3} C/mm respectively, Table 2.3. (The % change values give little indication of response in this context.)

2.6b Geometric Changes of the Seed, Neck, Crystal, i.e. Fat, Thin, Short, Long?

It is far easier, experimentally speaking, to generate a high radiation loss situation than a low radiation loss condition, e.g. by removal of the afterheater (thereby increasing

(T_M-T_A) and so B_i) and/or by growing irregularly shaped crystals (thereby increasing the surface area to volume ratio). Consequently, if the high radiation loss condition can be adequately controlled by careful manipulation of the seed-neck-crystal dimensions then the low radiation loss case simply becomes a more pronounced version of this one. The underlying theme throughout the study was one of reducing $DT_c(z)$ by such control. The results from the study presented here will consider the influence of each part of the model in turn on $DT_c(z)$ values.

In all the figures used in the discussion below "b" and "a" imply before and after the imposed perturbation respectively.

2.6b.i. The Seed

1. Varying the Seed Length

Fig. 2.5 shows that changes in the seed length had a negligible effect on temperature gradients in the crystal; typically, in silver and copper the increase in $DT_c(0)$ was≈1.0%, and in silicon and germanium 0.0% as shown in Table 2.4.

2. Varying the Seed Radius

Again the effect of this reduction was minimal in the metals ($DT_c(0)$ decreased by 4.8% in Ag and 3.5% in Cu) and not detectable in the semi-conductors (Fig. 2.6 and Table 2.5). In the seed the temperature gradients underwent a large % increase, Table 2.5, of approximately 265% in all cases. Evenso, the absolute magnitude of $DT_s(L_n)$ remained small, e.g. 0.238 C/mm

TABLE 2.4

Property / Element	$DT_c(0)$ °C/mm Before	$DT_c(0)$ °C/mm After	% Diff. in $DT_c(0)$ Before and After	$DT_s(L_n)$ °C/mm Before	$DT_s(L_n)$ °C/mm After	% Change in $DT_s(L_n)$
Ag	0.975	0.988	1.33	6.0×10^{-2}	6.12×10^{-2}	2.00
Cu	1.307	1.319	0.91	6.54×10^{-2}	6.65×10^{-2}	1.68
Ge	18.45	18.45	0.0	1.97×10^{-3}	1.96×10^{-3}	0.50
Si	20.99	20.99	0.0	7.90×10^{-3}	7.85×10^{-3}	0.69

Reducing L_s from 83 mm to 43 mm

High B_c

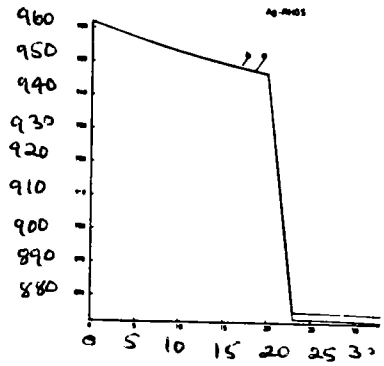
Fig. 2.5 Reducing the Seed Length from 60 mm to 20 mm (RHGS)

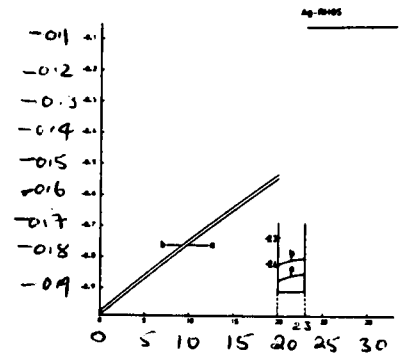
a. T(z) - vs - z (C-vs-mm)

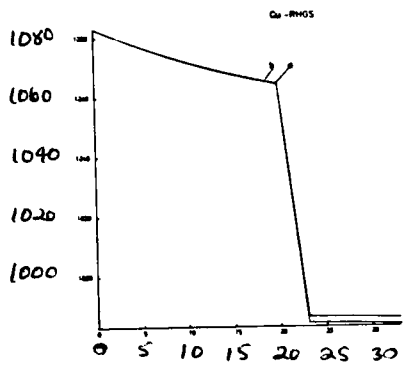
b. DT(z) - vs - z (C/mm - vs - mm)

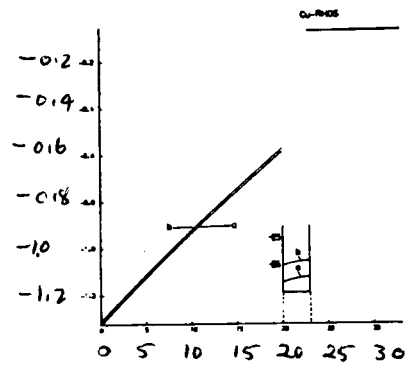
$DT_c(0)$ values were only slightly affected in metals; in semiconductors this change produced no visible effect

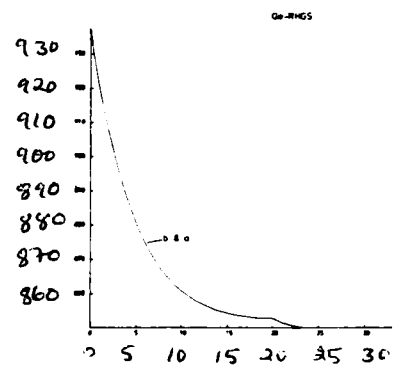
b = before; a = after

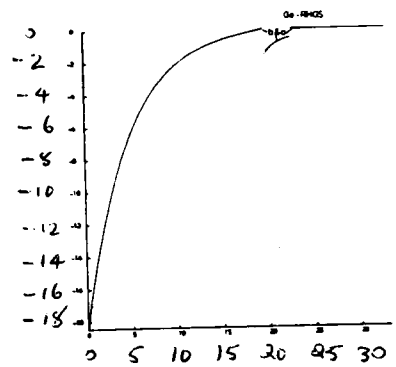

960
950
940
930
920
910
900
890
880
0 5 10 15 20 25 30

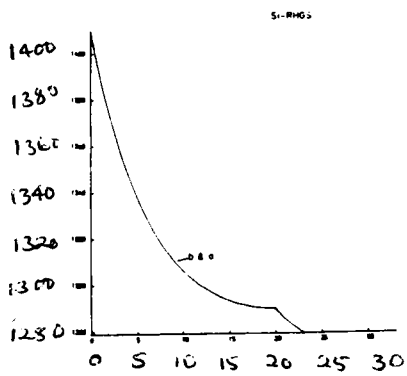

-0.1
-0.2
-0.3
-0.4
-0.5
-0.6
-0.7
-0.8
-0.9
0 5 10 15 20 25 30

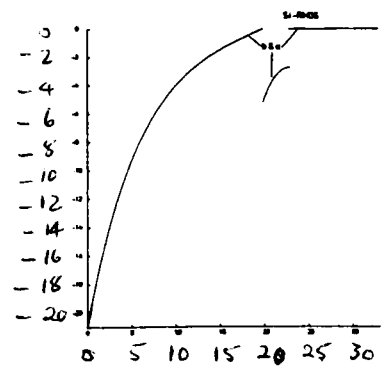

1080
1060
1040
1020
1000
0 5 10 15 20 25 30


-0.2
-0.4
-0.6
-0.8
-1.0
-1.2
0 5 10 15 20 25 30


930
920
910
900
890
880
870
860
0 5 10 15 20 25 30


-2
-4
-6
-8
-10
-12
-14
-16
-18
0 5 10 15 20 25 30


1400
1380
1360
1340
1320
1300
1280
0 5 10 15 20 25 30


-2
-4
-6
-8
-10
-12
-14
-16
-18
-20
0 5 10 15 20 25 30

(a) (b)

TABLE 2.5

Property / Element	$DT_c(0)$ C/mm Before	$DT_c(0)$ C/mm After	% Change in $DT_c(0)$ Before:After	$DT_s(L_n)$ C/mm Before	$DT_s(L_n)$ C/mm After	% Diff. in $DT_s(L_n)$ Before: After
Ag	0.975	0.928	4.8	6.54×10^{-2}	0.238	263
Cu	1.307	1.216	3.51	6.00×10^{-2}	0.217	261
Ge	18.45	18.45	0.00	1.97×10^{-3}	7.23×10^{-3}	261
Si	20.99	20.99	0.00	2.94×10^{-2}	7.90×10^{-2}	271

Reducing A_s by a Factor of 4
High B_c

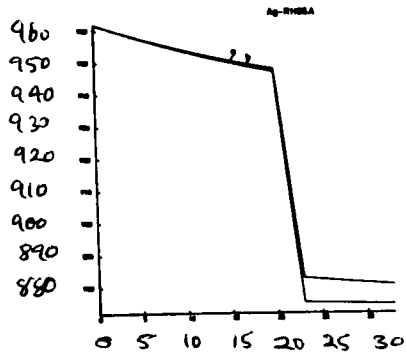
Fig. 2.6 Reducing the Seed Radius by a Factor of 2 from 3 mm to 1.5 mm (RHGSA)

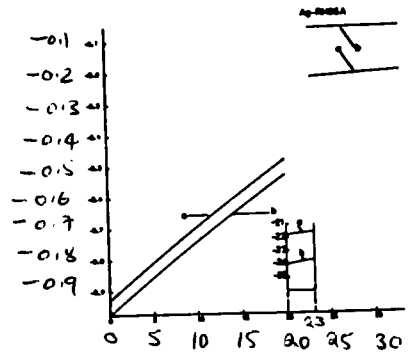
a. T(z) - vs - z (C-vs-mm)

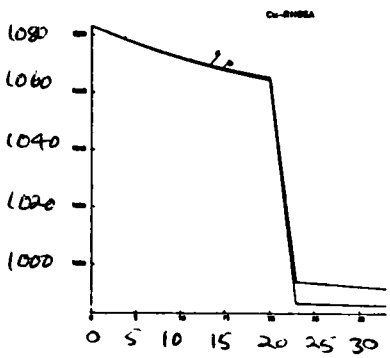
b. DT(z) - vs - z (C_{mm}-vs-mm)

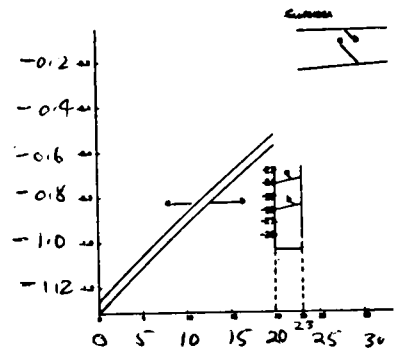
No change in semiconductor distributions was observed, whilst in the metals only a small decrease in $DT_c(z)$ could be obtained

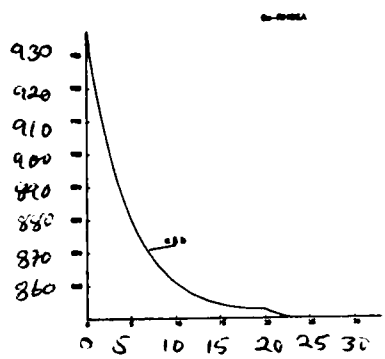
b = before; a = after

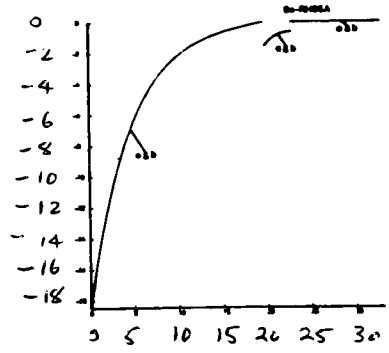

960
950
940
930
920
910
900
890
880
0 5 10 15 20 25 30

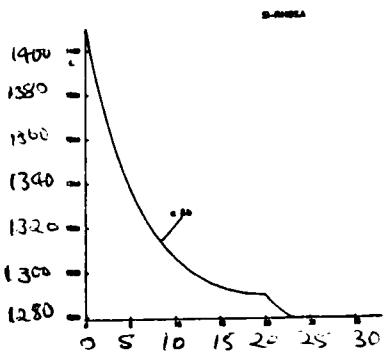

−0.1
−0.2
−0.3
−0.4
−0.5
−0.6
−0.7
−0.8
−0.9
0 5 10 15 20 25 30


1080
1060
1040
1020
1000
0 5 10 15 20 25 30

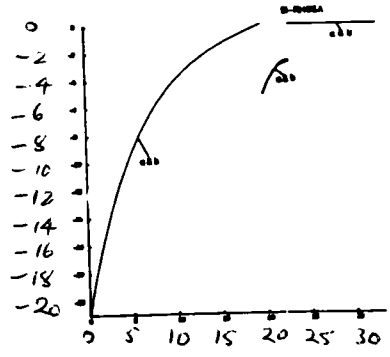

−0.2
−0.4
−0.6
−0.8
−1.0
−1.2
0 5 10 15 20 25 30


930
920
910
900
890
880
870
860
0 5 10 15 20 25 30


0
−2
−4
−6
−8
−10
−12
−14
−16
−18
0 5 10 15 20 25 30


1400
1380
1360
1340
1320
1300
1280
0 5 10 15 20 25 30

(a)


0
−2
−4
−6
−8
−10
−12
−14
−16
−18
−20
0 5 10 15 20 25 30

(b)

in silver and 7.23×10^{-3} C/mm in germanium. These results are fully substantiated in Fig. 2.6 where the area change of the seed is shown to be uninfluential.

By way of conclusion it is very clear from 1 and 2 that the seed played a small part in determining the temperature gradients of metal crystals, and an imperceptible part in the semi-conductor crystals. The area perturbations included for study were more effective than the length perturbations in the metals. As a guideline it is clear that for the seed to have any effect it must be long and thin to reduce crystal temperature gradients; also, the crystal temperature gradients cannot be easily controlled by seed dimension alterations. In practice it is known that seed dimensions imperceptibly affect crystal quality in metals (this thesis, Chapter I, p. 41), whilst in semi-conductors no systematic study appears to have been carried out.

2.6b.ii. The Neck

1. Varying the Neck Length

The results from this simulation fit in well with previous experimental work (Fehmer and Uelhoff[11]; Sworn and Brown[12]; Tanner[13], in particular): the neck length critically controls interfacial temperature gradients in metals. In silver and copper such changes in $DT_c(0)$ were 66.5% and 53.0% respectively (Table 2.6). In Fig. 2.7 it is abundantly plain how influential the neck length was. The situation in both silicon and germanium was quite different in that no important change in $DT_c(0)$ was monitored at all. It is relevant at this juncture

TABLE 2.6

Property / Element	$DT_c(0)$ C/mm Before	$DT_c(0)$ C/mm After	% Change in $DT_c(0)$ Before:After	$DT_n(L_c)$ C/mm Before	$DT_n(L_c)$ C/mm After	% Change in $DT_n(L_c)$ Before:After
Ag	0.975	1.624	66.5	24.04	54.37	126
Cu	1.307	2.0	53.0	26.24	59.48	126
Ge	18.45	18.45	0.0	1.531	2.625	71.4
Si	20.99	21.00	0.04	5.16	10.1	95.7

Reducing the Neck Length from 3 mm to 1 mm

High B_c

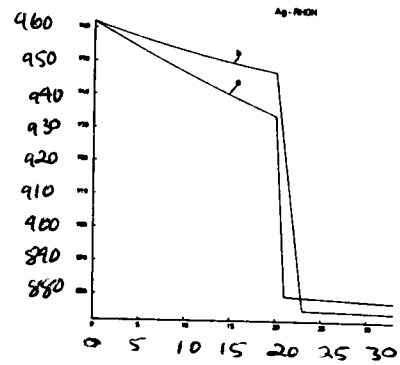
Fig. 2.7 Reducing the Neck Length ($L_s - L_n$) from 3 mm to 1 mm (RHGN)

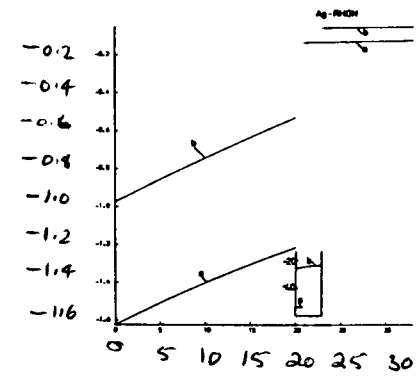
a. T(z) - vs - z (C - vs - mm)

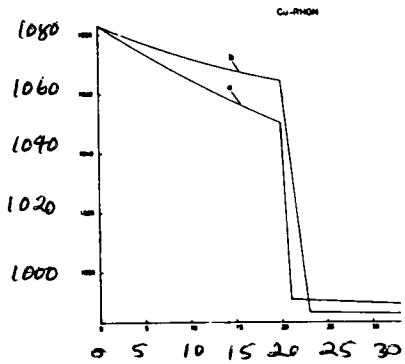
b. DT(z) - vs - z ($C/_{mm}$ - vs - mm)

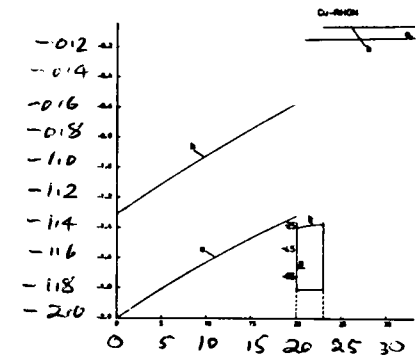
The temperature gradients (b) in the metal crystals increased markedly, but in the semiconductors no change was recorded. In all cases the neck temperature gradients rose sharply

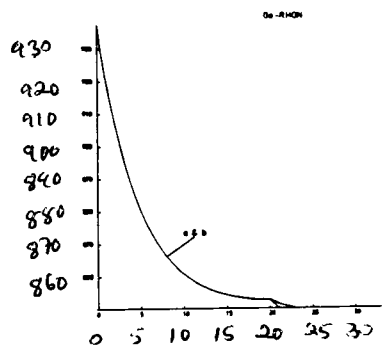
b = before; a = after

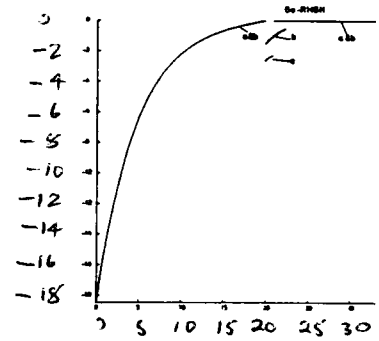

Ag-RHEN
960
950
940
930
920
910
900
890
880
0 5 10 15 20 25 30

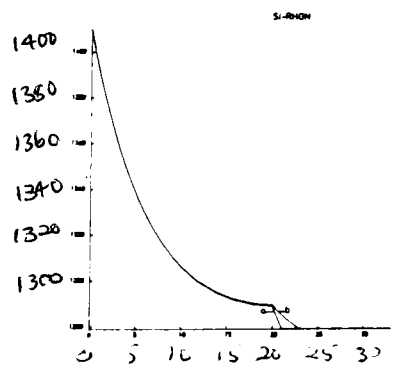

Ag-RHEN
-0.2
-0.4
-0.6
-0.8
-1.0
-1.2
-1.4
-1.6
0 5 10 15 20 25 30

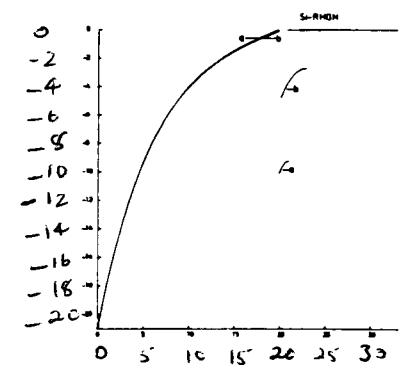

Cu-RHEN
1080
1060
1040
1020
1000
0 5 10 15 20 25 30


Cu-RHEN
-0.12
-0.14
-0.16
-0.18
-1.0
-1.2
-1.4
-1.6
-1.8
-2.0
0 5 10 15 20 25 30


Ge-RHEN
930
920
910
900
890
880
870
860
0 5 10 15 20 25 30


Ge-RHEN
-2
-4
-6
-8
-10
-12
-14
-16
-18
0 5 10 15 20 25 30


Si-RHEN
1400
1380
1360
1340
1320
1300
0 5 10 15 20 25 30


Si-RHEN
0
-2
-4
-6
-8
-10
-12
-14
-16
-18
-20
0 5 10 15 20 25 30

(a) (b)

to mention that in the original experiments by Dash[8] (1958) on silicon and Okkerse[9] (1959) on germanium the neck length required to promote dislocation-free growth was approximately 20 mm typically. Agreement between this work and that of the experimentalists does appear to be good, therefore, in that to effect an appreciable change in $DT_c(0)$ in semi-conductors (L_n-L_c) must be large. From the experimental work on dislocation-free metal crystals (see Sworn[4] for example) it is conversely known that the neck length required to initiate and sustain dislocation-free growth is much smaller than in the semi-conductor case, (approximately 3 mm); fitting in well with this work.

In the neck, the temperature gradients rose sharply when (L_n-L_c) was reduced. Typical increases were 126% in copper and 95.7% in silicon (Table 2.6). In order to reduce both $DT_c(0)$ and $DT_n(L_c)$ the neck must therefore be long.

2. Varying the Neck Radius

This change was of very useful effect in metals but not in semi-conductors as shown in Fig. 2.8. From Table 2.7 it is clear that the changes in $DT_c(0)$ induced were thermal conductivity linked, with silver, the best conductor considered, being much more dependent on R_n than germanium, the worst conductor analysed. For the two materials mentioned the change in $DT_c(0)$ was a decrease of 37.6% and 0% respectively. The only noticeable change in silicon was a splitting of the $DT_c(z)$ values around $z = L_c$ (Fig. 2.8b). Clear also from Fig. 2.8b is the equi-proportional effect that reducing R_n had on $DT_c(z)$

TABLE 2.7

Property / Element	$DT_c(0)$ C/mm Before	$DT_c(0)$ C/mm After	% Diff.in $DT_c(0)$ Before: After	$DDT_c(0\text{-}L_c)$	$DT_n(L_c)$ C/mm Before	$DT_n(L_c)$ C/mm After	%Change in $DT_A(L_c)$ Before: After
Ag	0.975	0.608	37.6	3.25	24.04	27.47	14.2
Cu	1.307	0.915	29.9	5.096	26.24	29.99	14.29
Ge	18.45	18.45	0.0	800	1.54	1.75	13.6
Si	20.99	20.98	0.04	1177	5.16	6.50	25.9

Reducing A_n by a Factor of 4

High B_c

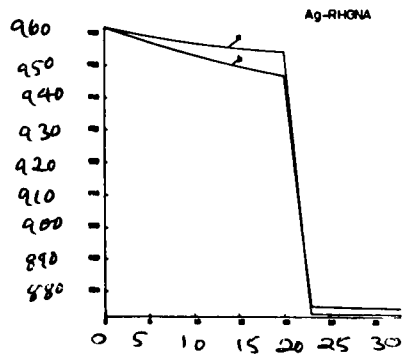
Fig. 2.8 Reducing the Neck Radius (R_n) by a Factor of 2 from 0.15 mm to 0.075 mm (RHGNA)

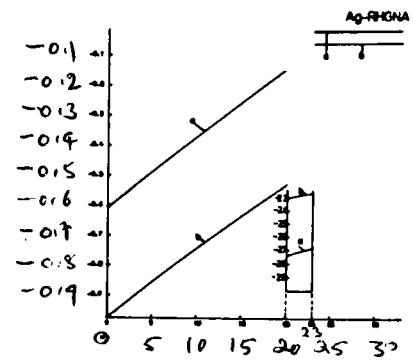
a. T(z) - vs - z (C-vs-mm)

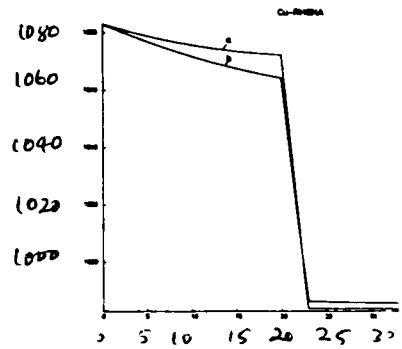
b. DT(z) - vs - z ($C|_{mm}$ — vs-mm)

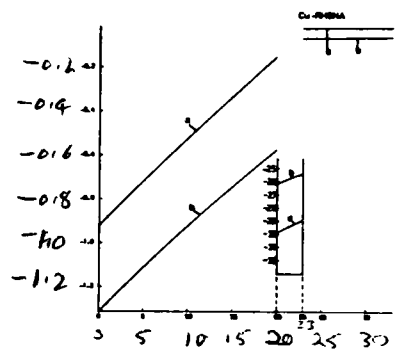
For the semiconductors the change was of no consequence (c.f. Fig. 2.7) but in the metal crystals a large reduction in $DT_c(z)$ values was observed and the neck temperature gradients rose markedly

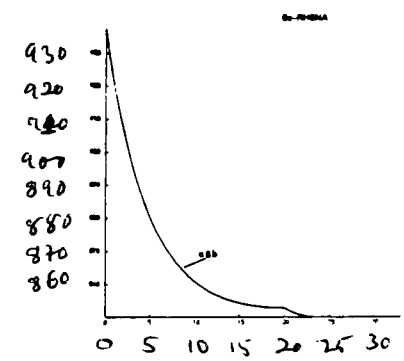
b = before; a = after

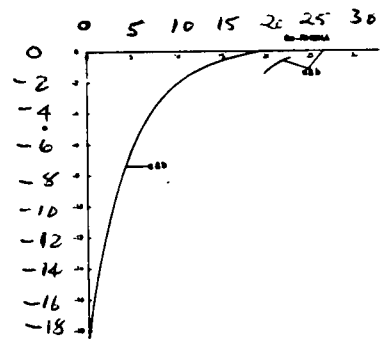

Ag-RHGNA
960
950
940
930
920
910
900
890
880
0 5 10 15 20 25 30

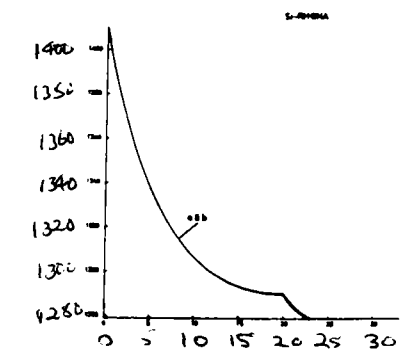

Ag-RHGNA
-0.1
-0.2
-0.3
-0.4
-0.5
-0.6
-0.7
-0.8
-0.9
0 5 10 15 20 25 30


1080
1060
1040
1020
1000
5 10 15 20 25

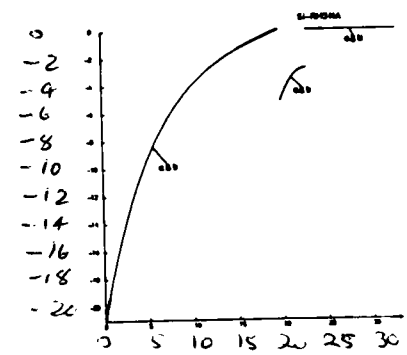

-0.2
-0.4
-0.6
-0.8
-1.0
-1.2
5 10 15 20 25 30


930
920
910
900
890
880
870
860
0 5 10 15 20 25 30


0 5 10 15 20 25 30
0
-2
-4
-6
-8
-10
-12
-14
-16
-18


1400
1380
1360
1340
1320
1300
1280
0 5 10 15 20 25 30

(a)


0
-2
-4
-6
-8
-10
-12
-14
-16
-18
-20
0 5 10 15 20 25 30

(b)

in both the silver and the copper, i.e. the crystal temperature gradients were reduced by an almost constant factor (not the same for the silver and copper) at all sampling points z. However, the effect that this reduction had on $DDT_c(0\text{-}L_c)$ was great, being 3.25 for silver (previously 0.836) and 5.096 for copper (previously 1.277). Therefore, while reducing $DT_c(0)$ in the metals, the reduction of R_n increased $DDT_c(0\text{-}L_c)$. This is an interesting result because it means that the afterheating properties required in the crystal puller need to be most efficient only around the growth face when the neck radius is small. As a consequence the afterheater can be shortened and the visibility increased, and dislocation-free crystals should still be produced. Experimental verification for this conclusion is available (this thesis, Chapter I). In this respect the metals and semi-conductors had reflected behaviour (compare this result to the not disimilar one at the end of (a.ii)). By reducing R_n the neck temperature gradients were not greatly increased, e.g. 14.3% in both copper and silver, 25.9% in silicon and 13.6% in germanium (Table 2.7).

The overall conclusion to draw, therefore, is that the neck can significantly influence the temperature gradients in metal crystals but not at all usefully in semi-conductor crystals (except when the neck is very long and thin of course). As a rider it must be remembered that what is good for the thermal properties of the crystal may be disastrous for the mechanical properties of the neck, i.e. too thin a neck may deform (and sometimes fracture at the elevated temperatures required to yield crystal growth) if a large crystal is attached to it.

2.6c The Crystal

1. Varying the Crystal Length

In the metal crystals the change in $DT_c(0)$ was marked, i.e. a reduction of 15.7% in silver and 20.7% in copper, Table 2.8; however, in the semi-conductor crystals the reductions were much less, being 3.0% in germanium and 7.5% in silicon. As shown in Fig. 2.9b it is further clear that reducing L_c by a factor of 2 affected the neck temperature gradients in germanium and silicon more than in silver and copper. In silver, for instance, $DT_n(L_c)$ was increased by 9.52%, whereas in germanium $DT_n(L_c)$ rose by 87.8% (Table 2.8). In the seed the temperature gradients increased but remained very low, e.g. in copper $DT_s(L_n)$ was 7.36×10^{-2} C/mm and in silicon $DT_s(L_n)$ was 3.80×10^{-2} C/mm (Table 2.8).

2. Decreasing the Crystal Radius

Table 2.9 shows quite clearly that when R_c was reduced by a factor of 2 $DT_c(0)$ increased dramatically in all cases, with the metals being more influenced by this change than the semi-conductors. Also, from Fig. 2.10b, it is clear that the temperature gradients in the germanium, for example, suffered a far greater change at the growth face than at z = 10 mm. Allied to this conclusion is the fact that the temperature gradient change at the growth face was positive while at the z = 10 mm point it was negative, implying that the change imposed caused a movement of the high temperature gradients towards z = 0 leaving the as grown crystal above z = 5 mm under the influence of a less severe temperature gradient. Similar

TABLE 2.8

›perty / ement	$DT_c(0)$ C/mm Before	$DT_c(0)$ C/mm After	% Diff. in $DT_c(0)$ Before:After	$DT_n(L_c)$ C/mm Before	$DT_n(L_c)$ C/mm After	% Diff. in $DT_n(L_c)$ Before:After	$DT_s(L_n)$ C/mm Before	$DT_s(L_n)$ C/mm After	% Change $DT_s(L_n)$ Before:Aft
Ag	0.975	0.821	15.7	26.57	24.04	9.52	6.00×10^{-2}	6.63×10^{-2}	10.5
Cu	1.307	1.036	20.7	29.52	26.24	11.00	6.54×10^{-2}	7.36×10^{-2}	12.5
Ge	18.45	17.88	3.0	12.63	1.53	87.80	1.97×10^{-3}	1.43×10^{-2}	625
Si	20.99	19.40	7.5	24.80	5.16	79.10	7.90×10^{-3}	3.8×10^{-2}	381

Reducing L_c from 20 mm to 10 mm

High B_c

Fig. 2.9 Reducing the Crystal Length (L_c) by a Factor of 2 from 20 mm to 10 mm (RHGC)

a. T(z) - vs - z (C-vs-mm)

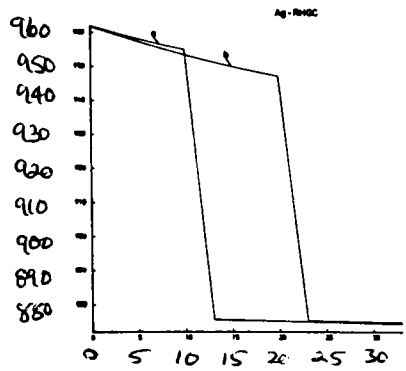
b. DT(z) - vs - z (C/mm-vs-mm)

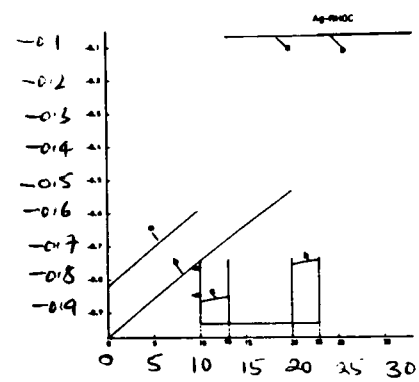
The temperature gradients in the metal crystals decreased, but in the semiconductors this change was not so obvious. Conversely, the temperature gradients in the neck for metals changed little; whilst for the temperature gradients in the semiconductor necks two effects were noticed:-

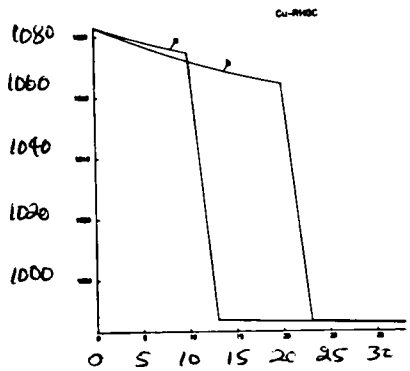
i. An increase in $DT_n(z)$ values

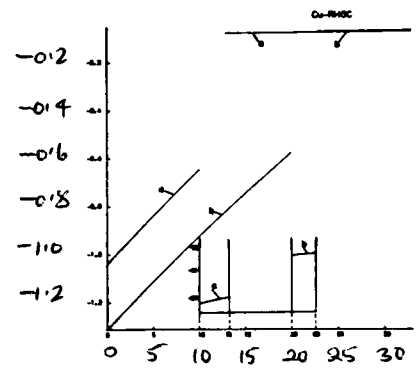
ii. An increase in the range of $DT_n(z)$ values

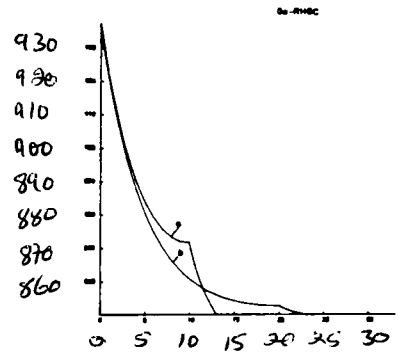
b = before; a = after

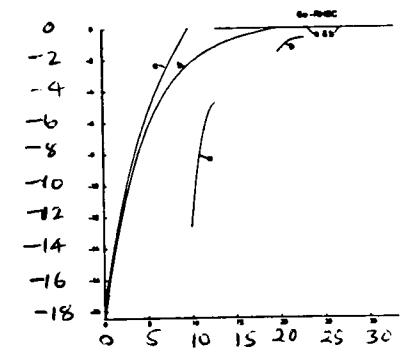

960
950
940
930
920
910
900
890
880
0 5 10 15 20 25 30

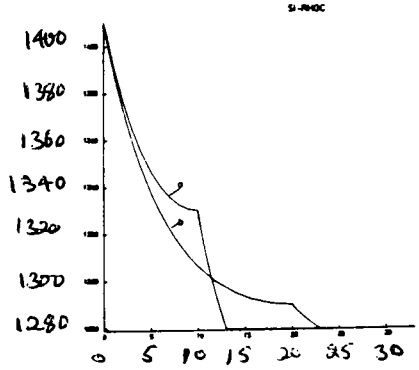

−0.1
−0.2
−0.3
−0.4
−0.5
−0.6
−0.7
−0.8
−0.9
0 5 10 15 20 25 30

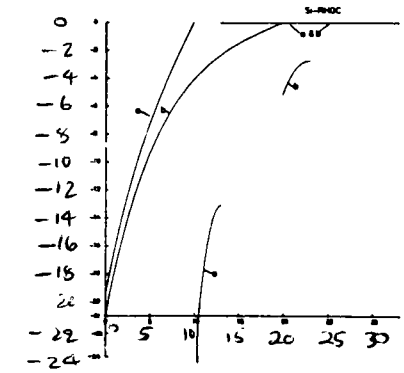

1080
1060
1040
1020
1000
0 5 10 15 20 25 30


−0.2
−0.4
−0.6
−0.8
−1.0
−1.2
0 5 10 15 20 25 30


930
910
900
890
880
870
860
0 5 10 15 20 25 30


0
−2
−4
−6
−8
−10
−12
−14
−16
−18
0 5 10 15 20 25 30


1400
1380
1360
1340
1320
1300
1280
0 5 10 15 20 25 30


0
−2
−4
−6
−8
−10
−12
−14
−16
−18
−22
−24
0 5 10 15 20 25 30

(a) (b)

TABLE 2.9

Property / Element	$DT_c(0)$ C/mm Before	$DT_c(0)$ C/mm After	% Change in $DT_c(0)$ Before:After	$DT_c(L_c)$ C/mm After	$DDT_c(0\text{-}L_c)$ Before	$DDT_c(0\text{-}L_c)$ After	$DT_n(L_c)$ C/mm Before	$DT_n(L_c)$ C/mm After	% Change in $DT_n(L_c)$ Before:After
Ag	0.975	1.682	72.5	1.55	0.836	0.451	24.04	18.06	24
Cu	1.307	2.869	119	1.624	1.277	0.766	26.24	18.12	30
Ge	18.45	25.98	40.8	1.31×10^{-2}	800	1982	1.531	0.242	84.1
Si	20.99	29.66	41.3	7.95×10^{-2}	1177	3720	5.16	1.20	76.7

Reducing A_c by a Factor of 4

High B_c

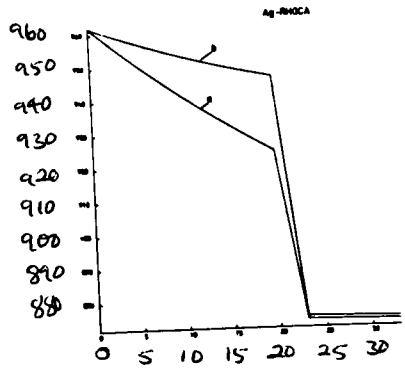
Fig. 2.10 Reducing the Crystal Radius (R_c) by 2 from 1 mm to 0.5 mm (RHGCA)

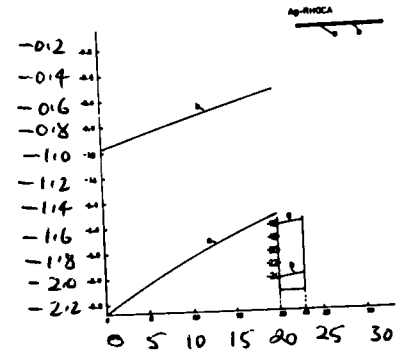
a. T(z) - vs - z (C – vs – mm)

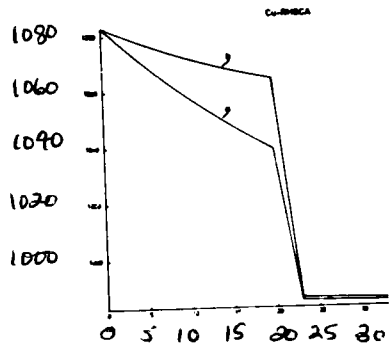
b. DT(z) - vs - z (C_{mm} – vs – mm)

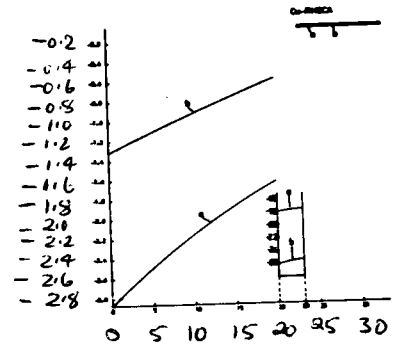
DT_c(z) in the metals increased noticeably at all sampling points, z. In the semiconductor crystals the temperature gradients underwent a large increase at the growth face but the as grown crystal experienced a successively smaller temperature gradient beyond a certain value ($\approx$5 mm in both silicon and germanium). The neck temperature gradients fell for all the elements studied

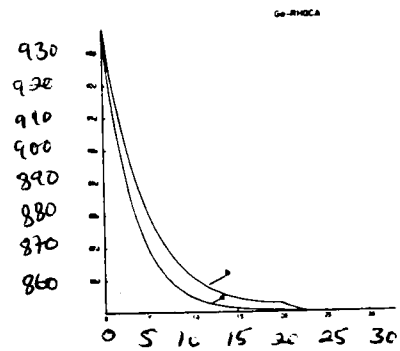
b = before; a = after

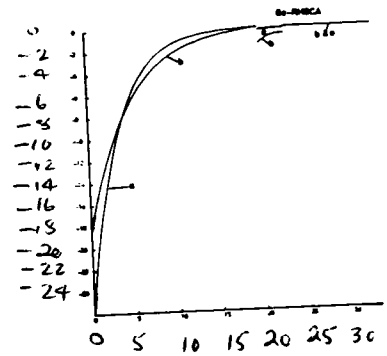

Ag-RHOCA
960
950
940
930
920
910
900
890
880
0 5 10 15 20 25 30

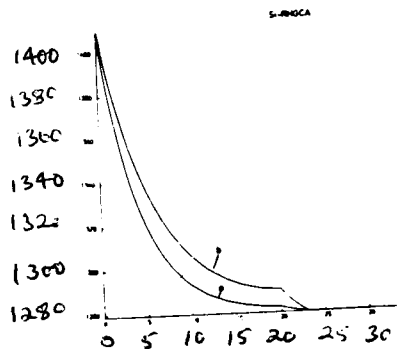

Ag-RHOCA
-0.2
-0.4
-0.6
-0.8
-1.0
-1.2
-1.4
-1.6
-1.8
-2.0
-2.2
0 5 10 15 20 25 30

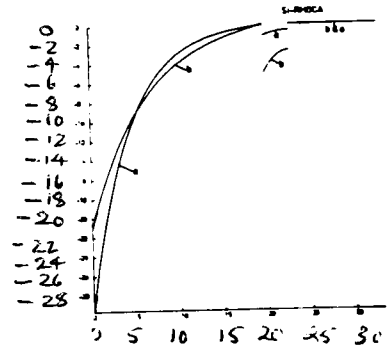

Cu-RHOCA
1080
1060
1040
1020
1000
0 5 10 15 20 25 30


Cu-RHOCA
-0.2
-0.4
-0.6
-0.8
-1.0
-1.2
-1.4
-1.6
-1.8
-2.0
-2.2
-2.4
-2.6
-2.8
0 5 10 15 20 25 30


Co-RHOCA
930
920
910
900
890
880
870
860
0 5 10 15 20 25 30


Co-RHOCA
-2
-4
-6
-8
-10
-12
-14
-16
-18
-20
-22
-24
0 5 10 15 20 25 30


Si-RHOCA
1400
1380
1360
1340
1320
1300
1280
0 5 10 15 20 25 30


Si-RHOCA
0
-2
-4
-6
-8
-10
-12
-14
-16
-18
-20
-22
-24
-26
-28
0 5 10 15 20 25 30

(a)

(b)

effects were noticed in the silicon case (Fig. 2.10b). In the metals, however, the perturbation applied to the model caused $DT_c(z)$ to increase everywhere. These two sets of behaviour were reflected in the $DDT_c(0\text{-}L_c)$ values; for instance, in germanium $DDT_c(0\text{-}L_c)$ was increased from 800 to 1982 and in silver $DDT_c(0\text{-}L_c)$ decreased from 0.836 to 0.451 (Table 2.9).

In the neck the temperature gradients were everywhere diminished implying that the thermal resistance effectiveness of the neck was reduced, e.g. $DT_n(L_c)$ was reduced by 84.1% in germanium and by 24% in silver (Table 2.9).

3. Increasing the Crystal Radius

The overall trend in this case was to reduce $DT_c(0)$ for all the elements studied. From Table 2.10 it is also clear that the metals were more affected, again, than the semi-conductors with the sensitivity ratio being approximately 2 : 1. From Fig. 2.11 an interesting parallel can be drawn with the behaviour of the metals under a low radiating condition, Fig. 2.4, i.e. for both the silver and the copper $DT_c(0)$ was less than that in the low radiating case. The semi-conductors were somewhat different in that the interfacial temperature gradients were still much higher than for the low radiating situation. The neck temperature gradients were increased in all cases, while the seed temperature gradients still remained small. It is further interesting to note that the values of $DDT_c(0\text{-}L_c)$ increased for the metals, from 0.836 to 1.66 in silver, for example, whereas in germanium $DDT_c(0\text{-}L_c)$ decreased from 800 to 67 (Table 2.10).

TABLE 2.10

operty / ement	$DT_c(0)$ C/mm Before	$DT_c(0)$ C/mm After	% Change in $DT_c(0)$ Before:After	$DDT_c(0\text{-}L_c)$ Before	$DDT_c(0\text{-}L_c)$ After	$DT_n(L_c)$ C/mm Before	$DT_n(L_c)$ C/mm After	% Change in $DT_n(L_c)$ Before:Afte
Ag	0.975	0.376	61.4	0.836	1.66	24.04	27.17	12
Cu	1.307	0.542	58.5	1.277	2.63	26.24	30.00	14.3
Ge	18.45	12.90	30.0	800	67	1.531	5.937	157
Si	20.99	14.45	31.1	1177	48	5.16	14.344	177

Increasing A_c by a Factor of 4

High B_c

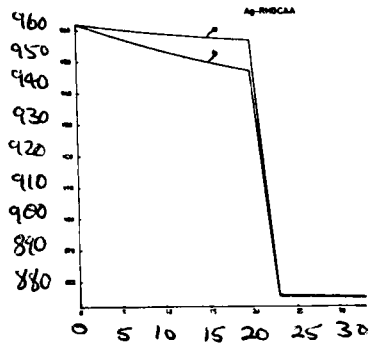
Fig. 2.11 Increasing the Crystal Radius (R_c) by 2 from 1 mm to 2 mm (RHGCAA)

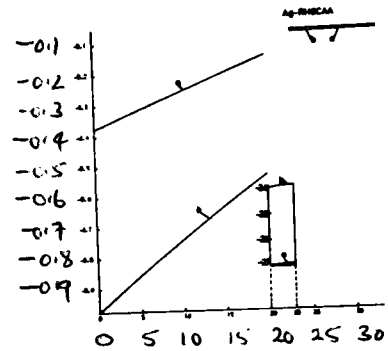
a. T(z) - vs - z (C-vs-mm)

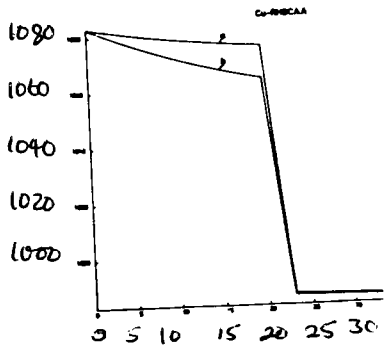
b. DT(z) - vs - z (C_{mm}-vs-mm)

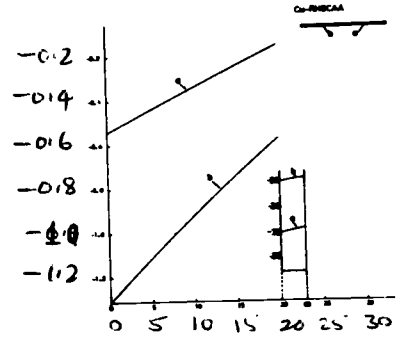
This perturbation had a profound effect on all crystals: a large reduction in $DT_c(0)$ was observed. Conversely, neck temperature gradients rose, implying that the thermal resistance effectiveness of the neck was increased

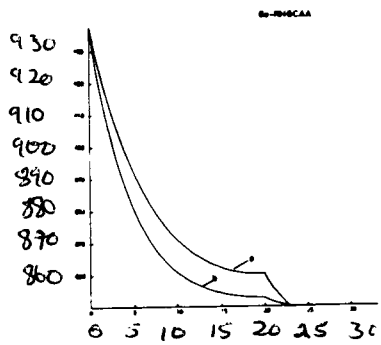
b = before; a = after

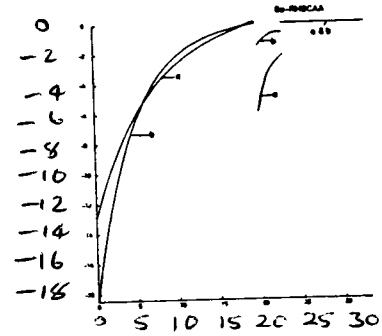

960
950
940
930
920
910
900
890
880
0 5 10 15 20 25 30

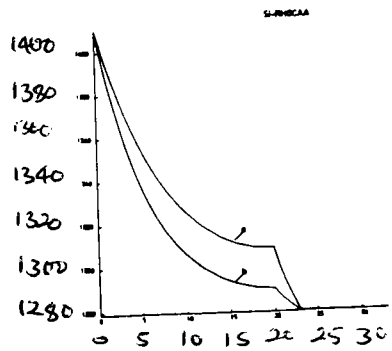

-0.1
-0.2
-0.3
-0.4
-0.5
-0.6
-0.7
-0.8
-0.9
0 5 10 15 20 25 30

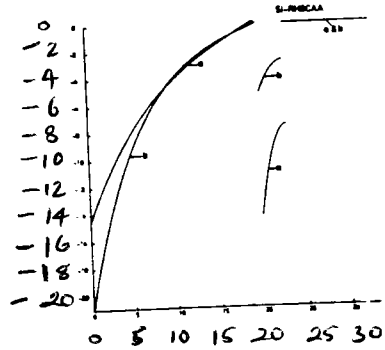

1080
1060
1040
1020
1000
0 5 10 15 20 25 30


-0.2
-0.4
-0.6
-0.8
-1.0
-1.2
0 5 10 15 20 25 30


930
920
910
900
890
880
870
860
0 5 10 15 20 25 30


0
-2
-4
-6
-8
-10
-12
-14
-16
-18
0 5 10 15 20 25 30


1400
1380
1360
1340
1320
1300
1280
0 5 10 15 20 25 30


0
-2
-4
-6
-8
-10
-12
-14
-16
-18
-20
0 5 10 15 20 25 30

(a)

(b)

2.7 Conclusions

The conclusions may be conveniently sub-divided into two sections: those which cover the metal-semiconductor comparison, and those which indicate how best to combat a harsh thermal environment by geometric methods.

i. The Metal Semiconductor Comparison

a. The Biot number is a useful guide to highlighting the effects monitored in all four elements.

b. When the radiation level was low (i.e. B_i was small) the greatest temperature gradient occurred in the neck for all four elements.

c. Both $DT_c(0)$ and $DDT_c(0\text{-}L_c)$ were greatest in silicon and germanium, implying that the semiconductors suffered a rapidly changing lattice parameter at the growth face, and that the range of temperature gradients experienced by the semiconductors was much larger than that in the metals.

d. Since the temperature gradients fall quickly in semiconductors only a short afterheater is necessary; however, in metals the temperature gradients are of like magnitude throughout the length of the crystal and so a long afterheater is required.

e. Under a high radiation condition (i.e. B_i large) the conclusions for the low radiation condition become more obvious, and the metals begin to emulate the semiconductors.

f. The neck became virtually redundant in the semiconductors but it still retained a great deal of influence in the metals.

ii. Geometric Variation Versus a Harsh Thermal Environment

g. In all cases studied the seed was of minimal importance in determining $DT_c(0)$, but a long thin seed is preferable to a short fat one.

h. Neck length changes can lower $DT_c(0)$ quite markedly in metals but not in semiconductors; and neck diameter changes, within the bounds of experimental possibility, are critically influential in metals but not in semiconductors. Therefore, long thin necks are preferable to short fat necks.

i. Reducing A_n pushes the temperature gradients to low values in metals and it may be possible to use a shorter afterheater therefore.

j. Large diameter crystals suffer smaller interfacial temperature gradients than small diameter crystals.

k. Long crystals suffer larger interfacial temperature gradients than short crystals, and so it seems better to grow short crystals than long ones. However, this effect was not very great in semiconductors and so a growing semiconductor crystal should experience a more stable temperature gradient distribution than a metal crystal.

It is therefore clear that to reduce the temperature gradients in a 'growing' crystal the seed should be long and thin; the neck should be long and thin; and the crystal should be short and fat (metal). A fat semiconductor crystal is preferable to a thin one but the length seems to be immaterial.

2.8 Suggestions for Further Work

a. The effect of a varying ambient temperature could be analysed. This would necessitate using a finite difference method, because it was found by the author to be difficult to adequately simulate the change in ambient temperature by any kind of analytical curve.

b. It would be interesting to measure the temperature of the growing crystal (in this Laboratory it would be of copper first) using grown in thermocouples, to see how far the assumptions made in the text were experimentally justified. Alternatively, with a certain amount of equipment redesign this problem could be tackled using a spot pyrometer. Spot sizes of 1 mm x 1 mm are easily available enabling the temperature of the crystal to be measured without actually interfering with the growth process. There is definitely a dearth of experimental data available in the literature in this area, and it would be further interesting to extend the experimental study to include the size effect of the crystal. It is because of this lack of information that the values generated in this study could not be reliably compared to any values from a practical crystal puller. The information that was available related to large crystals only ($\approx$20 mm in diameter) and it was consistently found that for silicon[19] the values of $DT_c(0)$ was about 10 C/mm, whilst for germanium[20] $DT_c(0)$ was about 11.5 C/mm.

c. The particular effects of convection on $DT_c(0)$ values could be investigated by inserting another term:-

$$h_c(T(z)-T_A)^{5/4} \qquad 2.26$$

into the right hand side of 2.1 and solving for T(z). Where h_c = convection constant.

APPENDIX A

The Heat Flow Equation of a Thin Rod

In the following derivation the temperature, T(z), at every point in a rod (here it is assumed to be a cylinder) is assumed to be constant across any plane perpendicular to the axis of the rod, which is defined by a co-ordinate z. Let the rod have a constant cross-sectional area, A; circumference, P; thermal conductivity, K; density, ρ ; specific heat, c; and heat radiation coefficient, h_R^*. Further, consider the section of the rod bounded by co-ordinates z and (z+dz). The rate at which heat flows into this element is given by:-

$$-\frac{KA\partial T(z)}{\partial z} \qquad 2.27$$

and the rate at which heat flows out of the element is given by:-

$$(\frac{K\partial T(z)}{\partial z} - \frac{K\partial^2 T(z)dz}{\partial z^2} - .....)A \qquad 2.28$$

Hence, the accumulation of heat in the element is given by:-

$$\frac{KA\partial^2 T(z)dz}{\partial z^2} \qquad 2.29$$

When the ambient temperature, T_A, and the temperature of the rod are similar then the radiation loss can be simulated as[16]:-

$$h_R P(T(z)-T_A)dz \qquad 2.30$$

and the rate of gain of heat can be accounted for by the expression:-

$$Ac\ \frac{\partial T(z)dz}{\partial t} \qquad 2.31$$

Consequently, the heat balance equation can be derived by equating 2.29 and 2.30 to 2.31:-

$$c\ A\frac{\partial T(z)}{\partial t} = \frac{KA\partial^2 T(z)}{\partial z} - h_R P(T(z)-T_A) \qquad 2.32$$

It is this last expression which was used to study the model formulated in this chapter.

USERID IGOLDER,NUPAAGG15

LISTING OF (WORKFILE,AAAA00011111(1/) PRODUCED ON 18MAY76 AT 19.39.20
OUTPUT BY LISTFILE IN 'IGOLDER,NUPAAGG15' ON 18MAY76 AT 19.41.32

DOCUMENT I

0001 *FORTRAN

FORTRAN COMPILATION BY FXFIV 11K 3A DATE 18/05/76 TIME 19/37/50

APPENDIX (B)

The computer program used in this study.

```
0000                PROGRAM (ABCD)
0001                INPUT 1=CRD
0002                OUTPUT 2=LPD
0003                TRACE 2
0004                END



0005                MASTER SUB
0006                DIMENSION TMAX(5),TMIN(5)
0007                DIMENSION R(3,3)
0008                DIMENSION PLOT(55)
0009                DIMENSION DT(10,11,3),RHO(10,11,3),TZ(11,3,2),TP(55)
0010                DIMENSION A(4,4),B(4),C(4),AA(4,4),WKS1(4),WKS2(4)
0011                DIMENSION T(10,11,3),DT(10,11,3),TAU(10,11,3)
0012                READ 2
0013                READ(1,45) RB
0014                WRITE(2,61) RB
0015          61    FORMAT(///' RB=',1PD13.6)
0016                READ(1,45) TAUY
0017                WRITE(2,60) TAUY
0018          60    FORMAT(///' TAUY=',1PD13.6)
0019                READ(1,45) RMU
0020                WRITE(2,12) RMU
0021                READ(1,45) ALPHA
0022                WRITE(2,13) ALPHA
0023                READ(1,53) INDEX
0024                WRITE(2,54) INDEX
0025                READ(1,7) IDATA1
0026                DO 30 I=1,IDATA1
0027                READ(1,1) (R(I,J),J=1,3)
0028          30    CONTINUE
0029                READ(1,7) IDATA2
0030                READ(1,45) (A1,A2,A3
                                    VO,VC
```

```
      READ(2,6) (TMAX(I),I=1,6)
      DO 606 I=4,6
      TMAX(I)=-1.0E+50
      TMIN(I)=1.0E+50
606   CONTINUE
      DO 8 JDATA=1,IDATA2
      READ(1,9)RL1,RL2,RL3,RK
      READ(1,55) DT1,DT2,DT3
      WRITE(5,57) DT1,DT2,DT3
57    FORMAT(///' DT1=',1PD13.6,' DT2=',1PD13.6,' DT3=',1PD13.6)
1     FORMAT(4D13.6)
45    FORMAT(3D13.6)
      WRITE(5,3) RL1,RL2,RL3,RK
3     FORMAT(///' L1=',1PD13.6,' L2=',1PD13.3,' L3=',1PD13.6,' RK=',1PD1
     13.6)
      WRITE(5,5) RA1,RA2,RA3
5     FORMAT(///' A1=',1PD13.6,' A2=',1PD13.6,' A3=',1PD13.6)
      WRITE(5,6) TM,VO,VC
6     FORMAT(///' TM=',F10.2,'  VO=',F10.4,'  VC=',F10.2)
7     FORMAT(I3)
53    FORMAT(10)
12    FORMAT(///' PHI=',1PE13.6)
13    FORMAT(///' ALPHA=',1PE13.6)
14    FORMAT(///' INDEX=',I3)
4     FORMAT(///' N1=',1PD13.6,' N2=',1PD13.6,' N3=',1PD13.6)
      DO 8 IDATA=1,IDATA1
      KDATA=(JDATA-1)*IDATA1*IDATA
      RN1=RK(IDATA,1)
      RN2=RK(IDATA,2)
      RN3=RK(IDATA,3)
      WRITE(5,4) RN1,RN2,RN3
C
      A(1,1)=COSH(RN2*RL1)
      A(1,2)=SINH(RN2*RL1)
      A(1,3)=-SINH(RN1*RL1)
      A(1,4)=0.0
      A(2,1)=RK*RN2*RN2*SINH(RN2*RL1)
      A(2,2)=RK*RN2*RN2*COSH(RN2*RL1)
      A(2,3)=(RA1**2)*(SQRT(RA1/3.142))*RK/2*(RA1-RA2)*SINH(RN1*RL1) =
     1RK*RA1*RN1*COSH(RN1*RL1)
      A(2,4)=0.0
      A(3,1)=COSH(RN2*RL2)
      A(3,2)=SINH(RN2*RL2)
      A(3,3)=0.0
      A(3,4)=-SINH(RN3*(RL2-RL3))
      A(4,1)=RK*RN2*RN2*SINH(RN2*RL2)
      A(4,2)=RK*RN2*RN2*COSH(RN2*RL2)
      A(4,3)=0.0
      A(4,4)=-RK*RA2*RN3*COSH(RN3*(RL2-RL3))*(RN3**2)*(SQRT(RA3/3.142))
     1*RK/2*(RA2-RA2)*SINH(RN3*(RL2-RL3)))
      B(1)=(TM-VO)*COSH(RN1*RL1)
      B(2)=RK*RA1*RN1*(TM-VO)*SINH(RN1*RL1) = (RN1**2)*(SQRT(RA1/3.142))
     1*RK/2*(RA1-RA2)*(TM-VO)*COSH(RN1*RL1)
      B(3)=0.0
      B(4)=0.0
      CALL FACTOR (A,4,B,4,C,AA,6,WKS1,WKS2,0)
C  THE ONE-DIMENSIONAL ARRAY, C, CONTAINS THE SOLUTION VECTOR.
      WRITE(5,40) (C(I),I=1,4)
40    FORMAT(//)' C3=',1PD13.6,' C4=',1PD13.6,' C2=',1PD13.6,'  C6=',1PD
     113.6)
      C3=C(1)
      C4=C(2)
      C2=C(3)
      C6=C(4)
      VO=VO
      DO 100 IZ=1,INDEX+1
      Z=(IZ-1)*RL1/INDEX
      TZ(IZ,JDATA)=Z
      T(KDATA,IZ,1)=VO+(TM-VO)*COSH(RN1*Z)+C2*SINH(RN1*Z)
      DT(KDATA,IZ,1)=(TM-VO)*RN1*SINH(RN1*Z)+C2*RN1*COSH(RN1*Z)
      DDT(KDATA,IZ,1)=DT(KDATA,IZ,1)-DT1
      TAU(KDATA,IZ,1)=PHI*ALPHA*DDT(KDATA,IZ,1)*SQRT(4.0*RA1/3.141)/2.0
      RHO(KDATA,IZ,1)=(ALPHA*ABS(DDT(KDATA,IZ,1))/PB)-(2*TAUV/(RMU*RB*SQ
     1RT(4*RA1/3.142)))
      IF(T(KDATA,IZ,1).GT.TMAX(1)) TMAX(1)=T(KDATA,IZ,1)
      IF(DT(KDATA,IZ,1).LT.TMIN(2)) TMIN(2)=DT(KDATA,IZ,1)
      IF(DDT(KDATA,IZ,1).LT.TMIN(3)) TMIN(3)=DDT(KDATA,IZ,1)
      IF(TAU(KDATA,IZ,1).LT.TMIN(4)) TMIN(4)=TAU(KDATA,IZ,1)
      IF(RHO(KDATA,IZ,1).LT.TMIN(5)) TMIN(5)=RHO(KDATA,IZ,1)
100   CONTINUE
C
      DO 200 IZ=1,INDEX+1
      Z=(IZ-1)*(RL2-RL1)/INDEX+RL1
      TZ(IZ,JDATA)=Z
      T(KDATA,IZ,2)=VO+C3*COSH(RN2*Z)+C4*SINH(RN2*Z)
      DT(KDATA,IZ,2)=C3*RN2*SINH(RN2*Z)+C4*RN2*COSH(RN2*Z)
      DDT(KDATA,IZ,2)=DT(KDATA,IZ,2)-DT2
      TAU(KDATA,IZ,2)=PHI*ALPHA*DDT(KDATA,IZ,2)*SQRT(RA2*4.0/3.141)/2.0
      RHO(KDATA,IZ,2)=(ALPHA*ABS(DDT(KDATA,IZ,2))/PB)-(2*TAUV/(RMU*RB*SQ
     1RT(4*RA2/3.141)))
      IF(DDT(KDATA,IZ,2).GT.TMAX(3)) TMAX(3)=DDT(KDATA,IZ,2)
      IF(TAU(KDATA,IZ,2).GT.TMAX(4)) TMAX(4)=TAU(KDATA,IZ,2)
200   CONTINUE
C
      DO 300 IZ=1,INDEX+1
      Z=(IZ-1)*(RL3-RL2)/INDEX+RL2
      TZ(IZ,JDATA)=Z
      T(KDATA,IZ,3)=VC+C6*SINH(RN3*(Z-RL3))
      DT(KDATA,IZ,3)=C6*RN3*COSH(RN3*(Z-RL3))
      DDT(KDATA,IZ,3)=DT(KDATA,IZ,3)-DT3
      TAU(KDATA,IZ,3)=PHI*ALPHA*DDT(KDATA,IZ,3)*SQRT(RA3*4.0/3.141)/2.0
      RHO(KDATA,IZ,3)=(ALPHA*ABS(DDT(KDATA,IZ,3))/PB)-(2*TAUV/(RMU*RB*SQ
     1RT(4*RA3/3.141)))
      IF(T(KDATA,IZ,3).LT.TMIN(1)) TMIN(1)=T(KDATA,IZ,3)
      IF(DT(KDATA,IZ,3).GT.TMAX(2)) TMAX(2)=DT(KDATA,IZ,3)
      IF(RHO(KDATA,IZ,3).GT.TMAX(5)) TMAX(5)=RHO(KDATA,IZ,3)
300   CONTINUE
C
      WRITE(5,20)
20    FORMAT(////1H ,' IZ ',6X,'TZ1',6X,6X,'T1',7X,6X,'T2Z',6X,
     1 6X,'T3',7X,6X,'T3Z',6X,6X,'T3',7X/)
      DO 30 IZ=1,INDEX+1
      WRITE(5,21) IZ,TZ(IZ,1,JDATA),T(KDATA,IZ,1),TZ(IZ,2,JDATA),T(KDATA
     1,IZ,2),TZ(IZ,3,JDATA),T(KDATA,IZ,3)
21    FORMAT(1H ,I3,6(1PD13.6,2X))
30    CONTINUE
```

```
C
      WRITE(2,22)
   22 FORMAT(/////1H ,' IZ ',6X,'TZ1',6X,6X,'DDT1',5X,6X,'TZ2',6X,
     1 6X,'DDT2',5X,6X,'TZ3',6X,6X,'DDT3',5X/)
      DO 31 IZ=1,INDEX+1
      WRITE(2,21) IZ,TZ(IZ,1,JDATA),DT(KDATA,IZ,1),TZ(IZ,2,JDATA),DT(KDA
     1TA,IZ,2),TZ(IZ,3,JDATA),DT(KDATA,IZ,3)
   31 CONTINUE
C
C
      WRITE(2,24)
   24 FORMAT(/////1H ,' IZ ',6X,'T1Z',6X,6X,'DDT1',5X,6X,'T2Z',6X,6X,'DD
     1T2',5X,6X,'T3Z',6X,6X,'DDT3',5X/)
      DO 35 IZ=1,INDEX+1
      WRITE(2,21) IZ,TZ(IZ,1,JDATA),DDT(KDATA,IZ,1),TZ(IZ,2,JDATA),
     1DDT(KDATA,IZ,2),TZ(IZ,3,JDATA),DDT(KDATA,IZ,3)
   35 CONTINUE
      WRITE(2,23)
   23 FORMAT(/////1H ,' IZ ',6X,'T1Z',6X,6X,'TAU1',5X,6X,'T2Z',6X,
     1 6X,'TAU2',5X,6X,'T3Z',6X,6X,'TAU3',5X/)
      DO 32 IZ=1,INDEX+1
      WRITE(2,21) IZ,TZ(IZ,1,JDATA),TAU(KDATA,IZ,1),TZ(IZ,2,JDATA),
     1TAU(KDATA,IZ,2),TZ(IZ,3,JDATA),TAU(KDATA,IZ,3)
   32 CONTINUE
      WRITE(2,25)
   25 FORMAT(/////1H ,' IZ ',6X,'T1Z',6X,6X,'RHO1',5X,6X,'T2Z',6X,6X,'RHO
     12',5X,6X,'T3Z',6X,6X,'RHO3',5X/)
      DO 34 IZ=1,INDEX+1
      WRITE(2,21) IZ,TZ(IZ,1,JDATA),RHO(KDATA,IZ,1),TZ(IZ,2,JDATA),RHOCK
     1DATA,IZ,2),TZ(IZ,3,JDATA),RHO(KDATA,IZ,3)
   34 CONTINUE
    2 CONTINUE
    3 CONTINUE
C
C
C GRAPHICS
      CALL GABGS(1)
      DO 67 I=1,5
      CALL PLACE(10,1)
      GO TO(63,60,70,72),I
   60 CALL TYPECS(20HDT(C) PLOTTED AGAINST Z(MM),26)
      CALL MAP(-0.1,33.0,TMIN(1),TMAX(1))
      GO TO 71
   69 CALL TYPECS(30HDDT(C/MM) PLOTTED AGAINST Z(MM),30)
      CALL MAP(-0.1,33.0,TMIN(2),TMAX(2))
      GO TO 71
   60 CALL TYPECS(31HDDT(C/MM) PLOTTED AGAINST Z(MM),31)
      CALL MAP(-0.1,33.0,TMIN(3),TMAX(3))
      GO TO 71
   70 CALL TYPECS(35HTAU(GM/MM**2) PLOTTED AGAINST Z(MM),35)
      CALL MAP(-0.1,33.0,TMIN(4),TMAX(4))
      GO TO 71
   72 CALL TYPECS(37HRHO(DISL/MM**2) PLOTTED AGAINST Z(MM),37)
      CALL MAP(-0.1,33.0,TMIN(5),TMAX(5))
      GO TO 71
   71 CONTINUE
      DO 78 K=1,3
      DO 77 NU=1,IDATA2
      DO 68 N=1,INDEX+1
   68 TP(N)=TZ(N,K,NU)
      DO 77 NP=1,IDATA1
      N=(NU-1)*IDATA1+NP
      GO TO(79,80,81,80,88),I
   79 CONTINUE
      DO 83 N=1,INDEX+1
   83 PLOT(N)=T(N,N,K)
      GO TO 82
   80 CONTINUE
      DO 84 N=1,INDEX+1
   84 PLOT(N)=DT(N,N,K)
      GO TO 82
   81 CONTINUE
      DO 86 N=1,INDEX+1
   86 PLOT(N)=DDT(N,N,K)
      GO TO 82
   88 CONTINUE
      DO 85 N=1,INDEX+1
   85 PLOT(N)=TAU(N,N,K)
      GO TO 82
   80 CONTINUE
      DO 81 N=1,INDEX+1
   81 PLOT(N)=RHO(N,N,K)
      GO TO 82
   82 CONTINUE
      IF(INDEX.LT.1) GO TO 999
      WRITE(2,808) (TP(N), N=1,INDEX+1)
      WRITE(2,808) (PLOT(N), N=1,INDEX+1)
  808 FORMAT(1H ,11E10.1)
  999 CONTINUE
      CALL CURVED(TP,PLOT,1,INDEX+1)
   78 CONTINUE
   76 CONTINUE
      CALL AXES
      CALL FRAME
   67 CONTINUE
      CALL GREND
C
      STOP
      END

END OF SEGMENT, LENGTH  2277, NAME  SUB


 0240                 FINISH
END OF COMPILATION =  NO ERRORS

    S/C SUBFILE  :      39 BUCKETS USED
  FIRST WORKFILE  :      62 BUCKETS USED
 SECOND WORKFILE  :      48 BUCKETS USED

   0002    *LINK LIB NAGF
   0003    *LINK LIB CUGHOST
   0004    *DATA BIN XSTLDISL
```

CHAPTER II REFERENCES

1. E. Billig, Proc. Roy. Soc., A235, 37, 1956
2. J. C. Brice, J.C.G., 2, 395, 168
3. H. S. Kuo and W. R. Wilcox, J.C.G., 12, 191, 1972
4. C. H. Sworn, Ph.D. Thesis, University of Cambridge, 1971
5. N. Kobayashi and T. Arizumi, J.C.G., 13/14, 615, 1972
6. K. Akiyama and J. Yamaguchi, J. Elect. Soc., 108, 1899, 1961
7. N. Kobayashi and T. Arizumi, Jap. J.A.P., 9, 361, 1970
8. W. C. Dash, J.A.P., 29, 736, 1958
9. B. Okkerse, Philips Tech. Rev., 21, 340, 1959
10. S. Howe and C. Elbaum, Phil. Mag., 6, 1227, 1961
11. H. Fehmer and H. Uelhoff, J.C.G., 15, 395, 1972
12. C. H. Sworn and T. E. Brown, J.C.G., 13/14, 247, 1972
13. B. K. Tanner, Z. für Naturforsch., 289, 676, 1973
14. I. M. Buckley-Golder, This Thesis, Ch. I.
15. H. S. Carslaw and J. C. Jaeger, "Conduction of Heat in Solids", O.U.P., 1971
16. H. Gröber, S. Erk and U. Grigull, "Fundamentals of Heat Transfer", McGraw-Hill, 3rd Ed., 1961
17. L. Fox, "Numerical Solution of 2-Point Boundary Problems in Ordinary Differential Equations", O.U.P., 1957
18. C.R.C., "Handbook of Chemistry and Physics", 55th Edition, 1974-75
19. B. M. Turovskii and K. D. Cheremin, Inorg. Mater., 4, 712, 1968
20. J. C. Brice and P. A. C. Whiffen, Solid State Electr., 7, 183, 1964

CHAPTER III

ASSESSING THE PERFECTION OF LOW DISLOCATION DENSITY ($<10^6/CM^2$) CRYSTALS ABOVE A 1 μm RESOLUTION LIMIT

List of Symbols Used in this Chapter

$K\alpha_1$, $K\alpha_2$ = Characteristic X-ray wavelengths

W = X-ray focus size

w = Incident beam slit width

a = Focus to slit distance

r_v = Vertical resolution

b = Specimen to film distance

ϕ = X-ray take-off angle

d = Interplanar spacing of a crystal

Θ_B = Bragg angle

λ = Wavelength

$d\Theta_B$ = Width of the rocking curve at half height due to the incident beam wavelength spread

$d\Theta_c$ = Perfect crystal rocking curve width at half height

t = Nuclear emulsion thickness

$\underline{E}$ = Electric field vector

$\underline{E}_o$ = Maximum value of $\underline{E}$

ν = Wave frequency

$\underline{k}$ = Wave vector

e = Charge on an electron

m_o = Rest mass of an electron

c = Velocity of light (vacuum)

ϵ_o = Permittivity of free space

ϵ = Permittivity of a crystal

R = Classical radius of the electron

χ = Dielectric susceptibility

n = Refractive index

ρ = Electronic charge density

χ_h = Pre-exponential factor of a Fourier series based on χ

$\underline{h}$ = Reciprocal lattice vector

$\underline{r}$ = Real space vector

F_h = Structure factor of reflection h

V_c = Volume of a unit cell

f_j = Atomic scattering factor of the jth atom in a unit cell

$\underline{r}_j$ = Position vector of the jth atom in the unit cell

χ_{rh}, χ_{ih} = Real and imaginary parts of χ_h respectively

μ_o = Forward linear absorption coefficient

χ_{io} = Dielectric susceptibility (imaginary) for the forward scattered beam

$\underline{D}$ = Dielectric displacement

$\underline{P}$ = Polarisation

$\underline{k}_{oj}$ = Wave-vector of a direct (forward-scattered) wave within the crystal

$\underline{k}_{hj}$ = Wave-vector of a diffracted wave within the crystal

C = Polarisation constant

ψ_o, ψ_h = Perpendicular distances of a tie point on the dispersion surface from the Ewald spheres

M = Amplitude ratio of the diffracted and forward scattered wavefields

$\underline{S}j$ = Poynting vector

$\underline{s}_o$, $\underline{s}_h$ = Unit vectors along $\underline{k}_j$ and $\underline{k}_{hj}$ respectively

$\underline{k}_{oj}^{i}$ = Imaginary part of $\underline{k}_{oj}$

I_j = Bloch wave intensity

$\underline{\Omega}$ = Surface normal

$\underline{k}_e$ = Incident wave-vector

μ_{eff} = Effective absorption coefficient of a Bloch wave

$\exp(-M)$ = Debye-Waller factor

Λ_o = Closest distance of approach of the dispersion surfaces

Θ_A = Angular deviation from the exact Bragg angle

$\underline{u}(\underline{r})$ = Crystal lattice point displacement vector

χ_r = Susceptibility of a strained crystal

χ_p = Susceptibility of a perfect crystal

$\underline{h}^l$ = Local reciprocal lattice vector

$\underline{k}_h^l$ = Effective wave-vector in a strained crystal

β_h^l, β_h = Deviation from the Bragg condition relative to the local reciprocal lattice, and the deviation of β_h^l from the perfect crystal reciprocal lattice respectively

Γ_o, Γ_h = Wave-functions of the forward scattered and diffracted wavefields respectively

ξ = Crystal-vacuum surface co-ordinate

x = Co-ordinate perpendicular to the Bragg planes

γ_o = Direction cosine between the inward drawn surface normal and $\underline{k}_e$

I_h^{Tr} = Traverse topograph intensity in the diffracted beam

v_h = A Green's function

r_e = Position vector on the crystal entrance surface

A = Proportionality constant

J_o = Zeroth order Bessel function

J_2 = Second order Bessel function

s_o^o, s_h^o = Position co-ordinates of a point on the exit surface of a crystal

s_o, s_h = Real space co-ordinates in the direction of $\underline{k}_{oj}$ and $\underline{k}_{hj}$

ϕ_e = Angle between the incident wave-vector, $\underline{k}_e$ or $\underline{s}_o$, and the Bragg surface

R = Radius of a cylindrical crystal

CONTENTS

		Page Number
	Contents	84
3.1	Introduction	86
3.2 (i)	Lang's Techniques	87
3.2 (ii)	Borrmann's Anomalous Transmission Method	88
3.3	Resolution in Lang X-ray Topography	90
3.4	Ilford Nuclear Emulsions	92
3.4 (i)	The Use of the Film on the X-ray Camera	93
3.4 (ii)	Development of the "Latent Image" in the Emulsion	94
3.4 (iii)	Optical Photography of the X-ray Topograph	96
3.5	Topographing a Cylindrical Crystal	96
3.6	X-ray Dynamical Theories	98
3.6 (i)	The Ewald-Laue Theory	98
3.6 (ii)	The Dispersion Surface and Highly Absorbing Perfect Cylindrical Copper Crystals	104
3.6 (iii)	The Borrmann Effect	106
3.6 (iv)	Boundary Conditions and Absorption Coefficients	108
3.6 (v)	The Dispersion Surface and a Cylindrical Crystal	110
3.6 (vi)	The Dispersion Surface, Spherical Waves and Cylindrical Crystals	112
3.6 (vii)	The Takagi-Taupin-Uragami Generalised Diffraction Theory (TTU)	114

3.7	A Calculation of the Integrated Intensity at the Exit Face of a Perfect Cylindrical Copper Crystal using the TTU Theory	117
3.7 (i)	The Model	117
3.7 (ii)	Boundary Conditions	119
3.7 (iii)	The Integrated Intensity in the Diffracted Beam	120
3.8	Conclusions	123
3.9	Suggestions for Further Work	124
	References	125

"..... whereupon Sommerfeld took a sheet out of the drawer on which were listed some ten or twelve topics for doctoral theses ..... At the end of the list stood the problem: 'To find the optical properties of an anisotropic arrangement of isotropic resonators' ..... Ewald was immediately struck by the last topic on the list ..... and he went home, determined that it would be this topic or none.

At the time of writing the thesis, it seemed a rather radical departure from the traditional theory. For this reason Ewald meant to discuss it with Laue who had a strong leaning towards fundamental physical issues.

When the time came, he found Laue listening in a slightly distracted way. He again insisted on knowing the distances between the resonators, and when he received the same answer as before, he asked; 'What would happen if you assumed very much shorter waves to travel in the crystal?'....."

Professor P. P. Ewald

"Fifty Years of X-ray Diffraction"
p. 37, 40, 41

3.1 Introduction

This chapter sets out to discuss the particular ways in which crystallographic information can be obtained from a single crystal by studying its interaction (experimentally and theoretically) with X-rays. Even more specifically, this interaction will be restricted to crystal-X-ray diffraction physics since X-ray diffraction topography has been extensively used throughout this work to assess lattice perfection. X-ray topography is only one of a number of techniques that could have been used for this purpose; the others being:-

i. Optical microscopy[1,2,3]
ii. Chemical etch pitting and thermal pitting[4,5]
iii. Infrared microscopy[6]
iv. Resistivity methods[7,8]
v. Neutron and γ -ray diffraction analysis[9,10]
vi. Electron microscopy[11]

In addition to the above particular references covering crystal lattice assessment techniques, a number of general books on the topic have been written[12,13,14]. X-ray topography was primarily used because it is the only non-destructive technique which can be used to examine low dislocation density, highly absorbing, thick metal crystals. Of the various types of X-ray topography available[(15-23)] only one hybrid method has been used: the Lang-Borrmann technique. In consequence only this method will be discussed from both a theoretical and experimental position, because to include the other methods would unnecessarily amplify the length of this thesis. For good reviews of the other techniques the reader is referred to references 13 and 24.

3.2.i Lang's Techniques[20]

In Lang's original paper (1958) he outlined a method for obtaining X-ray diffraction pictures of crystals using the well collinated characteristic radiation from a spot source, as shown schematically in Fig. 3.1. Since the incident beam was diffracted by a discrete set of lattice planes a "section topograph " of the crystal was produced, the contrast within which could be associated with lattice defects: primarily dislocations and stacking faults. Later, Lang showed that by traversing the crystal and X-ray plate synchronously across the main beam, that a 'full projection topograph' could be obtained of a very large crystal and its inherent defects.

Considering the diffraction process via a purely geometric construction (Fig. 3.2) it becomes clear that the diffracted beam has a finite width dictated by the incident beam width, the crystal thickness and the Bragg angle. Consequently, the diffracted beam slits can be placed to receive only a part of the diffracted beam. For instance, in Fig. 3.2, if the slits are reduced in lateral extent and placed into the centre of the diffracted beam (position S_4) then a central slice of the crystal, t_4, will be imaged. This indicates that surface strains, which can significantly impair quality, can be removed from the field of view.

A typical example of the usefulness of this method is shown in Fig. 3.3 where a diamond crystal is imaged in full projection mode (3.3a); in Fig. 3.3b a limited projection topograph of the same crystal is presented which shows a series of inclined lamellae not visible in 3.3a. This latter image

Fig. 3.1 Lang X-ray Topography - Schematically

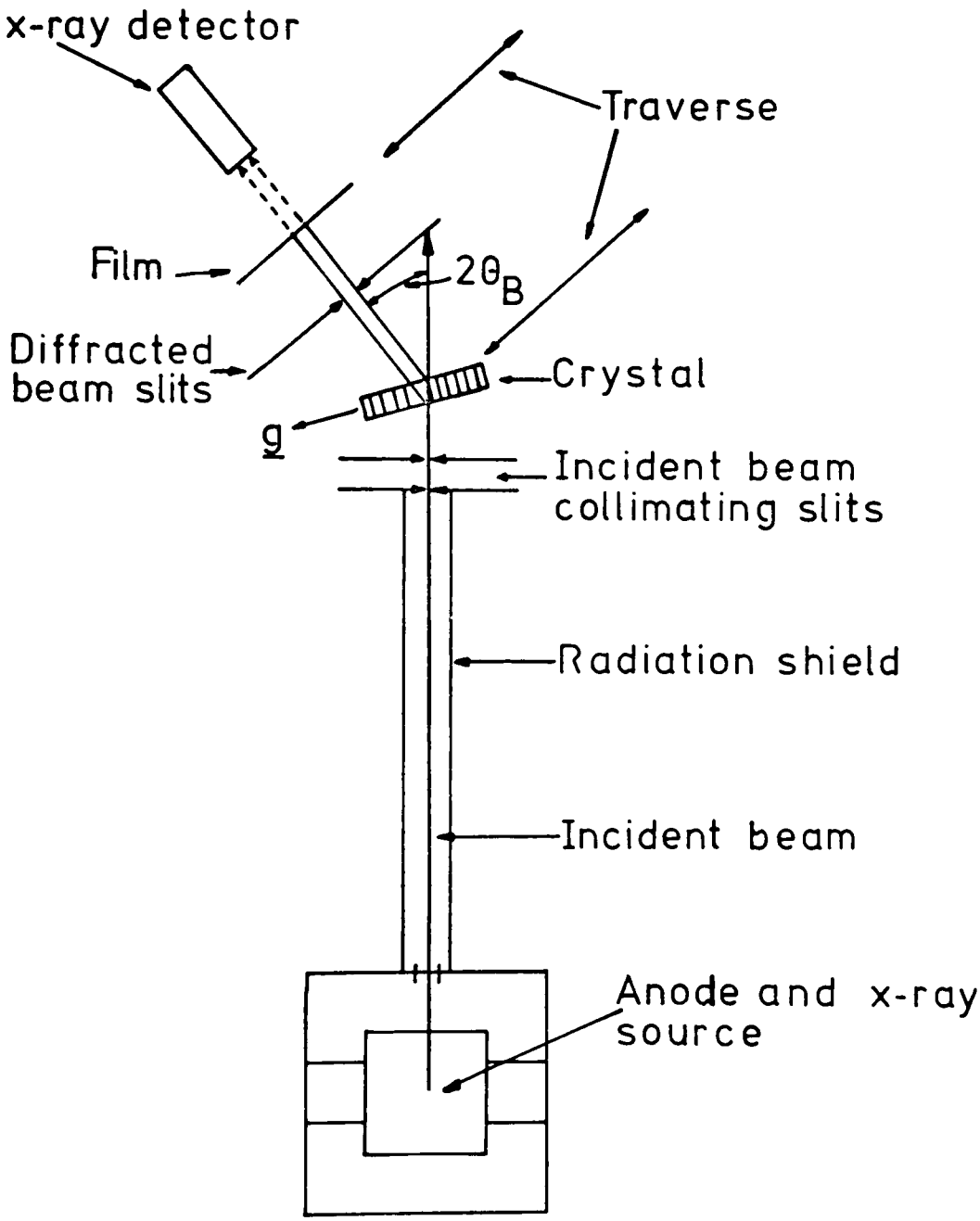

x-ray detector
Traverse
Film
$2\theta_B$
Diffracted beam slits
Crystal
g
Incident beam collimating slits
Radiation shield
Incident beam
Anode and x-ray source

Fig. 3.2 Limited Projection Topography - Schematically

By carefully positioning the diffracted beam slits, particular slices of the crystal can be imaged

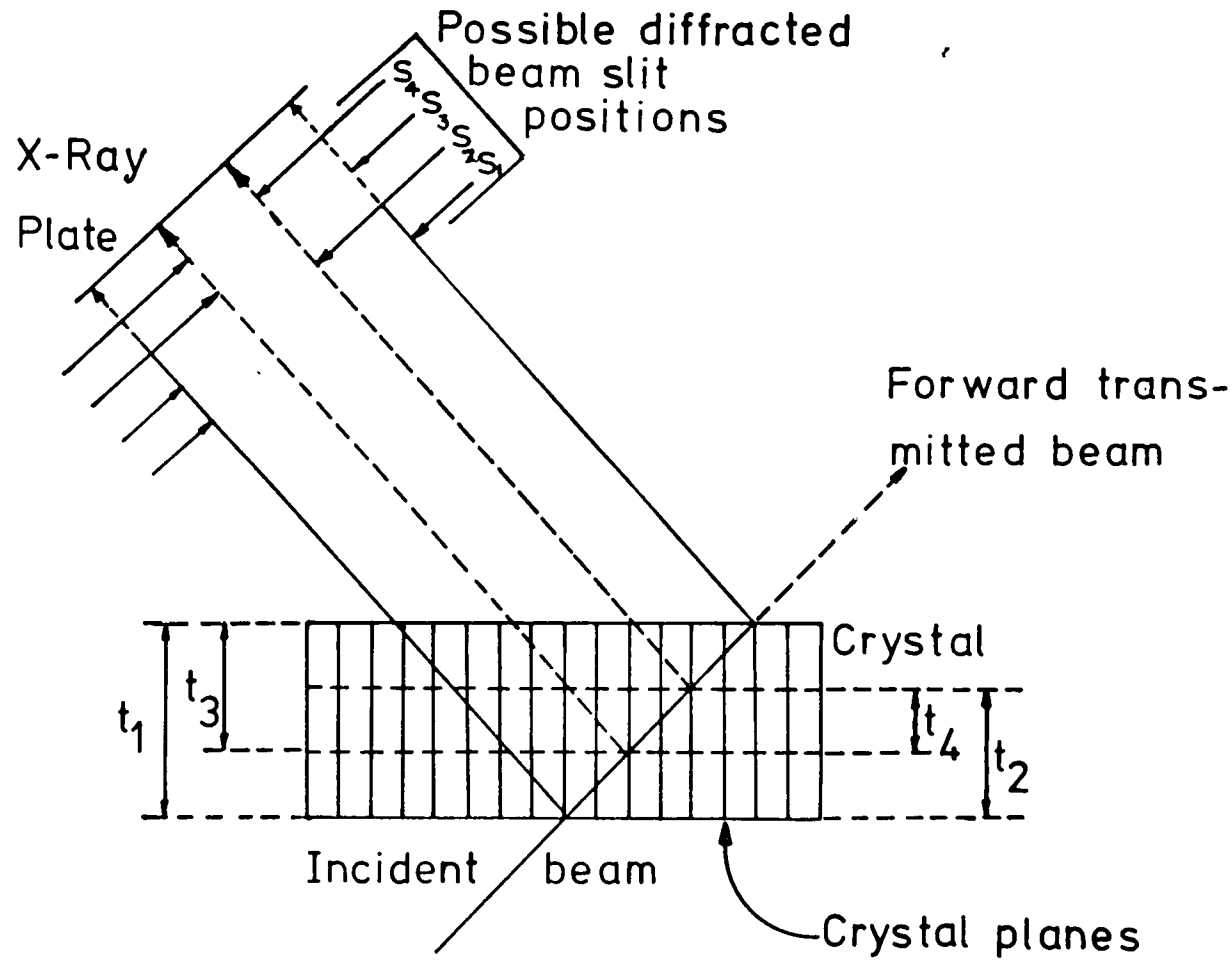
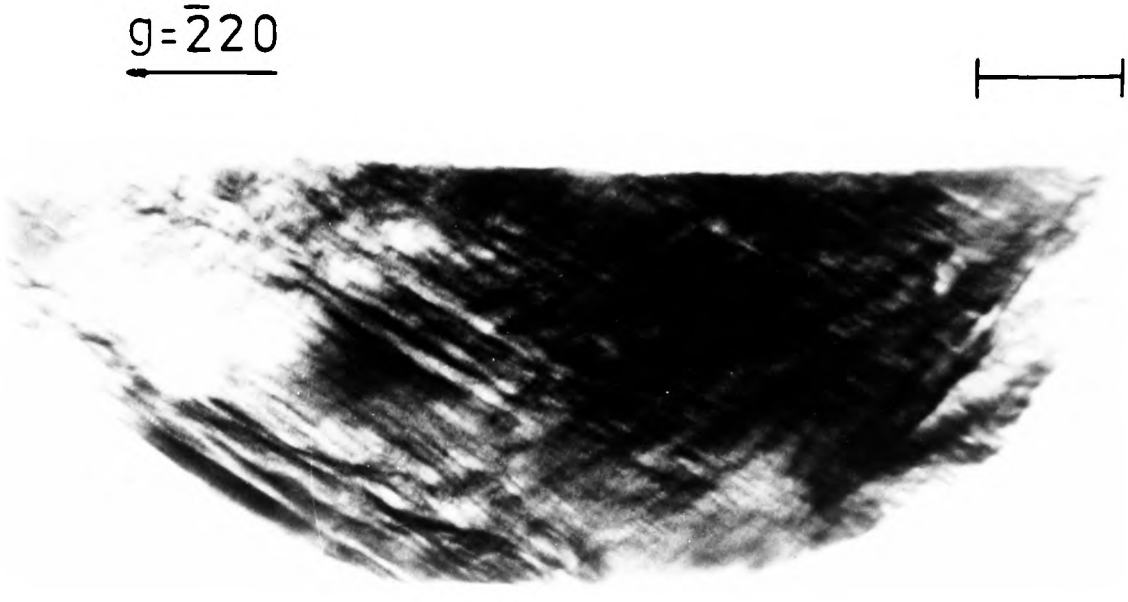

Possible diffracted
beam slit
positions
S_4 S_3 S_2 S_1
X-Ray
Plate
Forward trans-
mitted beam
Crystal
t_1
t_3
t_4
t_2
Incident beam
Crystal planes

Fig. 3.3 An Illustration of the Use of Limited Projection Topography of Diamond

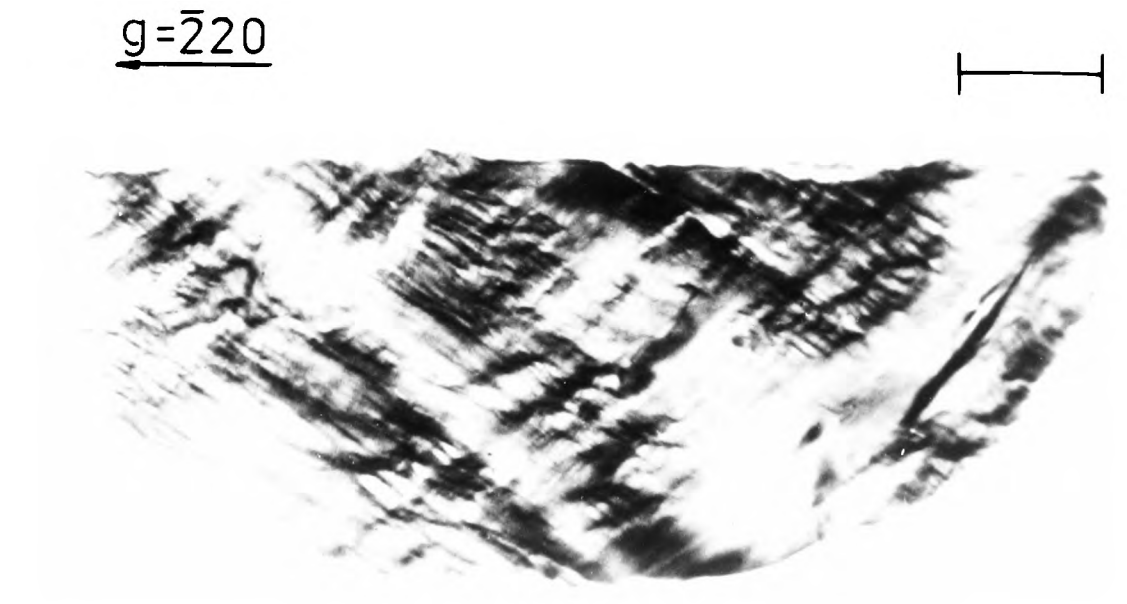
a. Full projection topograph

b. Limited projection topograph viewing a central slice (S_4 in Fig. 3.2) only. Notice the inclined lamellae, and the reduced influence of surface strains compared to a.

Scale mark = 0.5 mm $\mu ot = 0.545$



(a)



(b)

was produced by positioning the diffracted beam slits at position S_4 as shown in Fig. 3.2, and so minimising the influence of surface strains on the final topograph. These inclined lamellae were presupposed to be twins ($\approx$1 μm wide) in the crystal, and the aim of using X-ray topography was to either substantiate or invalidate this presupposition by obtaining diffraction from either the matrix or the twin. Unfortunately the evidence accrued was inconclusive, because it is thought that the strain fields associated with the twin boundaries were large and close together which gave a complicated image. However, the topographs in Fig. 3.3 do serve to show the advantage of limited projection topographs when the crystal does not absorb X-rays strongly, i.e. $\mu_o t$ is small (μ_o = linear absorption coefficient, t = crystal thickness). If $\mu_o t$ is large (as in Lang-Borrmann topography) then the width of the beam leaving the exit face of the crystal is very narrow and limited projection topographs are unobtainable.

3.2.ii Borrmann's Anomalous Transmission Method[21]

If the electric field vector, $\underline{E}$, of an X-ray wavefield inside a thick perfect crystal set to diffract is large at the atomic sites, then appreciable photoelectron absorption will occur which will greatly attenuate the transmitted intensity; conversely, if the magnitude of $\underline{E}$ is large in between the atomic sites minimal absorption will take place. In a thick ($\mu_o t \gg 1$) perfect crystal, therefore only the wavefield with a large value of $\underline{E}$ in between the atomic positions survives. Any deviation of the transmitted intensity from a theoretically calculable value will give an indication of a defective lattice,

e.g. from phonons, interstitials, vacancies, dislocations, stacking faults. Such calculations and comparisons with experiments have been performed with some success[25,26,27]. If the crystal contains an appreciable density of dislocations ($> 10^3/cm^2$), then sufficient atoms inside it will be displaced from their equilibrium positions so that the wavefield which exists largely between the atoms will be completely absorbed by a "defect absorption mechanism". (These three absorption methods are shown in Fig. 3.4)

If, however, the crystal contains a small dislocation density ($< 10^3/cm^2$) then it is possible to advantageously exploit the "defect absorption mechanism", so that the local absorption at a defect gives rise to a local reduction in transmitted intensity and therefore contrast on an X-ray plate in the form of a light line against a darker background. (This is analogous to both a bright field and dark field picture in electron microscopy of thick crystals) The technique can produce clear dislocation images from very highly absorbing crystals, as shown in Fig. 3.5 where $\mu_o t$ was $\approx$10-80. Ordinarily no transmission whatsoever would have been expected under these conditions: but because the crystal was very nearly perfect anomalous transmission was produced. Also note that the type of film used affects image clarity: Fig. 3.5a was taken using Ilford L4 and Fig. 3.5b with Ilford G5. The L4 is better than the G5.

In this investigation the Borrmann method has been used in conjunction with the scanning tachnique of Lang to produce X-ray topographs of the as grown metal crystals described in Chapter I. The theory relevant to the Borrmann method will be discussed later.

Fig. 3.4 Borrmann Topography

Only those wavefields (A) with nodes at the atomic positions reach the exit face of the crystal. Defects can cause local absorption of even these wavefields, giving rise to film contrast. Decoupling of the wavefields occurs at the exit face of the crystal.

d = interplanar spacing, Θ_B = Bragg angle

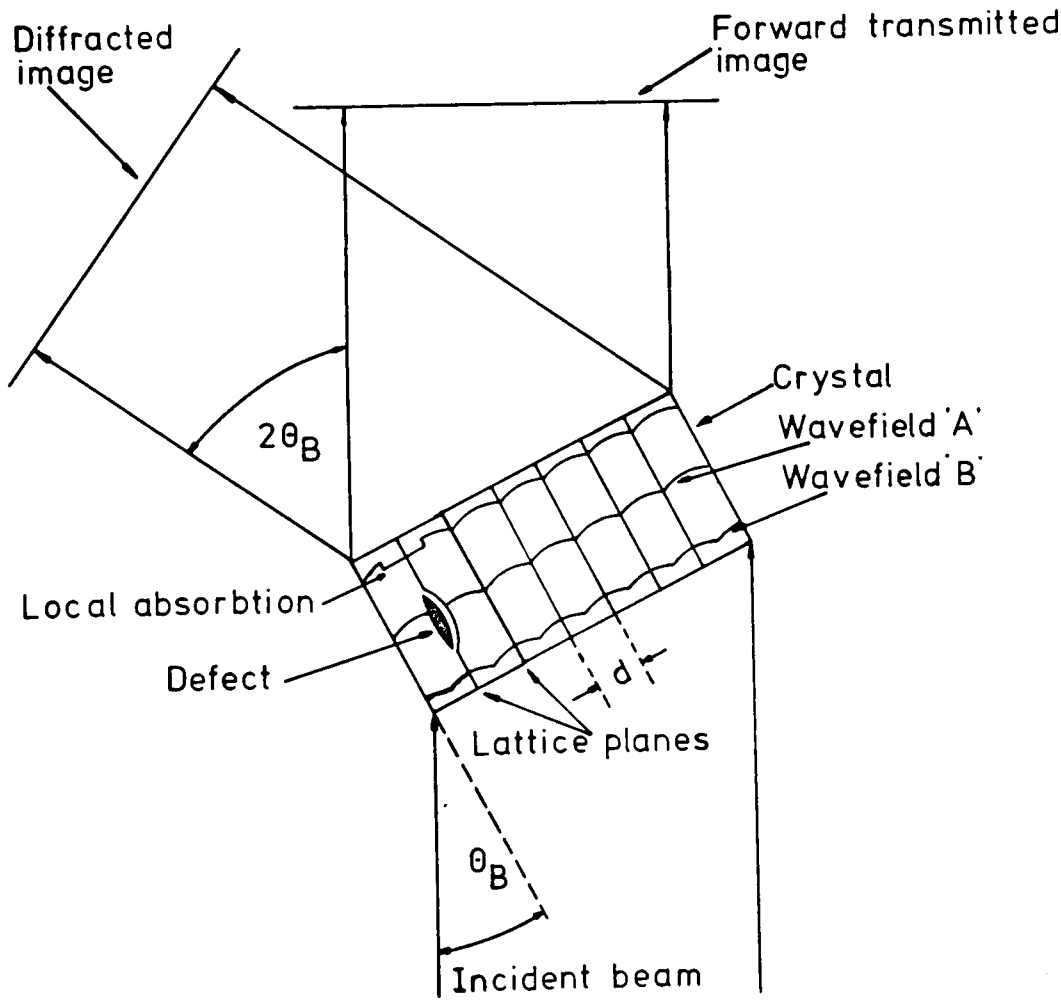
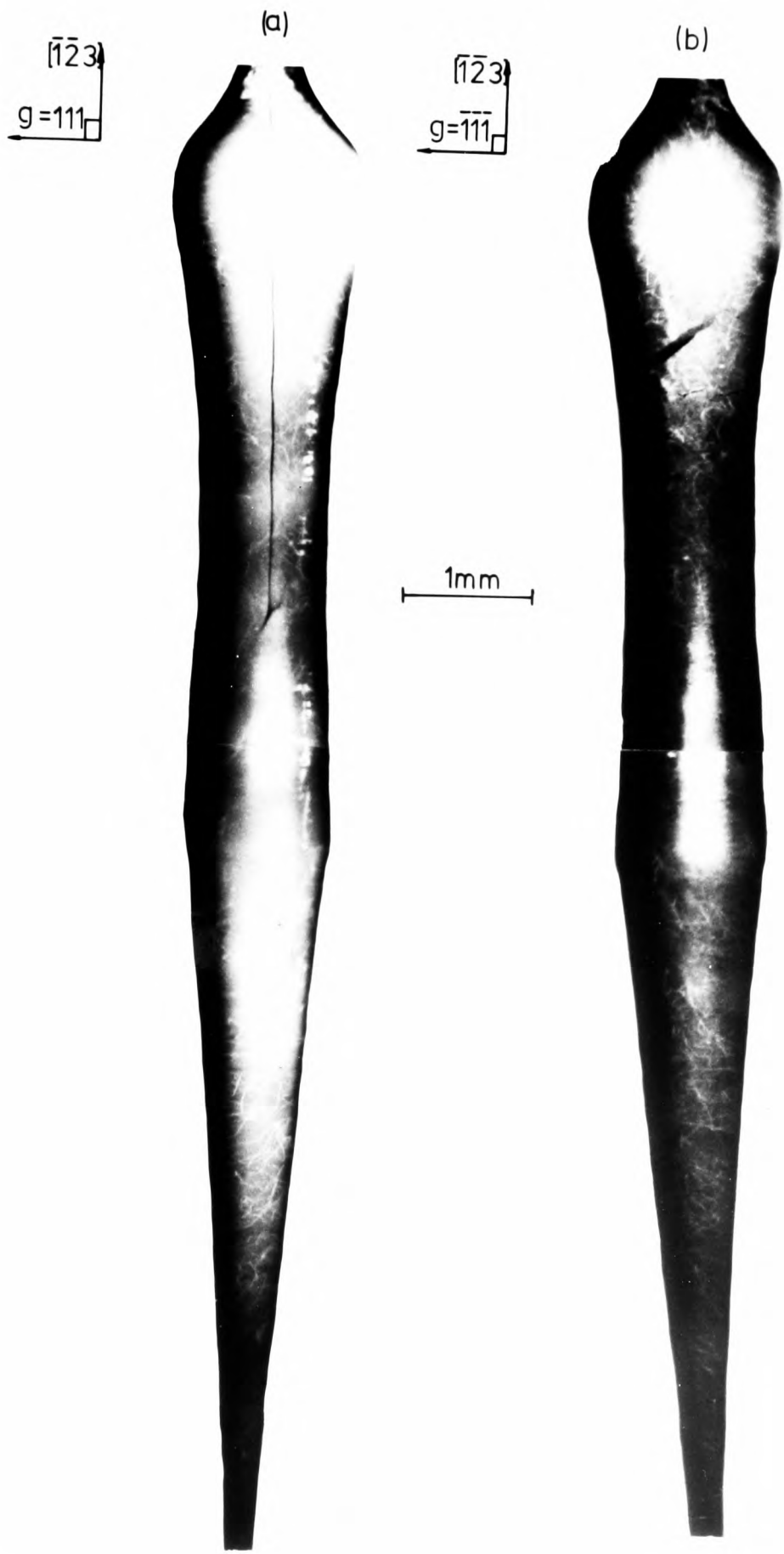

Diffracted image
Forward transmitted image
Crystal
Wavefield 'A'
Wavefield 'B'
$2\theta_B$
Local absorbtion
Defect
d
Lattice planes
θ_B
Incident beam

Fig. 3.5 An illustration of clear dislocation images in a $[\bar{1}\bar{2}3]$ copper crystal topographed under Lang-Borrmann conditions.

Notice that L4a emulsion gives better images than G5b


(a)
(b)
[1$\bar{2}$3]
g = 111
[1$\bar{2}$3]
g = $\bar{1}\bar{1}\bar{1}$
1mm

3.3 Resolution in Lang X-ray Topography

A strong requirement in Lang topography is that the incident beam must be well collimated, so that the crystal will discretely diffract a particular wavelength (normally K_{α_1}) thereby eliminating double-images on an X-ray plate. The major complication in this respect can be the influence of the K_{α_2} component which is normally about half the intensity of K_{α_1}[28]; therefore, unless the apparatus is carefully constructed to limit the divergence of the incident beam to less than the angular separation of K_{α_1} and K_{α_2} the crystal will diffract both at the same time.

Typically, the angular separation of K_{α_1} and K_{α_2} is $\approx$2'-4' of arc[28]. Hence, if 'W' is the X-ray tube focus size, 'w' the width of the incident beam slits, and 'a' the focus to slit distance then the relative magnitudes of these three parameters must conform to the following condition to prevent double diffraction:-

$$\frac{W+w}{a} < 2' \text{ of arc } (5.8 \times 10^{-4} \text{ radians}) \qquad 3.1$$

For the Lang cameras used in this study:-

$a = 70$ cm
$W = 200$ µm
$w = 200$ µm

Therefore, $\frac{W+w}{a} = 5.7 \times 10^{-4}$ radians, i.e. the cameras are within the collimation limits.

Resolution in the Lang technique is best considered in terms of the horizontal and vertical components. In the vertical direction the resolution, r_v, is given by:-

$$r_v = \frac{b}{a} W \sin \phi \qquad 3.2$$

Where,

b = specimen to film distance (1 cm)
a = focus to specimen distance (70 cm)
W = focus size (200 μm)
ϕ = X-ray take-off angle (3^{o}-6^{o})

For the Oxford cameras r_v is, at best, about 1 μm. To increase X-ray photon flux ϕ is normally held at 6^{o}, but to maximise resolution, e.g. in dislocation interaction studies, ϕ is normally limited to 3^{o}. Fig. 3.6 gives an overall view of the Lang cameras used in this study together with essential annotations. (For detailed information about them the reader is referred to references 29 and 30).

The horizontal resolution may be sub-divided into two parts: that contribution from the width of the perfect crystal reflection, as calculated from X-ray dynamical theory[31]; and that contribution which arises from the measurable wavelength spread of the characteristic peak. The latter component may be accounted for as follows. Beginning with Bragg's law:-

$$2d \sin\Theta_B = \lambda \qquad 3.3$$

Where,

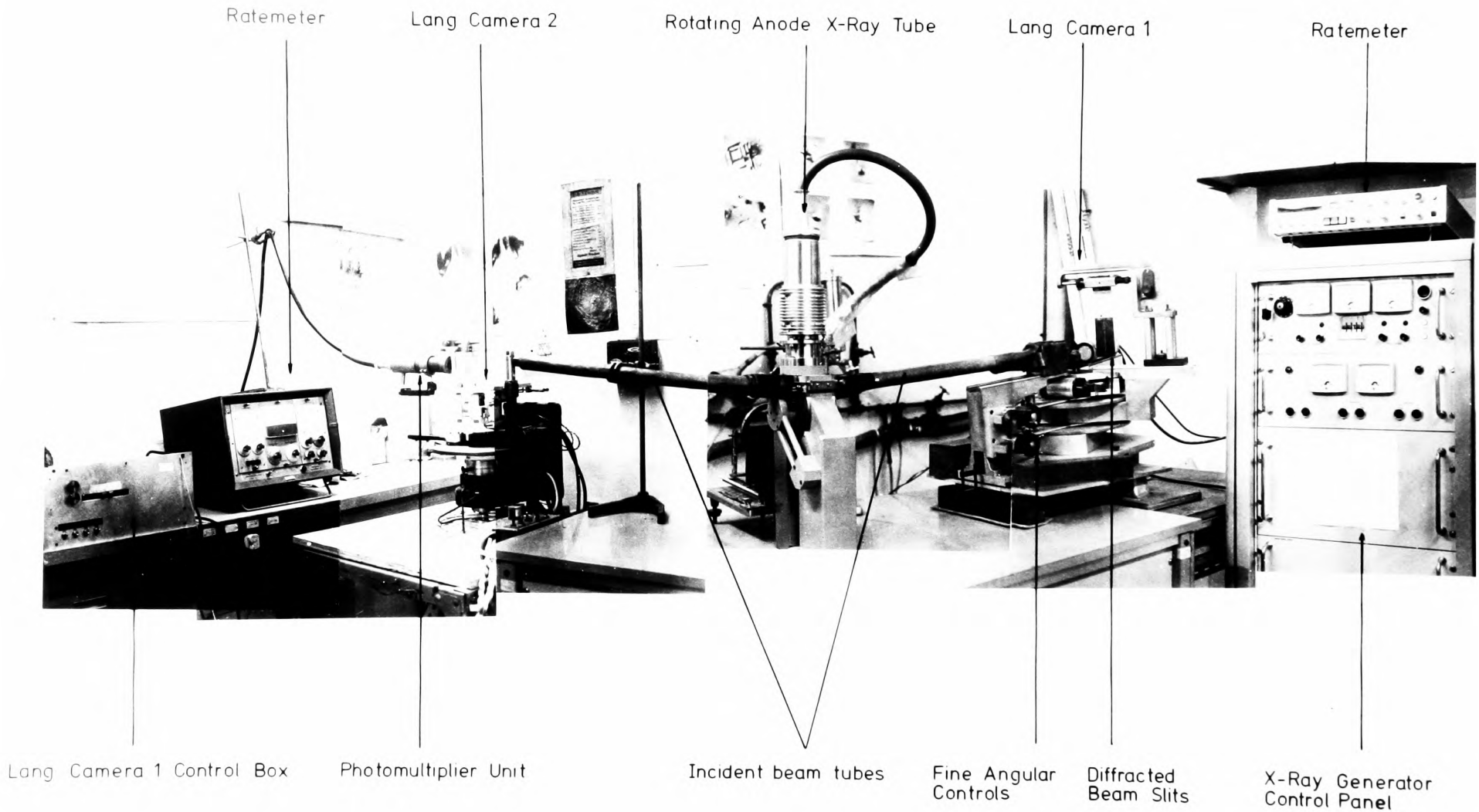
d = Interplanar spacing
Θ_B = Bragg angle
λ = Wavelength of radiation diffracted

Differentiating 3.3 with respect to λ :-

$$d\Theta_B = \tan\Theta_B \frac{d\lambda}{\lambda} \qquad 3.4$$

Typically $d\Theta_B$ is $\approx 2'$ of arc (or $\approx 6 \times 10^{-4}$ radians) except for large crystals, and since the magnitude of the perfect crystal rocking curve width, $d\Theta_c$, is usually $\approx 5''$ (or 2.5×10^{-5} radians) $d\Theta_c$ can normally be safely ignored. Furthermore, taking a representative value of $d\Theta_B$ as being 6×10^{-4} radians, and a specimen to film distance of 1 cm, then the best

Fig. 3.6 An Overall View of the Lang Cameras


Ratemeter
Lang Camera 2
Rotating Anode X-Ray Tube
Lang Camera 1
Ratemeter
Lang Camera 1 Control Box
Photomultiplier Unit
Incident beam tubes
Fine Angular Controls
Diffracted Beam Slits
X-Ray Generator Control Panel

horizontal resolution that can be achieved is 6.0 μm, unless the Bragg angle is very large. When Θ_B is very large, $d\Theta_B$ can become appreciable, whence the horizontal resolution can fall to 3-4 μm or even less, when the specimen to film distance is only a few mm.

To maximise resolution it is clear that the specimen to film distance must be small (in practice it is seldom feasible to place the film closer than 5 mm to the crystal); and that the use of small Bragg angles is preferred to large. Finally, it is worthwhile noting that the resolutions in both horizontal and vertical directions are very similar, which means that any improvement in one should be accompanied by an equal improvement in the other.

3.4 Ilford Nuclear Emulsions

In many respects the resolution limiting factor can be the film used to image the diffracted beam. Incorrect use of the film on the diffractometer, subsequent poor development and careless optical photography of the X-ray image can lead to both a loss of resolution and useful information. Throughout this work Ilford nuclear emulsions have been employed to record the X-ray topographic image and of the three types available, G5, K5, L4, only G5 and to a greater extent L4 have been used. From a resolution standpoint L4 is certainly the better emulsion (refer to Fig. 3.5) since it possesses the smallest undeveloped halide grain size (0.14 μm). Moreover, not only must the grain size be as small as possible and the halide density as high as possible ($\simeq 83\%$), but the emulsion thickness needs to be sufficiently large to increase the

probability of the dissociation of a halide molecule when an X-ray photon enters the film. Here, both 50 μm and 100 μm thicknesses have been used, because they were sufficient to reduce the intensity of $Mo_{K\alpha_1}$ and $Ag_{K\alpha_1}$ by approximately 50% and so produce a "latent image" which could be developed.

3.4.i The Use of the Film on the Lang Camera

When mounted on the diffractometer with the emulsion facing the diffracted beam, the normal to the film cassette must reside within 1^{o} of the diffracted beam direction otherwise a significant loss of image resolution can occur. For a film thickness, t, and angular deviation, α, such a resolution loss is given by R.L. = $t\tan\alpha$ and, for t = 100 μm and $\alpha = 1^{o}$, R.L. = 1.74 μm. In practice it was found that a simple way to overcome this difficulty was to measure the distance between the cassette and diffracted beam slits carefully with a ruler down either side of the cassette. Since the diffracted beam slits were most certainly perpendicular to the diffracted beam so would the cassette also be by this method. Magnets secured to the feet of the cassette (which was placed on a steel plate) maintained it in the correct position during exposure.

Prior to using a nuclear emulsion, a fast film topograph (fft) of the crystal was always taken to ensure that the correct diffraction conditions had been produced. Such fft's were taken using Ilford Industrial G film thereby enabling a rapid topograph to be produced in about 10 minutes. The Ilford Nuclear Emulsions required between 1 hr/mm and 5 hr/mm depending on diffracted beam intensity.

The Lang cameras must also traverse reasonably slowly, otherwise at the end of each half cycle the force induced on the specimen can cause it to move off the peak of the rocking curve. Even with very delicately mounted copper crystals this has never been a problem since the scan speed was so slow, i.e. 0·15 cm/min.

3.4.ii Development of the "Latent Image" in the Emulsion

As an X-ray photon traverses a nuclear emulsion it can dissociate halide molecules according to the following reaction:-

$$2Ag^{+} + Br^{-} \rightleftharpoons 2Ag + Br_2 \qquad 3.5$$

The silver is deposited as colloidal particles and it is these colloidal particles which constitute the "latent image" and which development aims to reveal. It must be remembered that the ionisation length of a $Mo_{K\alpha_1}$ photon can be $1\frac{1}{2}$-2 microns and that this can significantly affect image resolution; if harder radiations are used, e.g. $Ag_{K\alpha_1}$, this ionisation distance can rise to 2-3 microns[32].

Since the photographic emulsions are so thick it is necessary to arrange the development so that the diffusion rate of the developer into the emulsion is commensurate with the rate of development. The primary way in which this was done was by reducing the developing temperature to 0-4C (this affects development rate markedly but not the diffusion rate). In this work the developing procedure outlined in Table 3.1 was used for both the L4 and G5 emulsions.

TABLE 3.1

DEVELOPING PROCEDURE FOR ILFORD L4 AND G5 PLATES

		50 μm	100 μm
Soak:	distilled water at 4C to soften the emulsion	10 mins	20 mins
Develop:	Kodak D19B 3:1 or 1:1 with distilled H_2O, all at 4C	30-60 mins	45-60 mins
Stop:	1% Acetic acid in H_2O, all at 4C	10-15 mins	15-20 mins
Fix:	300 g/l Sodium Thiosulphate + 30 g/l Sodium Bisulphite with H_2O at room temperature	60-90 mins	60-120 mins
Wash:	running, filtered H_2O at room temperature	90-120 mins	120-150 mins
Drying:	Surface swabbed very gently with running water and cotton wool to remove any surface particles, and then washed in methanol which acted as a wetting agent. The plates were dried upside down on a watchglass in a dessicator. Normal drying was 120 mins for 50 μm and 360 mins for 100 μm		

Fluorescence around the main image could make subsequent optical photography difficult as it both interfered with optical negative exposure times and printing. To eliminate such a deleterious effect a subtractive reducing agent was used which oxidised the fluorescence image to a transparent silver salt, leaving a well defined diffraction image on an otherwise clear plate. A little overexposure was required to ensure that essential image detail was not lost too, because a subtractive reducer reduces all photographic densities equally. Fluorescent radiation is softer than diffracted radiation, however, which implies that it does not penetrate deep into the emulsion and thus even after overexposure of the main diffraction image the fluorescence can still be successfully reduced.

Reduction of the emulsion worked extremely well provided very long exposure times were not used ($\approx$ 30 hours), whence during reduction of the fluorescence image the corners of the diffraction image could be lost too. The reduction procedure is outlined in Table 3.2.

Intensification, the reverse of reduction, has not been used in this work because image resolution was invariably impaired. Also, the degree of densification which could be achieved was never satisfactory. It was always found to be better to repeat the experiment and increase the exposure time.

When completely dry ($\approx$ 2 days) the emulsion was covered with a solution of " Eukitt" (obtained from E. Mertens, Bonn, Königstrasse, W. Germany); then a well cleaned microscope slide cover glass was placed on top of the Eukitt and the preparation left to dry. This procedure ensured a well preserved topographic image for many years. The finally prepared plates were stored on trays and under cover to exclude dust.

TABLE 3.2

REDUCTION PROCEDURE

FARMER'S REDUCER

(Taken from reference 33)

Solution'A':	Potassium Ferricyanide	100 g
	Water to make	1000 cm^3
Solution 'B':	Sodium Thiosulphate	200 g
	Water to make	1000 cm^3

To 200 cm^3 of B was added a fresh batch of 5-10 cm^3 of A, which produced a pale yellow solution. The freshly washed plate was then immersed in the mixture and carefully watched whilst reduction took place. When sufficient image clearing had been produced the plate was immediately washed for $\approx$ 20 mins and then dried as in Table 3.1

3.4.iii Optical Photography of the X-ray Topograph

X-ray topography cannot be called X-ray microscopy inasmuch as X-ray cannot be focussed. Therefore, a crystal cannot be studied via an X-ray image which has been magnified on the Lang camera. Any magnification which is necessary must take place in an optical microscope.

A good optical microscope can accommodate magnifications between 3x and 2000x (the Reichert microscope used in this work was excellent in this respect). Understandably, the X-ray image should be magnified as much as possible to reveal every useful piece of information, but it is found that[32] the use of high numerical apertures is prohibited because of the photoelectron tack lengths (1-3 μm), and the reduction in counting statistics over a very small area (c.f. a newspaper when greatly magnified consists of black dots which can bear no resemblance to the original picture). In practice x800 is usually the best achievable (for $Co_{K\alpha_1}$ and $Cr_{K\alpha_1}$) whilst for $Mo_{K\alpha_1}$ the highest magnification to be profitably used was x200. Most X-ray topographs of metal crystals appearing in this thesis are at x10-15.

3.5 Topographing a Cylindrical Crystal

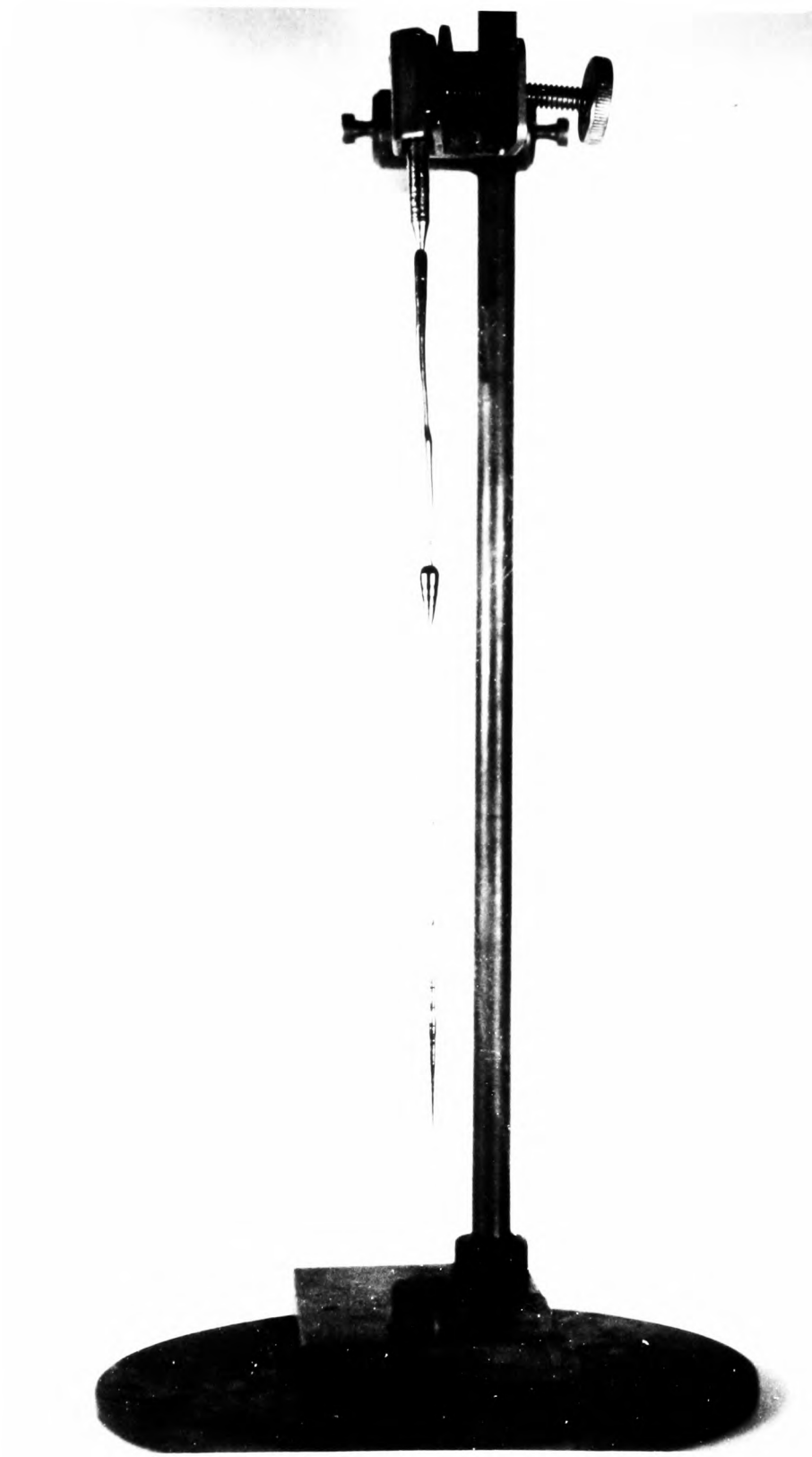
Normally, having taken a Laue photograph of a facetted crystal good enough for X-ray topography, it is easily possible to assign Miller indices to the various planes and directions which are visible. Moreover, from a simple subsequent sketch of the crystal, it is further possible to easily orient it to diffract from particular planes and so obtain X-ray

topographs using different g-vectors. When confronted with a dislocation-free cylindrical metal crystal the situation is much different, however: first, crystal symmetry makes an assessment of diffracting planes tedious; and secondly, the sample must remain attached to the seed in a vertical position otherwise dislocations may occur. This latter condition restricts g-vectors to those lying in the growth axis plane. It has been pointed out that of these g-vectors the 111's were the most useful (Chapter I) and the gist of the procedure to obtain such topographs will now be presented.

Intuitively it was clear that the Bragg surface of the crystal would diffract more strongly than the centre because the absorption was much less. (That this was true can be readily seen in Fig. 3.5.) The sample was clamped in a special stand which could fit directly onto the Lang Camera as shown in Fig. 3.7, (it had previously been Laue photographed to give the general g-vector direction to within 1^{o}); the tube power (35 kV and 5mA) was kept low to minimise irradiation of the operator; and the photomultiplier tube was positioned at $2\Theta_B$ to the incident beam to receive the diffracted radiation.

The crystal was then translated into the main beam until the leading edge just protruded into the incident X-rays. This was noticed by using a fluorescent stick placed in the incident beam and behind the crystal. By rotating the crystal slowly about its growth axis the diffracted beam was easily observed on a ratemeter coupled to the photomultiplier. To maintain the crystal on the peak of the rocking curve the fine angular control was used (Fig. 3.6). Finally, the normal setting-up procedure was adopted, e.g. insertion of the diffracted beam slits; taking a fft and so on.

Fig. 3.7 A Dislocation-free Copper Crystal Positioned in its Special Jig



3.6 X-ray Dynamical Theories

Having obtained an X-ray topograph it is necessary to interpret the intra-image contrast features and so work backwards to an understanding of defects in the lattice. For the present purpose, however, the crystal will be assumed to be perfect and two theories of X-ray diffraction will be presented (the Ewald-Laue and the Takagi-Taupin-Uragami theories) and used to analyse the diffraction phenomena associated with perfect, cylindrical copper crystals.

3.6.i The Ewald-Laue Theory[31,34]

It is assumed that, as a first approximation, the incident X-ray beam 'seen' by the crystal is a plane-wave. Strictly it is a spherical wave, but the plane-wave approximation is very useful when interpreting Borrmann topographs and some features of projection topographs. Added to this the study examines the interaction of plane-waves with a crystal which is also set at the Bragg position.

Let an electromagnetic plane-wave defined by:-

$$\underline{E} = \underline{Eo} \exp(-2\pi i(\nu t - \underline{k}.\underline{r}) \qquad 3.6$$

Where,

$\underline{E}$ = electric field vector at time, t, and position, $\underline{r}$
$\underline{Eo}$ = maximum value of $\underline{E}$
ν = frequency of wave
$\underline{k}$ = wave vector = $\frac{1}{\lambda}$ (where λ = wavelength)

be incident on a crystal which contains a periodic distribution of electrons. As a result the electrons will be set into motion under the influence of the applied field and will act as resonating dipoles under precisely defined conditions. By applying

simple electrostatic theory and Newtonian mechanics to this phenomenon, it can be shown that[31] the susceptibility, χ, of the crystal is given by:-

$$\chi = \frac{-e^2\lambda^2\rho}{m_o c^2 4\pi^2\epsilon_o} = \frac{-R\lambda^2\rho}{\pi} \qquad 3.7$$

Where,

(Units are in the S.I. system)
m_o = mass of the electron
e = charge of the electron
λ = wavelength of incident radiation
c = vacuum velocity of light
ϵ_o = permittivity of free space
R = classical radius of the electron

For X-rays χ is tiny (typically $\approx 10^{-5}$), negative and dimensionless and it allows the refractive index, n, to be written as:-

$$n = \left(\frac{\epsilon}{\epsilon_o}\right)^{\frac{1}{2}} = (1+\chi)^{\frac{1}{2}} = \left(1+\frac{\chi}{2}\right) \qquad 3.8$$

Where,

ϵ = permittivity of the crystal

3.7 clearly shows that χ is proportional to ρ; and since ρ possesses the 3-D periodicity of the crystal so also must χ. This can be done by expanding χ as a Fourier series based on the reciprocal lattice:-

$$\chi = \sum_h \chi_h \exp(2\pi i \underline{h}.\underline{r}) \qquad 3.9$$

This summation extends over all reciprocal lattice points, $\underline{h}$, and therefore gives the distribution of χ throughout the whole crystal; which is a necessary prerequisite to this study as first pointed out by von-Laue[35] in 1931.

In 3.9 the pre-exponential factor, χ_h, is related to the structure factor, F_h, for a particular Bragg reflection by the expression:-

$$\chi_h = \frac{-R\lambda^2}{\pi V_c} F_h = \frac{-R\lambda^2}{\pi V_c} \sum_j f_j \exp(2\pi i \underline{h}.\underline{r}_j) \quad 3.10$$

Where,

V_c = volume of the unit cell
f_j = scattering factor for an atom
r_j = position vector of the jth atom in the unit cell

χ_h is really sub-divided into two component parts:-

$$\chi_h = \chi_{rh} + i\chi_{ih} \quad 3.11$$

Where,

χ_{rh} = real part of χ_h
χ_{ih} = imaginary part of χ_h

χ_{ih} takes into account absorption phenomenologically. The normal linear absorption coefficient, μ_o, is given by:-

$$\mu_o = -2\pi k \chi_{io} \quad 3.12$$

Expression 3.7 is important because it shows that the interaction of the X-rays with the charged particles in the crystal is only strong for the electrons: the inverse mass term reduces any influence of the X-rays on the protons to $\frac{1}{2000}$ of that for electrons. Hence, the protons can be safely ignored.

For the problem in hand, the electrical conductivity is zero and the magnetic susceptibility is unity. Further, the dielectric displacement, $\underline{D}$, is related to the polarisation, $\underline{P}$, and the field, $\underline{E}$, by:-

$$\underline{D} = \epsilon_o \underline{E} + \underline{P} = \epsilon_o (1 + \chi)\underline{E} \quad 3.13$$

Using equation 3.13 Maxwell's equations[36] can be written so that they contain only one dependent variable. This variable for the current study is $\underline{D}$ and the waves within the crystal can be analysed via a 'propagation equation':-

$$\text{Curl}.\text{Curl}\ (1-\chi)\underline{D} = -\left(\frac{1}{c}2\right) \frac{d^2 D}{dt^2} \quad 3.14$$

In a periodic medium (the perfect crystal) a valid solution of 3.14 is a Bloch wave of the form:-

$$\underline{D}_j = \exp(-2\pi i \underline{k}_{oj} \cdot \underline{r}_j) \sum_h \underline{D}_{hj} \exp(2\pi i \underline{h} \cdot \underline{r}) \qquad 3.15$$

Where,

$\underline{k}_{oj}$ = wave-vector of a direct (forward-scattered) wave within the crystal

The Bloch wave concept is very useful because it accounts for many diffraction phenomena[37,38]. Each plane-wave component of 3.15 has a wave-vector of the form:-

$$\underline{k}_{hj} = \underline{k}_{oj} + \underline{h} \qquad 3.16$$

Where, from the Laue condition,

$\underline{k}_{hj}$ = wave-vector of the diffracted waves within the crystal.

3.15 then becomes:-

$$\underline{D}_j = \sum \underline{D}_{hj} \exp(-2\pi i \underline{k}_{hj} \cdot \underline{r}) \qquad 3.17$$

3.17 indicates that the waves are characterised by one wave-vector, $\underline{k}_{hj}$, one wave-amplitude, $\underline{D}_{hj}$, and that both Bragg's law and Maxwell's equations have been satisfied. Additionally, 3.17 describes not a single wave but a 'wavefield', composed of coupled plane waves travelling in the same direction: hence, the theory is concerned with dynamical X-ray interactions within the crystal.

Inserting 3.9 and 3.17 into 3.14 it is possible to derive the following vector wave equation:-

$$\underline{D}_{hj} - \left(\frac{\underline{k}_{hj}^2}{\underline{k}_{hj}^2 - \underline{k}^2}\right) \sum_{h^1} \chi_{(h-h^1)} \underline{D}_{h^1(h)j} = 0 \qquad 3.18$$

Where, $\underline{D}_{h^1(h)j}$ is the projection of $\underline{D}_{hj}$ on a plane normal to $\underline{k}_{hj}$. Ordinarily $\chi_{(h-h^1)}$ is the most influential part of the second term in 3.18, but when $\underline{k}_{hj} \approx \underline{k}$ a resonance condition can

be generated. This occurs when reciprocal lattice points reside on the Ewald sphere and, in a diffraction situation for X-rays, only two such points need be considered because the Ewald sphere is small compared to the reciprocal lattice spacing. Therefore, a two beam condition can be generated.

Under such a two beam condition 3.18 reduces to:-

$$\left.\begin{aligned}(\underline{k}_{oj}^2-\underline{k}^2(1+\chi_o))\underline{D}_{oj}-\underline{k}^2\chi_h-C\underline{D}_{hj} &= 0\\ -\underline{k}^2\chi_h C\underline{D}_{oj}+(\underline{k}_{hj}^2-\underline{k}^2(1+\chi_o))\underline{D}_{hj} &= 0\end{aligned}\right\} \quad 3.19$$

Where C is a polarisation factor accounting for whether the incident polarisation vector is parallel to the $\underline{k}_o\underline{k}_h$ plane (the so-called π polarisation) whence $C = \cos 2\theta_B$; or whether the polarisation vector is perpendicular to the $\underline{k}_o\underline{k}_h$ plane (the so-called σ polarisation), whence $C = 1$.

A solution to 3.19 exists for which the determinant is equal to zero, i.e. when:-

$$(\underline{k}_{oj}^2-\underline{k}^2(1+\chi_o))(\underline{k}_{hj}^2-\underline{k}^2(1+\chi_o)) = \chi_h\chi_{\bar{h}}\ C^2\underline{k}^4 \qquad 3.20$$

For centrosymmetric crystal structures (as used in this thesis) $\chi_h = \chi_{\bar{h}} \approx 10^{-5}$ and so the right hand side of 3.20 is very nearly zero. Thus, when one of the two left hand terms is nearly zero, i.e.:-

$$\underline{k}_{oj} \text{ or } \underline{k}_{hj} = \underline{k}(1+\frac{\chi_o}{2}) = n\underline{k} \qquad 3.21$$

3.19 has a solution.

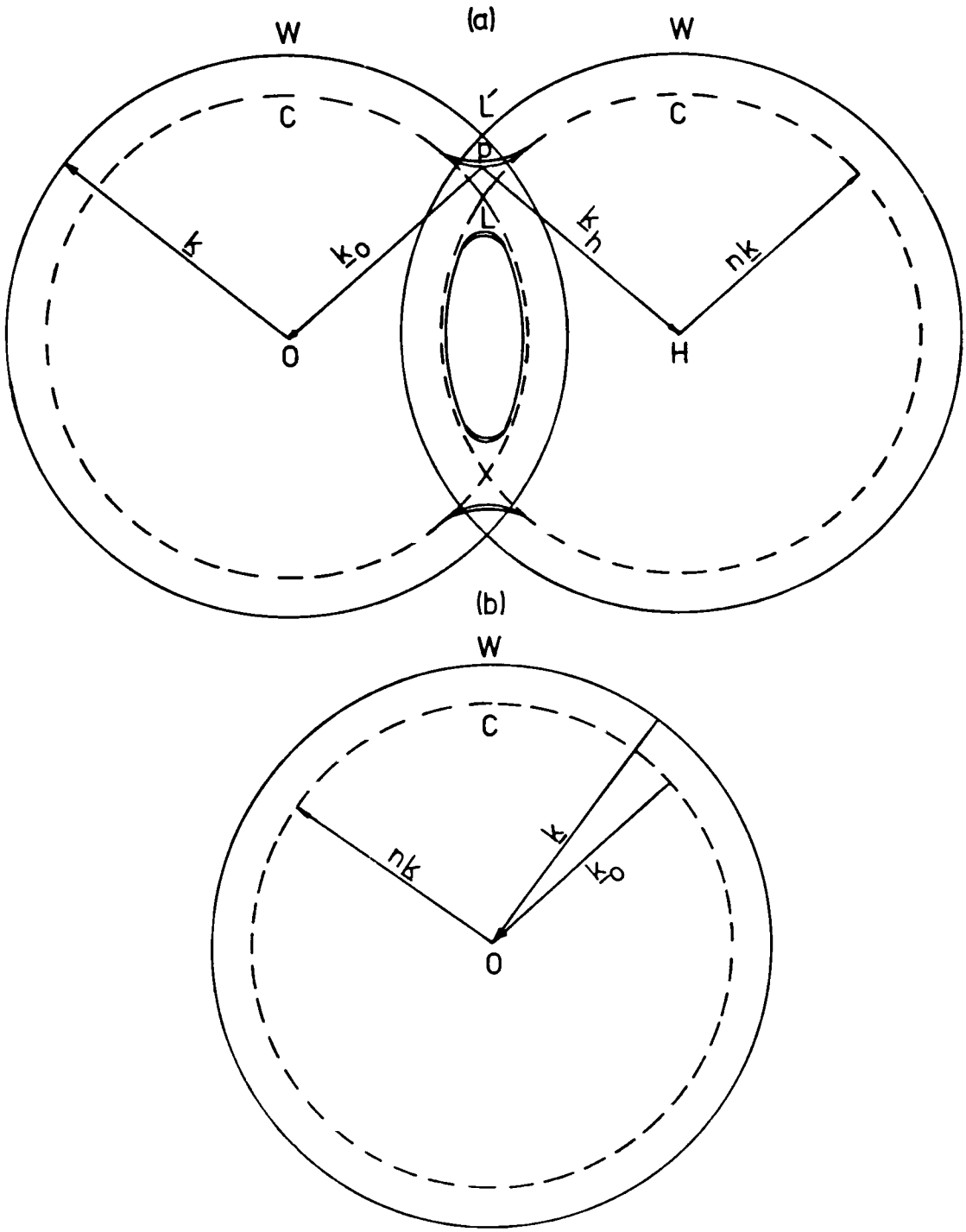
3.21 map out spheres centred on O and H as shown in Fig. 3.8a which are the ordinary Ewald spheres, W, corrected for the refractive index, n. Far from the intersection of these two spheres only one wavefield propagates inside the crystal (Fig. 3.8b), i.e. the refracted wavefield and so $\underline{D}_{oj}$ is large.

Fig. 3.8 Dispersion Surface Spheres for the Two Beam Case (a) and Single Beam Case (b)

The vacuum spheres are denoted by W and the crystal spheres by C. The tie point, P, in the two beam case, resides on the hyperboloid section of the model near to the intersection of the two crystal spheres centred on O and H

L^1 = Laue Point

L = Lorentz Point


(a)
W
W
C
C
L'
D
L
X
k
k0
kh
nk
O
H
(b)
W
C
nk
k
k0
O

At or very near to the intersection of the spheres it is possible for both:-

$$\underline{k}_{oj} \approx \underline{k}_{hj} \approx n\underline{k} \qquad 3.22$$

at the same time, i.e. this is very near to the Bragg condition. Accordingly the components of the left hand side of 3.20 may be written as:-

$$\left.\begin{aligned} \underline{k}_{oj}^2 - \underline{k}^2(1+\chi_o) &= 2\underline{k}\left[\underline{k}_{oj} - \underline{k}\left(1+\frac{\chi_o}{2}\right)\right] \\ \underline{k}_{hj}^2 - \underline{k}^2(1+\chi_o) &= 2\underline{k}\left[\underline{k}_{hj} - \underline{k}\left(1+\frac{\chi_o}{2}\right)\right] \end{aligned}\right\} \qquad 3.23$$

Here, the square bracketted terms on the right hand side of 3.23 represent the perpendicular distances of the two wave vectors $\underline{k}_{hj}$ and $\underline{k}_{oj}$ from the Ewald spheres of radius $n\underline{k}$ close to the Laue points, h, in Fig. 3.8. Denoting these distances by ψ_h and ψ_o respectively, 3.20 reduces to:-

$$\psi_o \psi_h = \underline{k}^4 \frac{c}{4} \chi_h \chi_{\bar{h}} \qquad 3.24$$

This is the "dispersion surface" equation, which is the mathematical representation of the locus of all the tie-points around the vicinity of the Laue and the Lorentz points. Ewald[34] originally termed this the 'dispersion surface' equation because it aptly represented the way in which the crystal could be encouraged to resonate, and so disperse energy in a well defined direction other than in the refracted direction.

3.24 is clearly the equation of an hyperboloid, which further means that by residing on this surface the wave-fields characterised by $\underline{k}_{oj}$ and $\underline{k}_{hj}$ possess locally different refractive indices n_{oj} and n_{hj} respectively compared to the average refractive index, n.

ψ_o and ψ_h are small compared to $\underline{k}_{oj}$ and $\underline{k}_{hj}$ ($\approx 10^{-5}\underline{k}_{oj}$, $\underline{k}_{hj}$) and so on a scale which clearly shows the variation of $\psi_o\psi_h$, X_o and X_h (i.e. the Ewald spheres corrected for the crystal refractive index) appear as planes in 3-D or, more usually, as straight line asymptotes to the two sheets (per polarisation) of the hyperbolae in 2-D, as shown in Fig. 3.9.

The dispersion surface so derived will now be used to discuss X-ray diffraction in perfect cylindrical crystals.

3.6.ii The Dispersion Surface and Highly Absorbing Perfect, Cylindrical Copper Crystals

The dispersion surfaces relevant to the 111 diffraction condition of $M_{oK\alpha_1}$ radiation in copper are shown in Fig. 3.9. These curves were plotted using the following information:-

a. $\chi_h = \chi_{\bar{h}}$ (Copper is centrosymmetric)

$F_h = F_{\bar{h}}$

b. $$\psi_o\psi_h = \left(\frac{CR\lambda}{V_c}\left|F_h\right|\right)^2 \qquad 3.25$$

(Derived by inserting 3.10 into 3.24 using a above)

c. $R = 2.81 \times 10^{-13}$ cm

$\lambda = 7.0926 \times 10^{-9}$ cm

$V_c = 4.725 \times 10^{-23}$ cm^3 39

$F_h = 80$

$2\Theta_B = 19.5638^\circ$

d. $\psi_o^{\pi}\psi_h^{\pi} = 1.0109 \times 10^7$ cm^{-2} ($C = \mathrm{Cos}2\Theta_B$)

$\psi_o^{\sigma}\psi_h^{\sigma} = 1.1386 \times 10^7$ cm^{-2} ($C = 1$)

It is clear from Fig. 3.9 that the effect of polarisation in this case is minimal: indeed, it is only when $\mathrm{Cos}2\Theta_B$ is large that polarisation effects can be influential. Only the C = 1 state will be considered in detail here.

Fig. 3.9 The 111 Dispersion Surfaces for $M_{oK\alpha_1}$ Radiation in Copper, Magnified to Reveal Tie Point Information

$\frac{1}{\Lambda_o}$ = Extinction length = $\frac{1}{({}^1P\sigma\ {}^2P\sigma)} = \xi_h$

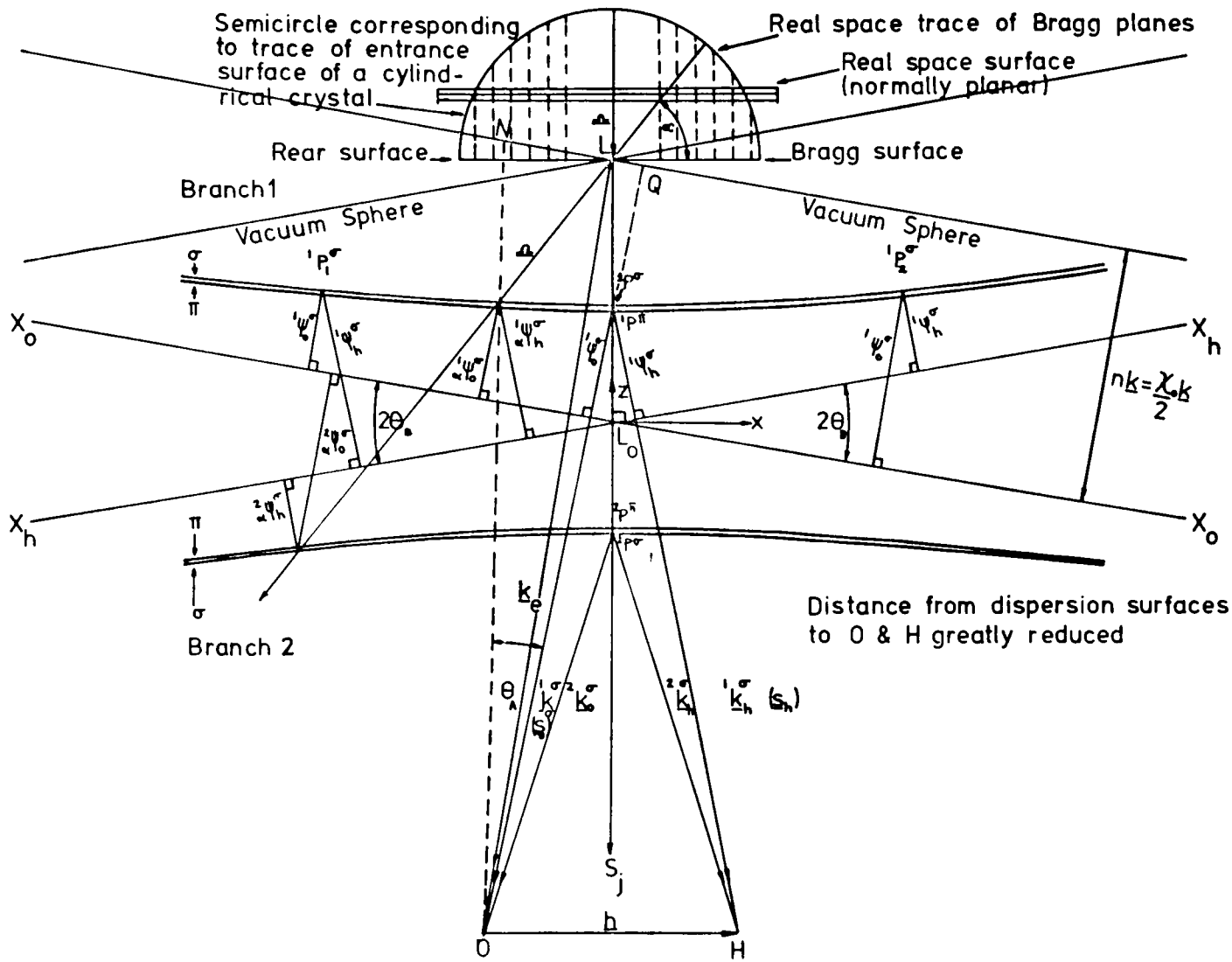
ξ_h = Extinction distance for the exact Bragg condition

X_o, X_h = asymptotes to the dispersion surfaces and in full reciprocal space are spheres centred on 0 and H respectively

For the case of anomalous transmission used in this thesis the Poynting vector, $\underline{S}_j$, must point down the atomic planes, as shown, to minimise absorption

$\underline{n}$ = real space surface normal

$\Theta_A = (\frac{QN}{k_e})$


Semicircle corresponding to trace of entrance surface of a cylindrical crystal
Real space trace of Bragg planes
Real space surface (normally planar)
Rear surface
Bragg surface
Branch1
Vacuum Sphere
Vacuum Sphere
Branch 2
Distance from dispersion surfaces to O & H greatly reduced
O
H

As well as giving the directions of the "crystal waves", the dispersion surfaces also provide information about the relative amplitudes of these same waves. Let M denote the ratio $\underline{D}_{hj} : \underline{D}_{oj}$; then by dividing either of 3.19 by $\underline{D}_{hj}$ or $\underline{D}_{oj}$, it can be shown that:-

$$M = \frac{\underline{D}_{hj}}{\underline{D}_{oj}} = \frac{2\psi_o}{\underline{k}C\chi_h} = \frac{\underline{k}\psi_h C}{2\chi_h} \qquad 3.26$$

Referring to Fig. 3.9 and using 3.26 it is clear that when the tie point, P, resides at the centre of the reflection domain the two wavefields $\underline{D}_{hj}$ and $\underline{D}_{oj}$ have amplitudes equal to ∓ 1. As the crystal is rocked so that ${}^1P^{\sigma}$ moves towards ${}^1P_1^{\sigma}$, i.e. the angular deviation, Θ_A, from the Bragg angle, Θ_B, is negative, $\underline{D}_{oj}$ increases at the expense of $\underline{D}_{hj}$; conversely, when Θ_A is positive and ${}^1P^{\sigma}$ moves towards ${}^1P_2^{\sigma}$, $\underline{D}_{hj}$ increases to the detriment of $\underline{D}_{oj}$. Thus a complementary interchange of energy occurs between the two wavefields implying that such wavefields are dynamically coupled.

This being the case, it is profitable to examine the associated energy flow direction for the various tie-points, P, as given by the corresponding Poynting vectors, $\underline{S}_j$. By definition, the time averaged Poynting vector is given by[41]:-

$$\underline{S}_j = \tfrac{1}{2}\,\mathrm{Re}(\underline{E}_j \wedge \underline{H}_j^{*}) \qquad 3.27$$

Where, Re means the real part of $\underline{E}_j \wedge \underline{H}_j^{*}$.

Further, it can be shown that[41] for the present case:-

$$\underline{S}_j = \frac{C}{\epsilon_o}\left((\underline{D}_{oj})^2\underline{S}_o + (\underline{D}_{hj})^2\underline{S}_h\right)\exp(4\pi\,\underline{k}_{oj}^{i}.\underline{r}) \qquad 3.28$$

Where,

$\underline{k}_{oj}^{i}$ is the imaginary part of $\underline{k}_{oj}$

$\underline{S}_o, \underline{S}_h$ are unit vectors along the refracted and diffracted beam directions respectively

Kato[42] has shown that $\underline{S}_j$ is in fact always perpendicular to the dispersion surface. Consequently, for points such as ${}^1P^{\sigma}$ at the centre of the rocking curve in Fig. 3.9, $\underline{S}_j$ is directed down the atomic avenues and it bisects $\underline{S}_o$ and $\underline{S}_h$. More importantly, the energy in both $\underline{D}_{oj}$ and $\underline{D}_{hj}$ will be the same for such a condition. In practice this is the particular case of Borrmann anomalous transmission as discussed in Section 3.2.ii. Experimental verification for this conclusion is shown in Fig. 3.10 where a dislocation-free cylindrical copper crystal is imaged in $\left|\underline{D}_{oj}\right|^2$ and $\left|\underline{D}_{hj}\right|^2$. It is noticed that the exposure times were comparable, and that for the central region of the crystal where anomalous transmission occurred that the intensity traces from a microdensitometer were very close. Along the purely Bragg leading surface, (BLS) the intensity profiles were complementary since this was not an anomalous transmission state, and so all the incident energy was directed into $\underline{D}_{hj}$, producing a region of high contrast in Fig. 3.10a and low contrast in Fig. 3.10b.

3.6.iii The Borrmann Effect

Borrmann first noticed[43] that a thick crystal which would otherwise absorb X-ray strongly could transmit them if it was highly perfect and set to diffract at the centre of the reflection domain. However, it was von Laue[44] who first propounded the following analysis of the effect.

The wavefield amplitude, $\underline{D}_j$, in the two beam case can be considered as the sum of the diffracted and refracted waves:-

Fig. 3.10 Part of a Cylindrical Crystal Imaged in $|\underline{D}_{oj}|^2$ and $|\underline{D}_{hj}|^2$

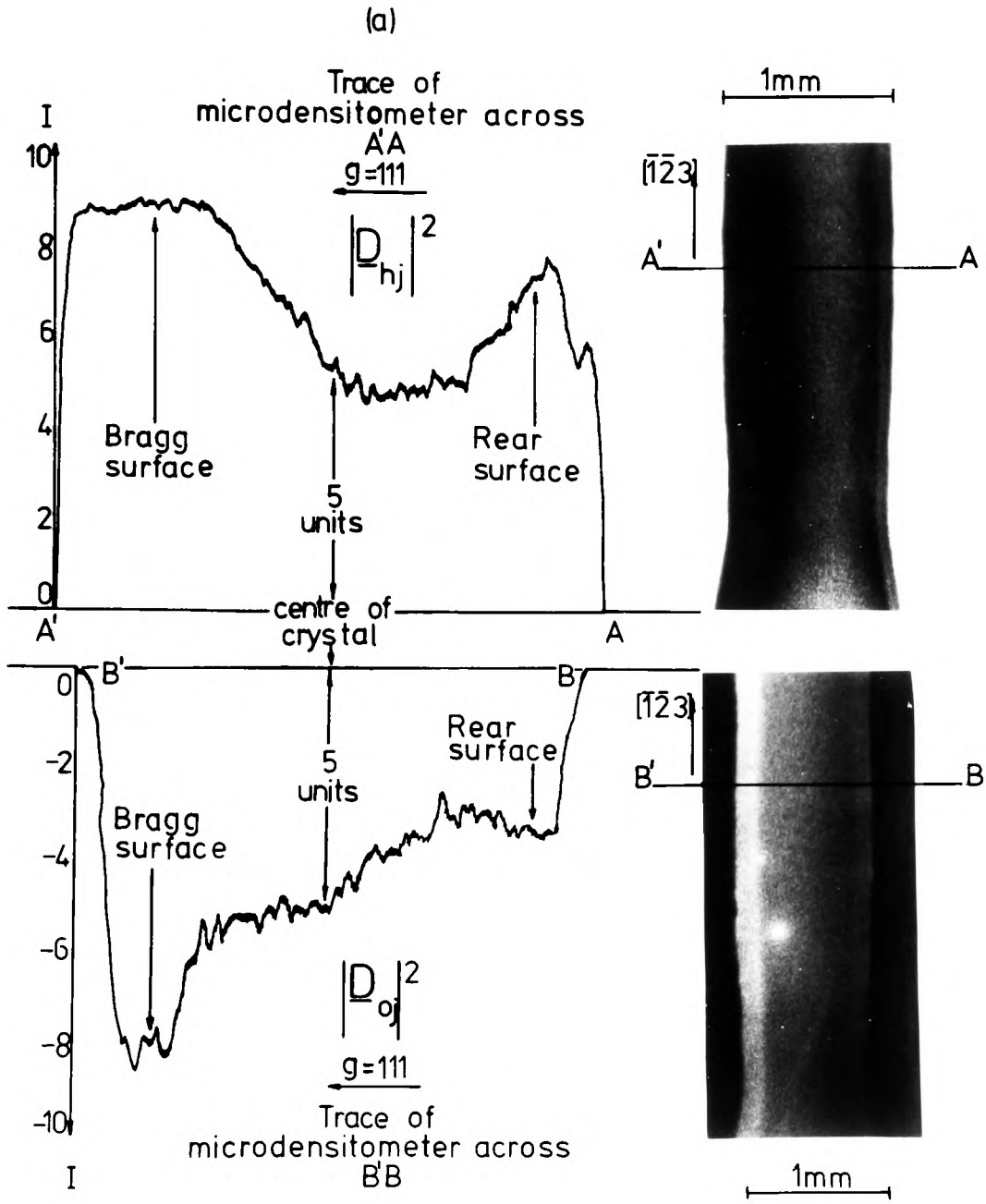
Exposure time for both = 3.5 hrs.
(50 kV 35 mA)

$\lambda = M_{oK\alpha_1}$ radiation

Note the absence of high contrast on the Bragg leading surface in (b), where all the energy has been transferred to $|\underline{D}_{hj}|^2$ in (a). The relative intensities for this surface are of equal magnitude but opposite sign as shown on the microdensitometer traces.

In the Borrmann state (at the exact centre of the crystal) $|\underline{D}_{oj}|^2$ and $|\underline{D}_{hj}|^2$ have equal intensities as shown, and predicted from plane-wave theory.

I = Intensity for that trace in arbitrary units


(a)
Trace of microdensitometer across A'A
g=111
$|D_{hj}|^2$
I
10
8
6
4
2
0
Bragg surface
Rear surface
5 units
centre of crystal
A'
A
1mm
$[\bar{1}\bar{2}3]$
A'
A
B'
B
0
-2
-4
-6
-8
-10
Bragg surface
Rear surface
5 units
$|D_{oj}|^2$
g=111
Trace of microdensitometer across B'B
I
$[\bar{1}\bar{2}3]$
B'
B
1mm
(b)

$$\underline{D}_j = \exp(-2\pi i \underline{k}_{oj} \cdot \underline{r})(\underline{D}_{oj} + \underline{D}_{hj} \exp(+2\pi i \underline{h} \cdot \underline{r})) \quad 3.29$$

In addition the intensity, I_j, can be written as:-

$$I_j = |\underline{D}_j|^2 = \exp(-4\pi \underline{k}_{oj}^{i} \cdot \underline{r})(|\underline{D}_{oj}|^2 + |\underline{D}_{hj}|^2 + 2\underline{D}_{oj}\underline{D}_{hj} C\cos 2\pi \underline{h} \cdot \underline{r}) \quad 3.30$$

Most important of all in 3.30 is the term $\cos(2\pi \underline{h} \cdot \underline{r})$ because this is the intensity modulating term. Since $\underline{h} \cdot \underline{r}$ = an integer only when $\underline{r}$ = a lattice vector, $\cos(2\pi \underline{h} \cdot \underline{r})$ is a maximum at lattice sites (i.e. at atom positions in simple structures such as Cu considered here).

From 3.26 it is clear the $\underline{D}_{oj}\underline{D}_{hj}$ is opposite to the sign of ψ_o since $\chi_h < 0$. When the tie point lies on branch 1 of the dispersion surface $\psi_o > 0$, $\underline{D}_{oj}\underline{D}_{hj} < 0$ and the maxima occur between the atomic planes; conversely, when ψ_o ends on branch 2 it is < 0, $\underline{D}_{oj}\underline{D}_{hj}$ is therefore > 0 and the maxima occur at the atomic positions. The added implications of these results are that only branch 2 wavefields are strongly absorbed, since photoelectron absorption is localised near to atom sites and, that to each wavefield must be assigned a specific absorption coefficient. Hence, although still suffering significant absorption, branch 1 wavefields still reach the exit face of the crystal with appreciable amplitude (refer to Section 3.6.iv). And, furthermore, the Poynting vector for such waves must point directly down the atomic planes (at the centre of the reflection curve) because any deviation would cause an increase in photoelectron absorption and hence a reduction of $\underline{D}_{oj}$ and $\underline{D}_{hj}$. This result further means that the wavefields do not decouple until the exit face of the crystal, which was first shown theoretically by von Laue[44]. The beam which then emanates

from the exit face of the crystal in the usually termed "forward direction" must now be re-named the "forward diffracted beam", since it arises from a dynamical interaction of wavefields with the lattice and is not generated in an isolated way within the crystal.

3.6.iv Boundary Conditions and Absorption Coefficients

Most experiments monitor wave intensities outside the crystal and so the boundary conditions at the crystal-vacuum (air) interface must be chosen to account for the decoupling and energy transfer of the Bloch waves at this junction. Hence, the resolved components of the wave-vectors must match on both sides of the boundary, i.e. the tangential component of the wave-vectors must be equal on both sides of the boundary. To satisfy this condition:-

$$\exp(-2\pi i \underline{k}_e \cdot \underline{\alpha}) = \exp(-2\pi i \underline{k}_h \cdot \underline{\alpha}) \qquad 3.31$$

Where,

$\underline{\alpha}$ = surface normal

$\underline{k}_e$ = incident wave-vector

$\underline{k}_h$ = wave-vector of the crystal Bloch waves

(Note: this is for the air-crystal interface, but the argument holds for the crystal-air interface too)

The wave-vectors inside and outside the crystal differ only slightly, and this can be represented as a vector equation in terms of a fraction of the surface normal, $\delta\,\underline{\alpha}$:-

$$\underline{k}_{oi} - \underline{k}_e = \underline{k}_{hi} - \underline{k}_e = \delta\,\underline{\alpha} \qquad 3.32$$

i = 1 or 2 depending on the branch of the dispersion surface

3.32 may be geometrically represented on a dispersion surface as shown in Fig. 3.9 by constructing a local surface normal, $\underline{\Omega}$, from the end of the incident wave-vector, $\underline{k}_e$, to cut the dispersion surfaces. The intersection points give the tie-points excited on the dispersion surface, e.g. ${}^1p^{\sigma}$, ${}^2p^{\sigma}$, ${}^1p^{\pi}$, ${}^2p^{\pi}$ in Fig. 3.9. In the Laue case, as used predominantly in this thesis, with each tie point one Bloch wave is associated, each having an effective absorption coefficient, μ_{eff}, given by[40]:-

$$\mu_{eff} = \mu_o(1 \mp |C| \epsilon_o \exp(-M)) \qquad 3.33$$

C = polarisation factor mentioned previously in equation 3.19

Where,

- refers to branch 1

+ refers to branch 2

μ_o is the normal linear absorption coefficient

ϵ_o is the pre-exponential of the Debye-Waller factor

exp(-M) is the Debye-Waller factor

To take the 111 diffraction condition of $M_{oK\alpha_1}$ in copper:-

$\mu_o = 445 \text{ cm}^{-1}$

C = 1 or 0.9422

Temperature = 20C, $\therefore$ exp(-M) = 0.988[39]

$\epsilon_o C(C=1) = 0.9983$

$\epsilon_o C(C=0.9422) = 0.9368$ [45]

Hence, the particular values of μ_{eff} are:-

Branch 1 σ polarisation $\mu_{eff} = 6.08 \text{ cm}^{-1}$

σ " $\mu_{eff} = 33.12 \text{ cm}^{-1}$

Branch 2 π polarisation $\mu_{eff} = 856 \text{ cm}^{-1}$

π " $\mu_{eff} = 883 \text{ cm}^{-1}$

Therefore, it is to be expected that only branch 1, σ polarised waves traverse these highly absorbing thick copper crystals.

3.6.v The Dispersion Surface and a Cylindrical Crystal

The dispersion surface size and shape is invariant of specimen shape and is determined only by $\underline{k}$, χ_h, χ_{h^-} and C (equation 3.24). But the specimen shape affects the boundary conditions discussed in Section 3.6.iv, and this subsection explores the imposition of boundary condition (3.32) on a crystal which possesses a cylindrical surface. In two dimensions this surface would obviously trace out a circle, and since only the entrance surface need be considered to analyse excited Bloch waves a semi-circle will suffice for the discussion as depicted in Fig. 3.9.

For every point along the circle in Fig. 3.9 the boundary condition (3.32) must be satisfied. Hence, by allowing the inward drawn normal, $\underline{n}$, to rotate about the Laue point, L, by an angle α, it is possible to define the deviation (Θ_A) of the crystal wave vectors from the exact Bragg angle as the crystal traverses the incident discrete wave-vector $\underline{k}_e$. (Θ_A is derived in Fig. 3.9.) It is also assumed that the exact Bragg condition is satisfied when the angle α is 90^o, i.e. the crystal is positioned centrally in the incident radiation.

Referring the dispersion surfaces in Fig. 3.9 to the new rectangular cartesian axes Ox and Oz, the dispersion surface equation becomes:-

$$z^2 = \frac{\Delta_o^2}{4} + x^2 \operatorname{Tan}^2\Theta_B \qquad 3.34$$

Where,

$\Delta_o = {}^1P^{\sigma}\ {}^2P^{\sigma}$ in Fig. 3.9 $\quad C = 1$

$\Delta_o = {}^1P^{\pi}\ {}^2P^{\pi}$ $\quad C = \operatorname{Cos}2\Theta_B$

Similarly, referred to Ox and Oz the line of the inward drawn normal, $\underline{\Omega}$, may be described by the equation:-

$$z = A + x\mathrm{Tan}\alpha \qquad 3.35$$

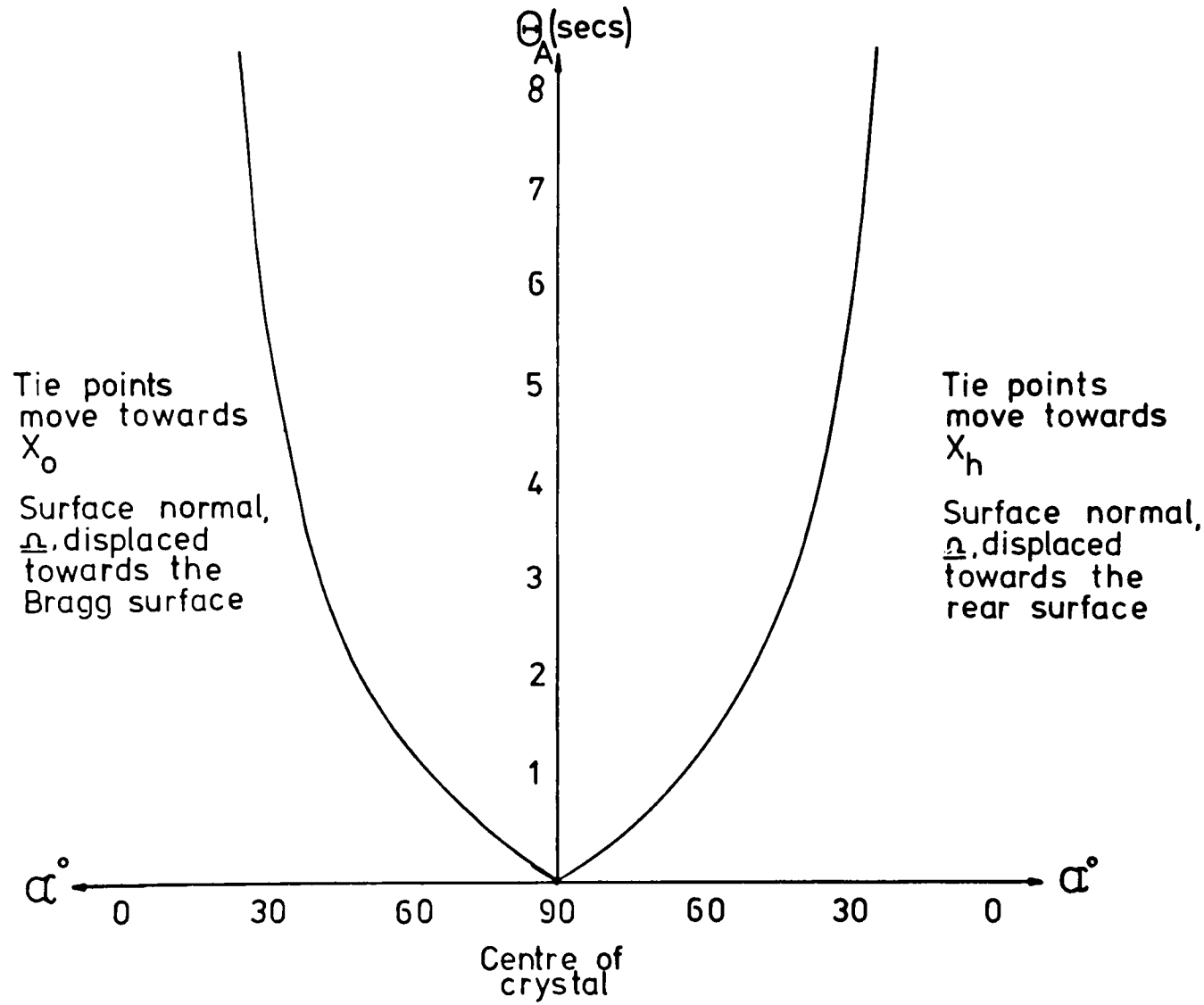
Where,

A = the distance between the Lorentz and Laue points in Fig. 3.9.

By solving the coupled equations 3.34 and 3.35 it was possible to characterise the particular tie-points, ${}^{1}_{\alpha}\psi^{\sigma}_{o}$, ${}^{1}_{\alpha}\psi^{\sigma}_{h}$, ${}^{2}_{\alpha}\psi^{\pi}_{o}$, ${}^{2}_{\alpha}\psi^{\pi}_{h}$ excited for each value of α and therefore position on the surface of the crystal cylinder as shown in Fig. 3.9. Furthermore, it was demonstrated in Section 3.6.iv that only σ polarisation, branch 1 wavefields are minimally absorbed and so the discussion will be restricted to these wavefields.

As α decreases from 90° to 80° in a sense towards the Bragg leading surface (BLS) it is clear from Figs. 3.9 and 3.11 that the tie points deviate little from the ${}^{1}P^{\sigma}$ position, and that Θ_A decreases from zero only slightly ($\approx 0.3''$ at $\alpha = 80^{\circ}$). As α tends towards 0° the intersection of $\underline{\Omega}$ with branch 1 of the dispersion surface occurs at larger and larger deviations from Θ_B, e.g. at $\alpha = 30^{\circ}$, $\Theta_A = 6.15''$ and so the tie point ${}^{1}P^{\sigma}$ migrates towards X_o. In terms of the amplitude ratio, M, as defined in 3.26, this means that $\underline{D}_{oj}$ increases at the expense of $\underline{D}_{hj}$ as discussed previously in Section 3.6.ii. Additionally, when $\alpha = 0^{\circ}$ no intersection of $\underline{\Omega}$ with the dispersion surface would be expected and so no crystal diffraction wavefields would be generated; only a refracted wavefield would exist. When α decreases from 90° to 0° in a sense towards the rear surface similar effects to those mentioned above would be expected. The only difference would be that since ${}^{1}_{\alpha}\psi^{\sigma}_{o}$ increases,

Fig. 3.11 The Variation of the Deviation from Ideal Bragg, θ_A, with angle α across a Cylindrical Crystal


Θ_A (secs)
8
7
6
5
4
3
2
1
Tie points move towards X_o
Surface normal, $\underline{\Omega}$, displaced towards the Bragg surface
Tie points move towards X_h
Surface normal, $\underline{\Omega}$, displaced towards the rear surface
α°
α°
0
30
60
90
60
30
0
Centre of crystal

then $\underline{D}_{oj}$ would decrease whilst $\underline{D}_{hj}$ increased by equation 3.26. These effects were never unambiguously monitored in this work for a real diffraction situation; the reason being one of spherical wave effects discussed in Section 3.6.vi.

In practice it was always found to be slightly advantageous to locate the diffraction peak using a surface reflection, traverse the crystal to the centre of the main beam, find the local Bragg maximum and then record the topograph. This marginally reduced the intensity of the surface reflection but maximised the Borrmann intensity and so led to a slightly shorter exposure time. Coupled with the curved surface effect noted here it must also be mentioned that the diffraction curves in Bragg and Laue geometries are dissimilar[46], with maxima in intensities occuring at different angular positions.

This effect would also give rise to a difference in exit face wavefield intensities and so could affect X-ray topography exposure times.

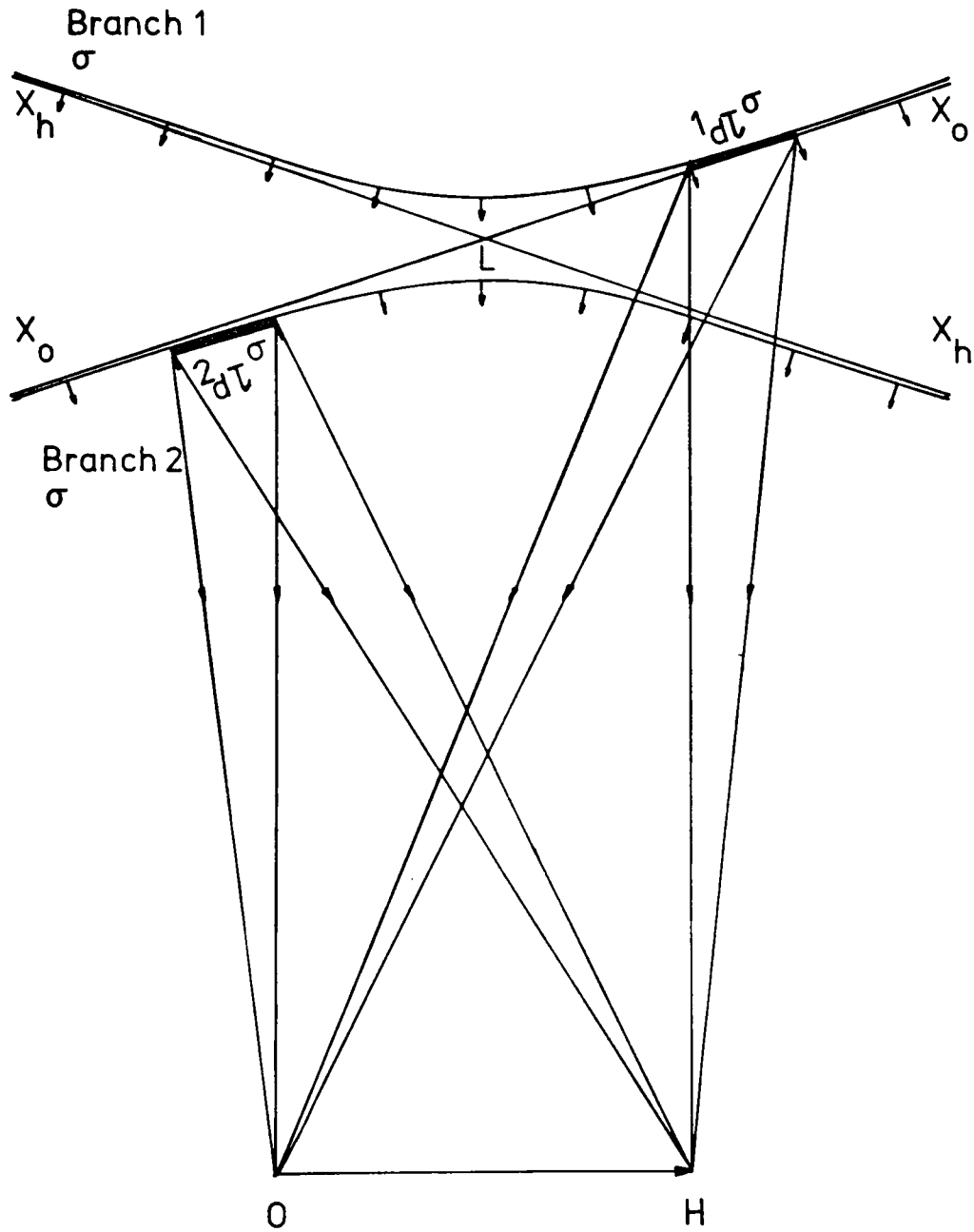
3.6.vi The Dispersion Surface, Spherical Waves and Cylindrical Crystals

In normal experimental arrangements the dispersion surface receives uniform illumination because the divergence of the incident beam ($\approx 10^{-4}$ radians) is usually much greater than the perfect crystal rocking curve width ($\approx 10^{-5}$ radians). The plane wave approximation used heretofore is therefore not strictly valid, and a discrete incident wave-vector, $\underline{k}_e$, cannot be used. Discrete dispersion surface tie-points do not exist either; rather, a continuous distribution along both branches is created, any one pair of wave-vectors of which will satisfy 3.24. It is therefore necessary to discuss all waves along the dispersion surfaces in Fig. 3.12.

Fig. 3.12 The Dispersion Surface and Spherical Waves

All tie points across the surfaces are excited, and interference occurs between "wave-packets" of angular extent $d\tau$ from opposing branches of the dispersion surfaces which are travelling in the same direction

L = Lorentz Point


Branch 1
σ
X_h
X_o
$_1d\tau^\sigma$
L
X_o
X_h
$_2d\tau^\sigma$
Branch 2
σ
O
H

The results discussed in Section 3.6.v are also not strictly real, but that an effect was monitored experimentally points to the action of these crystals as X-ray polarisers; and, furthermore, that only one sharply defined Borrmann wavefield left the crystal (because of absorption, p. 109), i.e. the crystal had produced a 'pseudo-plane' wave (as named by Authier[37]) which could be used to study the crystal shape effect noticed earlier.

Kato[42], who first applied spherical wave theory to wedge-shaped crystals, has shown that the dispersion surface remains a useful construction even for spherical waves. This is done by assuming the incident beam to be a superposition of plane waves characterised, therefore, by a spread of incident wave-vectors $\underline{k}_e$, each of which produces crystal wavefields. Along the dispersion surface, elements of angular extent $d\tau$, Fig. 3.12, can be isolated which correspond to crystal 'wave-packets' and which can be analysed in terms of wave-packet variables. The most important of these is the direction of propagation as it dictates whether the wave-packets from opposing branches of the dispersion surface give rise to interference fringes or not. Only when these wave-vectors are parallel (Fig. 3.12) will interference fringes occur. That interference fringes were never unambiguously recorded in these continuously varying wedge-angle specimens, highlights, once again, the selective nature of the crystals: only one wavefield (from branch 1) propagated along the atomic planes and so interference patterns could not be produced.

3.6.vii The Takagi-Taupin-Uragami Generalised Diffraction Theory[47,48,49] (TTU)

Plane wave theory gives a useful insight into X-ray diffraction but it is not strictly applicable to experimental problems, and this is where spherical wave theory can sometimes be usefully employed. However, spherical wave theory is extremely complex and other workers have attempted to produce a general diffraction theory which is less complicated but which gives the 'correct' results, i.e. a good simulation of experimental results. This theory will now be succinctly presented, discussed and then used to calculate the intensity distribution along the exit face of a cylindrical crystal.

The variation of the dielectric displacement, $\underline{D}$, in a crystal as a result of X-irradiation was shown by von Laue[35] to be obtained from:-

$$\nabla^2\underline{D} + 4\pi k^2\underline{D} + 4\pi \text{Grad. Curl}\underline{P} = 0 \qquad 3.36$$

Where,

(Note: the units here are c.g.s. and not S.I.)

$$4\pi\underline{P} = \chi\underline{D} \qquad 3.37$$

In a crystal which experiences a continuous strain gradient derived from a displacement vector, $\underline{u}(\underline{r})$, the susceptibility χ_r in the distorted crystal can be written as:-

$$\chi_r = \chi_p(\underline{r} - \underline{u}(\underline{r})) \qquad 3.38$$

Where,

$\underline{r}$ is the position vector of a lattice point

χ_p is the susceptibility at $\underline{r}$ in the perfect crystal.

By combining 3.38 with 3.9:-

$$\chi(r) = \sum_h \chi_h \exp(2\pi i\underline{h}.\underline{u})\exp(-2\pi i\underline{h}.\underline{r}) \qquad 3.39$$

Where,

χ_h is now 4π times the value in 3.10.

Using 3.37 and 3.39 it is possible to derive a solution for $\underline{D}$ which satisfies 3.36:-

$$\underline{D} = \sum_h \underline{D}_h(\underline{r}) \exp(-2\pi i(\underline{k}_h \cdot \underline{r} - \underline{h} \cdot \underline{u}(\underline{r})) \qquad 3.40$$

Where,

$\underline{k}_h$ is the diffracted wavefield vector which satisfies Bragg's law:-

$$\underline{k}_h = \underline{k}_o + \underline{h} \qquad 3.41$$

3.40 is where the TTU theory deviates from normal plane wave theory and it is important to understand the three prime differences:-

a. The argument of the exponential of 3.40 contains a a term $\underline{h} \cdot \underline{u}(\underline{r})$ which is not a linear function of position. Therefore, this theory is not concerned with plane-waves. Furthermore, the effective wave-vector inside the crystal, $\underline{k}_h^1$, is given by:-

$$\underline{k}_h^1 = \text{grad}(\underline{k}_h \cdot \underline{r} - \underline{h} \cdot \underline{u}(\underline{r}))$$

$$\underline{k}_h^1 = \underline{k}_h - \text{grad}(\underline{h} \cdot \underline{u}(\underline{r})) \qquad 3.42$$

For the general case of a distorted crystal it is necessary to develop the theory from now on in terms of a 'local reciprocal lattice vector', $\underline{h}^1$, given by:-

$$\underline{h}^1 = \underline{h} - \text{grad}(\underline{h} \cdot \underline{u}(\underline{r})) \qquad 3.43$$

$\underline{h}^1$ really represents the reciprocal lattice vector for a very tiny region of the crystal, i.e. a unit cell. Clearly, by combining 3.42 and 3.43:-

$$\underline{k}_h^1 = \underline{k}_o + \underline{h}^1 \qquad 3.44$$

b. $\underline{D}_h(\underline{r})$ in 3.40 is slowly position dependent and so the waves represented by 3.40 are quasi-plane waves. Mathematically, this means that second derivatives of $\underline{D}_h(\underline{r})$ may be ignored, and that $\underline{k}_o$ may assume an arbitrary value because any difference, Δk, in $\underline{k}_o$ can be allowed for in $\underline{D}_h(\underline{r})$ by multiplying it by $\exp(2\pi i \, \underline{\Delta k} \cdot \underline{r})$. However, $|\underline{\Delta k}|$ must be less than $|\underline{h}|$. For convenience:-

$$\left|\underline{k}_o\right| = \underline{k}$$

Where $\underline{k}$ is given by 3.21

c. Normal plane wave dynamical theory for a perfect crystal reduces an equation such as 3.40 (see 3.15) to a Bloch wave representation with constant $\underline{D}_h$ and no slowly varying function $\underline{h}.\underline{u}(\underline{r})$. In this case $\underline{D}_h$ can vary slowly and lattice displacements can therefore be included.

Inserting 3.40 into the relevant parts of 3.36 it is possible[47] to produce an equation to yield the allowed values of $\underline{D}_h$ for a given diffraction condition. This equation is:-

$$(\underline{S}_h.\text{grad})\underline{D}_h = i2\pi\underline{k}\beta_h^1\underline{D}_h - i\pi\underline{k}\sum_{g\neq h}\chi_{h-g}(\underline{D}_g)_h \qquad 3.45$$

Where,

$\underline{S}_h$ is a unit vector along $\underline{k}_h$ which is nearly parallel to $\underline{k}_h^1$. Also, β_h^1 is defined as:-

$$\beta_h^1 = \frac{1}{\underline{k}}\left(\left|\underline{k}_h^1\right| - \underline{k}\right) = \frac{1}{\underline{k}}\left(\left|\underline{k}_h\right| - \frac{d}{d\underline{S}_h}(\underline{h}.\underline{u}(\underline{r}) - \underline{k}\right)$$

$$\beta_h^1 = \beta_h - \frac{1}{\underline{k}}\frac{d}{d\underline{S}_h}(\underline{h}.\underline{u}(\underline{r})) \qquad 3.46$$

$$(\underline{D}_g)_h = -\frac{1}{\left|\underline{k}_h\right|^2}(\underline{k}_h^1 \wedge (\underline{k}_h^1 \wedge \underline{D}_g)) \qquad 3.47$$

$(\underline{D}_g)_h$ is the component vector of $\underline{D}_g$ perpendicular to $\underline{k}_h^1$. It therefore corresponds to the displacement of $\underline{k}_h^1$ from $\underline{k}_h$ induced by $(\underline{D}_g)_h$ changing to $(\underline{D}_g)_h^1$.

β_h^1 is the new term to arise and it is geometrically represented in Fig. 3.13. This term represents the deviation from the Bragg condition relative to the local reciprocal lattice. Correspondingly β_h represents the deviation of β_h^1 from the perfect crystal reciprocal lattice. For a perfect crystal, therefore, $\beta_h^1 = 0$.

Fig. 3.13 A Geometric Illustration of β_h^1

$$\beta_h^1 = \frac{1}{k}(\underline{k}_h^1 - \underline{k})$$

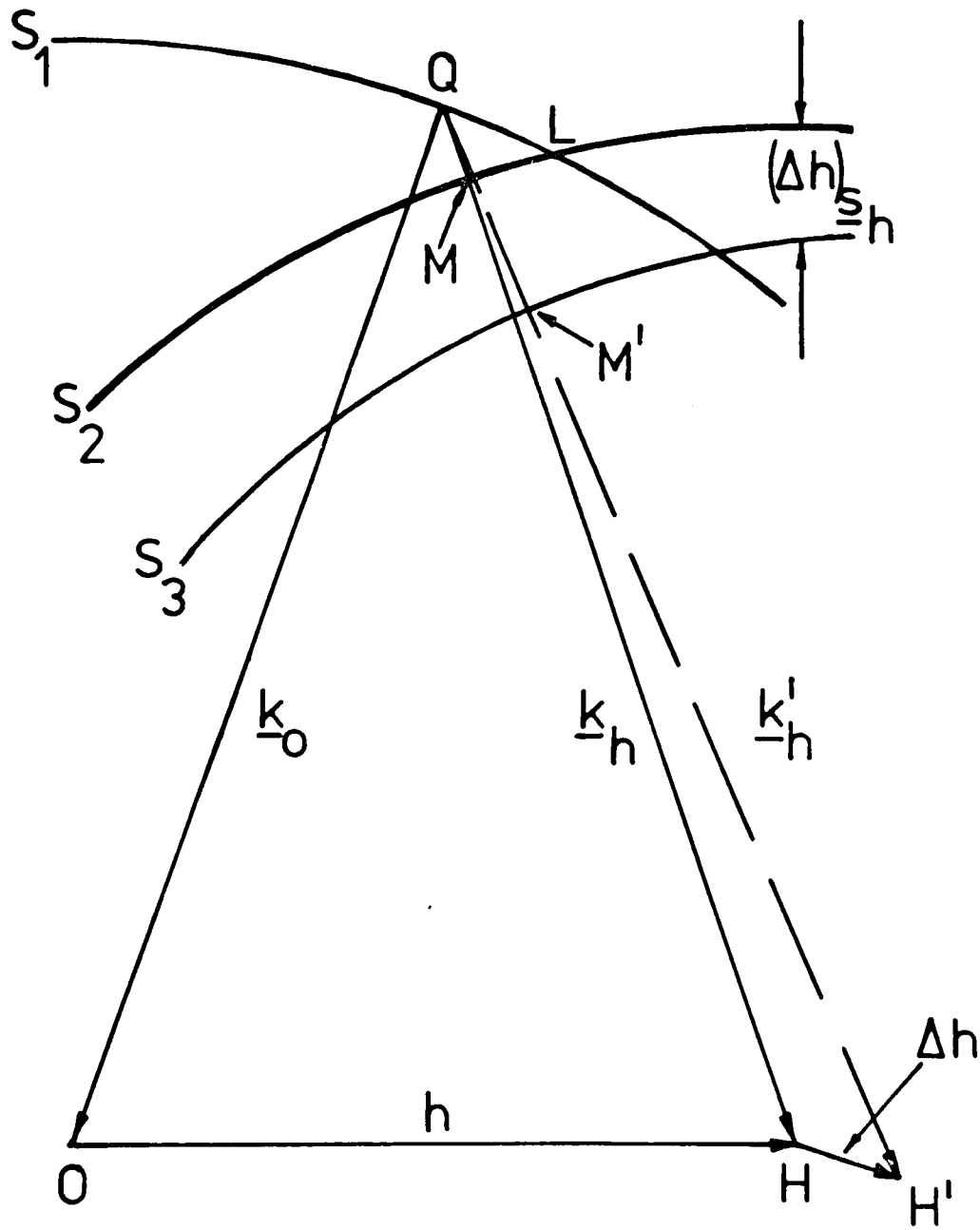
H and H^1 are the ideal and local reciprocal lattice points respectively

S_1, S_2, S_3 are spheres drawn around O^1, H and H^1 respectively

$QM = \underline{k}\beta_h$

$QM^1 = \underline{k}\beta_h^1$

The distance between S_2 and S_3 is $(\Delta_h)\underline{S}_h$ where $\underline{S}_h$ is a unit vector in the direction of $\underline{k}_h$


S1
Q
L
(Δh)s≡h
M
M'
S2
S3
k0
kh
k'h
Δh
h
O
H
H'

For the two beam case 3.45 reduces to:-

$$\frac{d\Gamma_o}{dS_o} = -i\pi kC\chi_{\bar{h}}\Gamma_h$$

$$\frac{d\Gamma_h}{dS_h} = -i\pi kC\chi_h\Gamma_o + 2i\pi k\beta_h^1\Gamma_h \qquad 3.48$$

(Note: $|\Gamma_o| = |D_o|$; $|\Gamma_h| = |D_h|$)

3.48 are now not vector equations but scalar equations and the wave-functions Γ_h and Γ_o are analytically soluble for a perfect crystal ($\beta_h^1 = 0$), and numerically soluble for an imperfect crystal ($\beta_h^1 \neq 0$). Being scalar equations it is clear that 3.48 now no longer enable a dispersion surface to be constructed (as did 3.19); all that can be determined are the wave-functions Γ_o, Γ_h at the exit face of the crystal subject to applying the correct boundary conditions to 3.48.

3.7 A Calculation of the Integrated Intensity at the Exit Face of a Perfect Cylindrical Copper Crystal using the TTU Theory

3.7.i The Model

The model used in the calculations is depicted in Fig. 3.14a. It consists of a cross-sectional view of a cylindrical crystal which possesses a radius, R. A set of Bragg planes are denoted by the trace OY, and a vacuum wave represented by a vacuum wave-vector, $\underline{k}$, is assumed incident at the exact Bragg angle, Θ_B. The "Takagi-fan"[47] is represented by PAB and therefore possesses an angle BPA of $2\Theta_B$. The "Takagi-fan" is subdivided into a grid, as shown in Fig. 3.14b, and can be considered as an inverse 'Borrmann-fan' as illustrated in Fig. 3.2. Accordingly, the intensity of the diffracted radiation at point P in Fig. 3.14a can be considered as

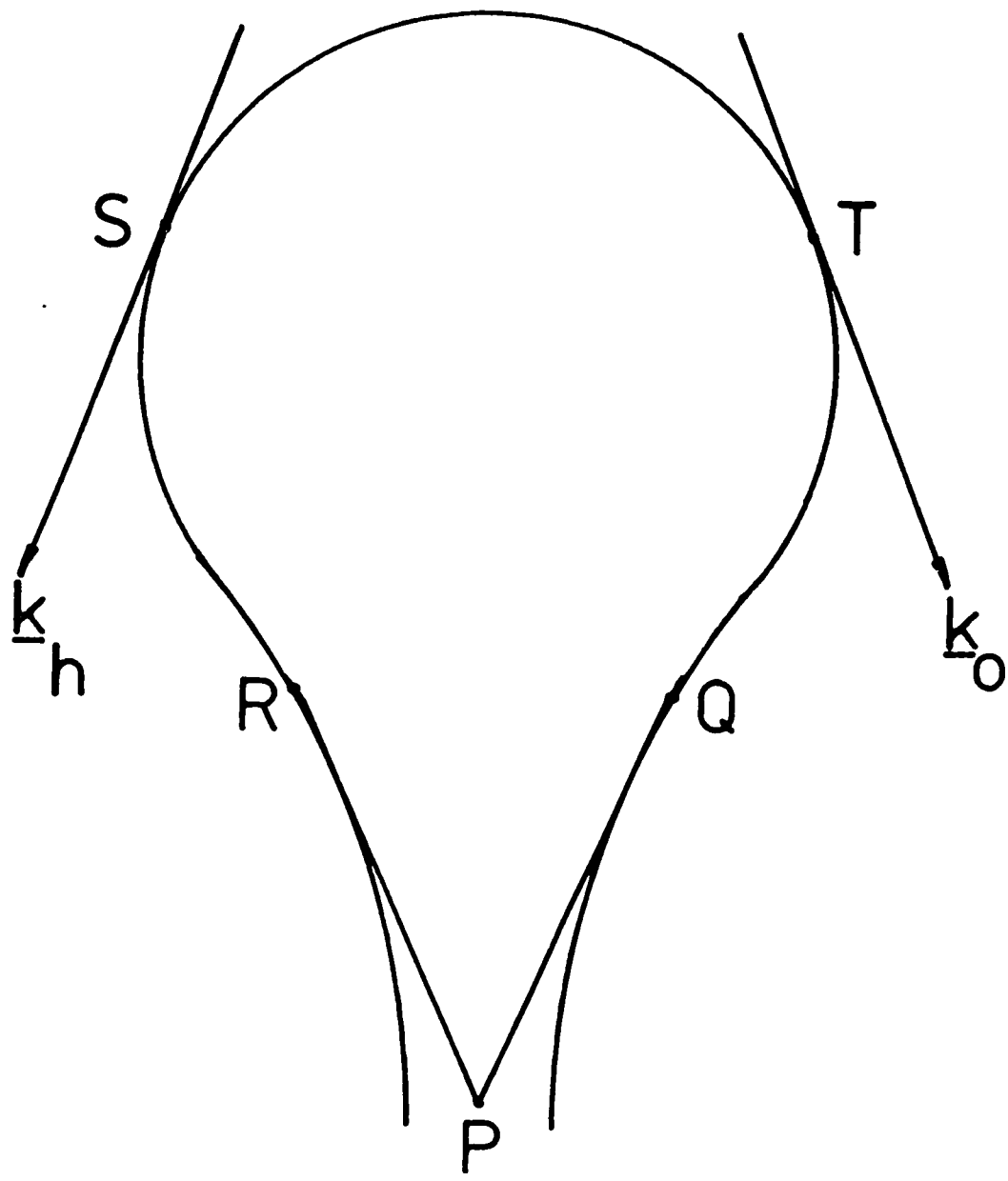
Fig. 3.14 a. The Model Used in the TTU Calculations

b. The "Takagi-fan"

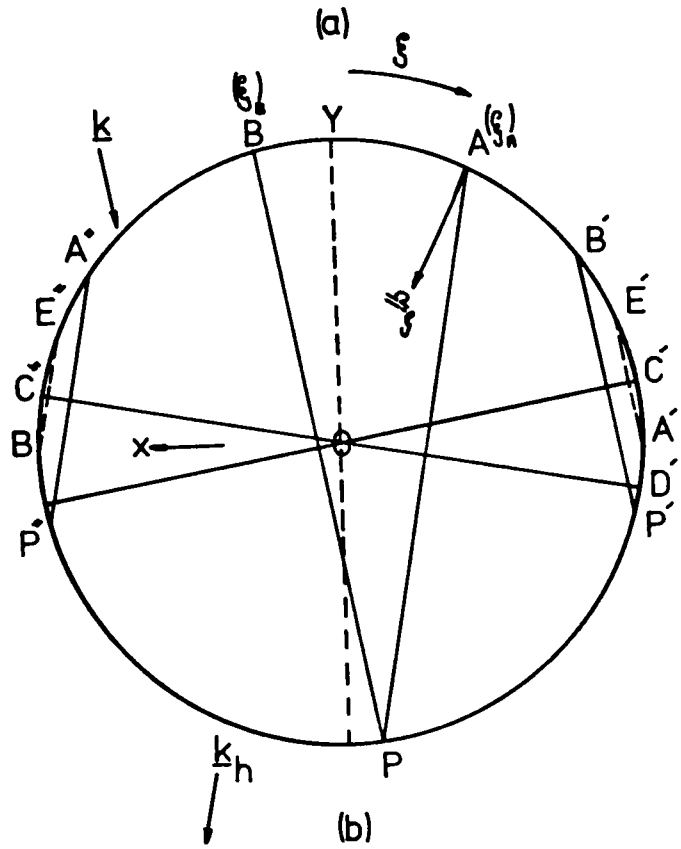
The integrated intensity at P is the summed contributions from MNOQR and so forth back up the crystal to AB. The reliability of the result depends on the fineness of the grid in the fan

c. The Boundary Conditions for the TTU Calculations were Derived using the Model Shown

ST = Pure Laue Surface
SR = Pure Bragg Surface
TQ = Rear Surface



(c)


(a)
ξ
k
B
Y
A
B'
E'
C'
A'
D'
P'
E
C
B
A'
P
x
k_h
P
(b)
k
B
A
Q
R
M
N
P
k_h
k_o

proportional to that falling on AB, and so the grid is necessary to sum the contributions from points MNOQR and so on back up the crystal as shown in Fig. 3.14b. It is both necessary and convenient to consider the circle in two distinct ways: first, the purely asymmetric transmission Laue diffraction case; and then the purely Bragg surface diffraction situation. For the current purpose this former condition is considered to hold when:-

$$\hat{POC''} > 4\Theta_B \qquad 3.49$$

and when, $\hat{POD'} > 2\Theta_B$

Outside these angular regions a mixed diffraction state can arise for which part of the surface AB is considered to be pure Bragg, C"B", and part pure Laue, A"C". In this case the surface C"B" (termed the forward Bragg surface) is considered to be a plane. When $P \rightarrow P^1$ (i.e. on the rear surface) and therefore $\hat{POD'} < 2\Theta_B$ (the rear mixed surface) the mathematics need only consider the Laue transmission arrangement, since this cannot be considered to be partly a Bragg surface as the waves do not enter and leave by the same surface.

The co-ordinate ξ represents the top crystal-vacuum surface along AB; X is a co-ordinate perpendicular to the Bragg planes; and γ_o is the direction cosine between the inward normal, $\underline{\Omega}$, along AB and $\underline{k}$. Assume incident a vacuum plane-wave given by:-

$$\Gamma(r) = \Gamma_o(r)\exp(-2\pi i\underline{k}.\underline{r}) \qquad 3.50$$

and assume also a two beam condition with the total wavefield, $\Gamma_c(r)$, in the crystal given by:-

$$\Gamma_c(r) = \Gamma_o(r)\exp(-2\pi i\underline{k}_o.\underline{r}) + \Gamma_h(r)\exp(-2\pi i\underline{k}_h.\underline{r}) \qquad 3.51$$

$\underline{k}_o$ is assumed to be parallel to $\underline{k}$ and its magnitude is given by 3.21; $\underline{k}_h$ is given by 3.41. It is also assumed here that β_h^1 is zero in 3.48 and therefore the study concerns a perfect crystal; this being a prerequisite to any study of distorted crystals.

3.7.ii Boundary Conditions

Using the diagram in Fig. 3.14c and following Uragami's[49] argument, the boundary conditions can be stated as follows:-

a. Along the rear surface from point T to Q,

$$\Gamma_h(r) = 0$$

$$\frac{\partial \Gamma_o(r)}{d\underline{S}_o} = 0$$

b. Along the Bragg surface from point S to R,

$$\Gamma_o(r) = \Gamma(r)$$

$$\frac{\partial \Gamma_h(r)}{\partial \underline{S}_h} = I_h \Gamma(r)$$

c. Along the Laue surface from T to S,

$$\Gamma_h(r) = 0$$

$$\frac{\partial \Gamma_o}{\partial \underline{S}_o} = 0$$

$$\frac{\partial \Gamma_h}{d\underline{S}_h} = I_h \Gamma(r)$$

Where,

$$I_h = -\pi ikC\chi_h$$

3.7.iii The Integrated Intensity in the Diffracted Beam

Takagi[47] has shown that the integrated intensity in the diffracted beam of an X-ray projection topograph ($\underline{T}_h^{Tr}$) can be derived by solving 3.48 subject to boundary conditions 3.7.ii. The solution is as follows:-

$$\underline{T}_h^{Tr} = \frac{\pi^2 kC^2 |\chi_h|^2}{\sin^2 2_B} \; J\int_A^B \gamma_o(\xi) \, |v_h(\xi)|^2 \exp(-\mu_m(\underline{r}(P)-\underline{r}_e(\xi)))d\xi \qquad 3.52$$

Where,

$$J = A\int_A^B |\Gamma_o|^2 \, dx$$

A = proportionality constant

$(\underline{r}(P)-\underline{r}_e(\xi))$ represents the difference in position vectors on the exit and entrance surfaces of the crystal

μ_m is the absorption coefficient

r_e is a position vector on AB

v_h is the Green's function relevant to the diffraction and boundary conditions for the appropriate component surfaces of the entrance surface

The Green's functions, v_h, used were taken from Uragami's work[49]:-

a. For the pure Laue surface (T to S) in Fig. 3.14c and from A" to B' in Fig. 3.14a,

$$v_h = v_h^k = J_o(\alpha((s_o^o-s_o)(s_h^o-s_h))^{\frac{1}{2}})$$

$$= J_o(\alpha (S_o^k . S_h^k)^{\frac{1}{2}})$$

$$\alpha = 2\pi kC(\chi_h \chi_{h-})^{\frac{1}{2}} = -2\underline{T}_h$$

s_o, s_h = real space co-ordinates parallel to the wave vectors $\underline{k}_o$ and $\underline{k}_h$ of the transmitted and diffracted waves respectively

s_o^o, s_h^o = position co-ordinates of point P in Fig. 3.14a

J_o = zeroth order Bessel function

$S_o^k = (s_o^o-s_o)$; $S_h^k = (s_h^o-s_h)$

b. From A" to B" in Fig. 3.14a part is a pure Laue surface, namely A" to C", and part is a pure Bragg surface (C"B"). From A" to E" (B"E"//P"A") it is clear that $v_h = v_h^k$, i.e. the same as for a above. From C" to B" the arc was replaced by a plane C"B" whence the relevant Green's function was,

$$v_h = v_h^{FIU} = v_h^k + \epsilon_o \frac{S_h}{S_o^{FIU}} J_2(\alpha(S_o^{FIU} . S_h^{FIU}))$$

$$S_o^{FIU} = \epsilon_o s_o^o - s_h; \quad J_2 = \text{second order Bessel function}$$

$$S_h^{FIU} = \epsilon_h s_h^o - s_o; \quad \epsilon_o = \frac{1}{\epsilon_h} = \frac{\sin(\phi_e)}{\sin(2\Theta_B - \phi_e)} > 0$$

ϕ_e = angle between the incident wave vector, $\underline{S}_o$, and the Bragg surface.

c. Over the entrance surface from B' to A" only the Laue integral need be considered to calculate the intensity at P^1, for example; hence, $v_h = v_h^k$ as in a above.

For the surface C'E' (i.e. the rear surface) the appropriate Green's function taken from Uragami's work was:-

$$v_h = v_h^{Bk} = v_h^k - J_o(\alpha(S_o^{Bk} . S_h^{Bk})^{\frac{1}{2}})$$

Where the product $S_o^{Bk} . S_h^{Bk}$ was equal to $S_o^k . S_h^k$ (in a above) so as to satisfy the boundary condition 3.8.ii(a).

For the surface E'B' (A'E'//P'B') the Green's function used was $v_h = v_h^k$, i.e. the same as for the surface A"B'. Again the arc C'A' was approximated by a straight line C'A'.

Before presenting the preliminary results of the calculations performed it is interesting to observe that 3.52 shows that I_h^{Tr} is proportional to the total energy incident on BA(Fig. 3.14a), and not on the intensity distribution or wavefront shape. Takagi further showed that the intensity of a projection topograph could be calculated by assuming incident plane-waves only. The justifications for this step were twofold: first, the wave function at a point on the exit surface

was linearly dependent on the wave-function at the entrance surface; and second, the intensity at a point in a projection topograph is the integrated intensity, i.e. the angular width of the incident beam covers the whole of the dispersion surface in Fig. 3.12. The TTU theory therefore provided the opportunity to simulate the intensity in the diffracted beam of an X-ray projection topograph from a perfect cylindrical crystal using the following constants:-

$$\Gamma_o = 1$$

$$R = 0.5 \text{ mm}$$

$$\Theta_B = 9.7819^o$$

$$\chi_h = -7.6177 \times 10^{-6} = \chi_{\bar{h}}$$

$$\mu_m = 6.08 \text{ cm}^{-1} \text{ (from Section 3.6.iv)}$$

(All other wavefields were assumed to be strongly absorbed)

The incident beam divergence was assumed to be infinite, i.e. plane-waves were assumed to be sufficient by the above reasoning.

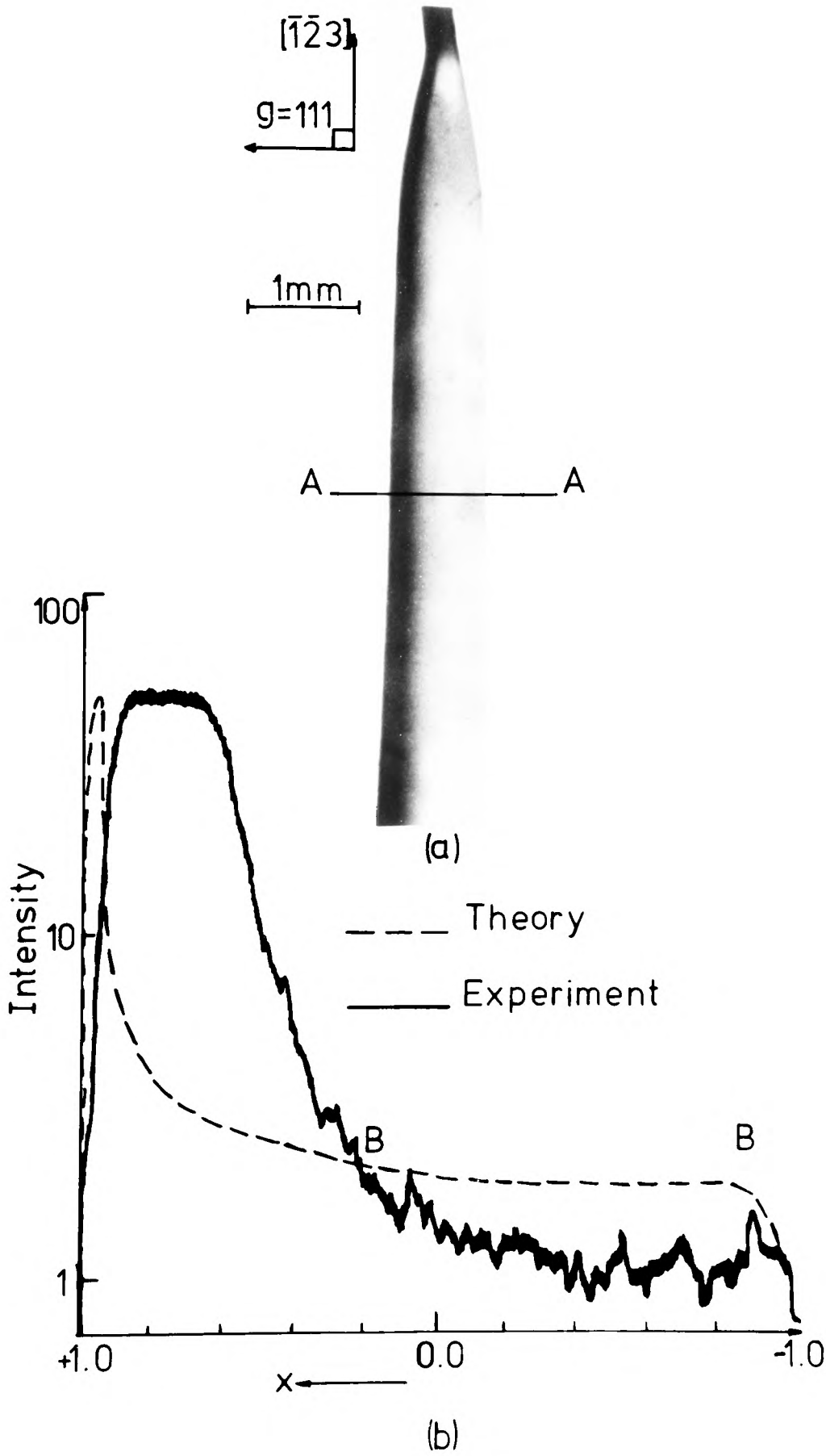
Equation 3.52 was then integrated for every section of the entrance surface A' to B" using the appropriate Green's functions outlined above. The result was an intensity profile of the diffracted X-rays along the exit face B" to A' for each point P.

Fig. 3.15b depicts the theoretically calculated intensity profile together with the microdensitometer trace across a $[\bar{1}\bar{2}3]$ growth axis dislocation-free copper crystal with the same radius shown in Fig. 3.15a. The trace line was across AA. Very encouraging agreement between the theoretical and experimental profiles is noticed, which indicates that the

Fig. 3.15 The Preliminary Results of the TTU Calculations

A. An X-ray topograph of the crystal simulated in the TTU calculations. Growth axis = $[\bar{1}\bar{2}3]$, microdensitometer trace = AA

B. Good agreement between theory and experiment was found. The small deviations are considered to be due to absorption and wavefield transmission mechanisms


[1̄2̄3]
g=111
1mm
A
A
(a)
100
10
1
Intensity
Theory
Experiment
B
B
+1.0
0.0
-1.0
x
(b)

TTU theory does provide reasonable results but with the loss of crystal-ray optical information. The theoretical curve adequately shows the large maximum in intensity along the Bragg surface C"B", although the lateral extent of the peak is not so great as in the experimental curve. Absorption is the prime reason for this discrepancy because the theoretical model assumed strong absorption across the cylinder of all waves except those belonging to branch 1, σ polarised. In the real situation absorption of the wavefields would be a variable quantity depending on the crystal thickness and the type of wavefields transmitted through to the exit face (refer to Section 3.6.iv for a short discussion of the effect). The lack of complete agreement along BB in Fig. 3.15b is again an absorption problem.

3.8 Conclusions

a. The calculations in Section 3.6.iv show that for the copper crystals grown in this work only one wavefield, from branch 1, would propagate through the crystal, since this possesses the smallest effective absorption coefficient.

b. The simple analysis in Section 3.6.v indicates that for plane-waves incident on the crystal that an effective deviation is placed on the crystal wavefields by the boundary, which causes the dispersion surface tie points to be displaced.

c. The TTU theory can be usefully employed to simulate the intensity of the diffracted beam in an X-ray projection topograph as shown in Section 3.8.

3.9 Suggestions for Further Work

a. It would be interesting to examine how far the effects discussed in Section 3.6.v really were attainable in practice. For this purpose a "quasi-plane" wave would be needed as in Authier's original experiment of 1960; hence, a cylindrical dislocation-free copper crystal would be required with which to diffract characteristic radiation and so obtain such a wave. A second cylindrical dislocation-free crystal would serve as the specimen in this now double crystal diffractometer. The aim would be to plot the intensity profile of the second crystal with position in the first diffracted beam, and with angular position about the Bragg peak to ascertain if Section 3.6.v is correct.

b. The calculations performed in Section 3.8 could be considerably expanded. For a crystal which exhibits a low absorption coefficient (e.g. aluminium, silicon, organics) for $M_{oK\alpha_1}$ radiation it would be interesting to observe if interference fringes could be produced from a cylindrical crystal. Having a low absorption coefficient, both branch 1 and branch 2 wavefields might propagate to the exit face of the crystal giving rise to interference fringes therefore. This phenomenon could be explored experimentally too.

The particular diffraction effects associated with a cylindrical crystal experiencing a strain gradient perpendicular to the longitudinal axis could be analysed. Such a study could be in conjunction with the plating experiments discussed in Chapter IV, where the strain was imposed on the copper crystal after plating with chromium at 55C and then cooling to room temperature. Again, low absorbing crystals could be analysed in this respect to examine the effects of a strain gradient on fringe spacing and visibility.

CHAPTER III REFERENCES

1. H. A. Meiers, Proc. Roy. Soc., 71, 439, 1903

2. H. A. Meiers, Phil. Trans. A., 202, 459, 1904

3. S. Amelinckx, "The Direct Observation of Dislocations", (Solid State Physics, Suppl. 6), Academic Press, New York

4. F. L. Vogel, W. G. Pfann, H. E. Corey and E. E. Thomas, Phys. Rev., 90, 489, 1953

5. T. Ejima, W. H. Robinson and J. P. Hirth, J.C.G., 7, 155, 1970

6. W. C. Dash, J.A.P., 30, 459, 1959

7. I. Kovacs, Acta Met., 15, 1731, 1967

8. Z. S. Basinski, J. S. Dugdale and A. Howie, Phil. Mag., 8, 1989, 1963

9. S. Kikuta, N. Minakawa and K. Doi, J. Phys. Soc. Jap., 31, 954, 1971

10. A. Freund and J. Schneider, J.C.G., 13/14, 247, 1972

11. P. B. Hirsch, A. Howie, R. B. Nicholson, D. W. Pashley and M. J. Whelan, "Electron Microscopy of Thin Crystals", Butterworths, 1965

12. D. K. Bowen and C. R. Hall, "Microscopy of Materials", Macmillan, 1975

13. S. Amelinckx, R. Gevers, G. Remaut and J. Van Landuyt, "Modern Diffraction and Imaging Techniques in Matls. Science", North-Holland Publishers, 1969, Nato

14. J. H. Richardson, "Optical Microscopy for the Materials Scientist", M. Dekker, N.Y., 1971

"Practical Methods in Electron Microscopy", Ed. A. M. Glauert, North-Holland, 1974

15. W. Berg, Naturwissen, 19, 391, 1931

16. C. S. Barrett, Trans. A.I.M.E., 161, 15, 1945

17. H. Barth and R. Hosemann, Z. Naturf, 13a, 792, 1958

18. A. Guinier and J. Tennevin, Acta Cryst., 2, 133, 1949

19. L. G. Schulz, J. Metals, 200, 1082, 1954

20. A. R. Lang, J.A.P., 29, 597, 1958
J.A.P., 30, 1748, 1959
Brit. J. Appl. Phys., 14, 904, 1963

21. G. Borrmann, W. Harting and H. Irmler, Z. Naturf., 13a, 423, 1958

22. U. Bonse and E. Kappler, Z. Naturf., 13a, 348, 1958
W. I. Bond and J. Andrus, Amer. Mineralogist, 37, 622, 1952

23. T. Tuomi, K. Nakkarinen, E. Laurilla and P. Rqbe, Acta Polytech. Scand., Ph.100, 1-4, 1973
T. Tuomi, K. Nakkarinen and P. Rqbe, Phys. Stat. Sol. (a), 25, 93, 1974

24. B. K. Tanner, "X-ray Diffraction Topography", Pergamon, 1976

25. P. H. Dederichs, Phys. Stat. Sol., 23, 377, 1967

26. P. H. Dederichs, Phys. Rev., B1, 1306, 1970

27. B. C. Larson, J. Appl. Cryst., 8, 150, 1975

28. A. H. Compton and S. K. Allison, "X-rays in Theory and Experiment", N.Y. Van Nostrand, 1935

29. C. J. Humphreys, Ph.D. Thesis, University of Cambridge, 1967

30. J. E. A. Miltat, D. Phil. Thesis, University of Oxford, 1971

31. M. von Laue, "Röntgenstrahlinterferezen", Akad. Verlagsgesellschaft, Frankfurt, 1960

32. A. R. Lang, "Modern Diffraction and Imaging Techniques in Materials Science", North-Holland, Nato, 1969, Ed. S. Amelinckx

33. A. Horder, "The Manual of Photography", Focal Press, London, 1973, p.544

34. P. P. Ewald, Ann. Physik, 49, 1, 1916; 49, 117, 1916; 54, 519, 1917

35. M. von Laue, Ergeb. Exakt. Naturw., 10, 133 1931

36. H. J. Pain, "The Physics of Vibrations and Waves", J. Wiley and Sons, 1970

37. A. Authier, C. R. Acad. Sci. Paris, 251, 200B, 1960

38. A. Authier, F. Balibar and Y. Epelboin, Phys. Stat. Sol., 41, 225, 1970

39. "International Tables for X-ray Crystallography", I.U.G., Kynoch Press, 1965

40. B. W. Battermann and H. Cole, Phys. Rev., 36, 681, 1964

41. A. Authier, "International Summer School on X-ray Dynamical Theory and Topography", Limoges, France, 1975

42. N. Kato, "X-ray Diffraction", by L. Azaroff, R. Kaplow, N. Kato, R. J. Weiss, A. J. C. Wilson, R. A. Young, McGraw-Hill, 1974

43. G. Borrmann, Physikal. Z., 42, 157, 1941

44. M. von Laue, Acta Cryst., 5, 619, 1952

45. T. O. Baldwin, F. W. Young and A. Merlini, Phys. Rev., 163, 591, 1967

46. R. W. James, "The Optical Principles of the Diffraction of X-rays", Bell, London, 1948

47. S. Takagi, Acta Cryst., 15, 1311, 1962
S. Takagi, J. Phys. Soc. Japan, 26, 1239, 1969

48. D. Taupin, Bull. Soc. Franc. Miner. Crist., 87, 469, 1964

49. T. S. Uragami, J. Phys. Soc. Jap., 27, 147, 1969
T. S. Uragami, J. Phys. Soc. Jap., 28, 1508, 1970
T. S. Uragami, J. Phys. Soc. Jap., 31, 1141, 1971

CHAPTER IV

A STUDY OF THE TENSILE DEFORMATION PROPERTIES OF CHROMIUM PLATED [$\bar{1}\bar{2}3$] GROWTH AXIS DISLOCATION-FREE COPPER CRYSTALS

List of Symbols Used in this Chapter

ΔM	= Mass of deposited chromium
ρ_{cr}	= Density of chromium
L	= Length
R	= Radius
ΔR	= Coating thickness
σ_R	= Radial stress from plating
σ_Θ	= Angular stress from plating
σ_z	= Longitudinal stress from plating
A_2, C_2	= Constants
a	= Inner radius of a composite cylinder
b	= Outer radius of a composite cylinder
$k_{1,2}$	= Coefficients of linear expansion
ν_1, ν_2	= Poisson's ratios
E_1, E_2	= Young's moduli
ϵ	= Strain
d_s	= Lattice spacing of strained planes
d_p	= Lattice spacing of non-strained planes
Θ_B	= Bragg angle
λ	= Wavelength
n	= Integer; number of dislocations in a pile-up
$\Delta\Theta$	= Angular displacement of a diffraction peak
σ_{Az}	= Applied longitudinal normal stress
L	= Gauge length of a crystal; dislocation source operation length; specimen to plate distance; pile-up length
d	= Gauge length diameter
τ	= Resolved shear stress

χ_o = Angle between tensile axis and the normal to the slip plane

λ_o = Angle between the tensile axis and the slip direction

γ = Resolved shear strain

$\dot{\gamma}$ = Shear strain rate

Δl = Extension of specimen corrected for araldite extension

α, β = Constants

μ = Shear modulus

b = Burger's vector

x = Dislocation velocity

N = Number of dislocations/cm^2

$\Theta_I, \Theta_T, \Theta_s$ = Initial, transitionary and stabilised work hardening rates

Θ = Divergence of a synchrotron beam

E = Energy of electron in a synchrotron

c = Velocity of light

M_o, m_o = Rest mass of an electron

A^I_F = Intensity of a given wavelength in a synchrotron beam

F_{hkl} = Structure factor

$P(\lambda)$ = Synchrotron intensity factor for a given wavelength,

μ_c, μ_a, μ_f = Absorption coefficients of a crystal, air and film respectively

t_c, t_a, t_f = Thickness of a crystal, air and film respectively

Tan α = Bending strain

δ = Image shift distance

CONTENTS

		Page Number
	Contents	128
4.1	Introduction	130
4.2	Specimen Selection	131
4.3	Specimen Preparation	132
4.3i	Etching and Electropolishing	132
4.3ii	Electroplating	133
4.3iii	Mounting the Crystals for Deformation	144
4.4	Macroscopic Deformation Studies in the Instron	145
4.4i	The Experiments	145
4.4ii	Processing Instron Data	146
4.4iii	Instron Results	148
4.4iii.a	The Elastic Region	148
4.4iii.b	The Work Hardening Region	157
4.5	Microscopic Deformation Studies in the Synchrotron	162
4.5i	Reasons for using the Synchrotron	162
4.5ii	Specimen Transport	165
4.5iii	The Synchrotron Experimental Arrangement	165
4.5iv	An Analysis of the Wavelengths Contributing to the Recorded Diffraction Image	169
4.5v	Synchrotron Results	170
4.5v.a	The Non-Loaded Crystal	170
4.5v.b	Loading the Crystal up to the Yield Point along the 'Elastic Line'	173
4.5v.c	Post Yielding Behaviour	177

4.6	A Review of the Instron and Synchrotron Results	179
4.7	Conclusions	186
4.8	Suggestions for Further Work	188
	References	190

Ut Tensio Sic Uis

(As the extension so the force)

Robert Hooke

Taken from an anagram in
De Potentia Restitutiva,
or, of a spring
(1679)

4.1 Introduction

In this final section and chapter an analysis is presented of the tensile deformation characteristics of chromium plated [I$\bar{2}$3] growth axis, dislocation-free copper crystals. Such an analysis is based on the information derived from two sets of experiments:-

i. Tensile deformation studies in an Instron, carried out in the Metallurgy Department at Oxford. These will be termed macroscopic studies, because they provided overall information of the deformation as determined from shear stress-shear strain curves.

ii. X-ray diffraction topography investigations using the S.R.C.'s Synchrotron Radiation Facility at the Daresbury Laboratory near to Warrington. These studies come under the general heading of microscopic studies because a great deal of crystallographic information was derived down to a 1 μm resolution limit.

The work was carried out with four primary aims in mind:-

i. To characterise the stress-strain curve of a dislocation-free copper crystal which had been surface treated with an electroplated layer of chromium.

ii. To determine the likely genesis of dislocations at the onset of plastic flow.

iii. To identify the influence, if any, of the plated layer on i. and ii.

iv. To assess the early stages of work hardening with particular reference to i., ii. and iii.

Electroplating was chosen because as a technique it could provide a uniformly deposited layer on the surface of the crystal in a short space of time[1]. Electro-evaporation techniques were not used because of the need to rotate the

specimen during deposition (the specimen was cylindrical) and because of the relatively slow deposition rates as shown in Chapter I, Section 1. Chromium was chosen as a deposited layer because it has been shown that[2] this metal can impart a significant increase to the yield stress of a dislocated copper crystal (yield stress increased by a factor of 2), but the reasons for this were by no means clear. Using these crystals it was hoped to clarify the effect a little more.

4.2 Specimen Selection

$[I\bar{2}3]$ growth axis copper crystals were chosen for this work for three important reasons. First, as discussed in Chapter I, with a $[I\bar{2}3]$ growth axis it was impossible for axial screw dislocations to exist and so propagate during crystal growth implying that a dislocation-free crystal could be confidently produced each time. Secondly, a crystal stressed along a <123> direction will initially slip on a single slip system during the early stages of deformation, rendering analysis of the aims i. to iv. in Section 4.1 that much easier. Thirdly, a wealth of information on the tensile deformation of <123> crystals containing a low dislocation density (10^4-10^6/cm^2) already existed,[3,4,5,6,7] which allowed profitable comparisons between this study and those to be made.

Laue photographs of the seed crystal showed that the actual growth axis orientation was $[I\bar{2}3]$ which, as indicated on the stereogram in Fig. 4.1a, meant that during deformation with the load applied along this axis the preferred slip system would be $(1\bar{1}1)$ $[\bar{1}01]$. Also indicated in the figure caption of

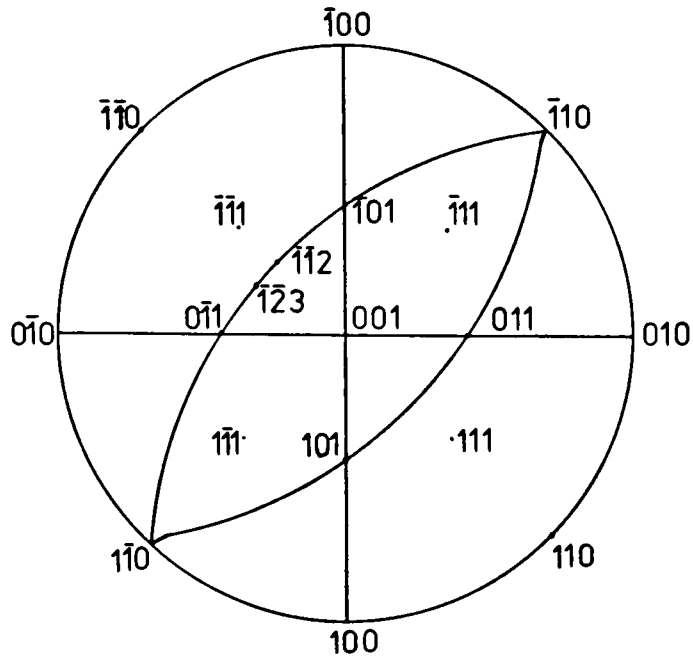
Fig. 4.1 The Deformation Crystallography

a. Stereographic projection on (001) showing the tensile axis, $[\bar{1}\bar{2}3]$, and the primary slip system $(1\bar{1}1)[\bar{1}01]$. The secondary slip system was $(\bar{1}\bar{1}1)[101]$.

Planes	Direction	Schmid Factor (S)
(111)	$[10\bar{1}]$	0
	$[0\bar{1}1]$	0
	$[\bar{1}10]$	0
$(1\bar{1}1)$	[110]	0.349
	$[\bar{1}01]$	0.465
	$[0\bar{1}\bar{1}]$	0.115
$(\bar{1}11)$	$[01\bar{1}]$	0.290
	[101]	0.116
	[110]	0.174
$(\bar{1}\bar{1}1)$	$[\bar{1}10]$	0.174
	[011]	0.174
	[101]	0.349

b. The Thompson tetrahedron oriented for this particular tensile axis

N.B. Apex of tetrahedron is into the page; All vector arrows reversed but indices remain the same


$\bar{1}00$
$\bar{1}\bar{1}0$
$\bar{1}10$
$\bar{1}\bar{1}1$
$\bar{1}01$
$\bar{1}11$
$\bar{1}\bar{1}2$
$\bar{1}\bar{2}3$
$0\bar{1}1$
001
011
$0\bar{1}0$
010
$1\bar{1}1$
101
111
$1\bar{1}0$
110
100

(a)

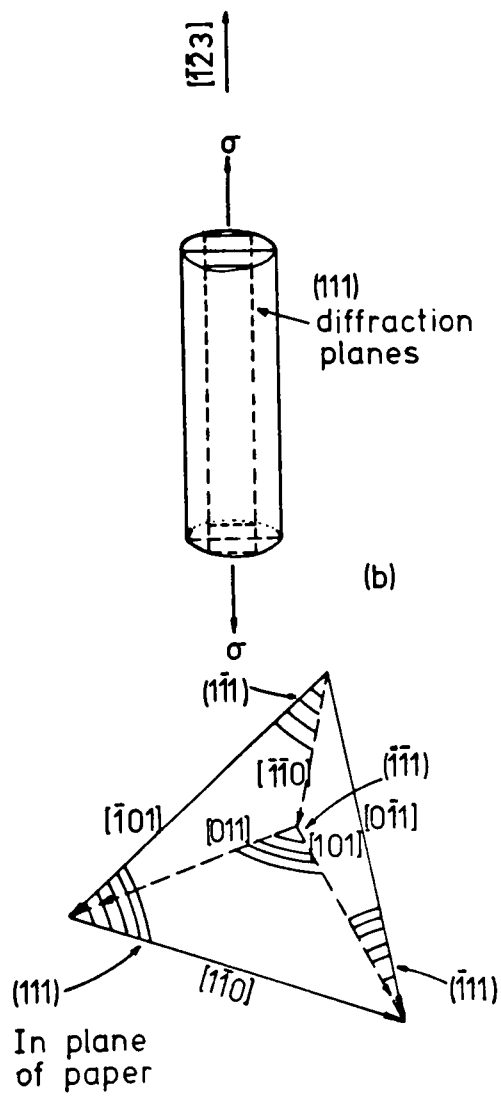

$[1\bar{2}3]$
σ
(111)
diffraction
planes
σ
(b)
$(1\bar{1}1)$
$[\bar{1}\bar{1}0]$
$(\bar{1}\bar{1}1)$
$[\bar{1}01]$
[011]
[101]
$[0\bar{1}1]$
(111)
$[1\bar{1}0]$
$(\bar{1}11)$
In plane
of paper

Fig. 4.1a are the Schmid factors (S) for the possible slip systems. For the $(1\bar{1}1)[\bar{1}01]$ system S = 0.465 and in Fig. 4.1b is shown the crystallographic geometry when the tension is applied along the $[\bar{1}\bar{2}3]$ axis of these crystals.

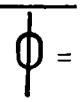
The external geometry of these samples was chosen so that they had a long ($\approx$1 cm), thin ($\approx$0.3 mm) double neck (as shown in Chapter I, Section 1) before the dislocation-free volume of interest. This measure aided specimen handling with tweezers far from the dislocation-free volume of interest. Such handling has been entirely acceptable because no contrast has ever been monitored on X-ray topographs of dislocations in the originally dislocation-free volume arising from specimen handling with tweezers at the beginning of the first neck. Two 'shoulders' were grown as a necessary part of the crystals, Fig. 4.2, to enable the specimen to be correctly mounted for subsequent deformation; and the 'gauge length', Fig. 4.2, was restricted to approximately 12 mm (total crystal length was $\approx$20 mm) so that the complete crystal could be imaged in the 25 mm high X-ray beam during a single exposure. The 'diameter' of the crystals, Fig. 4.2, was limited to about 1.0 mm to promote short X-ray exposure times on the Oxford Lang Cameras using a rotating anode set (see Chapters I and III). This latter set was exhaustively used to determine the state of perfection of the crystals at all stages of preparation prior to deformation.

4.3 Specimen Preparation

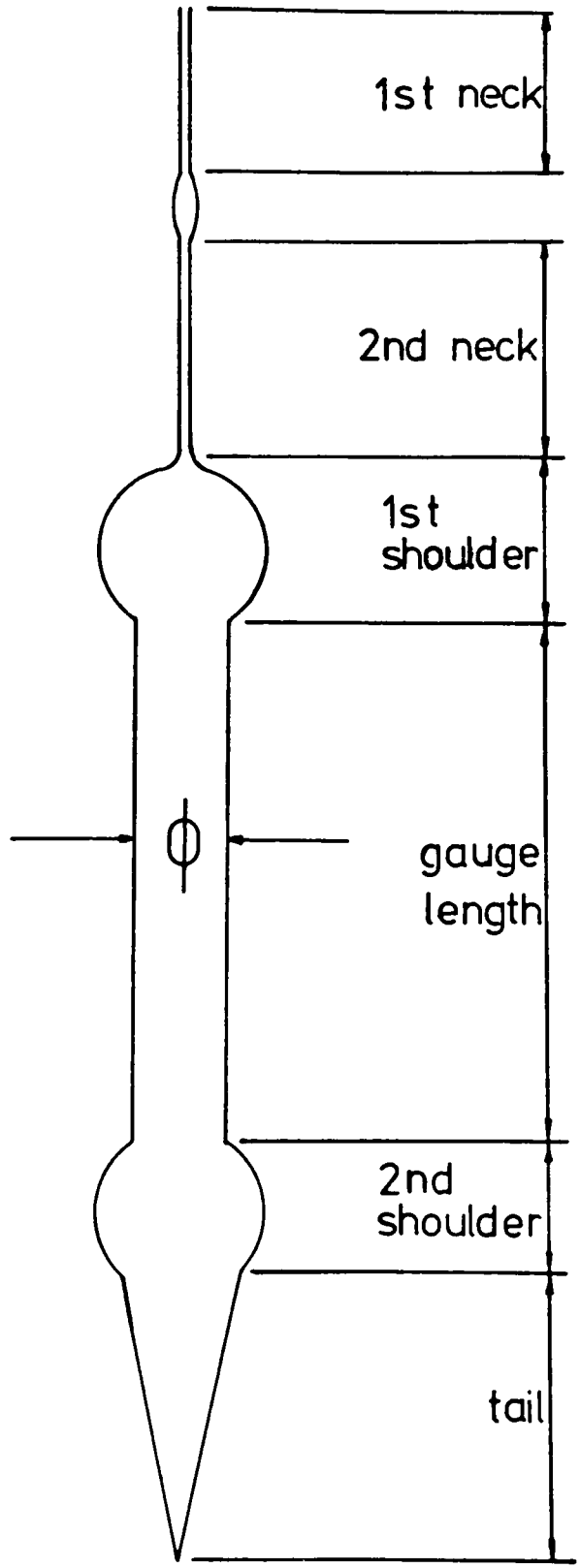
4.3i Etching and Electropolishing

Having ascertained the initial state of perfection of a crystal by the methods described in Chapters I and III,

Fig. 4.2 Specimen Shape and Definitions of Important Parts



= Gauge length diameter


1st neck
2nd neck
1st shoulder
gauge length
2nd shoulder
tail

the 'tail' was etched off in a concentrated solution of nitric acid while the crystal was still attached to the seed. The seed was clamped vertically in a micromanipulator and the attached crystal gently lowered into the acid. Etching took place in 3-4 minutes. During the early stages of this work a number of crystals were re-topographed following this etching procedure to maintain a check on perfection. It was sometimes noticed, Fig. 4.3b, that the very end of the crystal contained a small number of dislocations. These were sometimes removed from this end of the crystal by electropolishing in the following solution[8]:-

60% Orthophosphoric acid	250 ml	Freshly made
Copper carbonate	10 g	
Chromic acid, saturated soln. in water	1 ml	

A stainless steel cathode was used with a cell potential of 3V and a current of $\approx$ 0.01A. Polishing took place at room temperature for 15 minutes. This process in itself did not generate any detectable damage in the crystal as shown by comparing the topographs of a crystal before and after electropolishing as shown in Fig. 4.4. The electropolishing also served to remove any contaminating species from the surface of the crystals, e.g. oxides, greases, etc., so that the crystals could be subsequently electroplated reproducibly.

4.3ii Electroplating

While still attached to the seed the as electropolished, still dislocation-free crystal was washed in water for 2 minutes and then in methanol for another 2 minutes. After drying ($\approx$5 minutes) the crystals were finally electroplated at 55C using the following solution[9]:-

Chromic acid	450 g/litre
Sulphuric acid	4.5 g/litre
Current density	12-20 $A/_{dm^2}$
Voltage	4-5
Anode	Stainless steel

The solution was freshly made each time and during preparation it was reduced with 12.5 g/litre of citric acid as prescribed in the literature.

To obtain an estimate of the coating thickness, copper wire specimens 1 cm long x 1 mm diameter were plated for different times under the same bath conditions as for the dislocation-free crystals. Knowing the mass of the chromium deposited, ΔM; the density of the chromium, ϱ_{cr}; the length of the wire, L; and the radius, R; the thickness of the coating, ΔR, was determined from:-

$$\Delta R = \frac{\Delta M}{2 L \varrho_{cr} R} \qquad 4.1$$

when $\Delta R \ll 1$.

The results are plotted in Fig. 4.5 together with expression 4.1.

Clearly, plating the crystal with chromium at 55C and then cooling it to room temperature ($\approx$20C) would impose a stress on it depending on the relative magnitude of the thermal expansion coefficients of copper and chromium. Ultimately this stress could dislocate the crystal. To diminish the possibility of such an effect an initial attempt was made to chromium plate the crystals at room temperature, with two concomitant effects. Reference to Fig. 4.3c and Fig. 4.3d illustrates these two effects. A dislocation-free crystal, Fig. 4.3a, was etched to remove the tail, Fig. 4.3b; electroplated over half of the gauge length for 60 seconds (plating thickness ≈ 5 μm) at room temperature; and then re-topographed,

Fig. 4.3 Etching, and Electroplating at Room Temperature ($\approx$20C)

X-ray Topographs

a. An as-grown dislocation-free copper crystal

b. The same crystal as in (a) but with the 'tail' etched off. Note the presence of dislocations at the very bottom of the image

c. The crystal from (a) and (b) electroplated at 20C for 60 seconds with chromium over half the gauge length. A large reduction in anomalously transmitted X-rays over most of the plated region occurred except for the very intense double-line down the centre

d. The effect of removing the plated layer in HCl. Both dark lines from the centre had disappeared, and the once plated crystal region was badly damaged

Scale mark = 1 mm


[1̄2̄3]
g=111
(a)
(b)
(c)
(d)

Fig. 4.4 The Effect of Electropolishing

a. A dislocation-free crystal before and

b. after electropolishing. No detectable damage was induced.

Scale mark = 1 mm

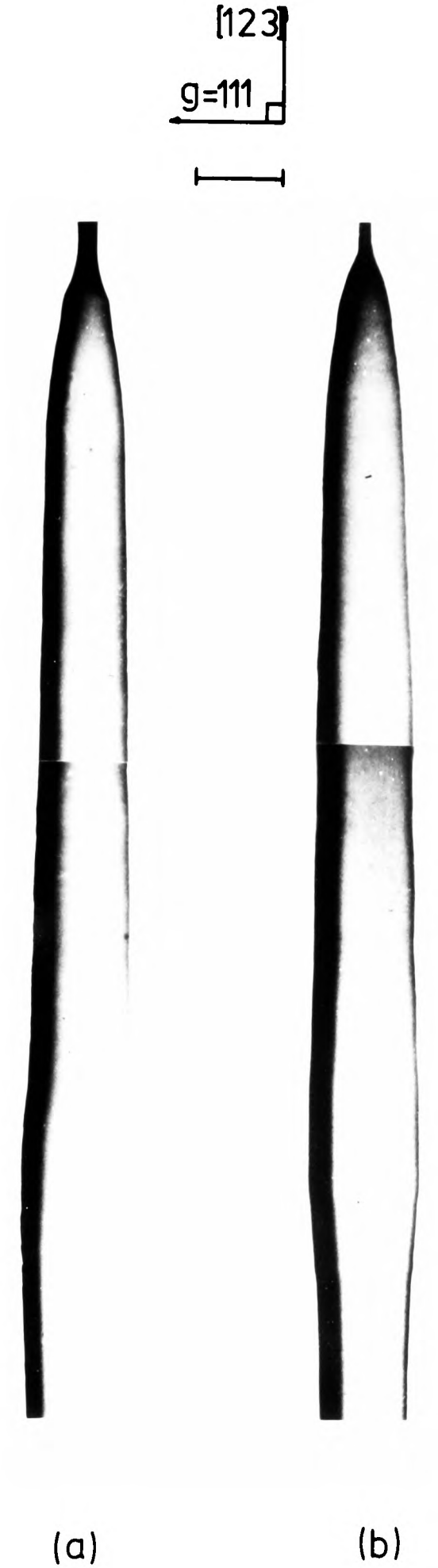

[123]
g=111
(a)
(b)

Fig. 4.5 A Plot of Plating Thickness versus Plating Time for Chromium Plated onto Copper at 55C

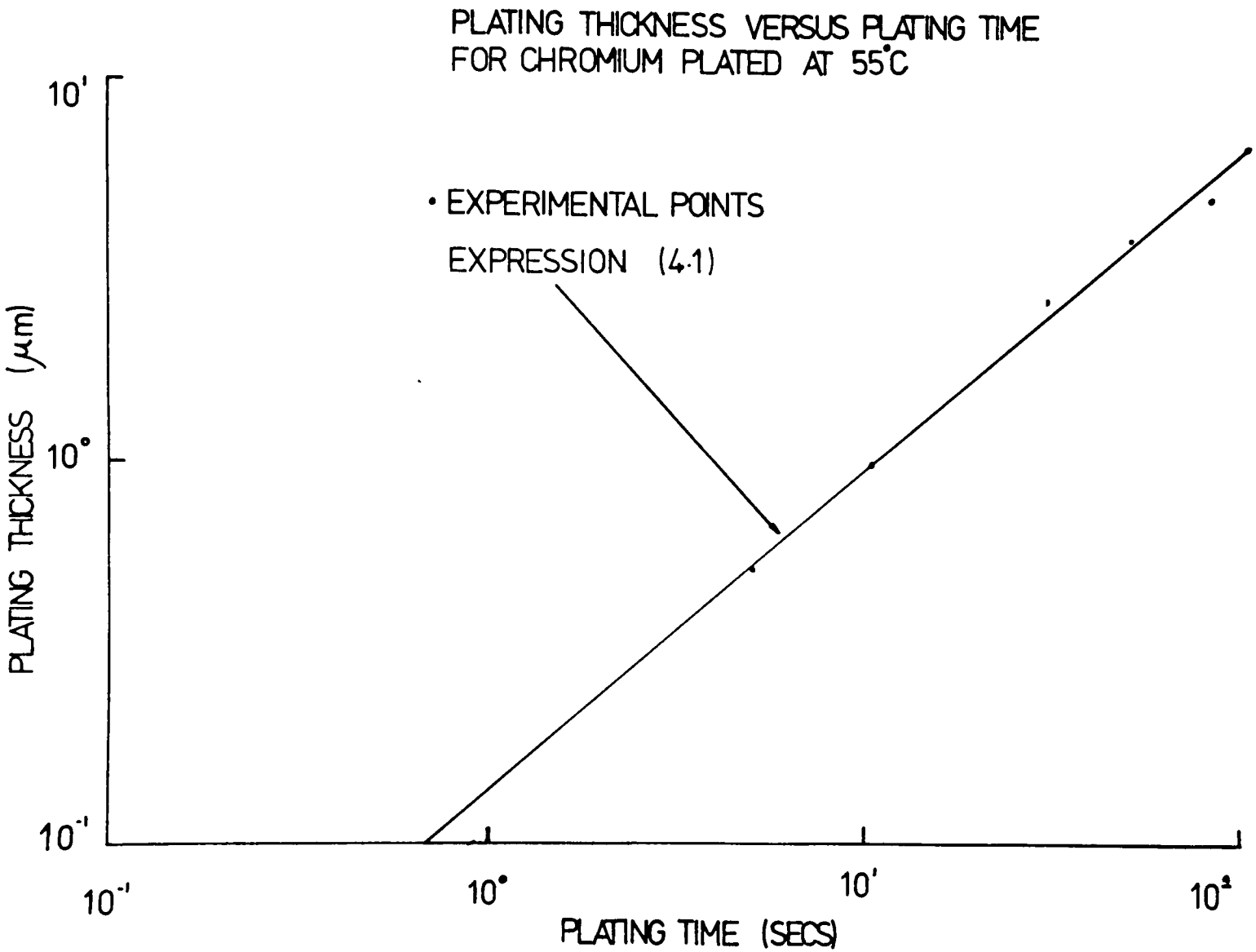

PLATING THICKNESS VERSUS PLATING TIME
FOR CHROMIUM PLATED AT 55°C
• EXPERIMENTAL POINTS
EXPRESSION (4·1)
PLATING THICKNESS (μm)
10'
10°
10⁻¹
10⁻¹
10°
10'
10²
PLATING TIME (SECS)

Fig. 4.3c. Only half of the crystal was plated so that any new contrast features could be compared to the upper dislocation-free volume.

It was noticed that an appreciable loss of anomalous transmission occurred over most of the plated region; and additionally, a very dark (corresponding to high X-ray intensity) 'double-line' appeared down $\frac{2}{3}$ of the plated region along the longitudinal axis of the crystal, Fig. 4.3c. The general loss of anomalously transmitted wavefields associated with the first effect could have arisen from three mechanisms: either the supposedly incoherent plating interface between the chromium and the copper significantly reduced the transmission of the Borrmann wavefields through the chromium; or, the chromium completely absorbed these Borrmann wavefields; or the crystal was completely dislocated along the plated region. As shown in Chapter III, the very worst absorption case occurs when the anomalous transmission coefficient is approximately twice the normal linear photoelectric absorption coefficient and therefore, for a 5 μm chromium layer, the Borrmann waves would be attenuated at the most by 20% (linear absorption coefficient of chromium $= 220\ cm^{-1}$ for $M_{oK\alpha_1}$[58]). Comparing the intensities in the upper and lower halves of the topograph in Fig. 4.3c qualitatively, readily shows that the intensity difference is far more than 20%; hence, the chromium absorption mechanism can be discarded.

To decide which of the two remaining absorption mechanisms was operative the plated layer was etched off in concentrated hydrochloric acid and the crystal topographed again, Fig. 4.3d. Not only was there total loss of anomalously

transmitted radiation along the once plated region, but also the 'double-line' had disappeared. It is therefore concluded that even at room temperature the plating could dislocate the crystal. The reason for the double line is still unclear and remains a subject for study in conjunction with the further work suggestions of Chapter III. Of further interest is the conclusion that the HCl did not produce any detectable evidence of dislocation production in the upper dislocation-free half of the crystal, because the complete crystal was immersed in the acid. Even plating for 10" gave evidence of dislocation production in the plated region as shown in Fig. 4.6a.

Recourse to the literature[1] gave every indication that the results above fitted in well with other reports of electroplating phenomena. For example, it has been shown that[1] at room temperature ($\approx$20C) the chromium is not deposited as bcc-Cr but as a hexagonal hydride. At 20C this hydride is dull, and, relative to 55C plating, porous((Fig. 4.6b,&c) provides good evidence for this conclusion for these crystals). Furthermore, decomposition of the hydride to bcc-Cr and H_2 may occur[1] and associated with this transformation is a volume shrinkage of $\approx$15%; therefore, it is to be expected that the chromium would subject the copper crystal to a compressive radial shear stress of approximately 200 $g/_{mm}{}^2$ when the plating thickness was 5 μm (note in Fig. 4.6b that the stresses involved at room temperature can fracture the chromium layer too). As shown in previous work by Kamada and Tanner[10] and later in this work, 200 $g/_{mm}{}^2$ is well above the upper yield stress ($\approx$90 $g/_{mm}{}^2$) of a dislocation-free copper crystal, and

Fig. 4.6 Chromium Plating Effects

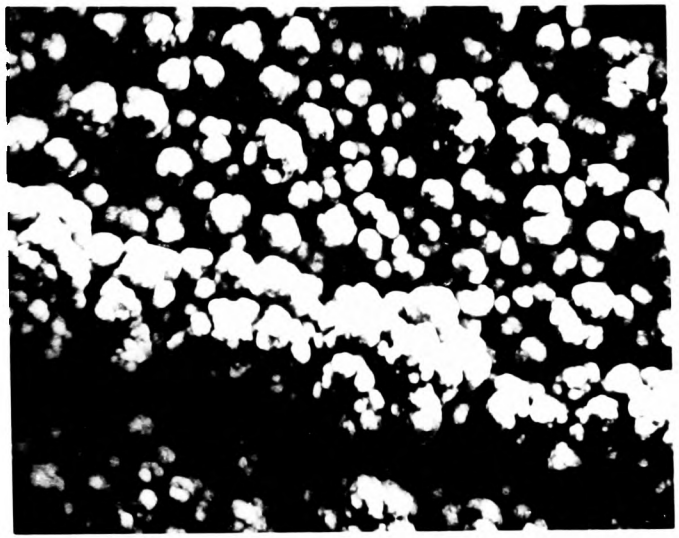
a. Electroplating a copper crystal with chromium for even 10 seconds at room temperature produced dislocations

b. S.E.M. micrographs of chromium electroplated onto copper at ≈20C. Note the lack of uniform deposition and the porous nature of the film, plus the cracking from residual stresses (bottom picture)

c. An S.E.M. micrograph of chromium electroplated onto copper at 55C. The film was continuous and evenly deposited

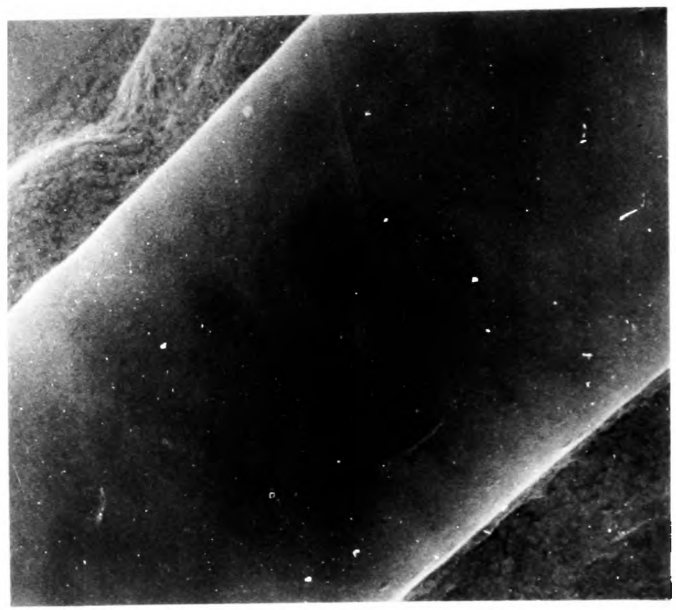


(a)





(b)



(c)

so dislocation of the crystal would still be expected at room temperature, despite the absence of differential expansion stresses as expected from plating at higher temperatures. This information further aids the interpretation of the topographs in Fig. 4.3° and supports the conclusion reached.

Another important consideration is that the crystal dislocated at a stress level comparable with that for non-plated crystals. This compatibility of results shows that the handling damage (e.g. when mounting the specimen for deformation) induced by Kamada and Tanner and later by the author was nil as it was in the crystal illustrated in Fig. 4.3. The yield stress measured by Kamada and Tanner therefore appears to be reliable and, what is more important still, the two sets of crystals grown by the author and Kamada and Tanner would appear to be similar as grown. This ameliorated the ease of interpretation of results.

A further study of plating stresses was carried out prior to deforming crystals in the Instron, but this time the plating temperature was 55C. The aim was to compare the theoretical and experimental stresses in the crystal as a result of plating at 55C and to assess the influence of these plating stresses on crystal perfection as monitored by X-ray topography.

The theoretical work to be presented follows closely the analysis of Poritsky[11] who derived expressions for the stress distributions in two concentric cylinders which fit together stress free at a temperature T, but which suffer thermal stresses at a different temperature T_o; the cylinders being completely elastic in deformation character. Poritsky's analysis neglects shear stress components, e.g. along the interfacial

circumference of the two cylinders, but since an order of magnitude estimate of the radial and longitudinal stresses was required here this error can be tolerated. Using a model similar to that shown in Fig. 4.7a Poritsky showed that the stress distributions may be calculated from:-

$$\left.\begin{aligned} \sigma_R &= A_2\left(1 - \frac{b^2}{R^2}\right) \\ \sigma_\Theta &= A_2\left(1 + \frac{b^2}{R^2}\right) \\ \sigma_z &= C_2 \end{aligned}\right\} \text{Outer cylinder} \qquad 4.2$$

$$\left.\begin{aligned} \sigma_\Theta &= \sigma_R = A_2\left(1 - \frac{b^2}{a^2}\right) \\ \sigma_z &= C_2\left(1 - \frac{b^2}{a^2}\right) \end{aligned}\right\} \text{Inner cylinder} \qquad 4.3$$

Where,

$$A_2 = \frac{-(k_2-k_1)(T-T_o)\left((1+\nu_1)\left(1-\frac{b^2}{a^2}\right)/E_1+(1-\nu_2)/E_2\right)}{\Delta} \qquad 4.4$$

$$C_2 = \frac{-(k_2-k_1)(T-T_o)\left((1-\nu_1)\left(1-\frac{b^2}{a^2}\right)/E_1-(1+\nu_2)/E_2\right)}{\Delta} \qquad 4.5$$

$$\Delta = \begin{vmatrix} 2\nu_2/E_2-\left(1-\frac{b^2}{a^2}\right)2\nu_1/E_1 & -1/E_2 + \left(1-\frac{b^2}{a^2}\right)/E_1 \\ (1-\nu_1)\left(1-\frac{b^2}{a^2}\right)/E_1-(1-\nu_2)/E_2 & \nu_2/E_2 - \frac{\nu_1\left(1-\frac{b^2}{a^2}\right)}{E_1} \end{vmatrix} \qquad 4.6$$

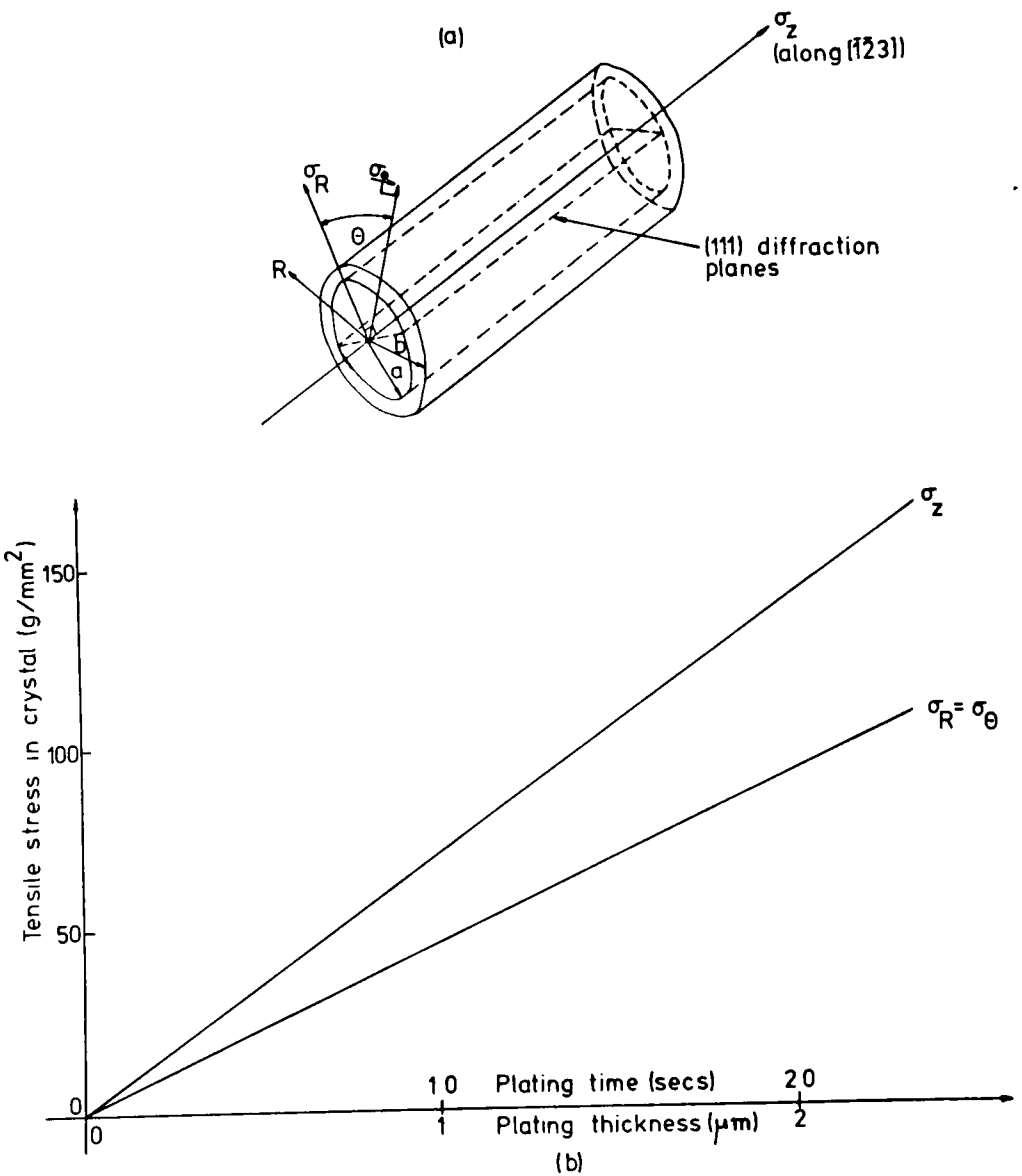
σ_R = Radial stress
σ_Θ = Angular stress
σ_z = Longitudinal stress
A_2, C_2 = Constants
a = Radius of inner cylinder
b = Radius of outer cylinder
R = Radial co-ordinate
k_1, k_2 = Coefficients of linear expansion of the inner cylinder (1) and the outer cylinder (2)
ν_1, ν_2 = Poisson's ratios for inner (1) and outer (2) cylinders
E_1, E_2 = Young's moduli for inner (1) and outer (2) cylinders

Fig. 4.7 Theoretical Modelling of Plating Stresses

a. The model used for the calculations

b. Plating stresses (theoretical) versus plating time and thickness for chromium deposited onto a 1 mm diameter copper substrate at 55C and then cooled to 20C

σ_R = Radial stress
σ_Θ = σ_R = Tangential stress
σ_z = Longitudinal stress
a = Radius of inner cylinder
b = Radius of outer cylinder
R = Radial co-ordinate


(a)
σ_z
(along [1̄1̄23])
σ_R
σ_θ
θ
R
(111) diffraction planes
b
a
Tensile stress in crystal (g/mm^2)
150
100
50
0
σ_z
$\sigma_R = \sigma_\theta$
10
20
Plating time (secs)
0
1
Plating thickness (μm)
2
(b)

The co-ordinates used for the analysis were cylindrical and this therefore implies that σ_R and σ_z are principal stresses. In this work σ_R and σ_z for the inner cylinder only were computed on the Oxford ICL 1906A computer. This inner cylinder was assumed to be a dislocation-free copper crystal and the outer cylinder was assumed to be a chromium plated shell. The constants were chosen as follows:-

1 = copper; 2 = chromium

$k_1 = 1.66 \times 10^{-5}\ C^{-1}$

$k_2 = 6 \times 10^{-6}\ C^{-1}$

$\nu_1 = 0.343$

$\nu_2 = 0.21$

$E_1 = 1.298 \times 10^{12}$ dynes/cm^2

$E_2 = 2.790 \times 10^{12}$ dynes/cm^2

$a = 5 \times 10^{-2}$ cm

$b = 5.005 \times 10^{-2}$ cm; 5.01×10^{-2} cm; 5.02×10^{-2} cm; 5.03×10^{-2} cm; 5.04×10^{-2} cm; 5.05×10^{-2} cm

$T = 55C$

$T_o = 20C$

The results are plotted in Fig. 4.7b

It is intuitively clear that since the thermal expansion coefficient of copper is greater than that for chromium, that the copper will be in a state of tension after cooling from 55C to 20C and the chromium in a state of compression. This is reflected in the results in Fig. 4.7b where the radial, longitudinal and angular components of stress are shown to be tensile. Typically, for a 1 μm thick plated layer the value of σ_R was 46.2 g/mm^2 and for σ_z the value was 71.5 g/mm^2.

Clearly, these normal stresses are appreciable compared to the shear yield stress ($\approx$90 g/mm^2) of the non-treated dislocation-free crystals. The implications of this result are two-fold: first, the plated dislocation-free crystal does not begin tensile deformation in the Instron under a zero stress condition, and therefore any stresses derived from the Instron tests must take into account plating stresses; and secondly, the stress state during Instron tensile deformation will not be uniaxial along the $[\bar{1}\bar{2}3]$ direction but triaxial. Considering the symmetry of the stress field imposed by plating this triaxial state can be reduced to a biaxial state, necessitating consideration of only σ_R and σ_z therefore. Because of the imposed stress field it is further obvious that the operative slip system need not be $(1\bar{1}1)[\bar{1}01]$ alone and that double slip may be prematurely induced; e.g. on the $(\bar{1}\bar{1}1)[101]$ system too.

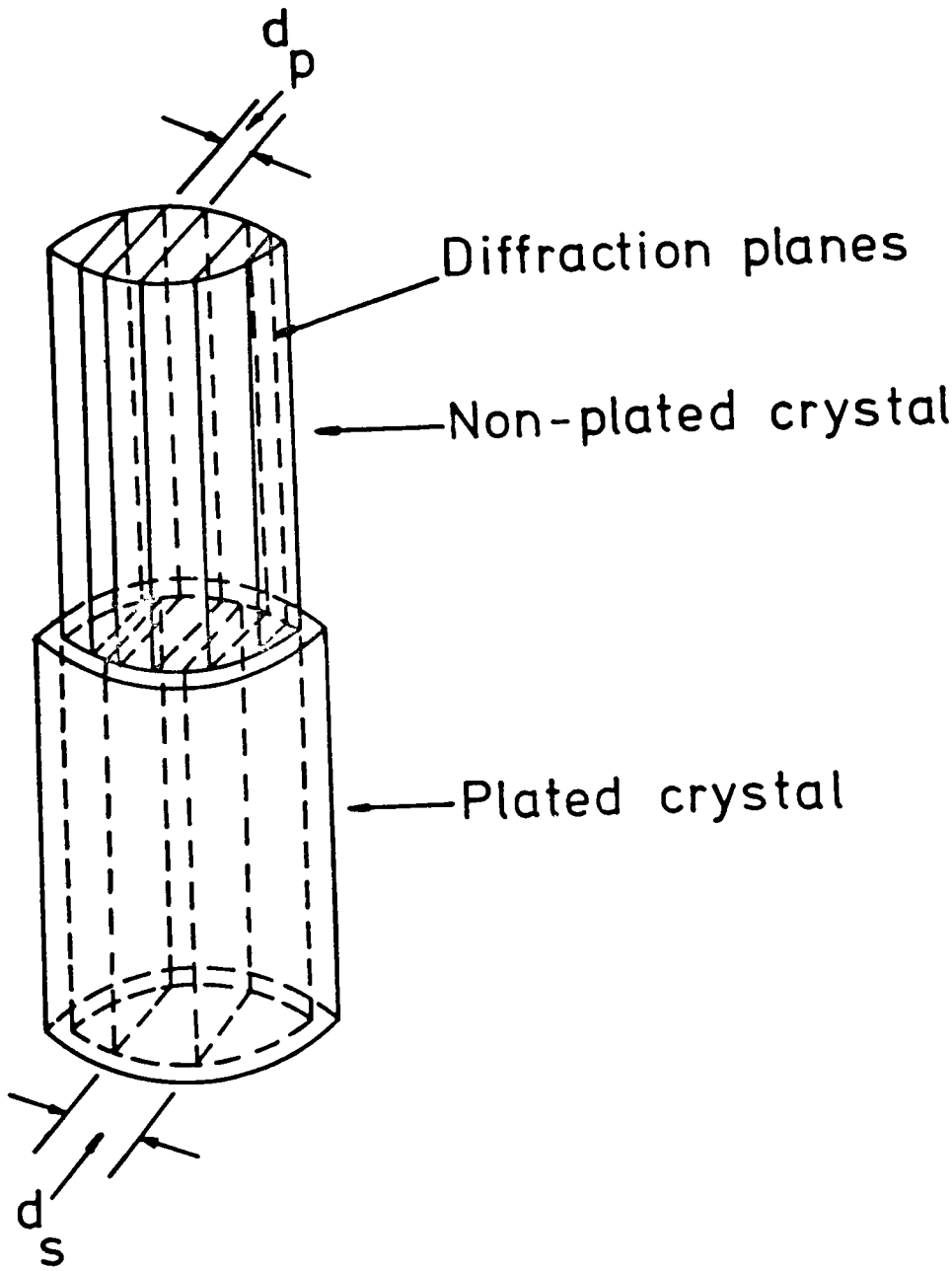
The experimental side of this investigation was concerned with the measurement of the stress induced in a dislocation-free copper crystal plated for 15 secs. at 55C with chromium and then cooled to 20C. The model used for subsequent calculations is shown in Fig. 4.8. By obtaining diffraction from a particular set of lattice planes in the non-plated region of the crystal on the Lang Camera with a lattice spacing of d_p, and then from the same planes in the plated half of the crystal with a lattice spacing d_s, it was possible to obtain an estimate of the strain, ϵ, in the plated region relative to the non-plated region from:-

$$\epsilon = \frac{d_s - d_p}{d_p} \qquad 4.7$$

Fig. 4.8 The Model Used for the Calculation of Plating Stresses from Diffraction Data

d_p = spacing of lattice planes in non-plated region

d_s = spacing of lattice planes in plated region


d_p
Diffraction planes
Non-plated crystal
Plated crystal
d_s

In both diffraction cases Bragg's law must be satisfied and so:-

$$2d_p \text{Sin}\,\Theta_{Bp} = n\lambda$$
$$2d_s \text{Sin}\,\Theta_{Bs} = n\lambda \qquad 4.8$$

Where,

Θ_{Bs} = Bragg angle of the plated substrate

Θ_{Bp} = Bragg angle of the non-plated crystal

n = Integer

λ = Wavelength of radiation used

Since λ can be the same in both cases, 4.8 can be combined to yield:-

$$d_p \text{Sin}\,\Theta_{Bp} = d_s \text{Sin}\,\Theta_{Bs} \qquad 4.9$$

If,

$$\Theta_{Bs} = \Theta_{Bp} - \Delta\Theta \qquad 4.10$$

then combining 4.9 and 4.10:-

$$d_s \text{Sin}(\Theta_{Bp} - \Delta\Theta) = d_p \text{Sin}\,\Theta_{Bp}$$

and expanding the left hand side, noting that when $\Delta\Theta$ is small $\text{Cos}\Delta\Theta \simeq 1$ and $\text{Sin}\Delta\Theta = \Delta\Theta$

$$\epsilon = \Delta\Theta \text{Cot}\,\Theta_{Bp} \qquad 4.11$$

Consequently by measuring the diffracted peak shift in seconds on the Lang Camera between the plated and non-plated regions of the crystal and converting this to radians, it was possible to determine the strain in the plated region relative to the non-plated region given Θ_{Bp}. Since all g-vectors in X-ray topography lie in a horizontal plane the method measured the radial component of strain, ϵ_R, for these cylindrical crystals. Theoretically[12] the Lang Camera used was capable of detecting a 1 second of arc peak shift, but this has never been

achieved in practice due to small amounts of slack at various linkages on the Camera which were difficult to eliminate. The machine error was estimated to be $\bar{+}$ 5 seconds of arc.

Fig. 4.9 depicts the X-ray topographs of the sample used at various stages in the study. Originally the complete crystal was dislocation-free, Fig. 4.9a, and it possessed a $[\bar{1}\bar{2}3]$ growth axis. It was etched to remove the tail, Fig. 4.9b, and then chromium plated at 55C for 10 seconds over half the gauge length, Fig. 4.9c. In Fig. 4.9c it can be seen that the upper half remained dislocation-free and the lower half appeared to be dislocated. By using a pair of collimating slits to reduce the vertical height and position of the incident beam it was possible to obtain diffraction from only the plated or non-plated regions respectively. The relative angular rotation, $\Delta\Theta$, needed to rotate the crystal so as to give one diffraction peak from the previous for the two regions was inserted into 4.11 and the strain calculated. This was carried out for the Bragg surface reflection, the central section of the crystal and the rear surface. Ideally, this type of experiment should have been performed on a double crystal spectrometer to increase sensitivity to strains and to reduce the influence of wavelength spread and diffracted peak profile on the final result. However, access to such apparatus was not available and so from this simple experiment all that could be hoped for was an order of magnitude estimate of ϵ_R. No attempt was made to measure the strain in the longitudinal direction because of the inherent problems of crystal dislocation during rotation; detecting the diffracted beam from a now much smaller diffracting volume; and a reduced diffracted intensity as a result of using a $\bar{2}\bar{4}6$ reflection with very small associated anomalous transmission coefficients.

Fig. 4.9 The Effect of Electroplating Chromium onto Copper at 55C and then Cooling to 20C

Scale mark = 1 mm

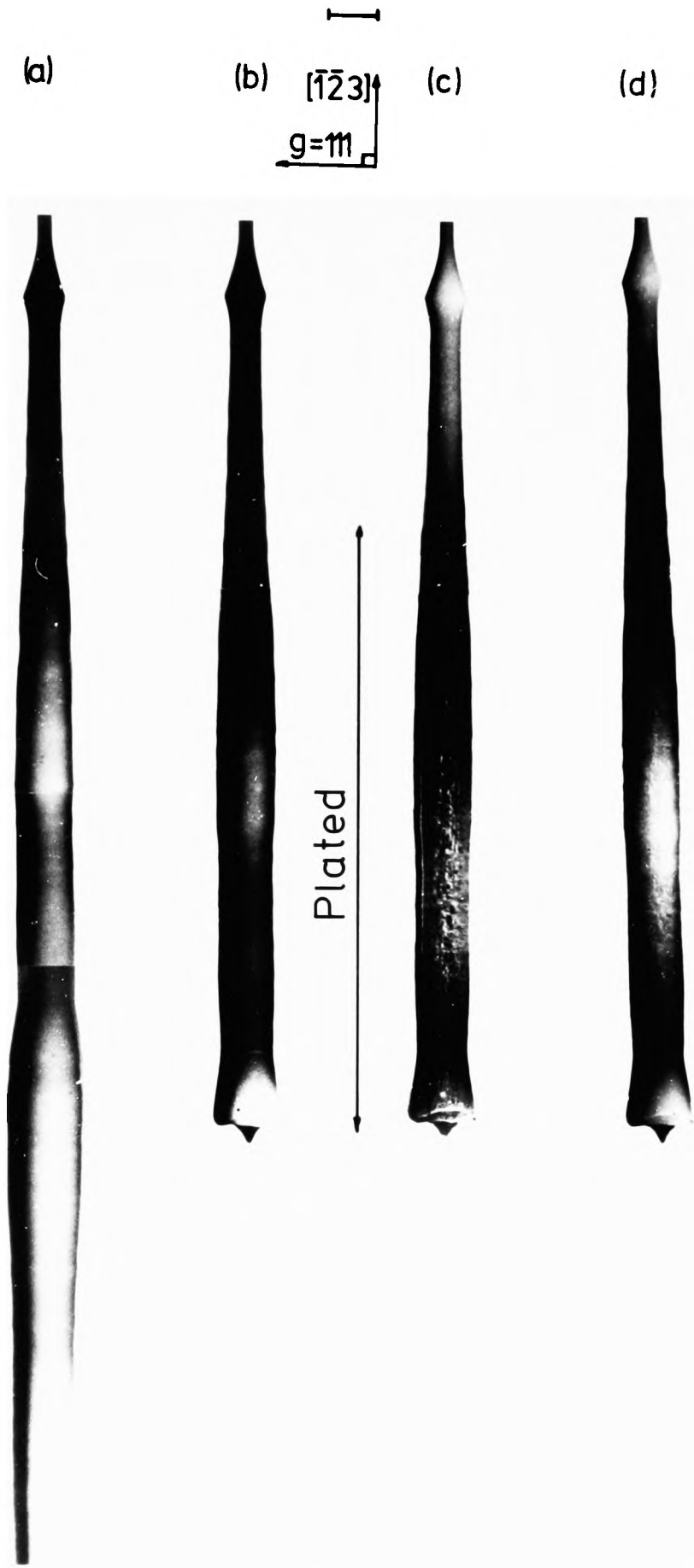
Plating time = 15 seconds
Plating thickness = 1.5 μm

a. Dislocation-free $[\bar{1}\bar{2}3]$ growth axis copper crystal

b. Same crystal as in (a) but with the tail etched off

c. The half plated crystal after electropolishing. Plating thickness ≈1.5 μm

d. The effect of removing the plated layer in HCl. Note the apparent retention of defects in the lattice as evidenced by the loss of anomalously transmitted X-rays locally


(a)
(b)
[1̄2̄3]
g=111
(c)
(d)
Plated

The crystal shown in Fig. 4.9c produced the following values for $\Delta\Theta$ and ϵ:-

	Bragg Surface	Central Section	Rear Surface
$\Delta\Theta$ (secs) $\mp$ 15	210	89	200
ϵ_R ($\times 10^{-3}$) $\mp$ 0.42	5.91	2.5	5.63
σ_R (g/mm^2) $\mp$ 22.4	335	142	319

The value for σ_R was estimated by assuming a value for the shear modulus, μ_{Cu}, for dislocation-free copper of $\approx$21kg/mm^2 from Kamada and Tanner's[10] work and converting this to a value for Young's modulus, E_{Cu}, using the well known[13] expression:-

$$E_{Cu} = 2(1 + \nu_{Cu})\mu_{Cu} \qquad 4.12$$

Where ν_{Cu} = Poisson's ratio for copper

Not unexpectedly the stress and strain in the crystal are seen to be symmetrical about the longitudinal axis of the crystal with a minimum value on that axis. Compared to theoretically derived stress values these results are approximately 2-4 times greater (σ_R for a 15" plated crystal was theoretically 70 g/mm^2). Some discrepancy therefore exists between the two sets of results, and whilst the experimental work shows an expected stress-strain gradient (as derived from a lattice spacing gradient) across the crystal, it is felt that the values generated are not too reliable for the reasons outlined previously with regard to the double-crystal arrangement. Consequently, for subsequent calculations the theoretical results will be used where plating stresses need to be incorporated into the analysis

of data. As a rider it must be noted that the theoretical results do not predict a strain gradient in the crystal and this is a failing which will be accounted for in the discussion of results.

When the plated layer was etched off the crystal, Fig. 4.9d, it was noticed that the contrast registered in Fig. 4.9c along the plated region and associated with dislocations remained faintly visible. It therefore appears that the 15 seconds plated layer induced defect generation and that by removing this layer a number of these defects ran back to their sources.

A final necessary conclusion is that at 55C chromium is deposited as a continuous surface layer as shown in Fig. 4.6c. Hence, the surfaces of the crystals tested can be considered as uniformly treated all over. All subsequently tested crystals were plated for either 10 secs. or 5 secs. at 55C over the whole surface. No dislocations were generated as a result of plating for these lengths of time, Fig. 4.21a.

4.3iii Mounting the Crystals for Deformation

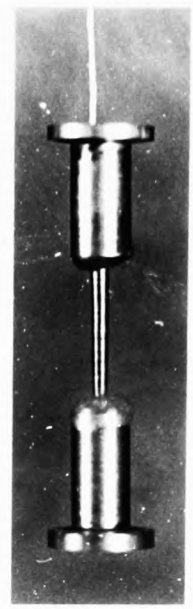
The seed and plated crystal were separated at the top of the long thin neck using a pair of very fine tweezers and scissors. The free crystal was then held vertically by the top of the neck in a crocodile clip attached to a micromanipulator, and the free end was gently dipped into a freshly made solution of rapid setting araldite which itself was held in a 'deformation-cup' made of brass, Fig. 4.10. The deformation-cup had previously been etched in nitric acid to increase the

Fig. 4.10 Crystal Mounting

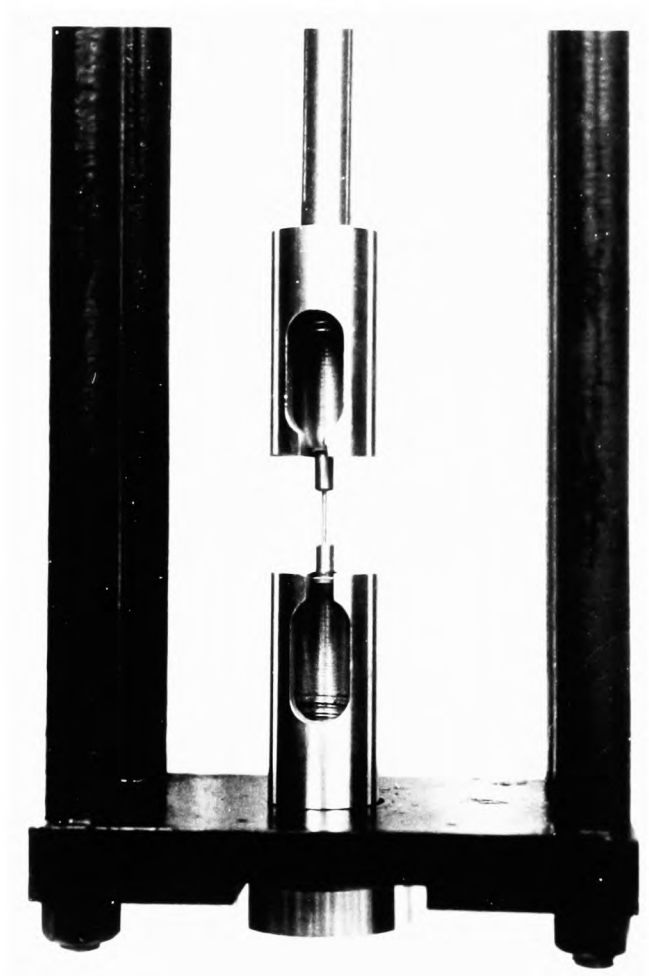
a. In the deformation cups

b. In the Instron

(a)



(b)



strength of the araldite-brass bond as recommended by the araldite makers. When set (≈ 8 hours), the crystal was very carefully turned upside-down, reclamped in the micromanipulator by the deformation-cup and the copper neck was etched off in concentrated HNO_3 (the chromium remained unaffected by this procedure). The second free end of the crystal was then mounted in a deformation-cup as before. Great perseverence was necessary throughout this period to ensure that the crystal was mounted vertically in the deformation-cups; that the deformation-cups were themselves aligned; and that no mounting stresses were induced in the crystal. The first two conditions can be seen to be satisfied in Fig. 4.10a, whilst the final requirement is shown to be satisfied in Fig. 4.21a where a 10 seconds plating time, mounted crystal has been topographed and gives no indication of dislocation contrast. Compare this topograph with that in Fig. 4.9c where such contrast from a 15 seconds plating time, non-mounted crystal was observed.

To transport the crystals the $\frac{1}{4}$ mile to the Instron a piece of cotton had previously been araldited to the end of one of the deformation-cups. The crystal was carried dangling from this cotton!

4.4 Macroscopic Deformation Studies in the Instron

4.4i The Experiments

The mounted crystals were assembled in specially designed cut-away coned grips (to reduce grip influence on deformation) which were attached to a 2kg load cell capable of

full scale deflections of 100g, 200g, 500g, 1000g and 2000g using the Instron chart recorder. The slowest crosshead speed was chosen (0.05 mm/min) which gave a strain rate of approximately 10^{-4} s^{-1} depending on the gauge length. This speed was chosen to allow correlation with Kamada and Tanner's results[10] and to allow a sensible record of the deformation to be obtained using a chart speed of 50 cm/min during the very early stages of deformation and 20 cm/min later on. Great care was taken to change the load cell range very smoothly since at low loads the merest knock to the Instron affected the recorded chart trace. A typical experimental arrangement is shown in Fig. 4.10b. All tests were carried out at room temperature.

4.4ii Processing Instron Data

The results from the Instron have been plotted as shear stress versus shear strain curves as shown typically in Fig. 4.12. To derive such information from the load, L, and crosshead extension, e, curves the following simple analysis was employed. The original cross sectional diameter, d, and gauge length, l_o, of the specimen were measured using a travelling microscope and average values obtained from five such measurements of each; the applied longitudinal normal stress, σ_{Az}, was then calculated from:-

$$\sigma_{Az} = \frac{4L}{\pi d^2} \qquad 4.13$$

The resolved shear stress, τ, on the slip plane could not be simply calculated from:-

$$\tau = \sigma_{Az} \cos\chi_o \cos\lambda_o \qquad 4.14$$

Where χ_o = Angle between the tensile axis and the normal to the slip plane

λ_o = Angle between the tensile axis and the slip direction

Rather, the composite stress system explained earlier (Section 4.3ii) had to be incorporated too. To obtain a value for the shear stress on the slip system $(1\bar{1}1)$ $[\bar{1}01]$ a Mohr stress circle analysis[14] could have been used, but more simply, as shown in Fig. 4.11, it was better to consider a unit cube and the residual plating stresses in the growth axis plane. Since the radial and tangential stresses were equal the resultant stress on the crystal could be considered to be composed of two parts: a hydrostatic part and a compressive part. Hence, only the compressive part needed to be incorporated into the modified Schmid equation as:-

$$\tau = ((\sigma_{Az} + \sigma_z) - \sigma_R)\cos\chi_o\cos\lambda_o \qquad 4.15$$

For a 10 secs. plating time crystal σ_z and σ_R were taken to be 71.5 g/mm^2 and 46 g/mm^2 respectively; whilst for a 5 secs. plating time crystal σ_z and σ_R were taken as 36 g/mm^2 and 22.5 g/mm^2 respectively. All values were taken from Fig. 4.7b.

Since the araldite in the deformation-cup possessed a large cross sectional area compared to the specimen ($\approx$11:1) the stress that it carried was small and therefore the extension too. Nevertheless the shear strain calculations for the crystal took into account the elastic extension of the araldite during deformation. The shear strain, γ, in the glide plane along the $[\bar{1}01]$ direction was finally calculated from[15]:-

$$\gamma = \frac{1}{\sin\chi_o}\left(\left(\left(\frac{l_o + \Delta l}{l_o}\right)^2 - \sin^2\lambda_o\right)^{\frac{1}{2}} - \cos\lambda_o\right) \qquad 4.16$$

Where, Δl = extension of the specimen corrected for araldite elastic extension

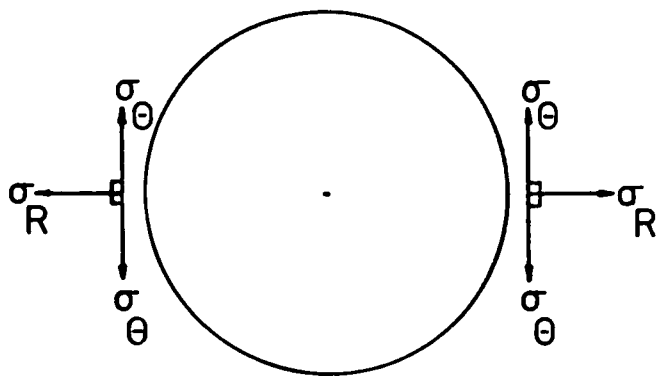
Fig. 4.11 Electroplating Stresses and Their Influence on the Interpretation of Instron Results

a. In the growth axis plane of the crystal the radial stress, σ_R, and the tangential stress, σ_θ, were equal, σ.

b. Considering a unit cube, then the radial and tangential stresses may be subdivided into a hydrostatic component and a compressive component as shown. Since a hydrostatic stress does not influence slip, the compressive component along the longitudinal axis need only be considered. In an Instron analysis, therefore, this must be subtracted from the applied stress to find the actual normal stress, σ_{AzA}, on the growth axis plane as:-

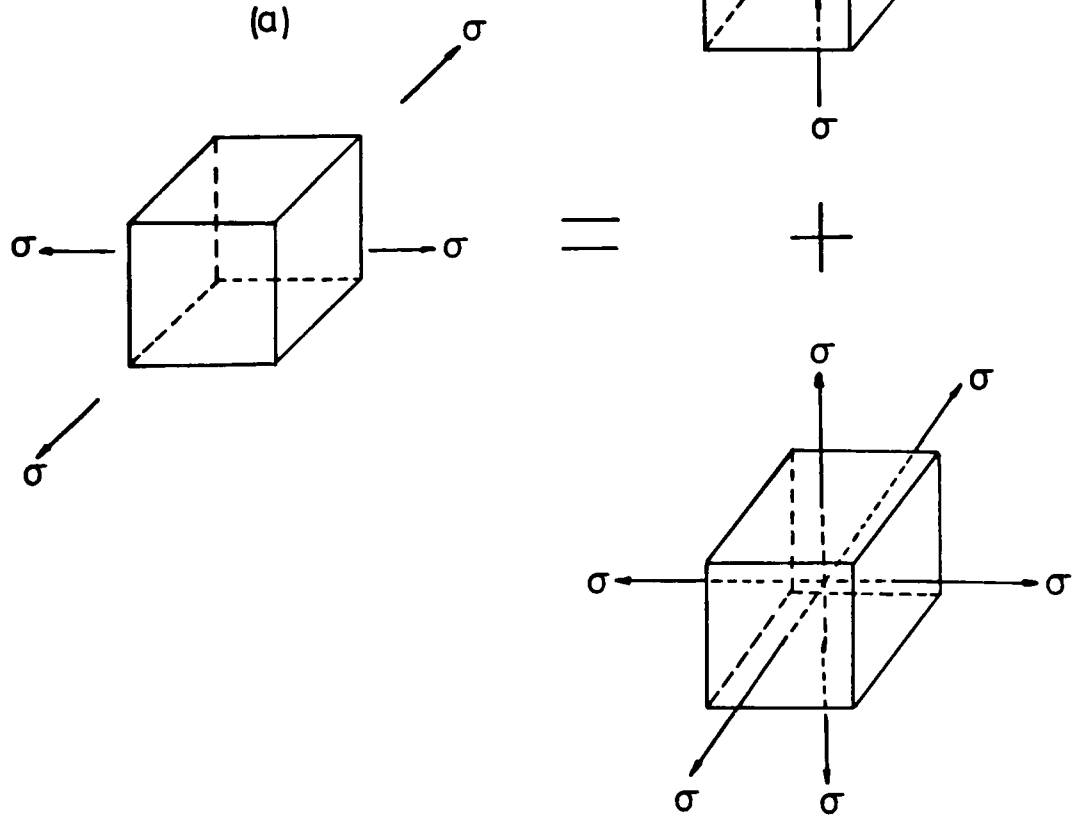
$$\sigma_{AzA} = ((\sigma_{Az} + \sigma_z) - \sigma_R)$$

σ_{Az} = applied stress in the Instron
σ_z = residual plating stress in longitudinal direction
σ_R = residual radial plating stress



$\sigma_R = \sigma_\Theta = \sigma$

(a)



(b)

Any extension of the deformation-cups and the Instron crosshead was considered to be insignificant because of the very low loads used, i.e. $\not>$2kg. For these tests the tensile apparatus was therefore considered to be hard.

4.4iii Instron Results

Four dislocation-free copper crystals plated for 10 seconds were tested and so were four 5 seconds plated dislocation-free copper crystals. Additionally, to aid interpretation of the results from dislocation-free crystals, two 10 seconds plated, dislocated crystals were tested as were two 5 seconds plated dislocated crystals. Finally, two dislocation-free non-plated copper crystals were strained in the Instron; again to aid interpretation of the results from the plated dislocation-free crystals. The important data from each test is tabulated in Table 4.1 and typical stress-strain curves are shown in Figs. 4.12 and 4.13.

4.4iii.a The Elastic Region

The most prominent feature of the elastic region was that in all dislocation-free crystals it was terminated by a yield point and thence a yield drop, Fig. 4.12a. In dislocated crystals, whether plated or not, no yield point or drop was ever recorded; for instance, refer to Fig. 4.12b. These results fit in well with those of other workers who have similarly observed yield points in dislocation-free semiconductor[16,17] and copper[10] single crystals but not in dislocated copper single crystals[10,19,20,3,21,22].

TABLE

Crystal Number ↓	Upper Yield Point g/mm^2	Lower Yield Point g/mm^2	Yield Drop g/mm^2	% Yield Drop	Initial Work Hardening Rate g/mm^2	Transitionary Work Hardening Rate g/mm^2
						DISLOCATION-FREE
C910"	80.5	77.5	3.0	3.7	18.6	5.53
C1110"	89.6	84.0	5.5	6.6	18.2	6.34
C1210"	78.3	70.5	7.8	9.9	18.5	5.01
C810"	85.3	81.4	3.9	4.5	18.8	5.89
$\bar{x}$	83.4	78.3	5.0	6.2	18.52	5.69
s	5.04	5.8	2.1	2.7	0.25	0.56
						DISLOCATION-FREE
C155"	47.5	38.0	9.5	20.0	18.2	2.06
C165"	55.7	50.8	4.9	8.7	18.9	2.45
C175"	63.3	58.6	4.7	7.4	21.1	2.74
C185"	54.1	46.1	8.0	14.0	19.0	2.59
$\bar{x}$	55.1	48.3	6.7	12.5	19.3	2.46
s	6.48	8.6	2.3	5.7	1.2	0.28
						DISLOCATED
C710"	42	-	-	-	22.5	3.7
C610"	38	-	-	-	27.9	5.8
						DISLOCATED
C145"	50	-	-	-	16-40	16.3
C135"	54	-	-	-	35.4	8.9
						DISLOCATION-FREE
C24	55	31	24	43.6	-	-
C25	85.5	40	45.5	53.2	-	-
$\bar{x}$	53.7	24.3	32.8	59.5	-	-
s	23.1	8.6	25.9	17.7	-	-

$\bar{x}$ = Average value

Final Work Hardening Rate g/mm^2	Region i g/mm^2 Magnitude of oscillation	Region i Extent of oscillation $\Delta\gamma$ % x 10-1	Region ii Magnitude of oscillation g/mm^2	Region ii Extent of oscillation $\Delta\gamma\% \times 10^{-1}$
PLATED FOR 10 SECONDS				
2.96	0	0	15	1.01
3.42	0	0	10	1.1
2.59	0	0	16.5	0.9
2.91	0	0	11	0.9
2.97	0	0	13.1	0.97
0.34	0	0	3.1	0.096
PLATED FOR 5 SECONDS				
1.01	1.5	0.2	4.5	0.70
2.00	1.9	0.3	5.1	0.61
1.83	2.5	0.32	7.5	0.51
1.77	1.6	0.25	6.2	0.59
1.65	1.87	0.26	5.8	0.60
0.43	0.45	0.053	1.3	0.082
PLATED FOR 10 SECONDS				
2.21	-	-	-	-
3.1	-	-	-	-
PLATED FOR 5 SECONDS				
1.3 to 2.9	-	-	-	-
1.2 to 2.5	-	-	-	-
NON-PLATED (Averaged values include Kamada and Tanner's results[10]				
0.787	-	-	-	-
0.850	-	-	-	-
0.594	-	-	-	-
0.230	-	-	-	-

s = Standard deviation

Fig. 4.12 Stress-strain Curves from Chromium Plated Copper Crystals

Plating thickness = 0.5 μm

a. The plated layer affected the work hardening rates markedly but not the yield point

Θ_I = 18.25 kg/mm^2
Θ_T = 2.06 kg/mm^2
Θ_s = 1.01 kg/mm^2
Θ_1 = 0.78 kg/mm^2

b. A chromium plated, dislocated crystal never showed a yield point but possessed high work hardening rates compared to a non-plated crystal

Θ_I = 16-40 kg/mm^2
Θ_T = 2.9 kg/mm^2
Θ_s = 1.31 kg/mm^2

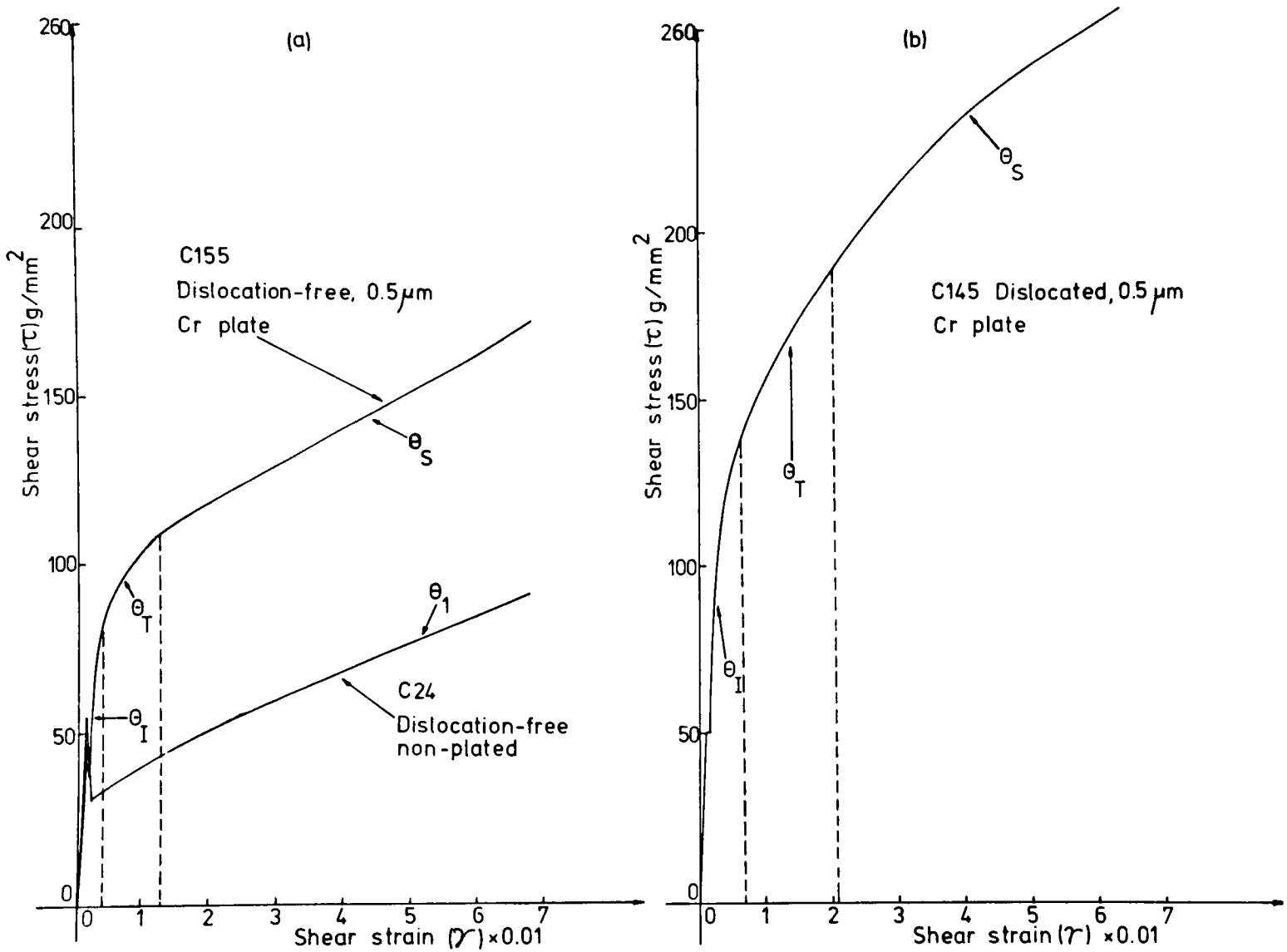

(a)
260
200
150
100
50
0
Shear stress(τ) g/mm²
C155
Dislocation-free, 0.5 μm
Cr plate
θS
θT
θ1
θI
C24
Dislocation-free
non-plated
0 1 2 3 4 5 6 7
Shear strain (γ) ×0.01
(b)
260
200
150
100
50
0
Shear stress (τ) g/mm²
θS
θT
θI
C145 Dislocated, 0.5 μm
Cr plate
0 1 2 3 4 5 6 7
Shear strain (γ) ×0.01

Fig. 4.13 Stress-strain Curves for Chromium Plated Crystals

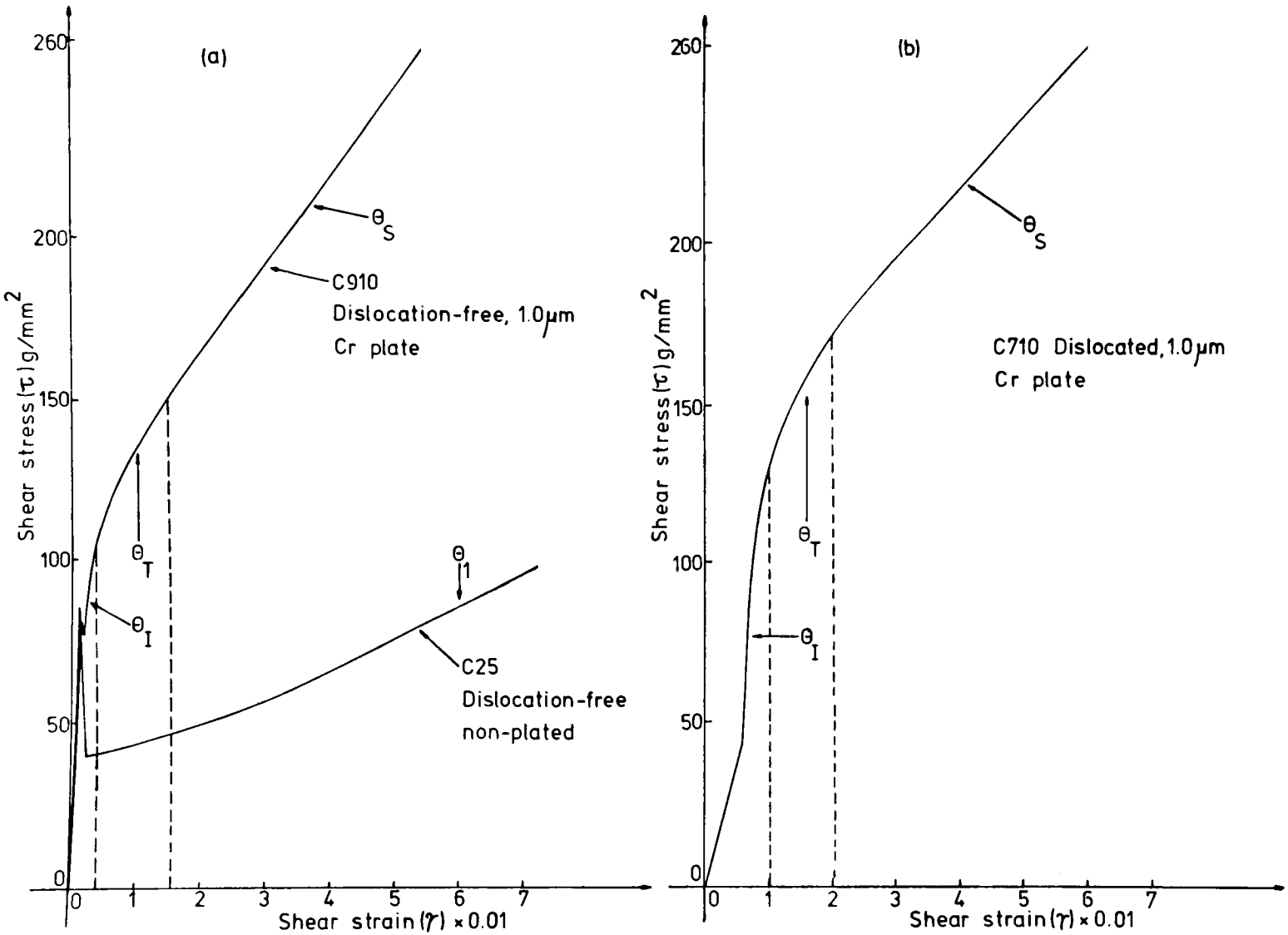
Plating thickness = 1.0 μm

a. Dislocation-free crystals

$\Theta_I = 18.6$ kg/mm^2
$\Theta_T = 5.5$ kg/mm^2
$\Theta_{s_1} = 2.9$ kg/mm^2
$= 0.85$ kg/mm^2

b. A typical stress-strain curve from a dislocated crystal

$\Theta_I = 22.5$ kg/mm^2
$\Theta_T = 3.70$ kg/mm^2
$\Theta_s = 2.21$ kg/mm^2


(a)
260
200
150
100
50
0
Shear stress (τ) g/mm²
θS
C910
Dislocation-free, 1.0μm
Cr plate
θT
θI
θ1
C25
Dislocation-free
non-plated
0 1 2 3 4 5 6 7
Shear strain (γ) × 0.01
(b)
260
200
150
100
50
0
Shear stress (τ) g/mm²
θS
C710 Dislocated, 1.0μm
Cr plate
θT
θI
0 1 2 3 4 5 6 7
Shear strain (γ) × 0.01

In all crystals which displayed a yield point it was noticed that such yield points were not very sharp. A typical example is shown in Fig. 4.14a, where, in the exploded diagram, the yielding region is very definitely curved very close to the yield drop. Any deviation from linearity of the elastic line can normally be taken to arise from pre-macroscopic yielding of a crystal due to dislocation motion. For example, the plethora of papers by Young[4,19,22,23,24] et al and other workers [20,25,26,27,28] on low dislocation density copper single crystals showed unequivocally that dislocations can glide at resolved shear stresses as low as 1.5 g/mm^2. In this work, however, dislocation motion at such stress levels has not been monitored by synchrotron topography (to be shown later) for a chromium plated dislocation-free crystal. For a dislocated crystal, evidence accrued from the Instron, Fig. 4.12b and Fig. 4.13b, did support this earlier work that dislocation motion could occur at low stresses below the normally recognised 'yield-knee', i.e. a gradual but definite change of stress-strain gradient between the elastic slope and the stage I part of the deformation curve. Note that in Fig. 4.14b the stress-strain curve was not linear at the start of the elastic region and neither was it linear at the end of the elastic region where a 'yield plateau' occurred. The absence of a yield point and the presence of these two curves indicates first that the crystal was dislocated and second that such dislocations moved prior to the large scale dislocation motion normally associated with macroscopic yielding.

For a dislocation-free crystal both these curves were not present: only the pre-yield curve was. Since the specimens possessed a variable cross sectional area, and since surface irregularities could lead to inhomogeneous yielding a curved pre-yield section is not unexpected.

The magnitude of the yield point was not comparable to either the theoretically calculable value[29] ($\approx$120 kg/mm^2) or the experimentally measured value[30] ($\approx$64 kg/mm^2) on copper whiskers by Brenner and others[31], for any crystal tested. Typically averaged values for the upper yield points in non-plated, 5 seconds plated and 10 seconds plated crystals were 53.7 $\mp$23.1 g/mm^2, 55.1 $\mp$6.4 g/mm^2, and 83.4 $\mp$5.0 g/mm^2 respectively. (All values taken from Table 5.1 and the non-plated values include Kamada and Tanner's[10] results) Shetty[32] has shown that for whisker crystals the upper yield stress, τ, does conform to the following empirical relationship:-

$$\underset{(kg/mm^2)}{\tau} = \frac{\alpha}{d} + \beta \qquad 4.17$$

Where, α, β are constants between 300-400 and 16-36 respectively

d is the diameter of the crystal in μm

Assuming that d = 10^3 μm the best value of τ that can be hoped for from these crystals assuming Shetty's work is applicable here is $\approx 9.1 \times 10^{-3}$ μ ($\mu \approx 4000$ kg/mm^2 [32]) and the worst value of τ would be $\approx 4 \times 10^{-3}$ μ. The crystals tested here had, at best, a value of τ of 2×10^{-5} μ. The factor of approximately 200 difference between these results could be explained by introducing an atomic surface source model of dislocation generation and gross stress concentration factors associated with the same. But as will now be shown other effects would have been expected if surface sources had been operating.

Viewed overall, the plating did not markedly affect the potential yield stress attainable by a non-plated crystal: Kamada and Tanner[10] achieved a best upper yield stress of 92 g/mm^2 with their non-plated crystals, whereas the best achieved here for a 10 seconds plated crystal was 89.6 g/mm^2 (Table 4.1). When averaged, however, the upper yield stress results did show a trend: the effect of the plated layer was to consolidate the values derived so that the certainty in the expected result from a crystal increased, e.g. the upper yield stress for a non-plated crystal was 53.7$\bar{+}$23 g/mm^2; for a 10 seconds plated crystal this was 83.4$\bar{+}$5.0 g/mm^2. The surface layer therefore had the effect of influencing the yielding behaviour of the crystals so that they yielded in a much more reproducible manner, but no definite increase in yield stress was noticed over and above that already measured for other dislocation-free copper crystals.

Surface corrugations arising from the growth of the crystals, as shown in Chapter I (Fig. 1.8), could have acted as stress concentrators during these Instron experiments. Even after the electropolishing prior to the chromium plating the surface was still ridged. The base radius of one of these ridges was estimated to be (from optical profile pictures taken on the Reichert optical microscope) approximately 0.25 mm. Hence, the normal longitudinal stress, σ_{Az}, would be locally raised by 1.18[33] which could not account for all the average yield stress difference monitored between say a non-plated and 10 seconds plated crystal, but it could account for the yield stress difference between the best non-plated and the best 10 seconds plated values.

Fig. 4.14 Parts of the Stress-strain Curves from Fig. 4.12 over the Region 0-1% Strain

Plating thickness = 0.5 μm

a. Dislocation-free
The yield point was non-sharp, which indicates non-homogeneous yielding. Serrated plastic flow was also observed

b. Dislocated crystal
The elastic "line" was curved which was a good indication of dislocation movement before macroscopic yielding. No definite yield point was registered. No serrated flow was monitored

α = residual plating stress on the glide planes (primary)

β = residual plating strain on the primary glide planes

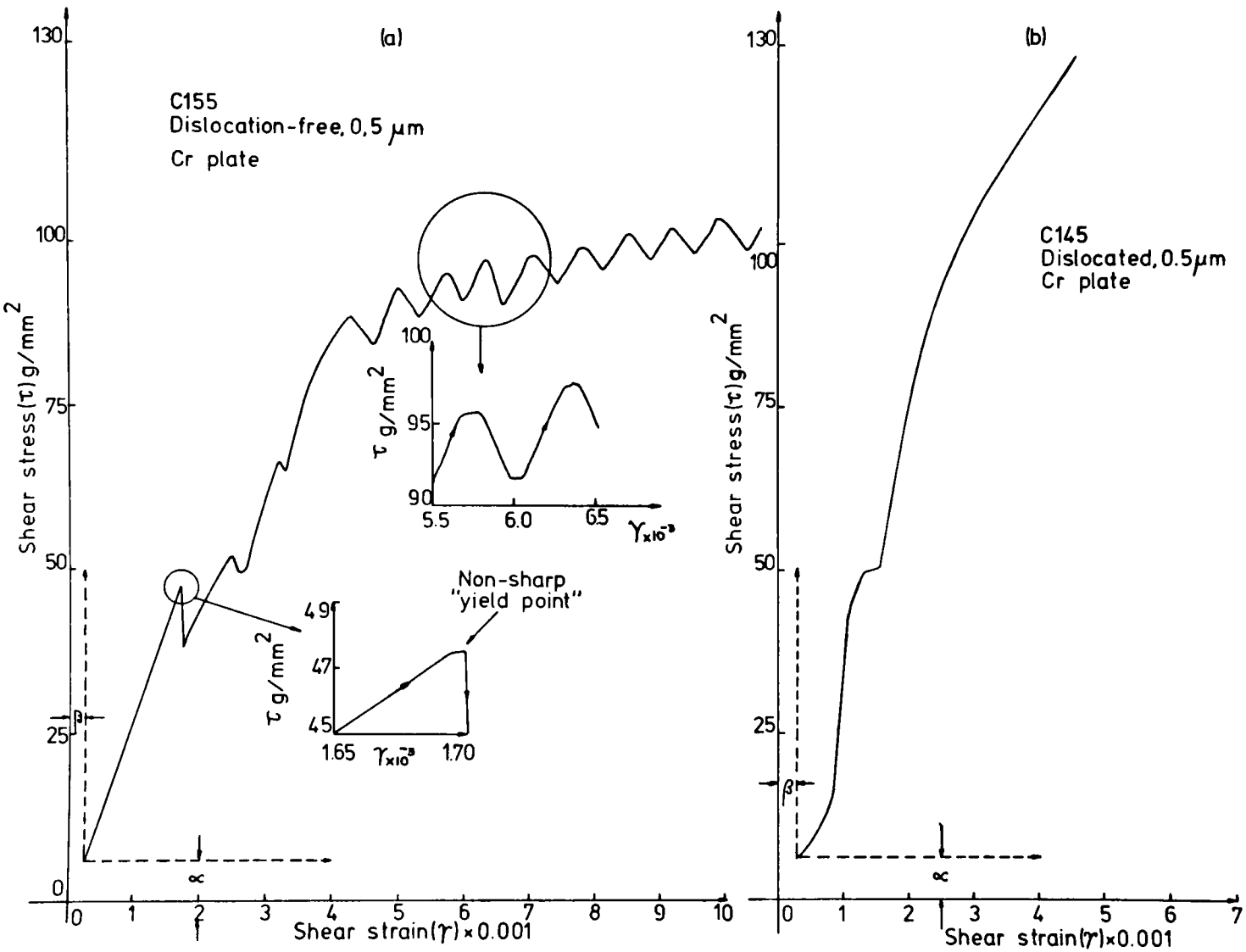

(a)
C155
Dislocation-free, 0,5 μm
Cr plate
Shear stress(τ) g/mm²
Shear strain(γ)×0.001
Non-sharp
"yield point"
τ g/mm²
β
∝
(b)
C145
Dislocated, 0.5μm
Cr plate

Fig. 4.15 Parts of the Stress-strain Curves from Fig. 4.13 over the Region 0-1% Strain

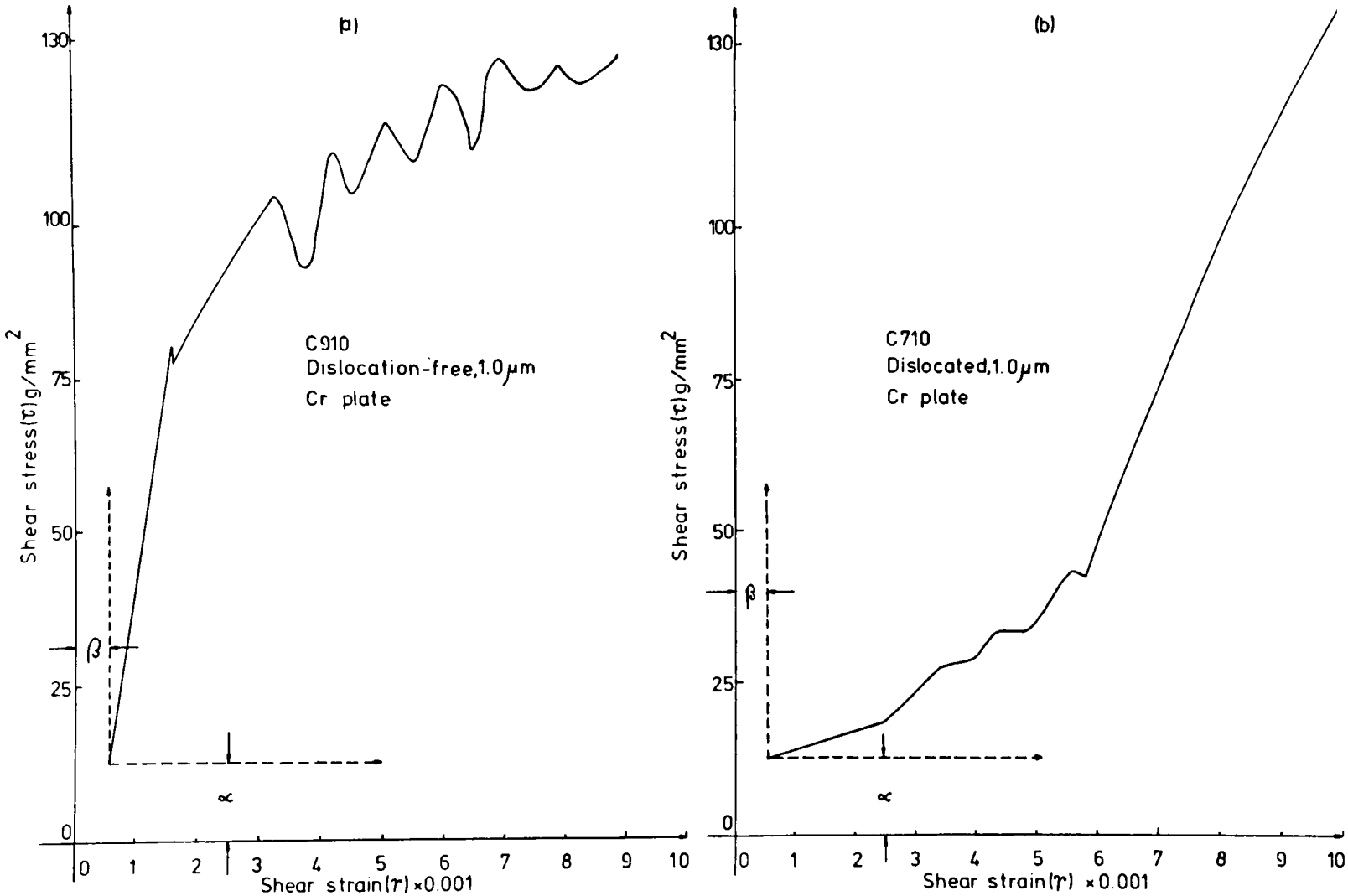
Plating thickness = 1.0 μm

a. Dislocation-free
Note the yield point and the serrated plastic flow

b. Dislocated
No yield point was observed and the elastic "line" was definitely non-linear. No serrated flow was recorded either.

α = residual stress on glide planes from plating

β = residual strain on glide planes from plating


(a)
C910
Dislocation-free, 1.0μm
Cr plate
Shear stress(τ) g/mm²
Shear strain(γ) ×0.001
β
α
(b)
C710
Dislocated, 1.0μm
Cr plate
Shear stress(τ) g/mm²
Shear strain(γ) ×0.001
β
α

Overall specimen geometry could also impose stress concentrations on the gauge length at the junction of the gauge length and the shoulders. Such a concentration factor is estimated to be ≈ 1.12[33]. Again this could not account for the yield stress differences noted in the results. The combined effect of a ridge and a shoulder together at the junction of the gauge length and shoulder would produce a stress concentration factor of 1.32, which would begin to explain the discrepancy in results between the 5 seconds plated and 10 seconds plated crystals but then not convincingly.

The final stress concentrator to consider is the junction between the end of the araldite film in the deformation-cup and the crystal surface. According to Friedel's[34] analysis, such a stress concentration factor is given by $(D/R)^{\frac{1}{2}}$, where D is the film thickness and R is the radius of the end of the film. Obviously, this quantity will vary from specimen to specimen but it is estimated to cover the range 1.5 to 3.0. It is felt that the discrepancy between the results can be attributed to this factor, because not only would it explain the internal variation of Kamada and Tanner's results where the yield stress covered the range 24-92 g/mm^2, but it would also explain the difference in yield stress values for the 5 seconds and 10 seconds plated crystals. In the case of the 10 seconds plated crystals the thicker chromium shell would accommodate a greater proportion of the stress concentration than in the thinner 5 seconds plated chromium shell. Accordingly the yield stress measured over a number of specimens would not be so variable in the 10 seconds case as for the 5 seconds, and this is borne out by the results in Table 4.1.

Consequently, plating a dislocation-free copper crystal with chromium for up to 10 seconds does not raise the yield stress of that crystal. All that happens is that the crystal is less susceptible to mounting problems. Such a conclusion therefore apparently invalidates the concept of an inherent surface source mechanism being the means of yielding in these crystals.

Consider the case of a Frank-Read source. It has been shown that[35] for a Frank-Read source deep within the crystal the source operation stress is given by:-

$$\tau_{F-R} = \alpha \frac{\mu b}{L} \qquad 4.18$$

Where,

τ_{F-R} = Source operation stress

μ = shear modulus of the matrix in which the dislocation of Burger's vector b is sited

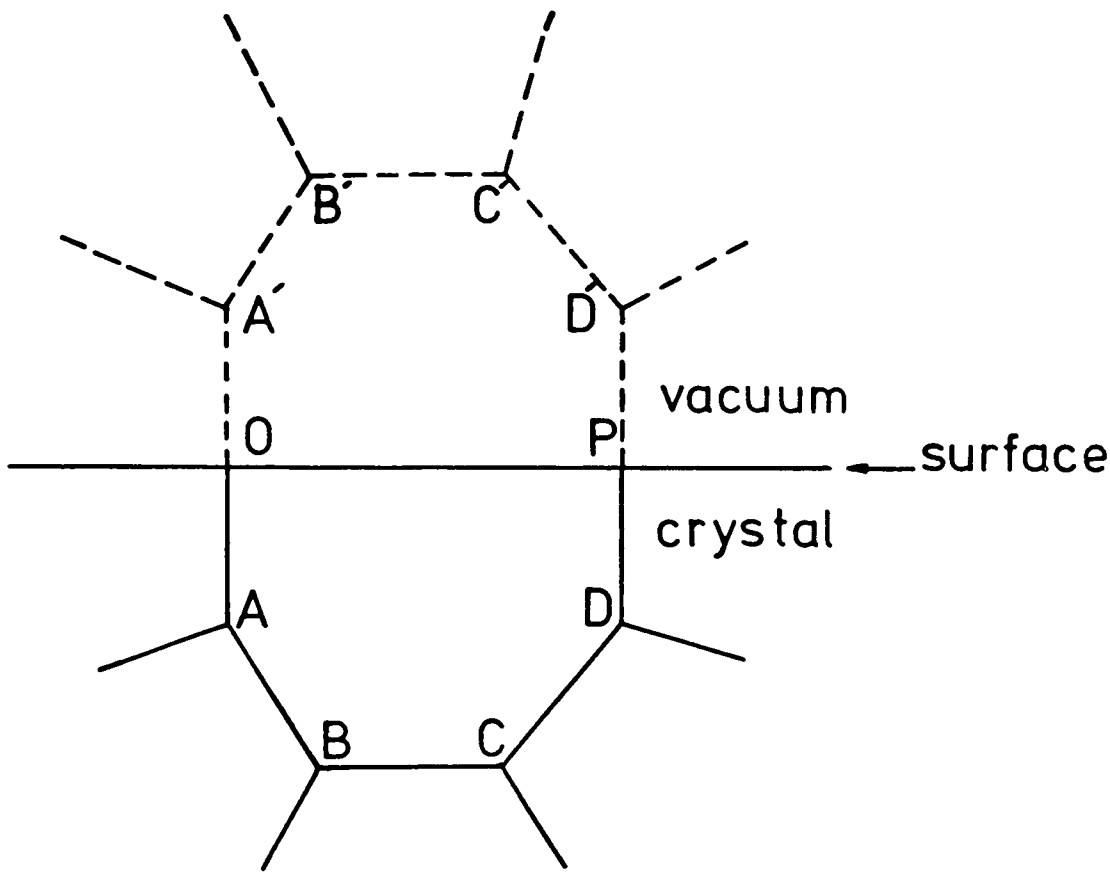
L = Source length

α = Constant between 1 and 1.3

If the Frank-Read source resides at the surface of a non-plated crystal as a half loop, then such an operation stress falls by a factor of 2, because the image of the loop outside the crystal effectively increases L by a factor of 2[36]. This is clearly shown in Fig. 4.16. If now the crystal containing such Frank-Read surface sources is electroplated, the image effects are destroyed (depending on the plating thickness and the shear moduli of the two materials) and the source operation stress once again assumes the value for the internal source of the same diameter. Thus, in a supposedly dislocation-free crystal which contained inherent surface sources of this type the yield stress (source operation stress) should be increased by a factor of approximately 2 if the image effect were destroyed by plating. A non-plated crystal is known to have, at best, a

Fig. 4.16 A Model for a Surface Dislocation Source

The operation stress of a Frank-Read source situated at the surface of a crystal is half of that for an internal source of the same size. This arises from image effects, since the effective source length is now A^1A and not OA


B
C
A
D
vacuum
O
P
surface
crystal
A
D
B
C

yield stress of about 92 g/mm^2 [10] which implies a source size, L, (calculated from 4.18) of approximately 9 μm ($b = \frac{a}{2}[110]$, $\alpha = 1$, $\mu \approx 4000$ kg/mm^2, $a = 3.6153$Å = lattice parameter of copper). In an X-ray topograph, therefore, these sources should be easily visible. Additionally, the yield stress of a 10 seconds plated crystal was, at best, 89.6 g/mm^2. The loops were not visible in an X-ray topograph and the yield stress of a plated crystal did not increase by a factor of about 2: therefore, inherent surface sources of this type were not, arguably, present in these crystals.

These results and conclusions are in disagreement with the particular results of other workers studying the effect of surface treatments on yield and flow stresses. For example, it has been demonstrated that a thin oxide film ($\approx$1200 atoms thick) could raise the measurable yield stress of a cadmium crystal by $2\frac{1}{2}$ times[37]; of a zinc crystal by a factor of ≈ 2[38]; and of aluminium by ≈ 2.3[39]. When metal single crystals were plated with other metals to approximately 1 μm in thickness, it was found that nickel on copper did not affect the yield stress of the copper[2] appreciably but a layer of 1 μm of chromium on top of the nickel increased the yield stress of the copper by 2[(2)]; silver and nickel on aluminium increased the yield stress of the aluminium by 1.27 and 1.59 respectively[40]; and chromium increased the yield stress of a copper crystal by about a factor of 2[41].

In other experiments it has been found that surface contamination increased the yield stress of silver crystals only slightly[42] but greatly increased the flow stress. Rosi[43],

using silver on copper found no large increase in the yield stress of the copper; yet when the silver was diffused into the copper to a depth of 3×10^{-2} cm (the specimen was 0.952 cm thick) the yield stress increased by 50%. The result of Harper and Cottrell[38] noted previously was found to be strain rate sensitive, which led them to conclude that the hardening effect was dynamical, involving dislocation pile-ups rather than being a surface source inhibition mechanism.

Clearly, a number of hardening mechanisms can exist and these can be reduced to six main types:-

i. Surface soure blocking[36]

Here, surface sources suffer anomalously high operation stresses because of the layer on the surface as already mentioned.

ii. Image forces[44]

A dislocation approaching an interface at which the shear modulus is discontinuous can either be attracted to or repelled by that interface. Alternatively the interface can exert no influence on the dislocation.

iii. Surface damage zone[45]

The surface layer locally modifies the surface dislocation structure, so that a hard crystal shell can surround a soft core which leads to strengthening.

iv. Film reinforcing[46]

A crystal with an adherent surface layer is essentially a composite material and therefore should be analysed as such.

v. Surface barrier to egression of dislocations[47]

The surface actually physically prevents dislocations from slipping out to the surface.

vi. Plastic constraint[48]

The substrate is surrounded by a layer of plastic incompatibility which gives rise to hardening.

In a truly dislocation-free crystal none of these mechanisms should be operative. Each has been used to varying extents to explain experimental results but not one appears to be fundamental enough to explain all results. The prime difference between this investigation and all others is that these crystals were, based on accumulated evidence, dislocation-free, whereas the other crystals studied were all Bridgman grown containing appreciable dislocation densities $\approx 10^6/cm^2$. Each of the above strengthening mechanisms is therefore instrumental in accounting for the observed results of other workers, but for these crystals only the film reinforcing[46] mechanism should be at all useful. Unfortunately this too appears to be redundant, because as noted by Brame and Evans[46] for a thin film (as used here) the film strength and substrate strength cannot be compounded to produce the total strength since this would make the film strength impossibly large. Moreover, since no real yield stress increase was recorded here this mechanism can also be neglected.

These crystals could have yielded as a direct result of internal source activation, because this is one method by which the crystals could have remained unaffected by the surface layer at yielding, and yet have been markedly influenced by such a layer during plastic flow. If such sources were even 9 μm in diameter, i.e. loops, and lay <u>deep</u> within the crystal (not near to the surface) it is arguable that they should have been detected in these crystals by Lang-Borrmann topography. Furthermore, only a small loop density is required to cause the effects noted here as will now be shown.

Let the imposed strain rate on the crystal be $\dot{\gamma}$; the velocity required by the dislocations to maintain such a strain rate be $\dot{x}$; the Burger's vector of the dislocations be b; and the dislocation density be N. It can be shown that[49] $\dot{\gamma}$ is related to the other parameters through the expression:-

$$\dot{\gamma} = Nb\dot{x} \qquad 4.20$$

To obtain an order of magnitude for N set $\dot{\gamma} = 10^{-4}s^{-1}$, b = $3.6153/\sqrt{2} \times 10^{-8}$ cm and $\dot{x} \approx 10^{4}$cm/sec[50] whence N ≈ 0.391 cm^{-2}. Assuming a loop diameter of 9 μm this renders a value for the loop density of only 69 cm^{-3}. Since these crystals possess a volume of $\approx 1.35 \times 10^{-2}$cm^{-3} this implies that only one glissile internal loop is required per crystal to account for the imposed strain rate straight after yielding.

It is noticed from Table 4.1 that the % yield drop decreased by a factor of 2 when the plating thickness increased by approximately two, but the absolute magnitude of the yield drop did not markedly change between the two sets of plated crystals. This result indicates that even though the defect distribution in the crystals was undetectable it was of like density in both cases because the yield drop gives a reliable indication of the number of activated, glissile dislocations in the crystal.

4.4iii.b <u>The Work Hardening Region</u>

Viewed in entirety, e.g. Fig. 4.12a, the work hardening curve of a plated, dislocation-free crystal can be compartmentalised into three distinct regions up to the measured shear strain of 6%:-

i. An initial rapid work hardening curve of average gradient Θ_I

ii. A transitionary curve of average gradient Θ_T

iii. A stabilised curve of average gradient Θ_S

In going from region i to iii the work hardening rate progressively decreased, e.g. from Table 4.1 it is seen that the three work hardening rates for a 5 seconds plated crystal are averaged to be 19.32 kg/mm^2(Θ_I), 2.46 kg/mm^2(Θ_T) and 1.65 kg/mm^2(Θ_S); for these same regions the extent of plasticity was 0.17% to 0.34%, 0.34% to 1.47% and 1.47% to 6% respectively.

Compared to dislocation-free non-plated crystals these work hardening rates are far in excess of any measured by the author (refer to Table 4.1 and Fig. 4.14a, for example) or by Kamada and Tanner[10]. Typically, the immediate post yield work hardening rate was $\approx$300-900 g/mm^2 for such crystals, i.e. during easy glide.

The work hardening rate results for a 10 seconds plated dislocation-free crystal, Fig. 4.13a, showed the same general trends as the 5 seconds plated crystals, i.e. an initially rapid rate of work hardening ($\Theta_I \approx 18$ kg/mm^2), followed by a transitionary region ($\Theta_T \approx 5.69$ kg/mm^2), and then a stabilised region ($\Theta_S \approx 2.97$ kg/mm^2). The shear strain extent of these regions in percentages was very similar to those for a 5 seconds plated crystal, i.e. 0.16% to 0.37% (region i), 0.37% to 1.5% (region ii) and 1.5% to 6% (region iii). These first two work hardening rates were greater than any measured previously during deformation up to a 6% shear strain on originally low

dislocation density copper crystals. Young's[22] work, for instance, rendered a maximum value for the post yield work hardening rate of $\approx$2800 g/mm^2 and similar results were found by Diehl[3]. Whilst the work final work hardening rate of the 5 seconds plated crystals ($\theta_s \approx 1.65$ kg/mm^2) and 10 seconds plated crystals commensurate with the work hardening rates ($\approx$1000 g/mm^2 to 2800 g/mm^2) measured by Young[22], the initial and transitionary rates were well above Young's values and Diehl's.

Considering a 10 seconds plated crystal, therefore, it is erroneous to term the initial part of the work hardening curve up to 6% shear strain as being an 'easy-glide' region, since the work hardening rates recorded were not commensurate with those normally associated with this phenomenon. In the case of a 5 seconds plated crystal the first two regions of work hardening can again be considered in the same way as the 10 seconds plated crystals: the stabilised region exhibited a work hardening rate similar to that for other crystals and the 'easy-glide' concept is therefore tentatively valid.

It is interesting to observe that the initial work hardening rate was only slightly dependent on chromium thickness, but the ratios of the transitionary and stabilised work hardening rates for 10 seconds and 5 seconds plated crystals were 2.3:1 and 1.8:1 respectively.

As shown clearly in Figs. 4.12b and 4.13b, depicting the stress-strain curves from two typical plated, but originally dislocated crystals, the only major feature which is absent is the yield point when compared to Figs. 4.12a and 4.13a. All

other features are similar when viewed on this scale, and the ratios of the work hardening rates for 5 seconds and 10 seconds plated dislocated crystals remained approximately the same as for the plated but originally dislocation-free crystals. The only real anomaly arose with the initial work hardening rate of crystal C145" as shown in Fig. 4.12b where it was 59.2 kg/mm^2. This result was associated with a crystal which exhibited a yield plateau, and since Θ_I was comparable to the slope of the elastic line it could be argued that the plateau corresponded to a yield source being activated, but then being quickly suppressed (hence no yield drop). If the source was very close to the surface it would quickly experience a back stress (from dislocation pile-up) which would make it passive and the crystal would then behave "elastically" again until other sources operated; or, the pile-up was diluted by dislocation loss to the chromium-copper interface, the chromium or, the free surface. These possibilities will be treated in depth later.

By plotting the stress-strain curves of these crystals up to 6% shear strain much fine detail is lost of the very early stages of work hardening. Consequently, the two typical curves in Figs. 4.12a and 4.13a have been replotted in Figs. 4.14a and 4.15a respectively up to a 1% shear strain to reveal this early fine structure in the work hardening behaviour. To take Figs. 4.14a and 4.15a together it is clear that there is a definite serration of plastic flow in region ii of a 10 seconds plated crystal, and in regions i and ii of a 5 seconds plated crystal. These serrations gave every indication of being reasonably periodic as shown in Figs. 4.15a and 4.14a: with a

magnitude of oscillation of about 15 g/mm^2 and a strain range of approximately 0.09% for region ii of a 10 seconds plated crystal; and a magnitude of oscillation of 4.5 g/mm^2 and a strain range of about 0.06% for a 5 seconds plated crystal in region ii. For region i of a 5 seconds plated crystal the magnitude of oscillation was $\approx$1.5-2.5 g/mm^2 and the strain range was $\approx$0.02-0.03%. The magnitude of the yield drop was comparable to the serration height which suggests that the serrations are connected with new source operation. Kamada and Tanner[10] observed a similar effect in their crystals during the immediate post yield region and argued that this was caused by Lüder's band propagation. These serrations were noticed for all plated, dislocation-free crystals but never for a plated dislocated crystal nor for a non-plated dislocation-free crystal as shown in Figs. 4.14b and 4.15b.

As such, therefore, this effect is considered to be real and the results derived from the two plated, dislocation-free crystals show that the plating thickness affected this behaviour. Other workers have not mentioned such an effect in the literature on single crystals and it is therefore considered to be a property peculiar to dislocation-free plated crystals which is dependent on chromium thickness, i.e. magnitude of stress oscillation was 3.3:1 (10":5") and the % strain range was 1.5:1 (10":5"). This effect will also be discussed in a little more detail once the synchrotron work has been presented.

4.5 Microscopic Deformation Studies in the Synchrotron

4.5i Reasons for Using the Synchrotron

The behaviour of the crystals outlined in Section 4.4 can be explained using a number of models, e.g. dislocation pile-up and surface layer cracking models. However, a deeper understanding of the recorded behaviour can be produced by probing the lattice strain in the crystal during deformation by using X-ray diffraction topography. Then, it is potentially easier to analyse the contribution of each model to the features of the stress-strain curves observed.

In the Oxford Laboratory these plated dislocation-free copper crystals could be topographed in approximately 5 to 8 hours (depending on specimen diameter) using $M_{oK\alpha_1}$ from an Elliot GX6 rotating anode X-ray set operating at 50kV and 35mA. Thus, any attempt to record the deformation of such crystals on the Oxford Lang Cameras would take an inordinately long time. Furthermore, during such long exposure times dislocation stability could not be guaranteed because of vibrations induced into the specimen by the traverse mechanism. Finally, as shown by Kamada and Tanner[10], once yielding is initiated in these crystals X-ray transmission through the yielded region is insignificant and, as shown by Young et al[19], any hope of detecting single dislocation movement inside the slip bands is minimal due to the density of dislocations in such bands. Kamada and Tanner's[10] work therefore shows that for these crystals yielding is a catastrophic process, although being discontinuous, and so only large area contrast differences can

be reliably analysed. Whereas Young and Sherrill[19] took the usefulness of X-ray topography in this field one step further and derived some information from the edges of slip bands, e.g. dislocation cross-slip. To make this X-ray diffraction study scientifically worthwhile a definite need arose to use a much more intense source of X-rays than the Oxford Laboratory source could provide: the synchrotron X-ray source admirably fulfilled this need.

It has been known for many years that when a charged particle is accelerated it can shed energy along all parts of the electromagnetic spectrum[51]. It has been further shown[51] that for a synchrotron such radiated energy intensity is proportional to $(E/M_o)^4$, where E is the energy of the particle and M_o its rest mass. As a result it turns out that this crystallographically useful radiation is only strong for electron synchrotrons since the inverse mass term greatly decreases the radiated intensity from proton synchrotrons. In addition the peak of the continuous distribution of wavelengths produced moves to shorter wavelengths as the energy of the electron increases, and at relativistic energies this peak lies in the X-ray region of the spectrum. Another important property of this radiated energy is that it is directed into a narrow cone of angle $\theta \approx M_o c^2/E$, where c is the vacuum velocity of light, in the forward direction, Fig. 4.17; consequently, the radiation is highly collimated when E is large.

For the British Electron Synchrotron (NINA) situated at Daresbury, typical curves of intensity versus wavelength and intensity versus angular divergence out of the electron plane for a given wavelength are shown in Fig. 4.18a and Fig. 4.18b

Fig. 4.17 Synchrotron Topography Schematically

An electron accelerated at relativistic energies radiates energy which can be strong in the X-ray region. By placing a crystal in the incident beam a Laue pattern can be recorded on a photographic plate. Since the complete crystal can be irradiated, each reflection contains the whole crystal and the defects visible for that particular g-vector

R = Radius of electron orbit

Θ = Angular divergence of the beam

E = Energy of the electron beam

m_o = Rest mass of the electron

C = Velocity of light

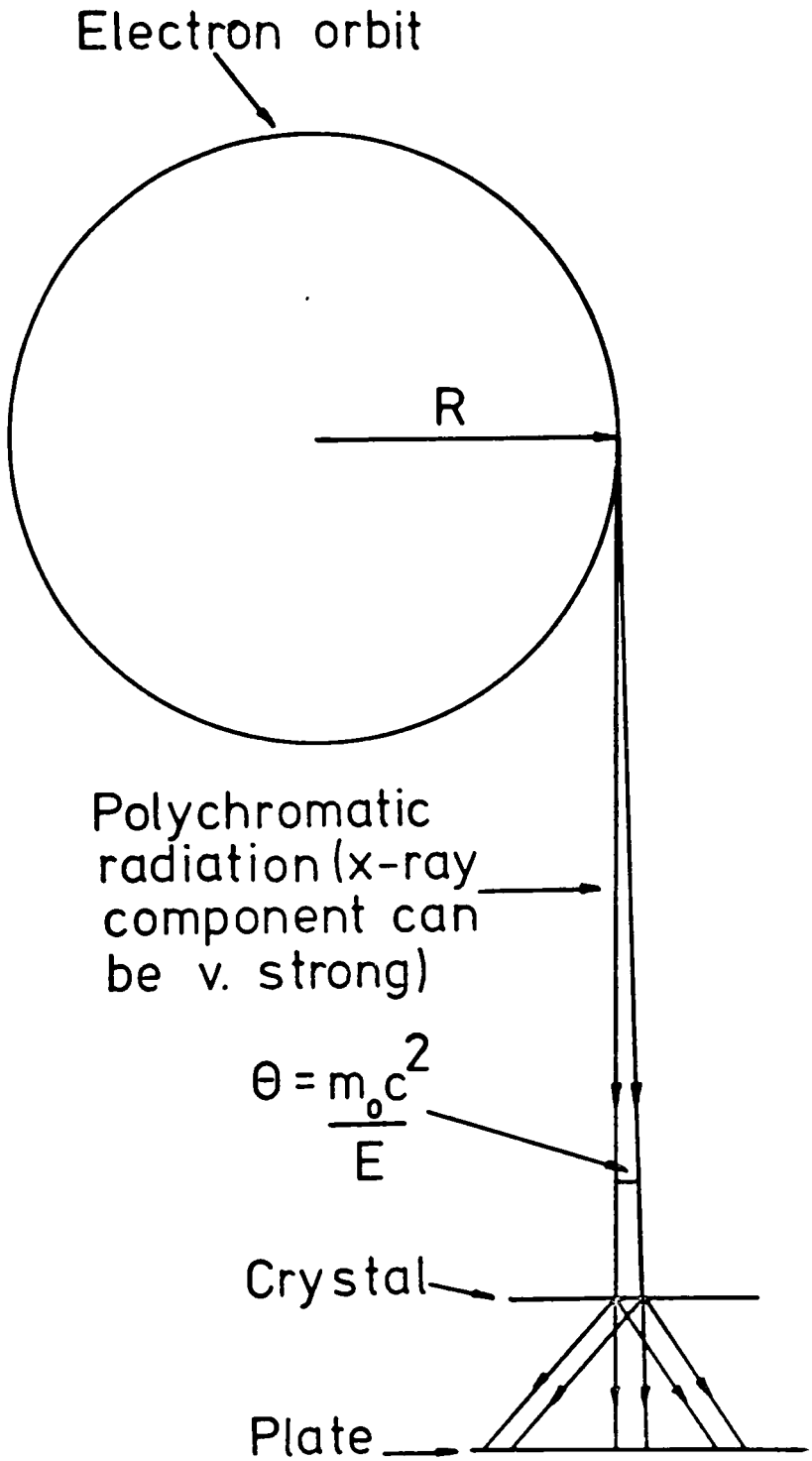
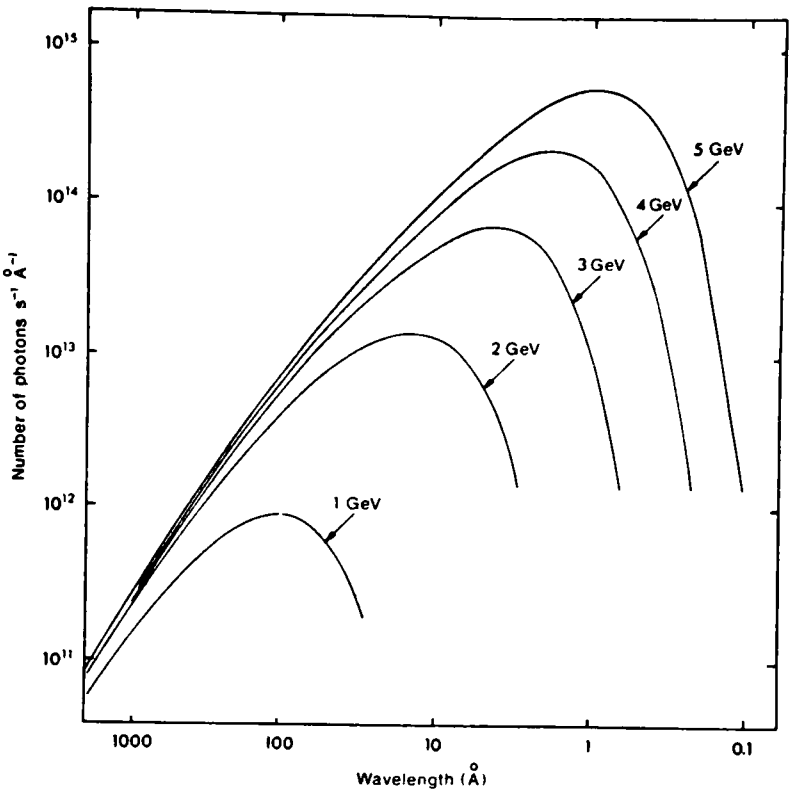

Electron orbit
R
Polychromatic radiation (x-ray component can be v. strong)
$\theta = \frac{m_0 c^2}{E}$
Crystal
Plate

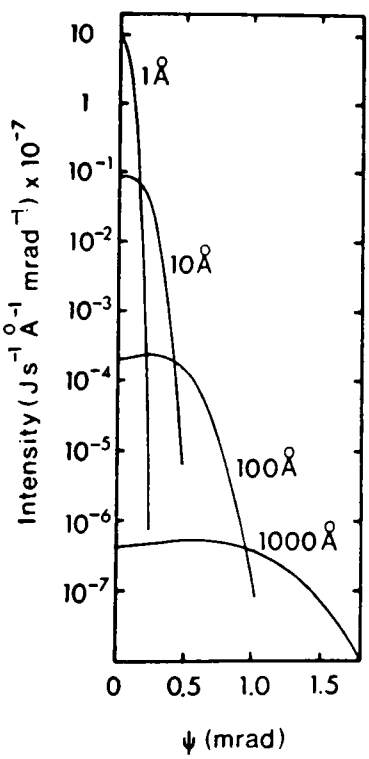
Fig. 4.18 Characteristics of Synchrotron Radiation

a. Intensity versus wavelength curves

b. Intensity versus angular divergence out of the orbital plane for a given wavelength



The intensity output from NINA versus wavelength for a monoenergetic electron.



The intensity output with respect to angular elevation for varying wavelengths, assuming a monoenergetic electron of energy 4 GeV and a circular orbit of radius 20·77 m.

respectively. It is seen that at 5GeV and 0.7Å ($\equiv M_{oK\alpha_1}$) that the divergence of the incident beam is $\approx 3 \times 10^{-4}$ radians. Also, as first shown in a simple investigation of synchrotron radiation for X-ray topography purposes by Tuomi et al[52] and later by Hart[53] for NINA the increase in X-ray flux for a given wavelength ($\approx$0.7Å) is approximately 1000x greater than a rotating anode source. Therefore, expected exposure times for these copper crystals would be $\approx$30 seconds.

Since the incident beam is composed of a well collimated, continuous distribution of wavelengths a complete Laue pattern of the crystal should be obtained in the forward direction under favourable absorption conditions; and, because the main beam can irradiate the complete crystal entrance surface, each Laue spot should be a record of the whole crystal and its observable defect distribution for that reflection. This was first conclusively proved by Tuomi et al[52], and is shown for a typical crystal studied in this work in Fig. 4.19 using the simple experimental arrangement illustrated in Fig. 4.17. In this basic format synchrotron topography is therefore analogous to the now little used Guinier and Tennevin[54] transmission technique, using white radiation.

The resolution of the technique is at least as good as in the Lang technique as shown by Hart[53], and when using a specimen to source distance of 47 m (source size $\approx$0.5 mm x 0.5 mm[53,55]) and a specimen to film distance of 10 cm, this resolution is $\approx$1 μm in both the vertical and horizontal directions.

Fig. 4.19 A Typical Synchrotron X-ray Laue Pattern

The picture depicts a forward diffracted Laue pattern of a copper crystal with a <110> growth axis (horizontal in this picture). The very dark centre arises from the influence of the main beam on the X-ray plate



The accumulated literature therefore gave every indication that synchrotron topography could be usefully employed to study the deformation of these crystals: because the exposure times were short; the resolution good; and the apparatus simple.

4.5ii Specimen Transport

Transporting these crystals the 160 miles from Oxford to Daresbury was an initial problem because of the very low yield stresses needed to dislocate the lattice and the intransit vibrations! This problem was, however, in most cases solved by immersing the crystal in a warm solution of 300 cm^3 of gelatine in a jar with a screw lid. The crystal was left hanging in the solution from its cotton until the gelatine had set (it turned opaque); and the screw top was then applied, with the cotton taken through a hole in this lid and then stuck down with tape to the top of the lid. The jar was then placed in a much larger plastic container (i.e. a chemical reagent carrier) which was filled with expanded polystyrene so that the jar and contents were completely surrounded by this vibration absorbing shell and medium. A screw top was applied to this container to keep the contents intact. The encased crystal was then kept as vertical as possible and transported by car to Daresbury.

4.5iii The Synchrotron Experimental Arrangement

At Daresbury the jar containing the crystal was immersed over $\frac{2}{3}$ of its length in hot water to melt the gelatine. At the same time the crystal was secured to a support from its cotton so that when the gelatine melted the crystal did not fall to the

bottom of the jar and so possibly dislocate. The free crystal was then washed very gently in water to remove excess molten gelatine solution and then left for half an hour to dry.

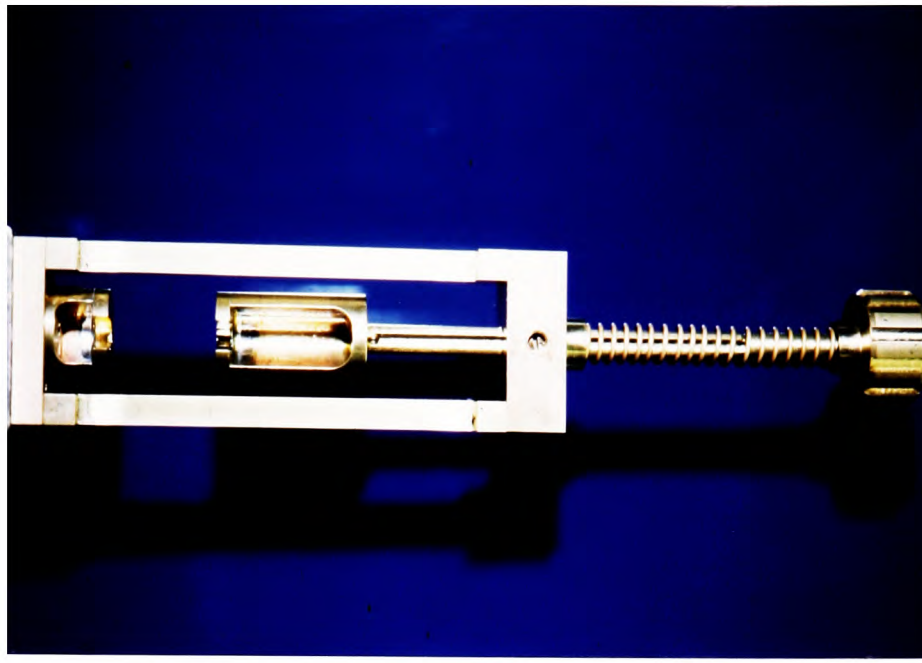
When dry the crystal was mounted in a deformation jig (Fig. 4.20a) similar in construction to Young's[19]. It consisted of two cut-away chucks, one of which could be translated along the common axis of the two by rotating a very finely threaded (40TPI) nut attached to its threaded end. The crystal could be loaded by screwing down this nut until it compressed a spring wound around this threaded end. Calibration measurements showed that one revolution of the nut applied a load of 40 g$\bar{+}$2 g to the crystal over the range 0 to 1000 g. As shown in Fig. 4.20a the jig was mounted on a standard laboratory goniometer to allow both specimen tilting to obtain desired reflections, and jig tilting to allow easier specimen insertion prior to X-ray exposure. Frequent cleaning and oiling of moving parts minimised frictional stresses.

Since synchrotron radiation is strongly polarised in the horizontal plane (reference to Fig. 4.18b shows the rapid decrease in short wavelength intensity as the observer moves out of this plane), it is to be expected that strong X-ray diffraction can only be produced for reflections which have g-vectors lying in a vertical circle parallel to the direction of the incident beam. In this work therefore the jig and crystal were rotated through 90^{o} so that the growth axis (and therefore the tensile axis) of the crystal was situated across the incident beam. This is shown in Fig. 4.20b and Fig. 4.20c. The position of the 111 g-vector had previously been determined in Oxford

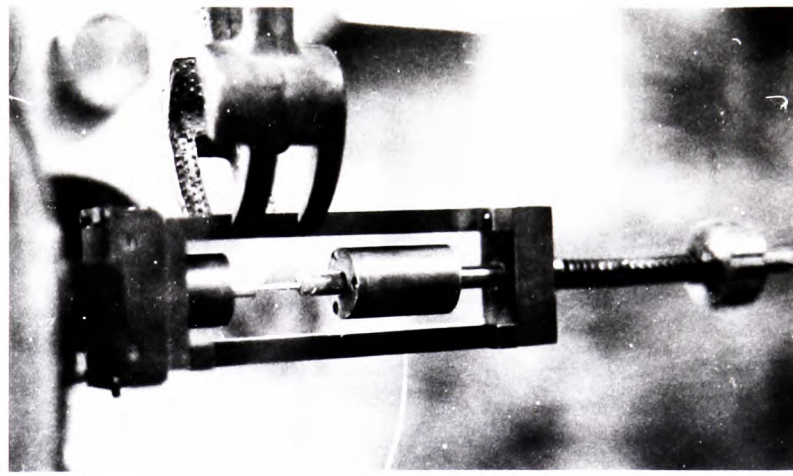
Fig. 4.20 The Synchrotron Experimental Arrangement

a. The deformation jig

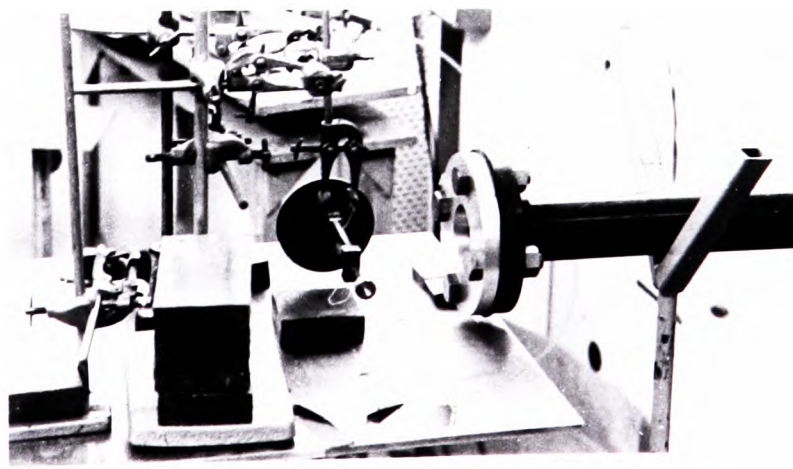
b, c. The deformation jig and a crystal set-up for study in the main synchrotron beam



(a)



(b)



(c)

by Laue work and a line corresponding to this direction was painted on the deformation-cups. This being the case it was easily possible to orient the crystal to diffract from the 111 planes in the copper using radiation of wavelength approximately equal to $M_{oK\alpha_1} \approx 0.7\text{Å}$.

The main beam exited from the polypropylene tube at the right hand side of Fig. 4.20b which was evacuated to reduce absorption losses by the air. This tube was not a part of the normal synchrotron radiation tube which ended another 10 m to the right of the picture. Because other equipment was clustered around this port it was impossible to set-up this experiment at the end of the beam line. Hence the use of the polypropylene tube. The diffracted radiation from the crystal was recorded on 2" x 2" Ilford L4 50 μm nuclear emulsion plates (not shown in Fig. 4.20b) placed perpendicular (as far as possible) to the 111 diffracted beam at a plate to specimen distance of 20 cm. Thus, only one reflection was recorded in the particular experiment to be described here; and, because the Bragg angle for this reflection was small ($\approx 9.7^{\circ}$), a larger than normal specimen to plate distance was necessary to separate the main transmitted and diffracted beams, so that only the diffracted beam was imaged. Therefore, main beam darkening of the emulsion was reduced. The plates were enclosed in lightight black plastic bags with the emulsion facing the beam.

Even though the main transmitted beam was eliminated from the plates fluorescence did prove to be a slight problem. To reduce this effect a very narrow main beam was used, sufficient only to irradiate the crystal and nothing else. Careful

positioning of the sample in the main beam was consequently important, and use was made of a spot laser to aid this positioning as follows. The spot laser was mounted in the main beam line but pointing in the opposite direction to the beam direction at a distance of approximately 15 m from the exit port. The port size was determined by two pairs of perpendicularly mounted thick lead shutters. The laser could be adjusted until the spot was travelling down the centre of the beam by using a screen stuck over the exit port. It was then a simple matter to adjust the specimen position on a moveable table to coincide with the spot and therefore to be in the centre of the main beam also.

The experiment to be discussed therefore took the following format:-

i. A known load was applied to the sample ($[\bar{1}\bar{2}3]$ tensile axis, dislocation free Cu, plated for 10" at 55C with Cr).

ii. An X-ray plate was positioned in the direction of the diffracted beam and perpendicular to it.

iii. The synchrotron was operating at 5.06 GeV and 18.1 mA and so an exposure time of just 30 seconds was used for each plate.

iv. Procedures i to iii were repeated up the stress-strain curve.

v. The plate processing technique discussed in Chapter III was used to develop the latent image, and the dried plates were finally optically reproduced in Oxford.

4.5iv An Analysis of the Wavelengths Contributing to the Recorded Diffraction Image

The incident beam is polychromatic and therefore although the crystal was set to diffract ≈ 0.7Å radiation from the 111 planes, a 222 reflection would also be expected using a ≈ 0.35Å wavelength, and a 333 reflection using 0.175Å radiation. The contribution of the first two wavelengths to the diffraction image will now be assessed: that due to the 0.175Å waves will be ignored for reasons soon to be made clear.

To calculate the % influence of each wavelength it is necessary to first calculate the anomalous absorption coefficient for each, noting that the electric vector is in the orbital plane of the accelerator[56] (i.e. horizontal) and that therefore the polarisation constant, C, is equal to unity. This is an important point because it means that the crystal transmitting in the Borrmann mode will be imaged with wavefields which have their tie-points on the same branch of the dispersion surface (i.e. branch 1) in both the Oxford and Daresbury experiments. Hence, no polarisation differences would be expected between images recorded at Oxford and at Daresbury. At Oxford, although the X-rays are non-polarised, the crystal acts as a highly efficient polariser by imposing a preferentially small absorption coefficient on the branch 1, σ-polarised wavefields (see Chapter III, Section 3.6iv). Table 4.2 gives the values of the anomalous absorption coefficients for the 0.7Å and 0.35Å waves.

Also considered in the calculations was the air absorption and the sensitivity of the L4 50 μm nuclear emulsion to the diffracted waves as first pointed out by Hart[53]. Taking

TABLE 4.2

hkl	111	222
Θ_B^o	9.653	9.653
$\lambda(A^o)$	0.7	0.35
F_{hkl}	80	54.7
$P(\lambda)$ (a) Photons $s^{-1}A^{o-1}$	6×10^{14}	9.5×10^{13}
$\mu_c(cm^{-1})$ (b)	6.08	2.34
$\mu_f(cm^{-1})$ (c)	138.6	25.67
$\mu_a(cm^{-1})$ (d)	10^{-3}	Effectively=0
t_c, t, t_f (cm)	0.1, 20, 5×10^{-3}	0.1, 20, 5×10^{-3}
$e^{-\mu_c t}$	0.544	0.790
$e^{-\mu_a t}$	0.98	1
$e^{-\mu_f t}$	0.500	0.879
${}_AI_F$ photons $s^{-1}A^2$	$1.592\times10^{17}(\pm100\%)$	$7.515\times10^{14}(\pm0.47\%)$

(a) Taken from Fig. 4.18a
(b) Calculation performed in same way as for Chapt.III, Sec.3.6i
(c) Taken from M. Hart's Ph.D. Thesis, University of Bristol, 1963 and the results extrapolated
(d) Taken from International Tables for Crystallography, 1962, accounting for λ.

into account all these factors it is possible to derive an expression to give a reliable indication of the intensity of each wavelength absorbed by the film, ${}_{A}I_{F}$ [52,53,57]:-

$$ {}_{A}I_{F} = \left(\frac{|F_{hkl}|\ P(\lambda)\lambda^3}{\mathrm{Sin}^2\Theta_B}\right) e^{-\mu_c t_c}.\ e^{-\mu_a t_a}.\ e^{-\mu_f t_f} \qquad 4.19 $$

Where,

$|F_{hkl}|$ = Magnitude of the structure factor for the reflection hkl

$P(\lambda)$ = Synchrotron intensity factor for the wavelength used, λ.

Θ_B = Bragg angle

μ_c, μ_a, μ_f = Absorption coefficients of the crystal, air and film respectively

t_c, t_a, t_f = Thickness of the crystal, air and film respectively

Table 4.2 shows the values chosen for each of the variables for each wavelength and also the results of the calculations. The not unexpected conclusion is that the image is made-up of predominantly 0.7Å radiation with the contribution from the 0.35Å X-rays being only 0.47%. Any contribution from shorter wavelengths can therefore be ignored. These calculations also show that to obtain a dense image in a short exposure time then not only must $P(\lambda)$ be large (therefore it is necessary to operate around the $P(\lambda)$-versus-λ peaks in Fig. 4.18a) but also the absorption coefficients of the crystal and film must be low and high respectively.

4.5v Synchrotron Results

4.5a The Non-loaded Crystal

Fig. 4.21a shows an X-ray topograph of the crystal in question just before it was mounted in gelatine and transported to Daresbury: it was dislocation-free according to this

Fig. 4.21 Synchrotron Topographs of a Crystal Strained along the [$1\bar{2}3$] axis originally

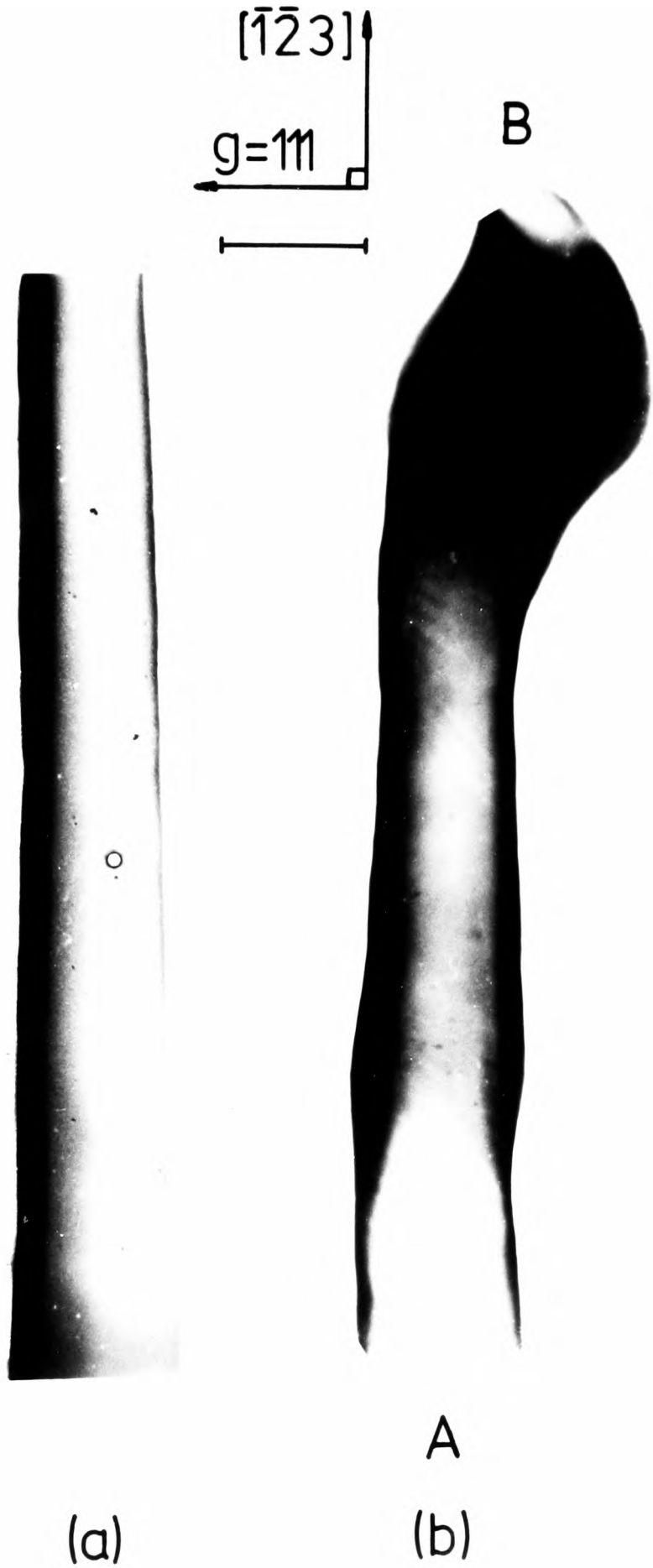
a. The non-loaded crystal topographed in Oxford using a standard X-ray source. No detectable dislocation contrast from plating for 10 seconds (1 μm thickness) was noticed.

b. The same crystal as in (a) topographed using synchrotron radiation. In transit deformation had occurred but the majority of the crystal remained dislocation-free. Non-loaded crystal again.

(Note the dislocated end at A and the asterism arising from lattice bending at B)

Residual stress on the primary glide planes from plating was ≈ 12.2 g/mm^2

Scale mark = 1 mm


[1̄2̄3]
g=111
B
A
(a)
(b)

picture but not, as noted previously, stress-free (the residual shear stress on the $(1\bar{1}1)$ glide plane was estimated to be ≈ 12.27 g/mm^2 as derived by the method in Section 4.4ii). In Fig. 4.21b is shown the same crystal topographed using the same reflecting planes (g = 111) as the Oxford topograph: it gives good evidence of the crystal being dislocation-free over a very large proportion of the gauge length. However, at one end (A) a reduction of anomalous transmission was noticed, while at the other end (B) a significant amount of reflection broadening had occurred. Both these effects can be attributed to deformation-cup influences; where, in the former case the crystal had been dislocated heavily because of the relative vibrations of the crystal and deformation-cup during transit (close examination shows that double slip was evident); and in the latter case the lattice has definitely been bent but not, it seems, heavily dislocated since the anomalous transmission was good. Towards this bent end images of slip bands corresponding to single slip are also visible with a spacing of ≈ 0.11 mm. From these projected traces of the slip bands and using the Thompson tetrahedron in Fig. 4.1b, it can be shown that the slip bands correspond to dislocation on the initially postulated primary slip plane, i.e. $(1\bar{1}1)$. Information about the slip direction cannot be gained. This crystal was therefore not wholly dislocation-free at the start of the deformation study, but as will be shown much useful information was nevertheless produced from the experiment.

Another interesting feature in Fig. 4.21b is the white line inside the bent region of the crystal. This line corresponds to a reduction of anomalous transmission and it is seen to

terminate at one end in the region of the interface between the copper and the chromium. This kind of contrast feature is indicative of an array of dislocations either in the surface of the copper; in the interface of the copper and the chromium (i.e. epitaxial dislocations); or in the chromium layer. Since it was not observed in Fig. 4.21a the epitaxial dislocations can be excluded from further enquiry. Further investigation of this line shows that it moves across the image as the asterism increases, as caused by an increase in the lattice-bending. Also, this white line traces a profile with the same shape as the reflection from the rear surface in this region. It is further observed that the reflection from the Bragg surface was straight until the very end of the image. From these three deductions it is possible to conclude that the lattice bending was a surface phenomenon restricted to the copper side of the copper-chromium interface, and that therefore the resultant dislocations giving rise to this white line reside in the surface of the copper. If the chromium too had been appreciably bent then the diffraction profile of the Bragg surface would not have been a line along the region considered.

To cause such asterism the lattice planes must have been bent in a concave fashion as shown in Fig. 4.22. Using Fig. 4.22 the bending strain Tan α is given by:-

$$\text{Tan}\alpha = \frac{\delta}{2L} \qquad 4.22$$

Where,

δ = image shift on the X-ray plate

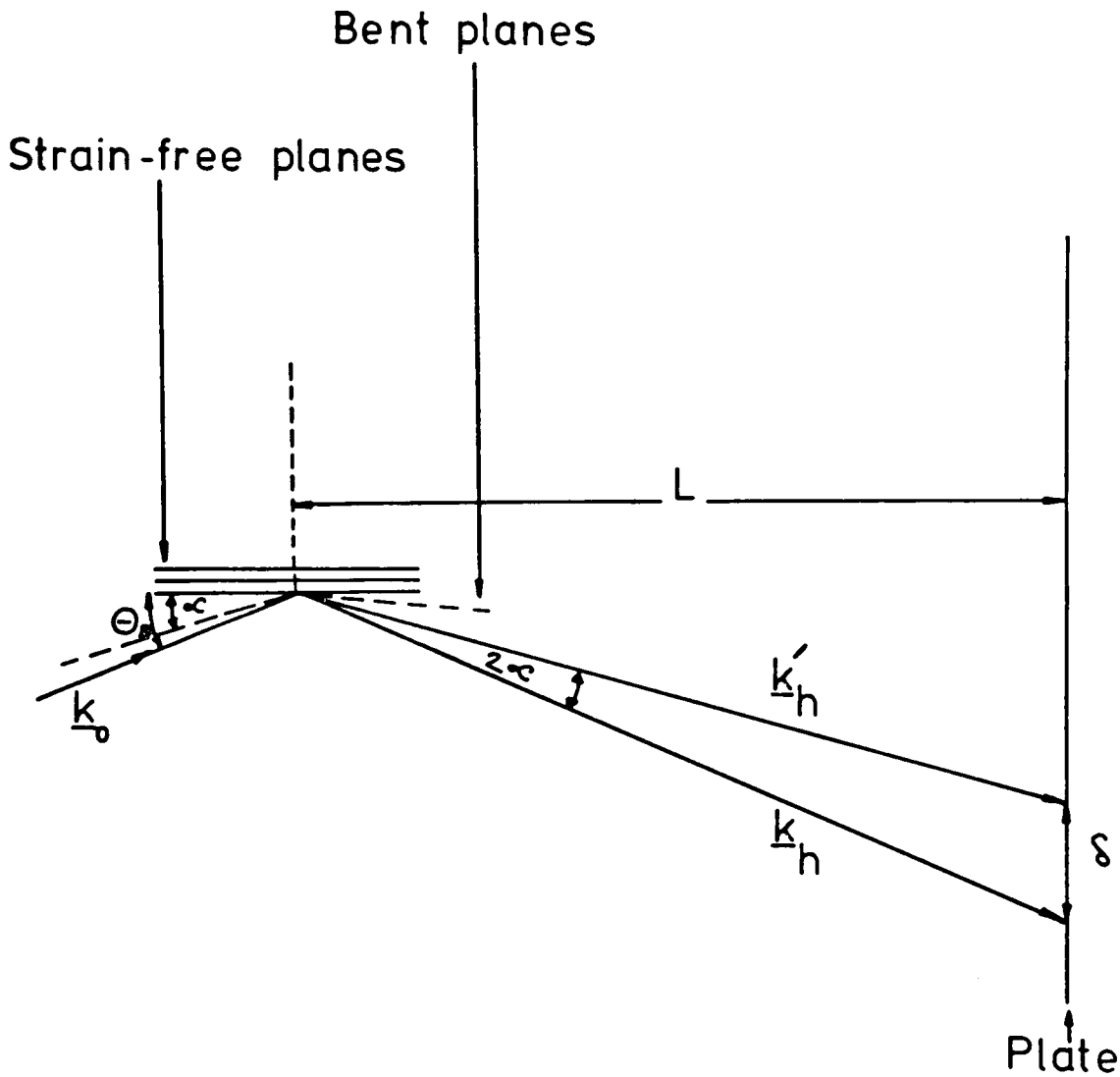
L = specimen to plate distance

Fig. 4.22 The Asterism in Fig. 4.21b was caused by Lattice Plane Bending

If α is the extent of the lattice bending then the strain in the planes is given by:-

$$\text{Tan}\,\alpha = \left(\frac{\delta}{2L}\right)$$

δ = image shift
L = specimen to plate distance
Θ_B = Bragg angle
$\underline{k}_o$ = incident wave-vector
$\underline{k}_h^o$ = diffracted wave-vector from non-strained lattice planes
k_h^1 = diffracted wave-vector from strained lattice planes


Bent planes
Strain-free planes
L
Θ_0
α
2α
$\underline{k}_0$
$\underline{k}'_h$
$\underline{k}_h$
δ
Plate

Measured for Fig. 4.21b, the maximum value of Tanα using L = 20 cm was 0.297% (δ = 1.25 mm). From Fig. 4.15a for a 10" plated crystal, it can be seen that the stress was approximately 100 g/mm^2 for this strain magnitude, i.e. greater than the recorded yield stress and so dislocation would be expected; hence the white line. It is to be further noted that bending would impose the greatest tensile stresses on the outside of the bend and therefore dislocation would occur there first. This fits in well with the observed contrast feature. A final feature to observe in Fig. 4.21b is the termination of the slip bands on this white line along the Bragg surface: but it is impossible to state which occurred first and therefore which sources (i.e. internal or near surface) operated first.

4.5vb Loading the Crystal up to the Yield Point along the 'Elastic Line'

Increasing the stress on the crystal from 12.27 g/mm^2 to 15.1 g/mm^2 (i.e. by 2.83 g/mm^2) produced no discernible change in image contrast as shown in Fig. 4.23a when compared to Fig. 4.21b, and increasing the stress still further to 16.5 g/mm^2 again produced no detectable change in the image. By increasing the stress still further to 17.99 g/mm^2 it was noticed that a white line, similar to the one discussed for the unloaded crystal, had appeared on the rear surface at the dislocated end of the crystal. No slip band activity was noticed. This is interesting because the stress on the glide plane had now increased by 5.72 g/mm^2, i.e. well above the 1.5 g/mm^2 found by Young et al[19] to be necessary to begin dislocation motion. The chromium layer therefore appeared to have an effect on the

Fig. 4.23 Synchrotron Pictures of a Crystal stressed to 22.2 g/mm^2

Note no detectable evidence for dislocation generation within the crystal. A certain amount of surface activity was noticed, e.g. the appearance of a second white line in (d)

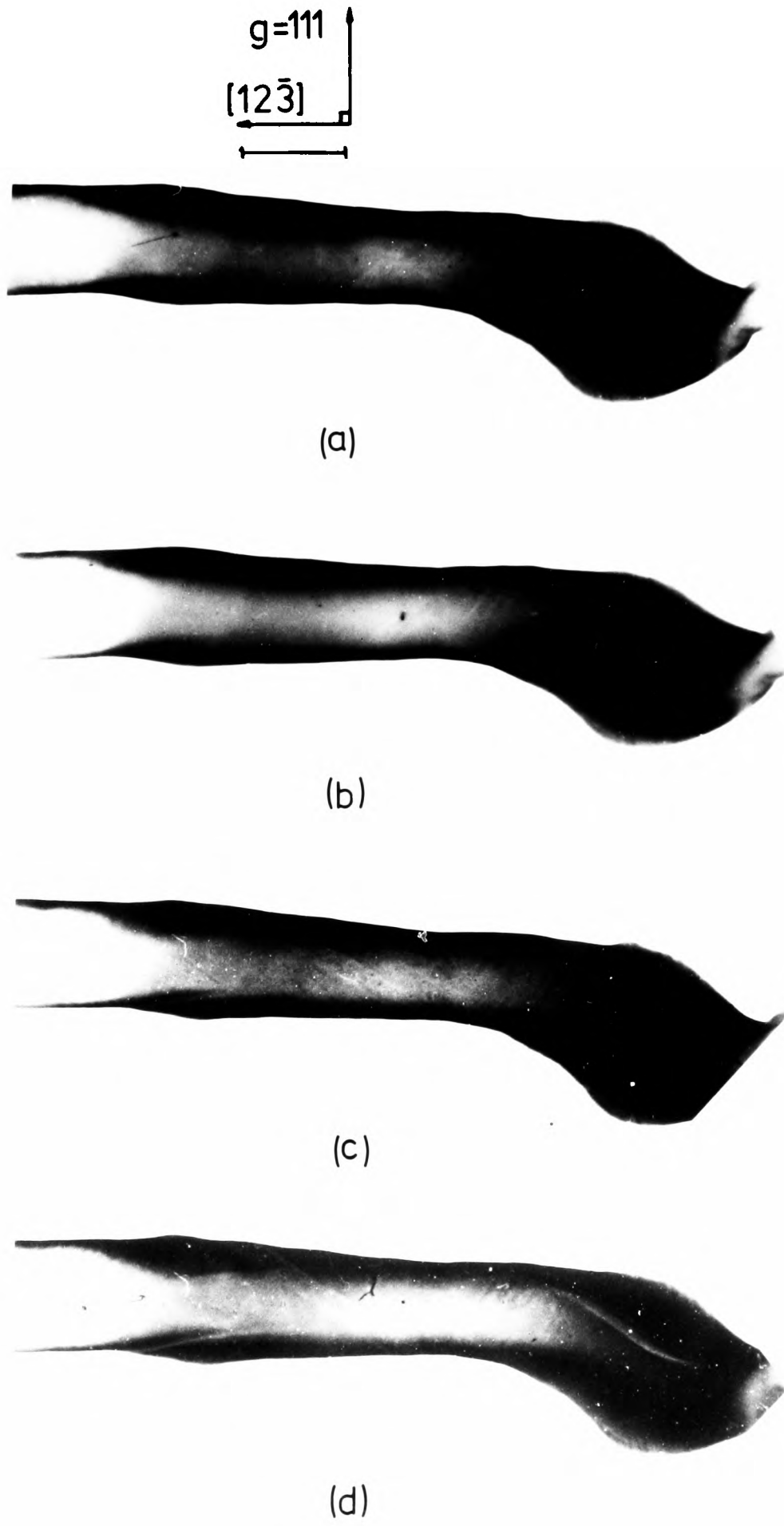
a. Stress = 15.1 g/mm^2

b. Stress = 16.5 g/mm^2

c. Stress = 17.9 g/mm^2

d. Stress = 22.2 g/mm^2

Scale mark = 1 mm


g=111
[12$\bar{3}$]
(a)
(b)
(c)
(d)

nucleated dislocations in the glide bands. Also no evidence for cross-slip was obtained. Minari[26] et al observed cross-slip in copper at very low stresses of the same order of magnitude as those applied here, and they also detected fresh dislocation production at a shear stress of 1.5 g/mm^2. No such evidence was available at this point in this deformation experiment

Upon increasing the stress still further to 22.2 g/mm^2, Fig. 4.23d, the second white line along the rear surface increased in length and there was a small increase in the asterism at this end of the crystal as well. It is therefore clear that the grips were imparting a bending moment to the crystal at this end. This unfortunate trend continued when the stress was increased to 30.9 g/mm^2, Fig. 4.24a, and it was noticed that part of the image from the dislocated end onwards had been completely displaced implying that part of the crystal had been rotated about the tensile axis: obviously the grips were not pulling uniaxially. By carrying out a calculation similar to that for the bending stresses previously it is possible to calculate the magnitude of this lattice rotation. It was found to be 4.7' of arc, and the associated strain was 1.38×10^{-3}. The torsional shear stress would therefore be about 60 g/mm^2 as derived from the stress-strain curve in Fig. 4.15a.

It is interesting to remember that in a normal Lang-Borrmann topography arrangement such lattice rotation would not be allowed, unless the crystal was rocked back onto the diffraction peak; and then only one part of the crystal would diffract. In synchrotron topography, however, such rotations can be accommodated by the technique because of the polychromaticity

of the main beam. From a diffraction standpoint this rotation was useful since it caused the rotated crystal to diffract a slightly shorter wavelength of incident radiation with a slightly lower anomalous absorption coefficient which gave rise to a denser image as shown in Fig. 4.24a. Also absent in Fig. 4.24a is the second white line, either because of the reduction of lattice bending (the asterism had decreased in this region) or as a direct consequence of the rotation stresses counteracting the bending stresses.

When the stress was increased further to 35.1 g/mm^2, Fig. 4.24b, the lattice rotation remained constant; the intensity from the centre of the crystal was slightly reduced; and the second white line reappeared along most of the rear surface of the crystal, together with a small increase in the associated asterism. No new slip bands were noticed and no intra-slip band activity could be detected. At this stress level Kamada and Tanner[10] had noticed a certain amount of dislocation activity on the Lang camera for a dislocation-free copper crystal. Also Pichaud et al[26] had good evidence for cross-slip and Minari[25] et al had detected dislocation generation; and in Young and Sherrill's[19] classic work on in-situ deformation of copper using a Lang Camera it was observed that new dislocations had been generated at sources (unidentified) other than the original grown-in dislocations. Outside the slip bands no such mechanisms were noticed here and inside these bands no activity could be detected.

After the next 12.8 g/mm^2 had been applied so that the shear stress on the glide plane was 47.9 g/mm^2 no change in image contrast could be monitored, Fig. 4.24c. Furthermore,

Fig. 4.24 Synchrotron Pictures of a Crystal stressed from 30.9 g/mm^2 to 47.9 g/mm^2

As shown in (a) lattice rotation had obviously occurred along part of the image since the grips were not pulling uniaxially. No deformation processes which could be isolated to dislocation motion could be detected. Up to this stress level the crystal obviously behaved "quasi-elastically". No direct evidence for cross-slip was found

a. Stress = 30.9 g/mm^2

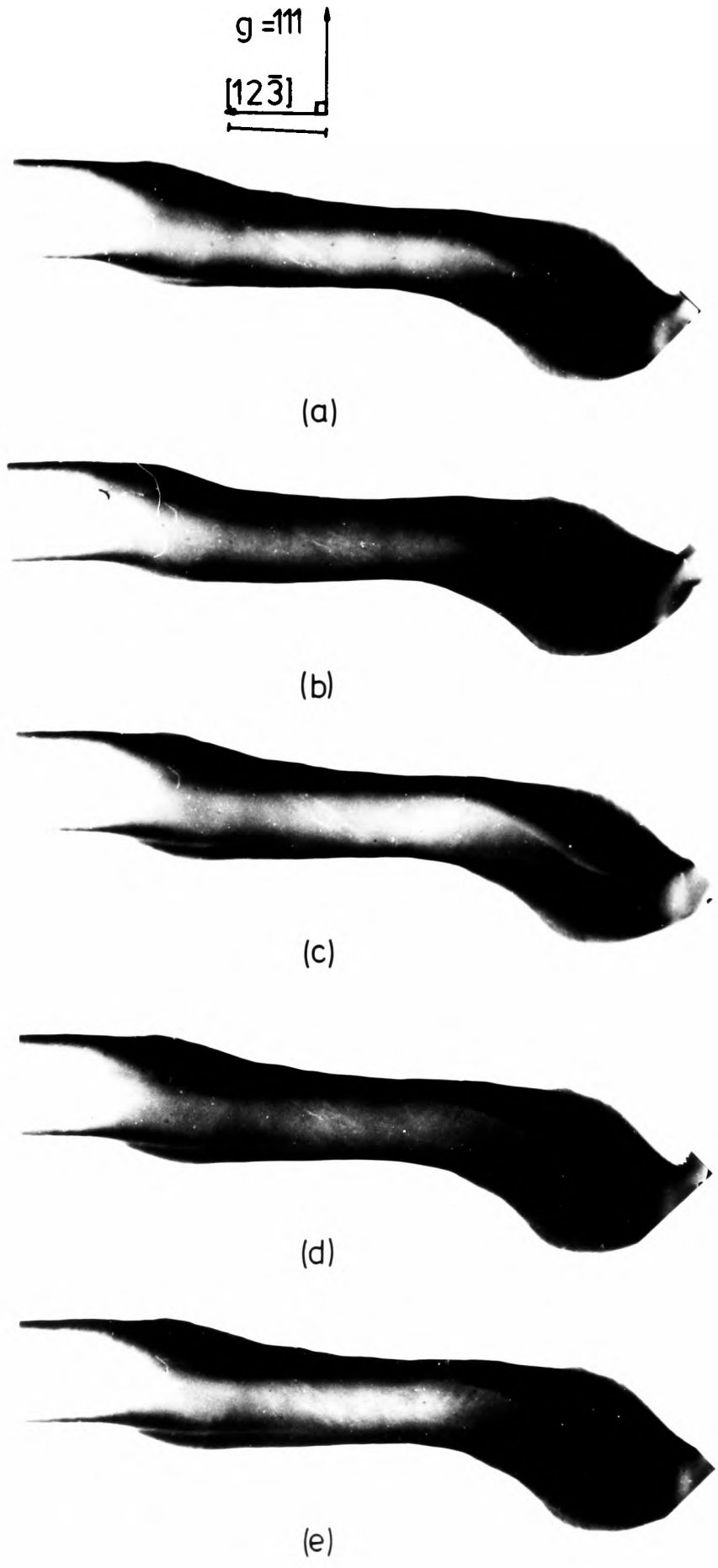
b. Stress = 35.1 g/mm^2

c. Stress = 47.9 g/mm^2

d. Stress = 12.2 g/mm^2

e. Stress = 47.9 g/mm^2

Scale mark = 1 mm


g =111
[12$\bar{3}$]
(a)
(b)
(c)
(d)
(e)

when the load on the crystal had been completely removed no general contrast changes were seen either, as indicated by comparing Fig. 4.24c and Fig. 4.24d. When the stress was again increased to 47.9 g/mm^2, Fig. 4.24e, exactly the same contrast features as shown in Fig. 4.24d and Fig. 4.24c were observed, indicating that the crystal was behaving 'quasi-elastically'. Since slip bands were clearly visible this could not be definitively called elastic behaviour, as dislocation motion within these bands could not be resolved. These topographs are valuable because they show, for the first time, that at the low stresses normally expected to produce cross-slip[19,26] in these low dislocation density crystals, that none was here apparent.

As the stress level was further increased to 65.1 g/mm^2 then to 73.7 g/mm^2 and then to 90.8 g/mm^2, Fig. 4.25, no change in anomalously transmitted intensity was observed until the 90.8 g/mm^2 level. Very diffuse images of slip bands lying along a different direction to the originally observed bands were present. Using the Thompson tetrahedron diagram in Fig. 4.1b, these diffuse lines correspond to the traces of the cross-slip planes $(\bar{1}\bar{1}1)$. The Schmid factor for the $(\bar{1}\bar{1}1)[\bar{1}0\bar{1}]$ system was below that for the primary $(1\bar{1}1)[\bar{1}01]$ system, being 0.349 and 0.465 respectively, and so glide on these planes would not be initially expected. However, in view of the complexity of the imposed stress system, initial glide on all these planes cannot be excluded as the normal Schmid factors are not strictly applicable.

Fig. 4.25 Synchrotron X-ray Pictures of a Crystal stressed from 90.8 g/mm^2 to 150.9 g/mm^2

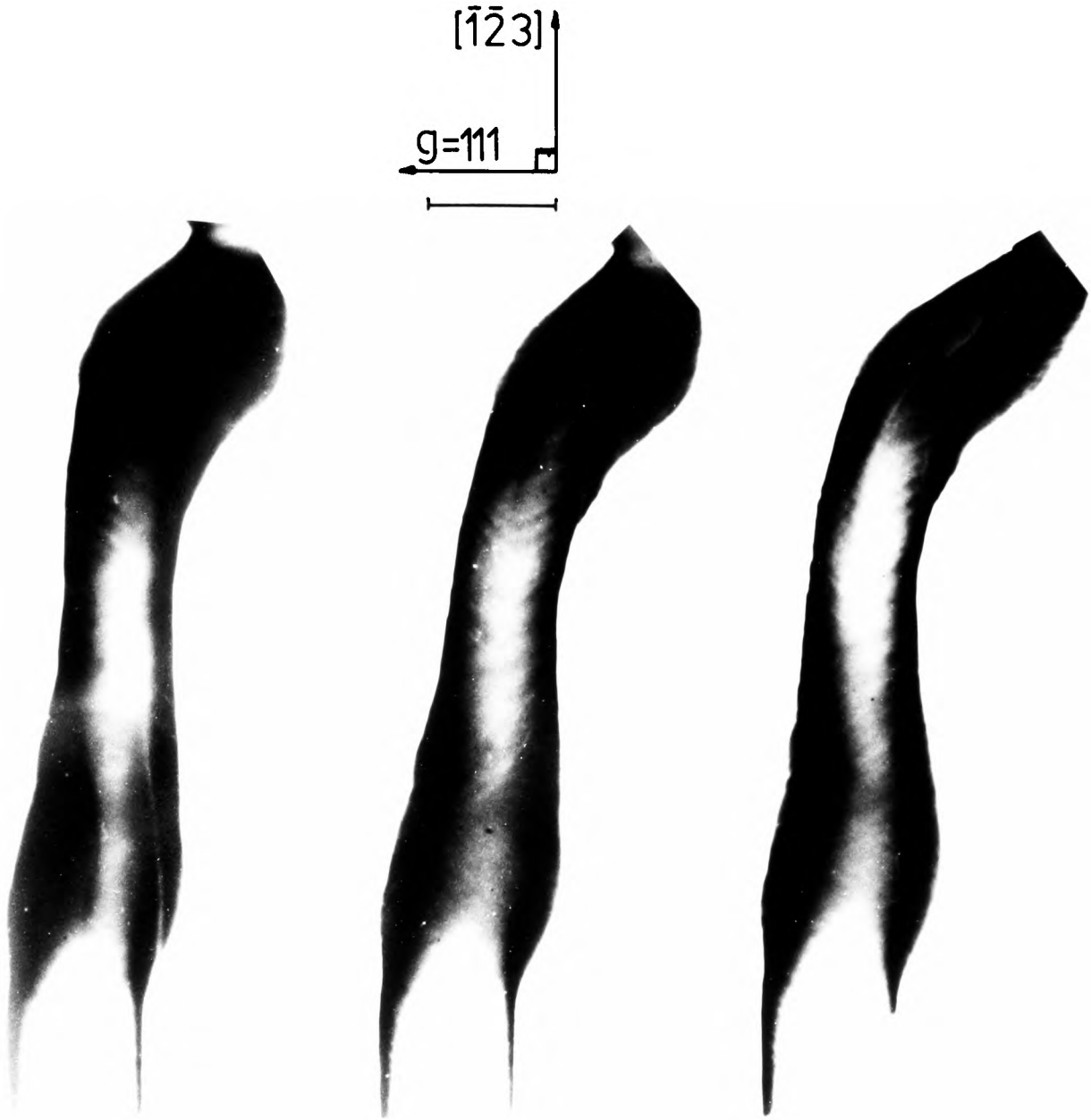
New slip bands were generated at the 90.8 g/mm^2 stress level (this is comparable to the yield stress measured in the Instron for comparable crystals). As the stress increased a herring-bone slip pattern occurred down part of the crystal. Deformation proceeded inhomogeneously.

a. Stress = 90.8 g/mm^2

b. Stress = 116.6 g/mm^2

c. Stress = 150.9 g/mm^2

Scale mark = 1mm



(a) (b) (c)

The asterism effects remained constant throughout these steps, implying that the load imparted to the crystal by the deformation jig was uniaxial during these stages. This 90.8 g/mm^2 stress level, which is the stress corresponding to yielding as evinced by the new slip band generation, is remarkably commensurate with that measured in the Instron for a 10" plated crystal. In this latter case the yield stress was 83.4 $g/mm^2 +^- 5.9$ g/mm^2, from Table 4.1. Moreover, since the new slip bands were a) remote from the originally observed slip bands and b) on a different slip plane, it is clear that the stress measured here was that for new dislocation generation and not that for cross-slip from the old slip bands. Additionally it can now be concluded that this being the case then the surface layer has not affected the production of new dislocations, but it has affected the motion of old ones. This conclusion dovetails well with the conclusion reached after studying the Instron results.

4.5vc Post Yielding Behaviour

Following the next stress increment from 90.8 g/mm^2 to 116.6 g/mm^2 three effects were noticed as depicted in Fig. 4.25b. First, at one end of the crystal an increase in slip band density had occurred; second, the slip band multiplication took place on the two planes $(1\bar{1}1)$ and $(\bar{1}\bar{1}1)$; third, the second white line disappeared at one end of the image. The first observation shows that deformation was proceeding inhomogeneously; whilst the second indicates that the stress was not uniaxially applied; and the third point indicates that the second white

line was associated with dislocations locked at the copper surface which left this region. This last result also indicates that the breakaway stress of these dislocations was comparable to the yield stress of the crystal. Again, no increase in asterism was observed so that the stress increase was uniaxial.

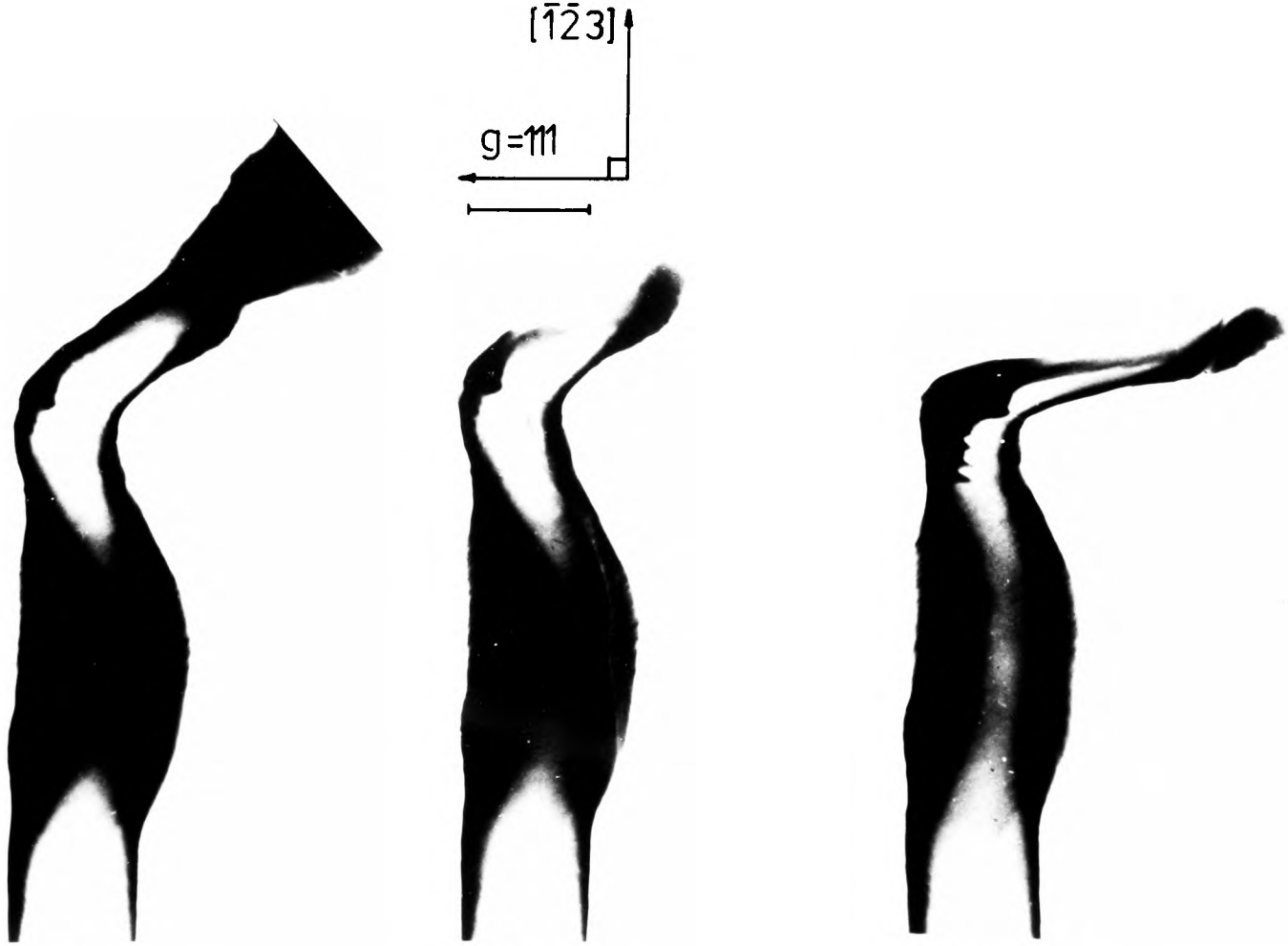
Consequent upon the next stress increment from 116.6 g/mm^2 to 150.9 g/mm^2, Fig. 4.25c, the slip band density increased, but slightly more on the secondary system than on the primary system. Also, a marked increase in contrast from the established slip bands occurred which is a clear indication of intra-slip band activity, i.e. the deformation of the already yielded region proceeded by dislocation motion on existing slip bands; whereas in the non-yielded region slip band initiation was clearly necessary. Deformation was therefore proceeding inhomogeneously down the crystal, on a duplex system, giving rise to a 'herring-bone' slip pattern.

The stress increases beyond this level bent the crystal badly at one end, and no information regarding individual dislocation motion or slip band progression could be gained since the complete crystal had yielded and individual slip bands could not be observed, Fig. 4.26a. It was instructive, however, to release the stress from 163.8 g/mm^2 to 99.4 g/mm^2, Fig. 4.26a, and then to increase it to 163.8 g/mm^2 again. At the centre of the crystal the X-ray intensity increased slightly when the stress was reduced (compare Figs. 4.26a and 4.26b) but when the stress was again increased the intensity of X-rays transmitted through the centre of the crystal fell noticeably, Fig. 4.26c. It was also noticed that at the 99.4 g/mm^2 stress level that a white line reappeared along part of the

Fig. 4.26 Synchrotron X-ray Pictures of a Crystal stressed well beyond the Yield Point

No individual slip bands could now be detected. However, when the stress was raised to 163 g/mm^2 (a) and then lowered to 99 g/mm^2 (b), a slight increase in anomalous transmission occurred from the centre of the crystal. Also a white line appeared along the rear surface. On increasing the stress to 163 g/mm^2 (c) again, the anomalous transmission was reduced and the white line disappeared. These pictures indicate that dislocations piled up at the centre of the crystal and when the stress was relieved they ran back to the surface, giving rise to the loss of X-ray transmission as shown by the white line.

Scale mark = 1 mm



(a) (b) (c)

rear surface of the crystal image, but this disappeared when the stress was again increased to 163.8 g/mm^2. From these observations it can be concluded that a number of dislocations ran back to the surface of the crystal when the stress was partially relieved; hence the white line corresponding to a local loss of anomalously transmitted intensity along the relaxed line of dislocations. When the stress was increased the disappearance of the white line signified the glide of the dislocations back into the crystal, and therefore the reduction of anomalously transmitted wavefields from the centre of the crystal.

4.6 A Review of the Instron and Synchrotron Results

As mentioned earlier the synchrotron work was aimed at clarifying the lattice processes contributing to the particular features of the stress-strain curves derived from the Instron experiments. In part this aim was fulfilled; for example, considerable justification for a lack of dislocation motion below the macroscopically observed yield stress (Figs. 4.23 to 4.25) was obtained, and the onset of yielding was clearly shown to be inhomogeneous, Fig. 4.25. Furthermore, the surface layer was shown to influence the motion of old dislocations (the contrast from old slip bands increased, implying that dislocations could not easily slip out to the surface, Fig. 4.25c) but not the operation of new glide bands (the yield stress from the synchrotron work was commensurate with that from the Instron studies, i.e. 90 g/mm^2, Fig. 4.25a). Of additional interest is the conclusion that the stress applied below the macroscopic yield stress gave rise to no direct evidence for cross-slip; and that the yield stress recorded was a measure of the stress required for new slip line generation therefore.

Since the resolution of the technique was ≈ 1 μm; and since the deformation jig used in the synchrotron studies imparted both torsional and bending stresses to the crystal, it was impossible to locate the dislocation sources that would have operated first had the applied stress been purely uniaxial. The evidence available (e.g. Fig. 4.24c and Fig. 4.25a,b) from the synchrotron work, clearly showed that the 'surface region' sources were encouraged to operate first because of the complex stress field which the crystal experienced in the deformation jig.

This being the case, in Fig. 4.26a,b,c the diffraction contrast evidence can be easily interpreted in terms of dislocation motion and interaction. Since slip occurred on two systems (fig. 4.25b) for which the deformation indices were $(1\bar{1}1)\,[\bar{1}01]$ (primary system) and $(\bar{1}\bar{1}1)\,[101]$ (secondary system) as derived from the relvant Schmid factors, Fig. 4.1, it is possible for the dislocations to dissociate into partials according to the following reactions:-

$$\frac{a}{2}[\bar{1}01] \longrightarrow \frac{a}{6}[\bar{2}\bar{1}1] + \frac{a}{6}[\bar{1}12] \qquad (1\bar{1}1) \text{ Primary Plane}$$

$$+$$

$$\frac{a}{2}[101] \longrightarrow \frac{a}{6}[112] + \frac{a}{6}[2\bar{1}1] \qquad (\bar{1}\bar{1}1) \text{ Cross-slip Plane}$$

$$\downarrow$$

$$\frac{a}{6}[\bar{1}03]$$

The first two partial dislocations can therefore combine to form a stair-rod dislocation of Burger's vector $\frac{a}{6}[\bar{1}03]$ which has a lower energy than the sum of the two partials. Since such a dislocation is sessile it is to be expected that pile-ups behind the stair-rod would occur at the centre of the crystal where the

two slip systems cross as shown in Fig. 4.25b. Extending this analysis to include Fig. 4.26a,b,c the white line in 'b' can be argued to correspond to the equilibrium position of the dislocations, normally piled-up at the stair-rods at the centre of the crystal, once the applied stress had been reduced causing them to relax. In a normal Instron test, double-slip from surface sources in these crystals would not be expected initially and so this work hardening mechanism must be restricted to this specific synchrotron study.

Regarding the Instron work hardening behaviour of these crystals the synchrotron study could only provide a little evidence to aid the interpretation of the curves. These curves can only be analysed in a superficial way therefore, and from the available information it will be assumed that the operational dislocation sources were internal. Additionally, the experimental conclusions reached by other workers (and reviewed, amongst others, by Hirsch[59], Mitchell[60], and Kovacs and Zsoldos[49]) for stage I deformation in copper (without a surface layer) are best summarised first.

i. The displacement of dislocations emitted by sources is approximately constant, and large compared to the average distance of the sources from one another. A number of dislocations reach the surface.

ii. Few lattice obstacles occur and may be neglected.

iii. Within each glide plane, the distance between neighbouring dislocations is larger than source to source distances. Hence, pile-ups are unexpected.

iv. The number of active sources is a constant, except during the v. initial stages of deformation when they increase continuously with time.

What has been monitored in this work has been the modification of the stage I behaviour by the crystal surface layer and the general shape of the stress-strain curves can be accounted for in terms of this layer.

At yielding the internal sources operated inhomogeneously (i.e. continuously with time, iv above) as shown in Fig. 4.25a,b,c and generated dislocations which ran unhindered to the surface of the copper. The normal egress of dislocations at this surface was impeded by the chromium layer causing dislocation pile-ups. (The tentative evidence for this conclusion from Fig. 4.25c has previously been discussed.) As shown by Stroh[61] the pile-ups cause shear and normal stresses ahead of the pile-up line in the obstacle (here, this is the surface layer) given by:-

$$\tau = \beta \tau_s \left(\frac{L}{r}\right)^{\frac{1}{2}} \qquad 4.20$$

$$\sigma = \frac{3}{2}\left(\frac{L}{r}\right)^{\frac{1}{2}} \tau_s \sin\Theta \cos\frac{\Theta}{2}$$

Where,

τ = shear stress in the film
β = constant ≈ 1
τ_s = shear stress on the glide plane
L = pile-up length
r = distance into the film (obstruction) at an angle Θ to the pile-up line
σ = normal stress in the film

Typically,

L = 0.5 mm (i.e. half the crystal diameter)
τ_s = 90 g/mm^2
r = maximum value of 1 μm

Consequently, at the free surface an induced shear stress in the chromium from the pile-up would be $\approx$1850 g/mm^2, rising towards the end of the pile-up. The most highly stressed plane in the surface layer, as shown by Stroh[61], would be at an angle of 70.5° to the pile-up line. This effect has three ramifications:

first, the chromium layer can be dislocated by the pile-up stresses; second, the source operation can be inhibited by the back stress from the pile-up; third, the chromium and copper can de-adhese. Therefore, if the chromium does not dislocate and the two layers do not de-adhese the copper would work harden rapidly as the sources were suppressed. This would explain the rapid work hardening rate during the immediate post yield section of the curves in Fig. 4.12 and Fig. 4.13. It is to be further noted that very few dislocations would actually exist in the pile-up. Typically the number, n, piled-up from one source on one slip plane would be ≈15 to 25 as calculated from[62]:-

$$n = \frac{k \pi \tau_s L}{4\mu b} \qquad 4.21$$

k = (1-ν) for edge dislocations
k = 1 for screw dislocations
ν = Poisson's ratio
τ_s = shear stress on the glide plane
L = pile-up length
b = Burger's vector

As the load was increased either the pile-up would break loose and cause dislocation of the chromium, or de-adhesion of the Cu-Cr interlattice would take place, or new sources on new glide planes would operate. Each of these processes would be sudden, causing rapid dislocation motion and therefore a decrease in the stress required to maintain the imposed strain rate. Hence, serrations in the plastic flow region of the stress-strain curve would be expected (because of the low dislocation density), as shown previously in Figs. 4.14a and 4.15a. In other researchers' work serrated flow would not be expected because of the random dislocation distribution, and consequently source position and type throughout the crystal. Any suppression

of one type and position of source could be compensated for by increased activity from other sources as the applied stress increased.

In the early stages of work hardening the above three possibilities reduce to one because as shown originally by Stroh[61] the slip line must contain ≈ 1000 dislocations if cracks in the obstacle-matrix interface are to occur. Since only then will the stress at the pile-up tip be sufficiently high ($\approx \mu/_{30}$) to initiate a crack by the coalescence of the first few piled-up dislocations. For similar reasons slip in the chromium layer would not be expected during the initial work hardening rate region. The serrations during this part of the plastic flow curve are therefore considered to be associated with new source operation on the same primary glide system but at different sites. Correspondingly, little difference in Θ_I values would be expected for 5 seconds and 10 seconds plated crystals, and as noted experimentally.

The decrease in work hardening rate between region i and region ii of the stress-strain curves is considered to be due to slip initiation on the secondary slip system as shown in the synchrotron work, Fig. 4.25b. This would provide a greater number of mobile dislocations and therefore decrease the stress required to maintain the strain rate. At the same time pile-up of these secondary dislocations would be expected at the chromium layer, causing secondary source suppression by back stresses, as before, and therefore new sources would need to operate to maintain the strain rate. Serrated flow would still be expected. Hence, during region ii a number of competitive dislocation processes would occur, but the greater number of available dislocations belonging to discrete slip bands (Fig. 4.25a,b,c) would decrease the work hardening rate.

It is instructive to note from equation 4.15 that the ratio of the shear stresses on the primary and secondary slip systems was ≈ 1.38. Therefore, when slip on the secondary system by the internal source operation mechanism alluded to earlier, began at ≈ 84 g/mm^2 (Fig. 4.15a) the stress on the primary system would be ≈ 124 g/mm^2. From Fig. 4.13a it is seen that the change in work hardening rates started at ≈ 115 g/mm^2 which provides good foundation for the argument that the work hardening rate decrease was associated with slip on the secondary slip system.

The decrease in work hardening rate between regions ii and iii is considered to arise from crack formation at the chromium-copper interface, thereby releasing dislocation pile-ups and, therefore, causing unimpeded operation of suppressed sources belonging to discrete slip planes. This is argued to be so because the complete crystal would be heavily dislocated and many slip lines would be present. Optical and scanning electron microscopy failed to reveal these slip lines on the surface of the chromium because the slip step height was so small (estimated to be ≈ 100Å). Typically the shear stress on the glide planes during this region was ≈ 150 g/mm^2, Fig. 4.13a, which, using expression 4.21, would place approximately 40 dislocations in each pile-up. As noted in a similar case by Stroh[61], it is possible to achieve the 1000 required dislocations to produce the stress required for crack formation, by dislocations from adjacent slip lines contributing to a total pile-up stress as a result of correctly summing the individual pile-up stresses. In this case approximately 25 slip lines would be needed for the

mechanism to work. Once cracks of this type had been initiated dislocation loss to the surface would be decreasingly impeded and the work hardening rate would fall to that for an initially unplated, dislocated crystal as noted in Section 4.4iiib. Extra dislocation sources, once suppressed would contribute to the decrease in work hardening rate.

4.7 Conclusions

a. Plating a dislocation-free copper crystal with chromium imparts a residual stress on the copper at both room and 55C plating temperatures.

b. Dislocation-free chromium plated copper crystals exhibited a yield point. This yield point was not affected in any noted way by plating thickness. Dislocated crystals did not show a yield point.

c. The work hardening rate of the crystals was initially high ($\approx$18 kg/mm^2), and then progressively decreased to a level commensurate with that measured by other workers, i.e. $\approx$3 kg/mm^2 for originally dislocated crystals.

d. A closer analysis of the early parts of the stress-strain curves revealed a serrated plastic flow curve for dislocation-free, plated crystals only, with a serration magnitude comparable to the yield drop of the crystal. This phenomenon was explained in terms of new internal source operation.

e. The yield stress measured from the synchrotron experiment was comparable to that measured in the Instron, i.e. $\approx$ 90 g/mm^2 for a 10" plated crystal.

f. Below this macroscopically measured yield stress no dislocation motion or generation was observed which could be directly attributable to the application of a uniaxial stress to the crystal. Due to bending and rotational stresses dislocations were generated at the surface of the crystal.

g. No information was gained concerning the likely origin of dislocations at the onset of plastic flow. Dislocation sources could therefore not be unambiguously identified.

h. The surface layer affected the motion of already existing dislocations but not the production of new dislocations.

i. Yielding was inhomogeneous and occurred on two slip systems due to non-uniaxial crystal loading in the synchrotron experiment.

j. The surface layer impedes source operation, through pile-up back stresses, once the source begins operation. This causes new source operation at different sites on the same glide planes giving rise to serrated plastic flow. Double slip can be invoked to account for the decrease in work hardening rate from region i to ii.

k. The decrease in work hardening rate from region ii to iii is considered to occur by crack initiation at the chromium copper interface, causing pile-up release and re-operation of the suppressed sources associated with the pile-ups.

l. No information regarding the likely dislocation mechanisms giving rise to the magnitude of the serrated flow nor the strain extent of the same could be gained.

5.8 Suggestions for Further Work

i. It would be interesting to repeat the synchrotron experiment using a more automated system. Also, a better design of tensile-jig would be useful which would not impose torsional and rotational stresses on the crystal. Then it would be possible to decide whether double slip really was occuring in these crystals or not at the assumed stress levels.

The automation part of this suggestion has been started. This is a necessary part of any future study because although the exposure time required for the X-ray plates was only 30 seconds, the total plate turnround time was ≈ 3 minutes, because of the need to clear the experimental area of personnel and open the shutter.

To promote rapid insertion of the plates into and out of the diffracted beam a slide projector has been used in reverse as follows. The focussing lens was removed and a hollow brass cylinder was inserted in its place to eliminate X-ray damage to the plastic casing. Each X-ray plate (2" x 2") was mounted in a frame and placed consecutively in one of the 80 slide slots of the horizontally mounted circular slide magazine. The frame was necessary to prevent the thin plates from jamming. The loaded projector was then encased in a light tight black plastic bag and positioned in the experimental area so that an X-ray plate would receive a particular X-ray reflection when moved into the normal slide position: the quartz halogen lamp was removed. A lead screen was placed in front of the projector to cover all but the brass tube so that polymer degradation by the main beam could be eliminated.

The experiment could then be completely automated and remotely controlled from outside the experimental area: the in-situ deformation being controlled from a safe distance, and multiple exposures were effected by advancing the slide magazine by one. This latter operation was found to take about $1\frac{1}{2}$ seconds, meaning that the plate changing time could be significantly reduced. This apparatus could be easily used for in-situ deformation studies once the tensile-jig has been drastically improved.

ii. It would be worthwhile to deform dislocation-free or dislocated copper crystals electro-evaporated with chromium in the high voltage electron microscope. This would give direct evidence for the dislocation processes outlined previously as being operative at various stages in the deformation. Electro-evaporation of the chromium would be necessary because of the need to deposit only a very thin layer and so allow passage of the electron beam.

iii. More information regarding the effect of plating thickness on flow stress values is needed. This would best be done using a combined Instron, synchrotron and electron microscope study.

CHAPTER IV REFERENCES

1. G. Dubpernell, in "Modern Electroplating", 3rd Edition, p. 87, Ed. F. A. Lowenheim

2. J. Garstone, R. W. K. Honeycombe and G. Greetham, Acta Met., 4, 485, 1956

3. J. Diehl, Z. Metallkunde, 47, 331, 1956

4. F. W. Young, Jr., J. Appl. Phys., 33, 963, 1962; "Dislocation Dynamics", p. 313, 1968, New York: McGraw-Hill

5. T. E. Mitchell, Ph.D. Thesis, University of Cambridge, 1962

6. R. Berner, Z. Naturf., 15a, 689, 1960

7. J. Diehl and R. Berner, Z. Metallkunde, 51, 522, 1960

8. J. S. Askearn, J. P. Monaghan and J. W. Mitchell, Rev. Sci. Instr., 41, 1853, 1970

9. "Metals Reference Book", Fourth Edition, III, p. 1086, Ed. C. J. Smithells, Publ.

10. K. Kamada and B. K. Tanner, Phil. Mag., 29, 309, 1974

11. H. Poritsky, Physics, 5, 406, 1934

12. C. J. Humphreys, Ph.D. Thesis, University of Cambridge, 1967

13. A. H. Cottrell, "An Introduction to Metallurgy", p. 308, 1967, Publ. Ed. Arnold

14. J. F. Nye, "Physical Properties of Crystals", p. 43, 1969, Publ. Oxford U.P.

15. E. Schmid and W. Boas, "Plasticity of Crystals", p. 59, 1968, Publ. Chapman and Hall

16. J. R. Patel and A. R. Chaudhuri, J. Appl. Phys., 34, 2788, 1963

17. H. Alexander and P. Haasen, Solid St. Phys., 22, 27, 1968

18. G. L. Pearson, W. T. Read and W. L. Feldman, Acta Met., 5, 181, 1967

19. F. W. Young and F. A. Sherrill, J. Appl. Phys., 42, 230, 1971

20. J. D. Livingston, J. Appl. Phys., 31, 1071, 1960

21. A. S. Argon and W. T. Brydges, Phil. Mag., 18, 817, 1968

22. F. W. Young, J. Appl. Phys., 33, 963, 1962

23. F. W. Young, J. Appl. Phys., 32, 1815, 1961

24. F. W. Young, J. Appl. Phys., 33, 3553, 1963

25. F. Minari, B. Pichaud and L. Capella, Phil. Mag., 31, 275, 1975

26. B. Pichaud and F. Minari, Phil. Mag., 34, 1121, 1976

27. P. Petroff and J. Washburn, J. Appl. Phys., 37, 4987, 1966

28. J. Marukawa, J. Phys. Soc. Jap., 22, 499, 1967

29. A. Kelly, Strong Solids, O.U.P., 1966

30. S. S. Brenner, J. Appl. Phys., 28, 1023, 1957

31. S. Z. Bokstein and I. L. Svetlov, Soviet Phys. Solid St., 7, 2697, 1966

32. M. N. Shetty, J. Phys. Soc. Jap., 24, 1264, 1968

33. G. H. Neugebauer, Product Eng., 14, 82, 1943

34. J. Friedel, "Dislocations", 1964, Pergamon Press

35. F. C. Frank and W. T. Read, "Symposium on Plastic Deformation of Crystalline Solids", 1950, p. 44 (Held at Carnegie Institute of Technology, Pittsburgh)

36. J. C. Fisher, Trans. A.I.M.E., 194, 531, 1952

37. R. Roscoe, Phil. Mag., 21, 399, 1936
R. Roscoe, Nature, 133, 912, 1934

38. S. Harper and A. H. Cottrell, Proc. Roy. Soc., B63, 331, 1950

39. J. Takamura, Mem. Fac. Eng. Kyoto Univ. 18(3), 255, 1956

40. T. Takasugi and O. Izumi, Acta Met., 24, 1107, 1976
T. Takasugi and O. Izumi, Acta Met., 23, 1111, 1975

41. R. M. Johnson, Scripta Met., 8, 965, 1974

42. E. N. Da C. Andrade and C. Henderson, Phil. Trans. Roy. Soc., (A), 244, 177, 1951

43. F. D. Rosi, Acta Met., 5, 348, 1957

44. A. K. Head, Phil. Mag., 44, 92, 1953
D. M. Barnett, Acta Met., 15, 589, 1967

45. J. C. Bilello, Scripta Met., 4, 493, 1970

46. D. R. Brame and T. Evans, Phil. Mag., 3, 971, 1958

47. C. S. Barrett, Acta Met., 1, 2, 1953

48. J. Pridans and J. C. Bilello, Acta Met., 20, 1339, 1972

49. I. Kovacs and L. Zsoldos, "Dislocations and Plastic Deformation" Pergamon Press, 1973, p. 214

50. Z. S. Basinski, Phil. Mag., 4, 393, 1959

51. J. Schwinger, Phys. Rev., 75, 1912, 1949
See also, R. P. Godwin, Springer Tracts, Mod. Phys., 51, 1, 1969

52. T. Tuomi, K. Naukkarinen and P. Robe, Phys. Stat. Sol. (a), 25, 93, 1974
See also the first synchrotron topography paper:
T. Tuomi, K. Naukkarinen, E. Lawila and P. Robe, Acta Polytech. Scand., Ph100, 1, 1973

53. M. Hart, J. Appl. Cryst., 8, 436, 1975

54. A. Guinier and J. Tennevin, Acta Cryst., 2, 133, 1949
For the reflection version of this technique read:
L. G. Schulz, J. Metals, 200, 1082, 1954

55. J. H. Beaumont and M. Hart, J. Phys. E, 7, 823, 1974

56. K. Codling, Rep. Prog. Phys., 36, 541, 1973

57. R. W. James, "The Optical Principles of the Diffraction of X-rays", Publ. Bell and Sons, 1948, p. 269

58. "International Tables for Crystallography", 1962, Kynoch Press

59. "The Physics of Metals", 2, C.U.P., 1975

60. T. E. Mitchell, "Dislocations and Plasticity in Single Crystals of F.C.C. Metals and Alloys". Cavendish Laboratory, Cambridge, Internal Report

61. A. N. Stroh, Proc. R. Soc., A223, 404, 1954
A. N. Stroh, Proc. R. Soc., A232, 548, 1955

62. J. D. Eshelby, F. C. Frank and F. R. N. Nabarro, Phil. Mag., 42, 351, 1951